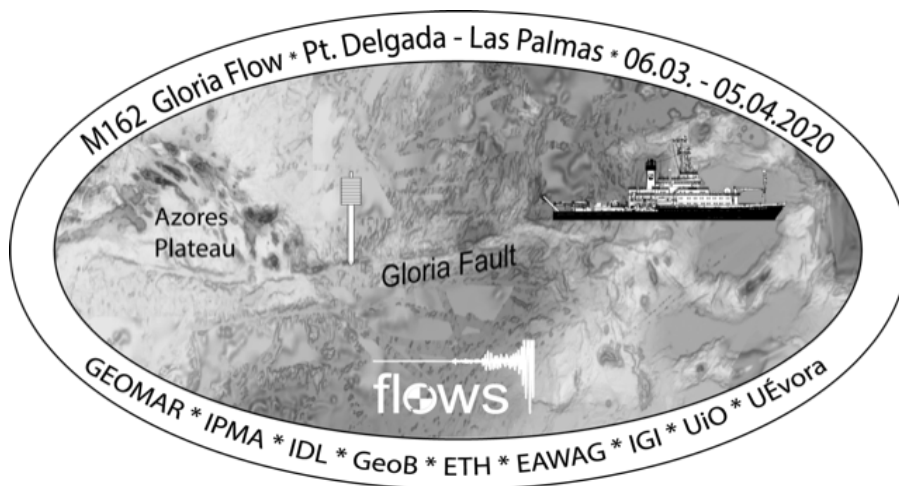METEOR Berichte

Exploring subsurface fluid flow and active dewatering along the oceanic plate boundary between Africa and Eurasia (Gloria Fault)

Cruise No. M162

06.03.2020 – 11.04.2020

Ponta Delgada (Portugal) – Emden (Germany)

GLORIA-FLOW

C. Hensen, H. Adao, S. Arn, L. Batista, L. Belosa, A. Bodenbinder, S. Cherednichenko, B. Domeyer, J. Duarte, C. Glombitza, N. Kaul, M. Koppe, J. Li, V. Liebetrau, T. Müller, P. Nogueira, M. Nuzzo, A. Petersen, M. Schmidt, J.-N. Schmidt, T. Schmidt, K. Sroczynska, M. Stelzner, P. Terrinha, N. Warnken, U.W. Weber

Chief Scientist: Christian Hensen

GEOMAR Helmholtz-Zentrum für Ozeanforschung Kiel

2020

Table of Contents

1   Cruise Summary

1.1   Summary in English

R/V Meteor cruise M162 was conducted as a systematic continuation of ongoing work dedicated to understand if and how fluid flow through crust and sediments continues along transform-type plate boundaries and fracture zones away from mid-ocean ridges and continental margins. Central target was the Gloria Fault in the central Northeast Atlantic. Previous findings along the eastern continuation of the Gloria Fault revealed fault-controlled fluid advection and mud volcanism along strike-slip faults in the Horseshoe Abyssal Plain and the Gulf of Cadiz, where fluid geochemistry revealed the admixture of fluids from deeply buried oceanic crust and oldest sediments on top of it. The Gloria Fault itself is an old, reactivated, and seismically active oceanic fracture zone. During M162 a systematic survey along the main trace of the Gloria Fault between the Azores Plateau and the Madeira-Tore Rise was carried out, including sub-bottom profiler surveys, heat flow transects, gravity corer sampling, as well as video-guided CTD and multicorer deployments. In accordance to recently recorded seismic activity along the fault, there is evidence for tectonic motion both in sub-bottom profiler records and sediment cores. Heat flow measurements revealed values significantly elevated above the background in many places, predominantly along the main fault trace and other active faults. In a number of places fluid geochemistry revealed enhanced diagenetic processes in the sediments, implying the potential relation to upward-directed fluid flow. In summary, cruise M162 revealed the first complementary data set on heat flow and fluid geochemistry along an oceanic fault zone, which will further our understanding on themes like the alteration of oceanic lithosphere and crust-ocean element exchange.

1.2   Zusammenfassung

Wesentliches Ziel der R/V Meteor Reise M162 war es, die Existenz von Fluidaustritten am Meeresboden im Bereich von Transformstörungen und Bruchzonen - außerhalb der bekannten Gebiete an mittelozeanischen Rücken und Kontinentalrändern – zu erkunden. Das zentrale Arbeitsgebiet war dabei die Gloria Störung im östlichen Nordatlantik. Vorausgegangene Untersuchungen entlang der östlichen Verlängerung der Gloria Störung, im Bereich der „Horseshoe" Tiefsee-Ebene sowie des Golfes von Cádiz, hatten gezeigt, dass dort der Aufstieg von Fluiden aus der ozeanischen Kruste sowie den ältesten Sedimentablagerungen an Blattverschiebungen gebunden ist. Die zentrale Gloria Störung stellt eine reaktivierte, seismisch aktive Bruchzone dar. Auf der Reise M162 wurden systematische Erkundungsarbeiten entlang der Hauptstörungslinie zwischen dem Azorenplateau und dem Madeira-Tore Rücken durchgeführt, die im westlichen Untersuchungen des Meeresbodens mit dem Parasound-System, Wärmestrommessungen, Sedimentkern-Beprobungen sowie videogesteuerte Probenahmen mit der CTD und dem Multicorer umfassten. Hochauflösende, seismische Daten und Beobachtungen an Sedimentkernen zeigen dabei eindeutige Hinweise auf rezente tektonische Aktivität. Die Wärmestromwerte sind vielfach im Vergleich zu Erwartungswerten erhöht. Darüber hinaus weisen erste Ergebnisse der Porenwasser-Geochemie an einigen Kernlokationen auf diagenetische Veränderungen hin, die mit Fluidaufstieg in Verbindung stehen könnten. Zusammenfassend ist zu sagen, dass insbesondere der einzigartige, komplementäre Datensatz von Wärmestrom und Porenwasser-Geochemie an einer ozeanischen Bruchzone zu einem besseren Verständnis von Krustenalteration und dem möglichen Einfluss auf globale Stoffhaushalte beitragen wird.

2　　Participants

2.1　　Principal Investigators

Name	Discipline	Institution
Dr. Christian Hensen	Geochemistry	GEOMAR
Dr. Pedro Terrinha	Geology, Sedimentology	IPMA
Dr. Norbert Kaul	Heat flow	GeoB
PD Dr. Mark Schmidt	CTD, Gas geochemistry	GEOMAR
Dr. Clemens Glombitza	Microbiology	ETH
Dr. Helena Adao	Benthos Biology	MARE - UÉvora

2.2　　Scientific Party

Name	Discipline	Institution
Dr. Christian Hensen	Chief Scientist, Geochemistry	GEOMAR
Dr. Pedro Terrinha	Geology, Sedimentology	IPMA
Dr. Joao Duarte	Geology, Tectonics	IDL
Dr. Pedro Miguel Nogueira	Sedimentology, Petrology	UÉvora
Dr. Luis Batista	Geology, Hydroacoustics	IPMA
Lea Belosa	Geology, Hydroacoustics	CEED-UIO
Bettina Domeyer	Geochemistry	GEOMAR
Thilo Schmidt	Geochemistry	GEOMAR
Andrea Bodenbinder	Geochemistry	GEOMAR
Dr. Volker Liebetrau	Isotope Geology	GEOMAR
PD Dr. Mark Schmidt	CTD, Gas geochemistry	GEOMAR
Dr. Thomas Müller	CTD, Gas geochemistry	GEOMAR
Dr. Norbert Kaul	Heat Flow	GeoB
Jan-Niklas Schmidt	Heat Flow	GeoB
Niklas Warnken	Heat Flow	GeoB
Dr. Clemens Glombitza	Microbiology	ETH
Jiaqi Li	Microbiology	ETH
Silvan Arn	Microbiology	ETH
Asmus Petersen	Coring	GEOMAR
Sergiy Cherednichenko	Video	GEOMAR
Matthias Koppe	Hydroacoustics	GEOMAR
Dr. Marianne Nuzzo	Geochemistry	IGI Ltd.
Dr. Helena Adao	Benthos Biology	MARE - UÉvora
Dr. Katarzyna Sroczynska	Benthos Biology	MARE - UÉvora
Ulrich Wolfgang Weber	Noble gas geochemistry	Eawag, UIO
Martin Stelzner	Bordwetterwarte	DWD

2.3　　Participating Institutions

GEOMAR	Helmholtz-Zentrum für Ozeanforschung Kiel, Germany
CEED-UIO	Centre for Earth Evolution and Dynamics, University of Oslo, Norway
DWD	Deutscher Wetterdienst, Geschäftsfeld Seeschifffahrt

EAWAG	Eidgenössische Anstalt für Wasserversorgung, Abwasserreinigung und Gewässerschutz, Dübendorf, Switzerland
ETH Zürich	Eidgenössische Technische Hochschule Zürich, Switzerland
GeoB	Fachbereich 5 – Geowissenschaften, Universität Bremen, Germany
IGI-Ltd.	Integrated Geochemical Interpretation, Bideford, Devon, Great Britain
IPMA	Instituto Portugues do Mar e da Atmosfera, Lisbon, Portugal
IDL	Instituto Dom Luiz, University of Lisbon, Portugal
MARE - UÉvora	Marine and Environmental Sciences Centre - University of Évora, Portugal

3   Research Program

3.1   Description of the Working Area

The major working area of cruise M162 was the Gloria Fault (located between the Azores Plateau in the west and the Madeira-Tore Rise in the east; Fig.3.1), which is representing a major section of the Azores-Gibraltar Fracture Zone (AGFZ). The AGFZ itself corresponds to the set of faults that define the plate boundary between African and Eurasia in the North Atlantic. The AGFZ extends for more than 2300 km, from the active oceanic spreading centre of the Mid-Atlantic Ridge across the East Central Atlantic all the way to the Southwest Iberia, where it connects to the Gibraltar Arc (Terrinha et al., 2009; Duarte et al., 2011, 2013; Zitellini et al., 2009). The Gloria Fault corresponds to the discrete, linear transform segment of the Eurasia-Africa plate boundary and its trace is clearly depicted on the ocean floor bathymetry and trends East-West. The Gloria Fault segment is characterized almost exclusively by dextral strike-slip fault mechanisms and is seismically active (Krueger et al., 2020), including high-magnitude events of up M=8.4 (Buforn et al 1988). Along the major trace line of the Gloria Fault, a number of distinct working areas (WA) 2-6 had been identified for detailed investigation on M162. In addition to the initially proposed work plan, WA1 (located in the Hirondelle Basin, NW of São Miguel) was added to the work schedule. Pore water data from sediment cores in this area obtained on cruise M141 provided evidence for ongoing hydrothermalism and fluid flow in the subsurface (Schmidt et al., 2019). Hence, some complementary work was dedicated to examine this working area within the context of obtaining a more comprehensive understanding of fluid flow along the AGFZ.
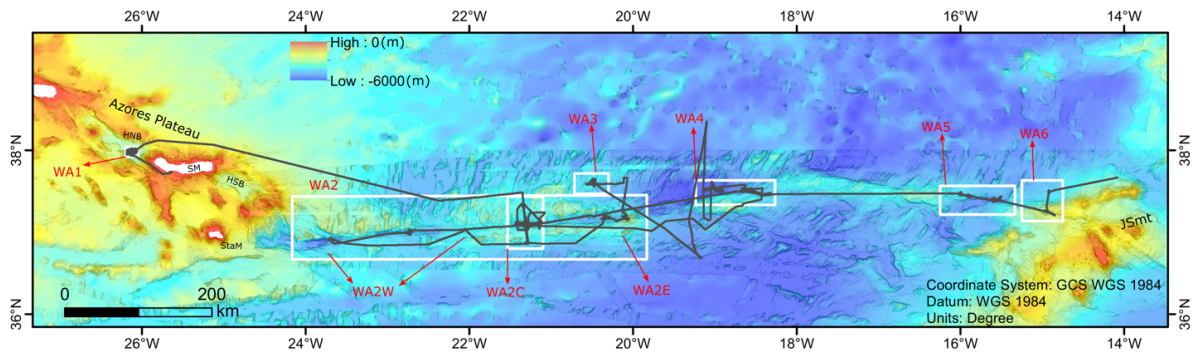
Fig. 3.1 Track chart of R/V Meteor for working areas (WA) 1-6 during cruise M162.

3.2   Aims of the Cruise

The overarching aim of cruise M162 was to find out if seismically active oceanic fracture zones like the Gloria Fault are places of active fluid circulation that could represent a link between fluid flow processes between mid-ocean ridges and continental margins. The verification of active fluid flow along the Gloria Fault is relevant with respect to (i) the relationship between fluid flow and seismic activity, (ii) the spread of (chemoautotrophic) ecosystems in the abyssal ocean, (iii) the control of fluids on the strength of the fault interfaces, and/or (iv) the role of fluids in triggering or supporting high magnitude fracture zone earthquakes. Specifically, the following key tasks were to (i) find out if there are sites of active fluid discharge along the Gloria Fault (and more general along transform faults and oceanic fracture zones) and (ii) to constrain the origin of the fluids and decipher processes involved, (iii) search for evidence for ongoing serpentinization, (iv) find indications for existing deep-sea chemoautotrophic ecosystems along the fault system, and (v) analyse the sedimentary record with respect to paleo-seismic events.

3.3   Agenda of the Cruise

After departure from Ponta Delgada, working areas WA1 to WA6 (Fig. 3.1) were investigated roughly in numerical order from west to east. Station work within the working areas typically consisted of a site survey with multibeam and sub-bottom profiler (Parasound) followed by V-CTD surveys, heat flow measurements, and GC/V-MUC coring. There were no major technical problems during the cruise that affected the scientific program. Some time was lost though due to bad weather conditions (see section 4). The program was, however, modified in a few points with respect to the initial proposal. As mentioned above, a short survey program in WA1 was added to the schedule, because relevant new information had become available prior to the cruise that scientifically justified the addition to the work program. Another minor addition to the initial work program was a lateral W-E gravity core transect within the major fault trace of the Gloria Fault between the Azores Plateau and WA2-central. Together with cores obtained on M141 this will allow for a systematic investigation of changes in sediment composition and pore water geochemistry over a large distance and thus allow for a better connection of information obtained in WA2-central. Moreover, minor adaptations were made based on findings during the cruise. Unfortunately, the working area located in the Madeira Abyssal Plain (West of Madeira Island) and a reference station that were suggested in the initial proposal had to be dropped due to time limitations. This decision was also corroborated by the change of destination harbour from Gran Canaria to Emden. Carrying out additional station work West of Madeira would have meant an inappropriate loss of ship time.

In addition to the scientific work performed during M162, specific measures were taken with respect to sustainable ocean research. On request of the Foreign Ministry of Portugal, the Parasound system was only used for station work, but not on transits between working areas within the Portuguese EEZ. In addition, when using the Parasound system a whale-observation team (H. Adao, K. Sroczynska) was operating on the bridge during daytime. In one instance, a Parasound survey had to be interrupted due to the sight of whales.

4   Narrative of the Cruise

(C. Hensen[1])

[1]GEOMAR

On March 5, 2020 an international group of 25 scientists arrived on RV Meteor in Ponta Delgada. The collaborating group was formed by members of the GEOMAR Helmholtz-Centre for Ocean Research Kiel, the Faculty of Geosciences at Bremen University, the IPMA in Lisbon, the Dom Luiz Institute (IDL) at Lisbon University, the University of Évora (Portugal), the ETH Zürich, the EAWAG Dübendorf (Switzerland), the IGI Ltd. Bideford (UK), and the CEED at Oslo University. This first day onboard was used to set up laboratories and prepare all scientific equipment. Unfortunately, due to a severe damage of the AUV "Abyss" that occurred on cruise AL532 this cruise had to be conducted without AUV and team members.

RV Meteor departed from Ponta Delgada in the morning of March 6, 2020. After a transit of only 3 hours Meteor reached the first working area (WA) 1 located in the Hirondelle Basin between the islands São Miguel and Terceira. This WA was added to the initial plan as findings made during a previous Meteor cruise suggested the existence of active fluid discharge at the seafloor in this area, hence providing a direct link to the proposed work. Within 48 hours we carried out surveys with Multibeam/Parasound (MB/PS) and the video-guided CTD (VCTD), conducted a heat flow (HF) transect across previous coring locations, and sampled sediments by gravity corer (GC) and video-multicorer (VMUC). Around midday on the 8th of March, we started a transit of about 240 NM to the central working area WA2. Here, all investigations could fortunately be based on available seismic information collected during M79. Station work in this area started on March 9 with a long MB/PS survey following the main N-S seismic line recorded on M79. Until March 15 this area was intensely investigated with alternating program of HF- and VCTD-surveys as well as GC and VMUC deployments.

In the night of the 16th of March, we left the central WA2 for a systematic continuation of a set of gravity cores along the major fault trace, which was commenced during Meteor cruise M141. Within 2 days we conducted 3 MB/PS-surveys, 1 HF-profile and 3 GC-deployments up to ~22°40'W. In the night of the 18th of March, we left the western part of WA2 and headed east to the end of the major trace of the Gloria Fault at about ~20°20'-20°05'W. In this area, station work was carried out for 2 days, including MB/PS-surveys, one HF-profile and several GC-deployments. In the night of the 20th of March, we started a combined transit and MB/PS-survey to WA3. Station work in WA3, again including MB/PS- and HF-surveys as well as GC-deployments, was carried out for 2 days. Video-guided instruments could not be used due to increasingly rough weather conditions.

In the night of the 22nd of March, the planned transit to WA4 had to be dropped because of bad weather conditions, which lasted for the whole day and made it impossible to carry out any useful

station work. In the morning of the 23rd of March, station work could finally be resumed in WA4. Investigations in this area were carried out until the 26th of March in the morning. Again, rough weather conditions made it impossible to continue useful station work thereafter during this day. The time was used for a transit back to the central WA2, where a number of GCs were retrieved and another HF-profile was carried out in order to fill some gaps in the data set within the next 2 days. In the night of the 29th of March, we started the longer transit to WA5, with another stopover in WA4, where again some data gaps were filled by GC-coring and a short HF-survey. WA5 was reached on the 30th of March. Station work in this area was conducted until April 1, 2020, which again had to be interrupted on March 31 due to bad weather conditions.

In the early morning of the of the 2nd of April we arrived in the last working area (WA6). Luckily, weather conditions finally allowed for the deployment of all gears. Station work had to be resumed in the night of the 4th of April to allow for a timely arrival in Lisbon on the 5th of April, 2020. Due to the Corona-Virus Pandemic, the subsequent cruise M163 had been cancelled and Meteor was recalled to Germany, instead of calling at Las Palmas (Canary Islands). The stopover in Lisbon was used to drop 7 scientists based in Portugal and Croatia. The final transit with destination Emden was used for packing of the equipment, final analyses and data evaluation. RV Meteor moored after a successful cruise in Emden at about 14:00 on the 10th of April.
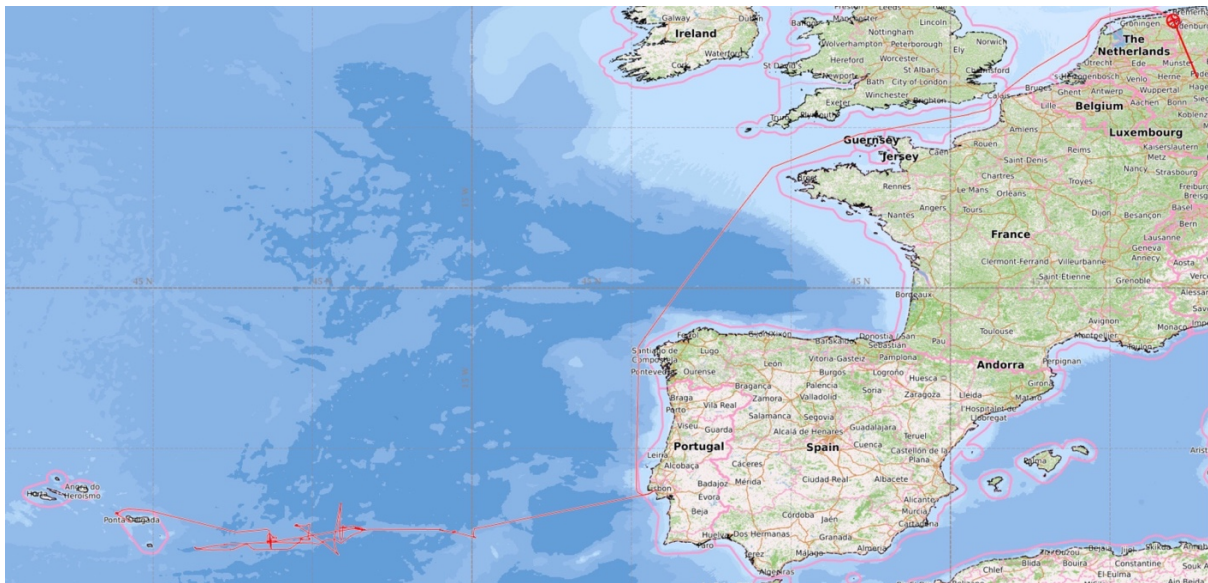
Fig. 4.1 Overall track chart of R/V Meteor cruise M162.

5   Preliminary Results

5.1   Hydroacoustics

(P. Terrinha[1], L. Batista[1], L. Belosa[2], J. Duarte[3], M. Koppe[4], P. Nogueira[5])

[1]IPMA, [2]CEED-UIO, [3]IDL, [4]GEOMAR, [5]UÉvora

5.1.1   System Overview

Multibeam

Two multibeam systems are available onboard R/V METEOR for bathymetric mapping of the seafloor: a KONGSBERG EM122 for deep-water mapping and a KONGSBERG EM710 for shallow water. Due to depths between 3500 m and 4900 m in the Gloria Fault working areas, the EM122 System was used for surveying the seafloor.

The EM122 system is a deep-water multibeam echosounder that provides accurate bathymetric mapping of the seafloor (Fig. 5.1.1). Basic components of the system are two linear transducer arrays in a Mills cross configuration with separate units for transmitting and receiving. The nominal sonar frequency is 12 kHz with an angular coverage sector of up to 150° and 256 beams per ping. The emission beam is 150° wide across track, and 1° along track direction. The reception is obtained from 256 beams, with widths of 2° across track and 20° along track. Thus, the actual footprint of a single beam has a dimension of 1° by 2°. Achievable swath width on a flat bottom will normally be up to six times the water depth depending on the character of the seafloor.

Fig. 5.1.1   Basic principle of a multi-beam echosounder.

In addition to travel times, the Simrad EM122 also records the amplitude of the backscattered signal that is used to produce seafloor backscatter maps. The acoustic backscatter acquired by multibeam carries important information about the seafloor geomorphology and physical properties. With the proper radiometric and geometric correction, acoustic backscatter mosaics can aid in the mapping of surficial seafloor features and facies, an important task toward remote seafloor characterization.

Parasound

The Ship is equipped with a hull mounted parametric sub-bottom profiler Parasound P70 (Atlas Hydrographic GmbH, Bremen) whose operation provides high resolution information of the uppermost 50-100 m of the sediments. Parasound P70 works as a narrow beam sediment echo-sounder, providing primary high frequencies (PHF) of 18 kHz and adjustable to 18.5-28 kHz, thus generating parametric secondary low frequencies (SLF) in the range of 0.5-10 kHz and secondary high frequencies (SHF) between 36.5-48 kHz. The secondary frequencies develop through nonlinear acoustic interaction of the primary waves at high signal amplitudes. This takes place only in the emission cone of the PHF signal, which is limited to an aperture angle of only 4° for the Parasound P70. This is achieved by using a transducer array of 128 transducers on a rectangular plate of approximately 1 m² in size. Therefore, the footprint size is only 7% of the water depth and vertical and lateral resolution is significantly improved compared to conventional 3.5 kHz echosounder systems. The fully digital system provides important features like recording of the 18 kHz PHF signal and both secondary frequencies, SLF and SHF, continuous recording of the whole water column, beam steering, different types of source signals (continuous wave, chirp, barker coded) and signal shaping. However, many of the new features are still in an experimental state. Digitization takes place at 96 kHz to provide sufficient sampling rates for the SHF. A down-mixing algorithm in the frequency domain is used to reduce the amount of data and allow data distribution over ethernet. For the standard operation a parametric frequency of 4 kHz and a sinusoidal source

wavelet of 2 periods was chosen to provide a good relation between signal penetration and vertical resolution. The transmission sequence was established as a single pulse mode with manual system depth at the beginning of the acquisition and afterwards controlled by the PHF arrival. The PHF signal was recorded permanently. All raw data were stored in the ASD data format (Atlas Hydrographic), which contains the data of the full water column of each signal as well as the full set of system parameters. Additionally, a 200 m long reception window of the onboard processed data was recorded in compressed PS3 data and SEGY format. All lines were then loaded to a Kingdom Suite Project. Vertical scale was converted in meters using a sound velocity in water of 1500 m/s.

5.1.2 Preliminary results

The multibeam data recovered during the M162 mission needs further processing that will be made shortly. Various gaps were filled in and almost full coverage of the Gloria Fault Fracture Zone will be available. This will be useful for geomorphologic and tectonic analysis in trying to understand the possible mechanisms that control the very large topographic variation along the fault zone.

Results from the Parasound acoustic survey
A total of 24 profiles of high-resolution ATLAS Parasound parametric sub-bottom profiler were acquired in the cruise (Table 5.1.1). In total, around 710 nm during the M162 cruise were acquired. The profiles were acquired at speed of 5 to 7 knots. All the profiles were acquired to help on the decision for gravity core location. The location of the Parasound profiles is shown in Figures 5.1.2 to 5.1.6.

Table 5.1.1 List of Parasound profiles

FID	W Area	line_id	length (m)	length (nm)
1	WA1	PS01	72422.93	39.08
2	WA2	PS02	69384.50	37.44
3	WA2	PS03	73825.67	39.84
4	WA2	PS04	24881.06	13.43
5	WA2	PS05	98277.22	53.03
6	WA2	PS06	9720.18	5.24
7	WA2	PS07	20786.02	11.22
8	WA2	PS08	9330.07	5.03
9	WA2	PS09	6745.32	3.64
10	WA2	PS10	32765.44	17.68
11	WA2	PS11	36665.81	19.78
12	WA2	PS12	2052.54	1.11
13	WA3	PS13	89407.44	48.24
14	WA4	PS14	4019.51	2.17
15	WA4	PS15	403685.01	217.82
16	WA4	PS16	92907.65	50.13
17	WA4	PS17	26519.40	14.31
18	WA4	PS18	94048.56	50.75
19	WA5	PS19	866.18	0.47
20	WA5	PS20	35062.74	18.92
21	WA5	PS21	32473.20	17.52
22	WA5	PS22	18037.35	9.73
23	WA6	PS23	21109.48	11.39
24	WA6	PS24	28560.90	15.41
		TOTAL	1303554.20	703.38
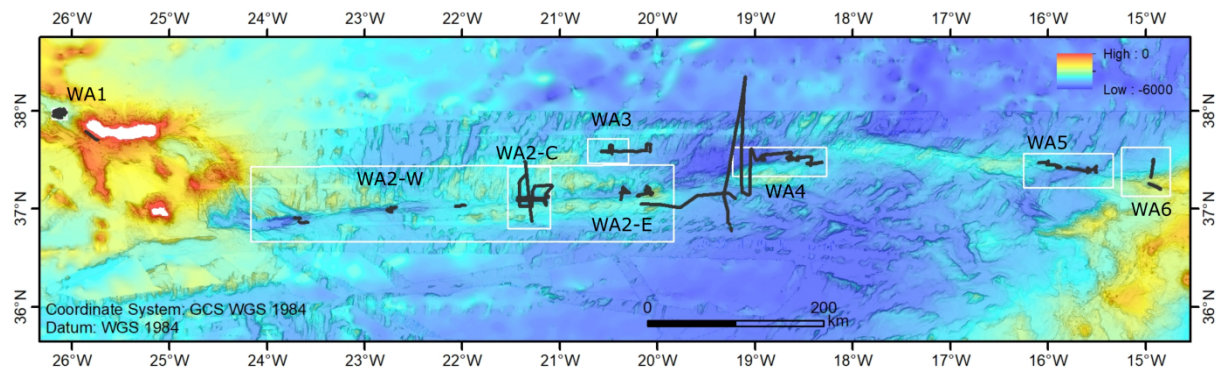
Fig. 5.1.2   Location of PARASOUND stations profiles in the working areas recorded during the M162 cruise.
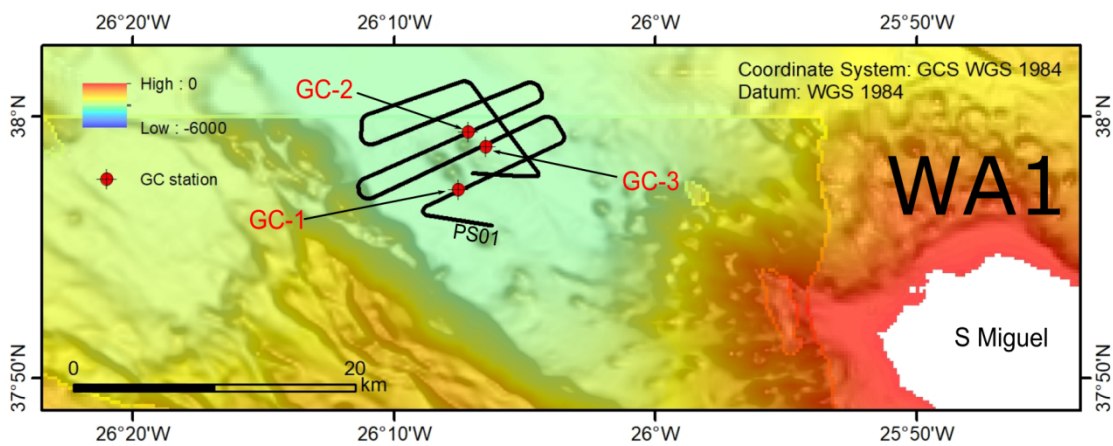
Fig. 5.1.3   Parasound profile acquisition and gravity core locations in WA1.
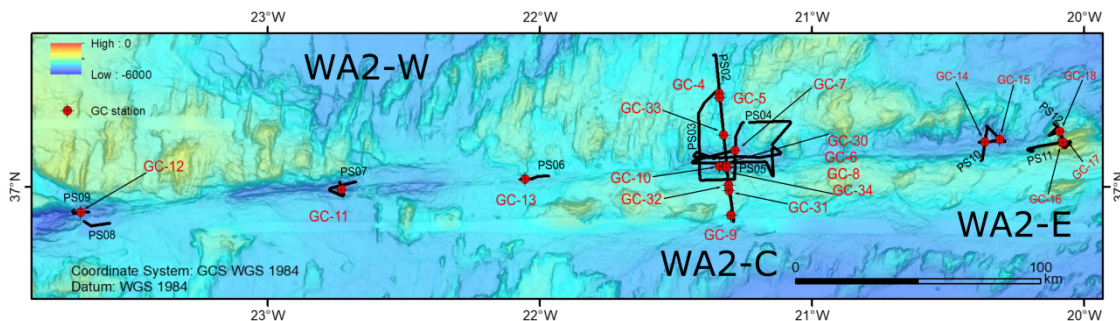
Fig. 5.1.4   Parasound profiles acquisition and gravity core locations in WA2.

These new data provide insights into the uppermost Quaternary sedimentary architecture over the surveyed zones, as well as into the subsurface tectonic geometry of the faults and fault systems observed there. To our knowledge this was the first systematic sub-bottom profiling survey conducted along and across the Gloria Fault Fracture Zone. Previous work on the eastern prolongation of the Gloria Fracture Zone investigating the deep circulation of seawater or hydrothermal fluids had been successfully reported by Hensen et al. (2015, 2017).

The ATLAS Parasound parametric data show detailed stratigraphic information of the uppermost tens of metres below the seafloor (up to 75 m at an assumed sediment velocity of 1.5 km/s). The best results were obtained in the flat areas with highly penetrative sediments, while steep slopes displayed very low penetration.

     Although the Gloria Fault is known to be kinematically and seismically active at Present the new profiles show that very recent tectonic activity is also occurring off the fault, which is also

compatible with off the fault large earthquakes of M>7. Tectonic deformation off the fault is well displayed in profiles PS 13, PS14, PS15 and PS24.
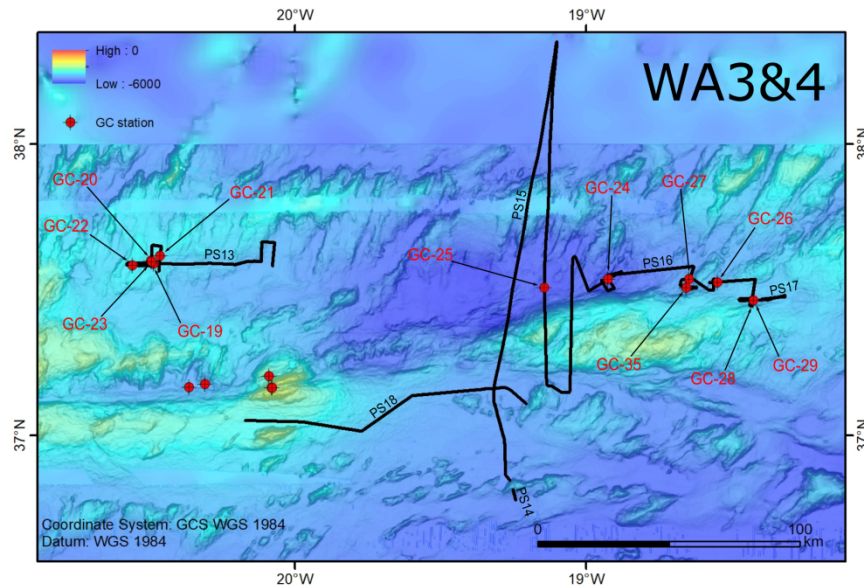
Fig. 5.1.5   Parasound profiles acquisition and gravity core locations in WA3 and WA4.
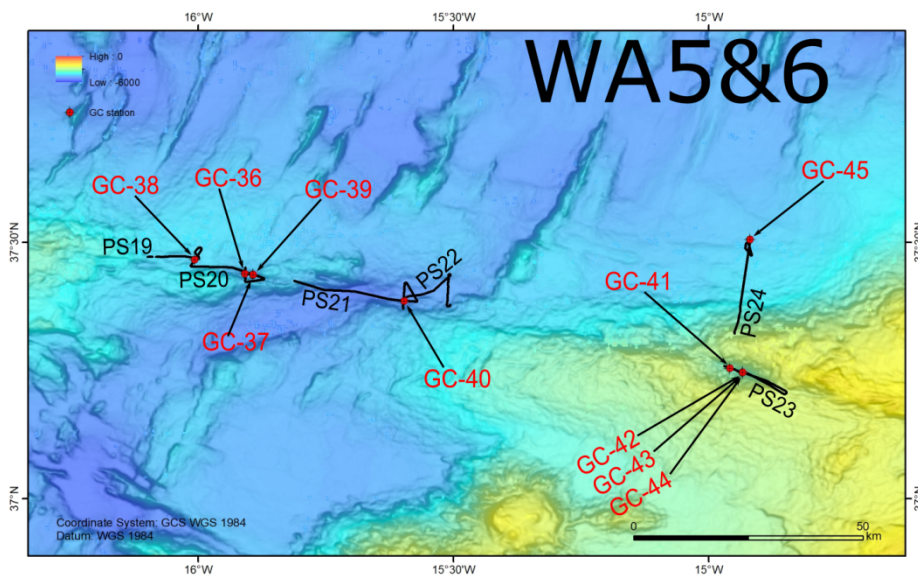
Fig. 5.1.6   Parasound profiles acquisition and gravity core locations in WA5 and WA6.

Working Area 1 (WA1) – The Terceira rift

These profiles were made in the axial part of the Terceira Rift in order to select adequate sites for sampling for fluid flow in the sedimentary cover. Places were chosen where active faults off main extrusive bodies could be observed. These sites and WA-1 were chosen after the successful work by Schmidt et al (2019) on evidences of hydrothermalism in the Terceira Rift. It is worthwhile to note that i) the tectonic deformation and volcanic intrusions vary along the same sub-basin axis on juxtaposed profiles, such as in the sub-basin imaged at offsets 2000 and 2500 and that ii) the highly reflective uppermost layers are underlain by a transparent discontinuous unit that pinches out towards structural highs; this is probably a layer made of mass transport deposits (Fig. 5.1.7).
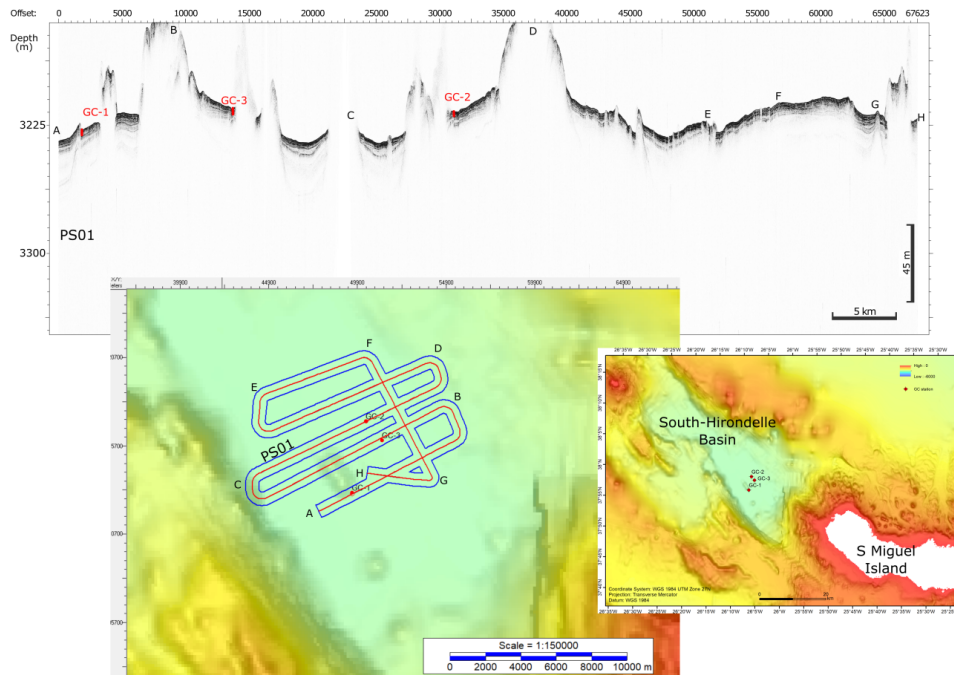
Fig. 5.1.7   Location of profile PS01 in the Terceira Rift (WA1). Inset shows the location of the gravity cores. The segments of the profile are separated by the turning points. See text for description.

Working Area 2 (WA2) – The west strike-slip segment of the Gloria Fault

The WA2 is more than 500 km in length, very rectilinear, with no bends and contains some basins with local basement depressions of almost 1 km. This is considered the pure strike-slip segment of the Gloria Fault. WA2 extends from the connection of the Terceira Rift with the Gloria Fault in the west to the restraining bend, the locus of the 1941 M8.4 earthquake (Buforn et al., 1998) in the east. WA2 is sub-divided in three sub-areas described below.

Sub-working area WA2-W: the connection between the Terceira Rift and the west Gloria Fault
Sub-bottom profiles were acquired at the intersection of the Terceira Rift with the Gloria Fault in order to ensure the existence of sufficient thickness of well bedded layers and vertical offsets (PS09, GC-12, Fig. 5.1.8). Other sub-bottom profiles were acquired in neighbouring basins to locate the sampling for gravity cores, PS07 for GC-11 and PS06 for GC-13 (Figs. 12.1.1-2).

Sub working area WA2-C: The GF M79 Basin
The WA2-C encompasses the GF M79 Basin (21º 15'W) (Batista et al., 2017). The basement is downthrown by approximately 0.8 km mainly by flexure of the northern flank of the Gloria Fault. Crustal and uppermost mantle was modelled as consisting of five layers (L1- sediments, L2- basalts, L3-gabbros, L4-hydrated mantle and L5, mantle). A series of Parasound profiles and gravity cores were acquired in this sub-area (Figs. 5.1.9 and 12.1.3).

Sub working area WA2-E: The transition from the pure strike-slip to the transpressive domain
Line PS10 was shot within a basin domain similar to GF M87 Basin. However, it shows both compressive (at GC-15) and extensional (north of GC-14) deformation faults, possibly an evidence of flower structures (Fig. 5.1.10). Lines PS11 and PS12 show no penetration within a sedimentary cover, which means that either the outcrop is barren of sediment cover or it is very thin. This is in agreement with an uplifted basement block (Fig. 12.1.4).
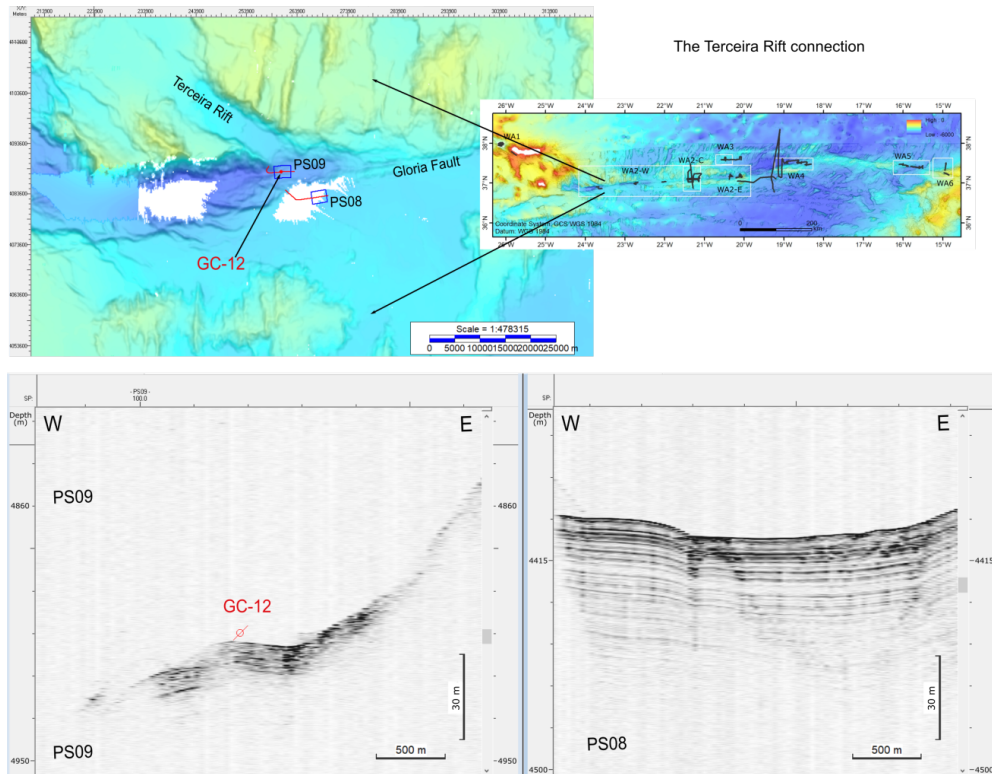
Fig. 5.1.8 Sub working area WA2-W: the connection between the Terceira Rift and the Gloria Fault.
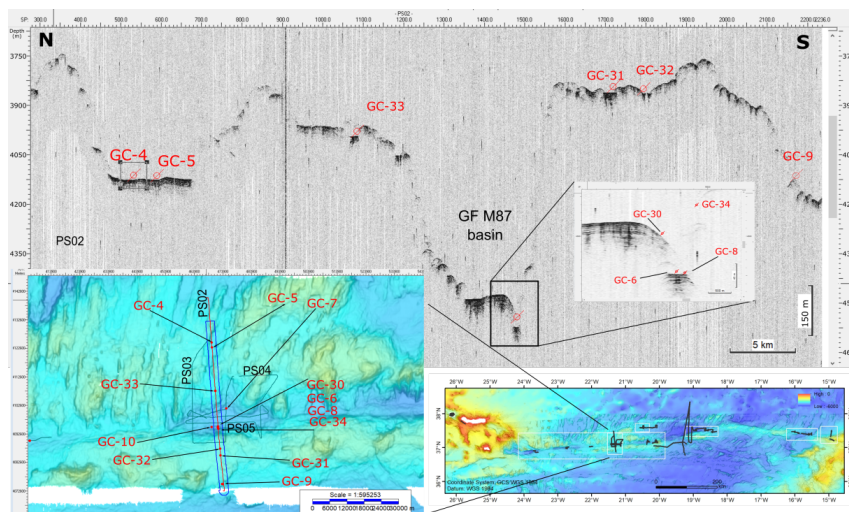
Fig. 5.1.9 Parasound profile PS02 and location of gravity cores within and across GF M87 Basin.

Working Area 3 (WA-3) – Off the Gloria Fault in the Eurasia Plate

Profile PS13 was shot approximately 70 km north of the Gloria Fault, most of it along the East-West direction across approximately N-S striking ridges that are interpreted as rotated blocks formed in late Cretaceous times at the Mid-Atlantic Ridge. The thin package of sediments deposited is controlled by this ridge and trough morphology. In some places tectonic deformation structures affecting the most recent sediments are observed, such as at GC-20 and GC-23 and near the seamount by GC-19 and GC-22 (Fig. 5.1.11 – 5.1.13).
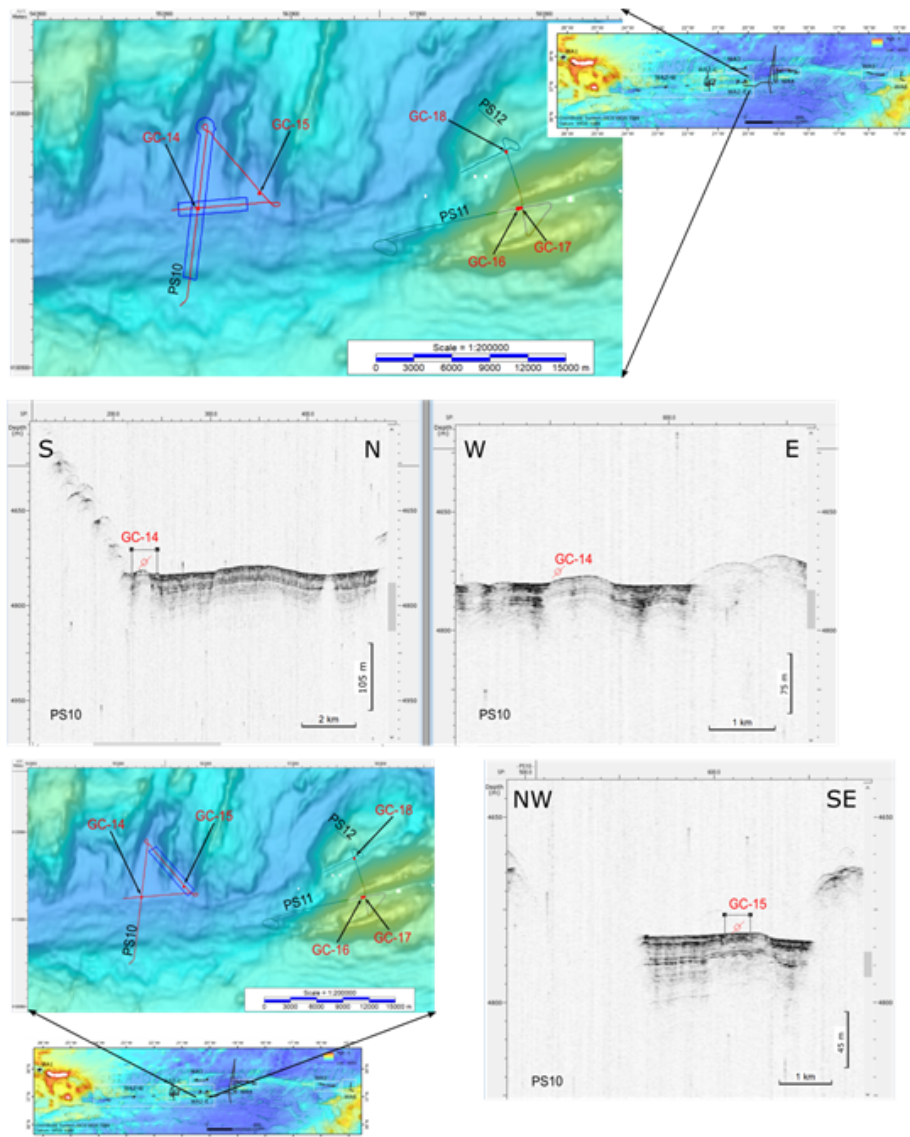
Fig. 5.1.10   Map showing locations of profiles PS10, PS11 and PS12 and gravity cores GC-14 to GC-18. Note compressive and extensional deformation around GC 14 and compressive ones under GC-15.

Working Area 4 (WA-4) – The restraining bend segment

WA-4 encompasses part of the restraining bend of the Gloria Fault where the epicenter of the 1941 M8.4 magnitude earthquake occurred (Buforn et al., 1988). To the north of this high the bathymetry drops to over 6 km depth, locally, suggesting a flexural relationship between the structural high and this sub-basin.

Inspection of the bathymetry map of Figures 5.1.14-5.1.15 and 12.1.5-12.1.7 shows the N-S striking ridges of the Cretaceous tilted blocks abruptly cut by the Gloria Fault trace. All segments of PS15-16-17 shown in Figures 5.1.14-5.1.15 and 12.1.5-12.1.7 show short segments of well layered sediments cut by transparent segments of profile, possibly zones of extremely fractured sediments with sudden vertical offsets of tens of meters.
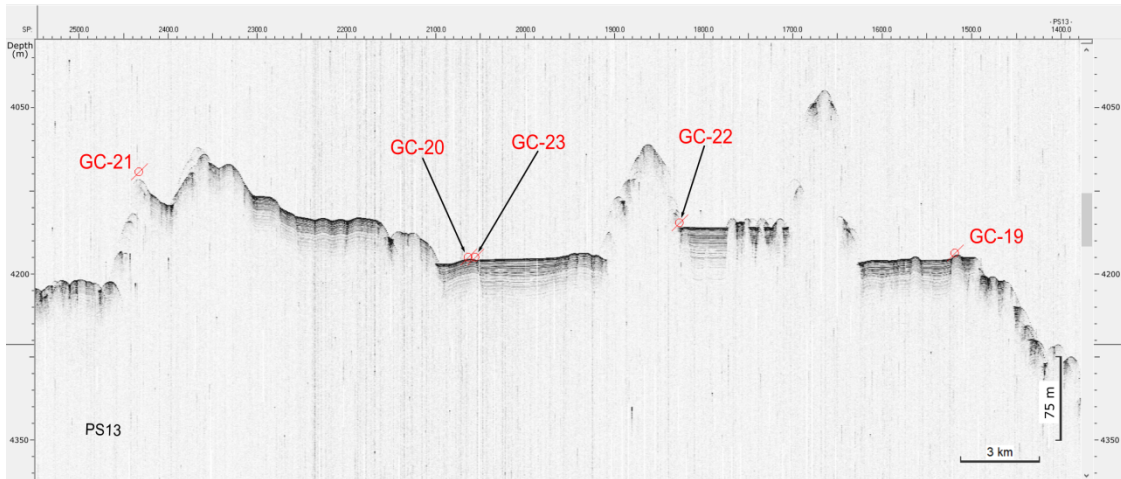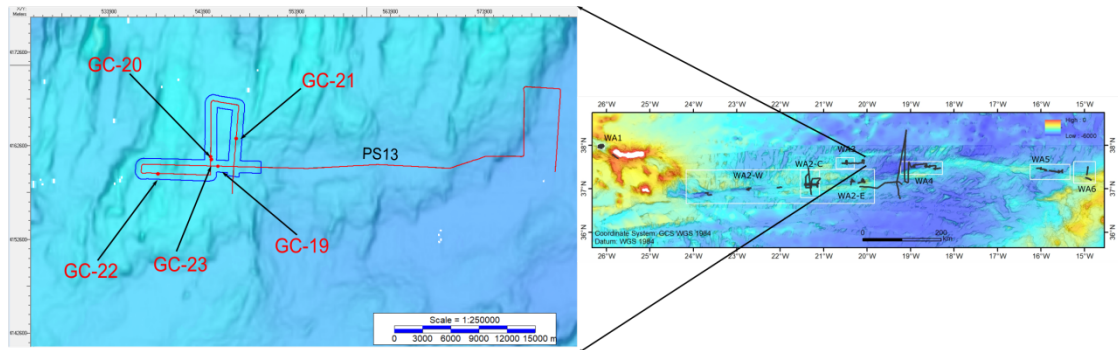
Fig. 5.1.11   Various examples of profile PS13 off the Gloria Fault, ~70 km to the north in the Eurasia plate. See text for description and Figure 5.1.12.
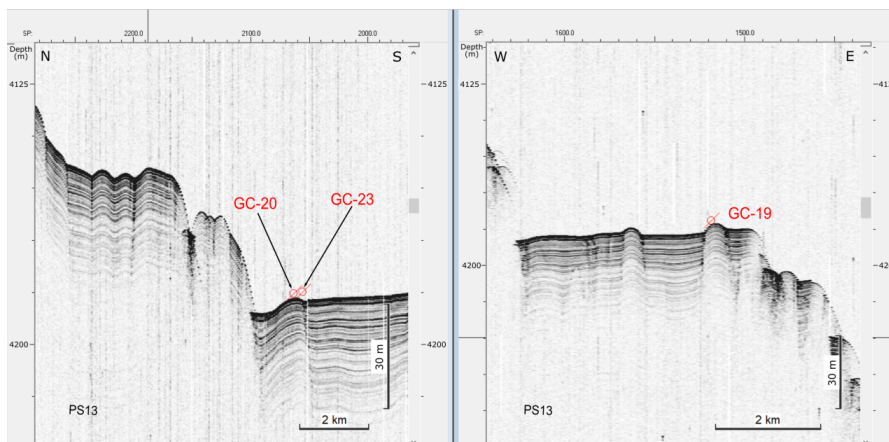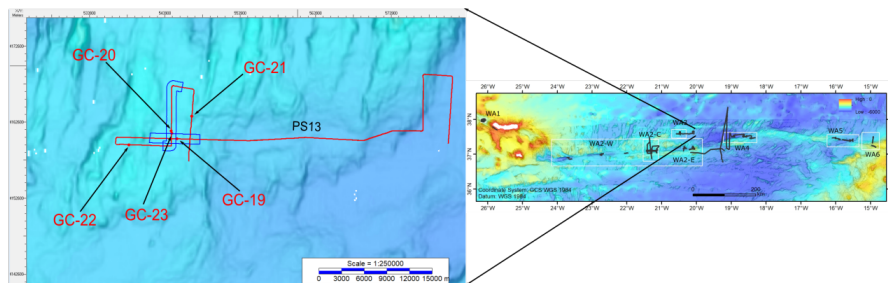
Fig. 5.1.12   Detail of PS13. Note the shallow and recent extensional deformation around GC-20 and GC-23, probably associated with a releasing bend. Compressive structures near GC-19.
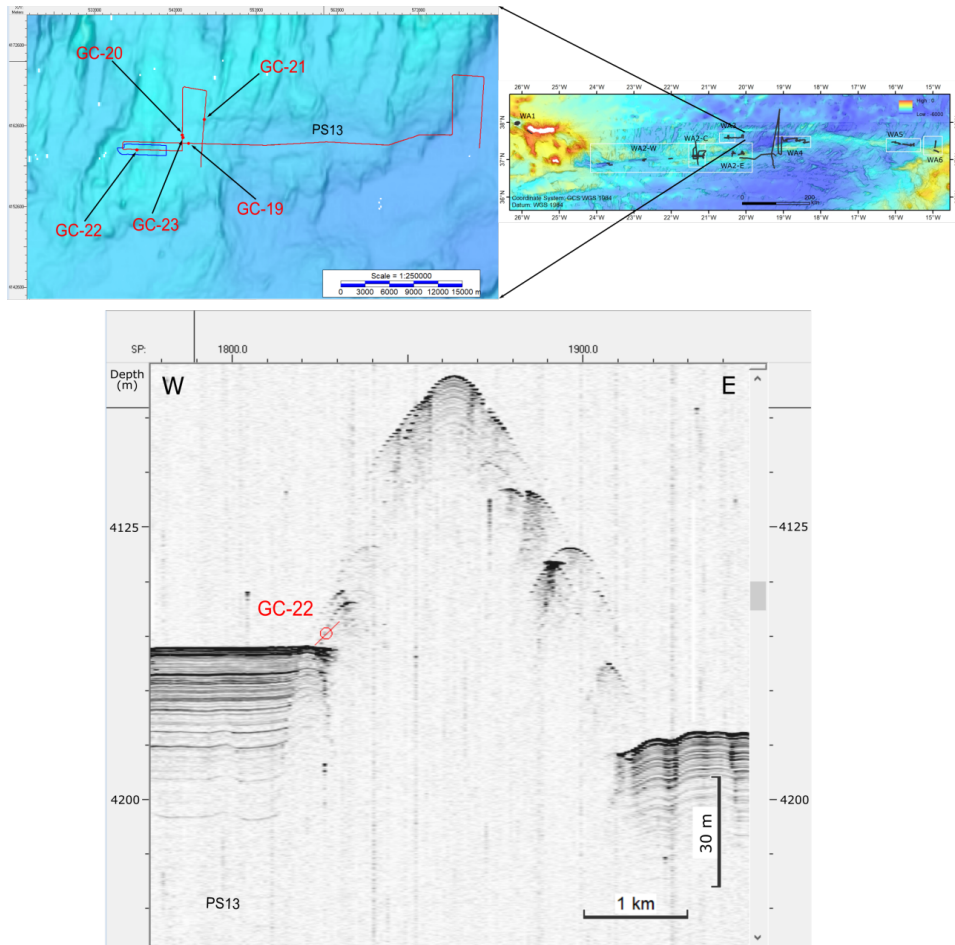
Fig. 5.1.13   Detail of PS13. Example of deformation structures near GC-22.
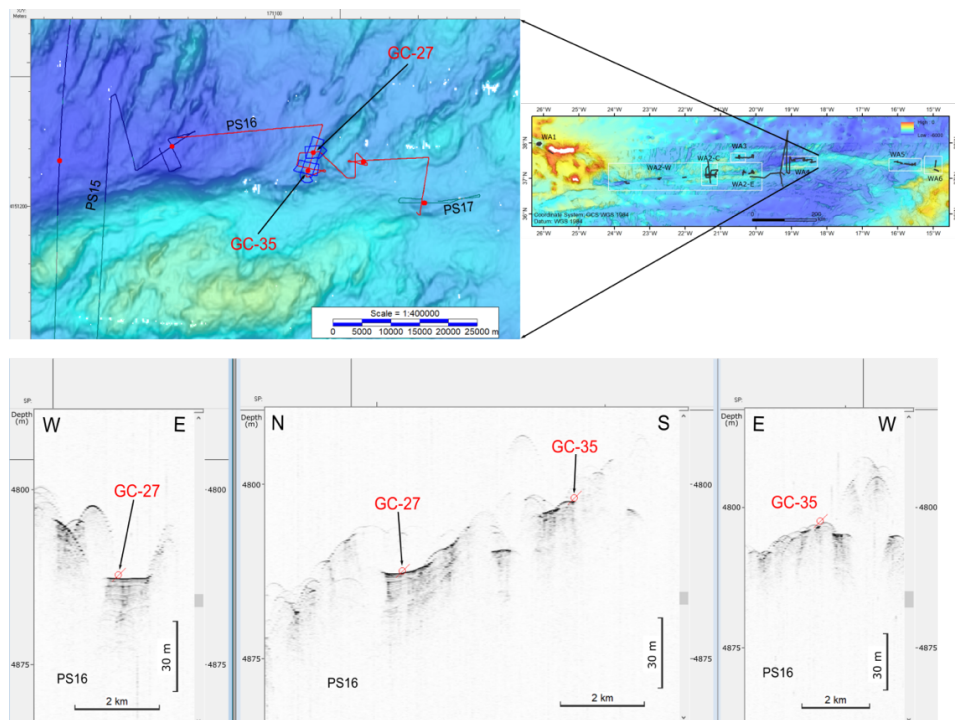
Fig. 5.1.14   Sections of Parasound profile PS16 and locations of gravity cores GC27 and GC35 in WA-4.
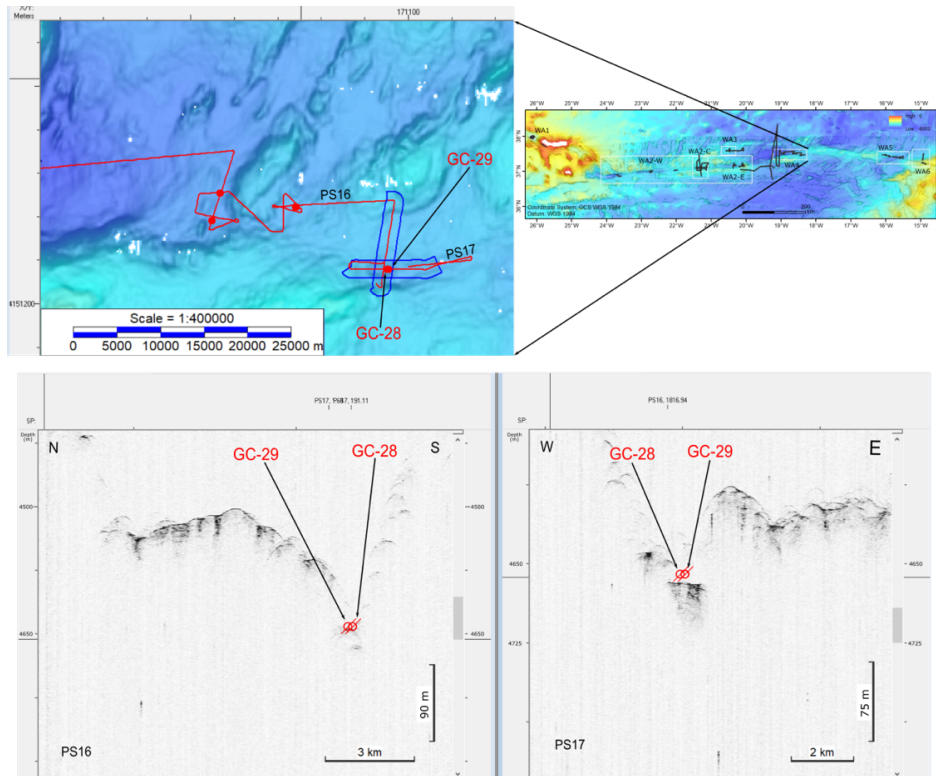
Fig. 5.1.15   Sections of Parasound profile PS16 and locations of gravity cores GC28 and GC29 in WA-4.

Working Area 5 (WA-5) – A strike-slip segment

WA-5 is again dominated by dextral strike-slip kinematics (Neres et al., 2016). The goals were small basins with scarce sedimentary cover. Because the basins were narrow the records show many diffractions and lateral echoes (Figs. 5.1.16 and 12.1.8).
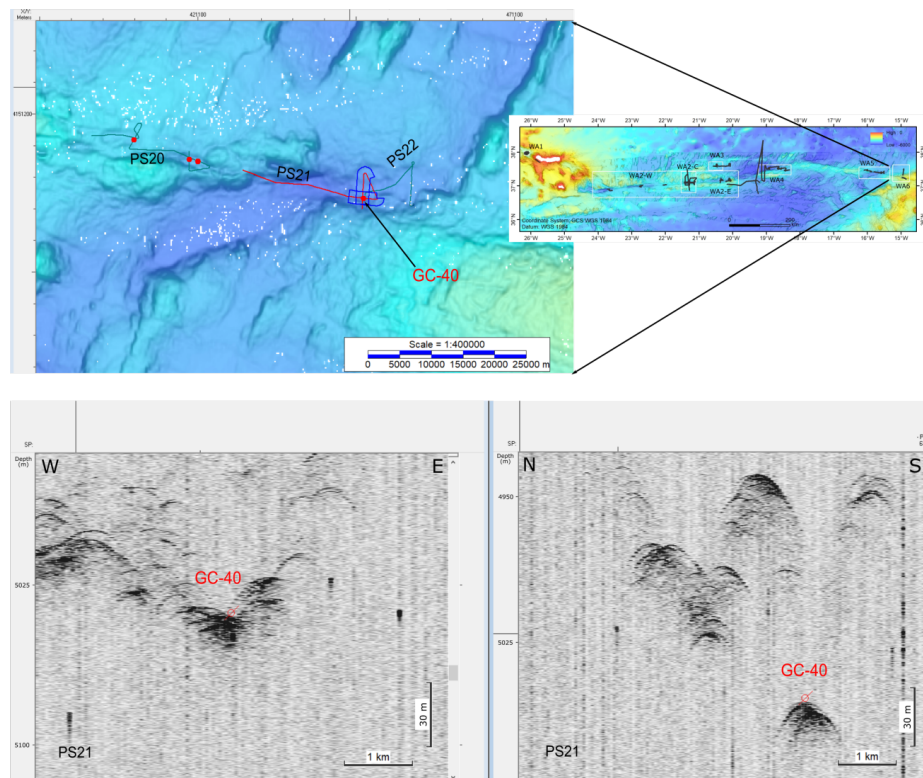
Fig. 5.1.16   Examples of Parasound profile PS 21 in WA-5.

Working Area 6 (WA-6) – The connection to the Madeira-Tore Rise

The Gloria Fault rotates from ~W-E to WNW-ESE strike within the Madeira-Tore Rise. The record of PS23 shows a thin sediment cover within a small oval basin at 15º W (Fig. 5.1.17) and some short cores could be retrieved here. The N-S trending profile PS24 shows the descent from the Madeira-Tore Rise towards the abyssal plain in the north. The wrinkled seafloor surface marks vertical offsets and folds indicating tectonic deformation and draping of sediments (Fig. 5.1.18).
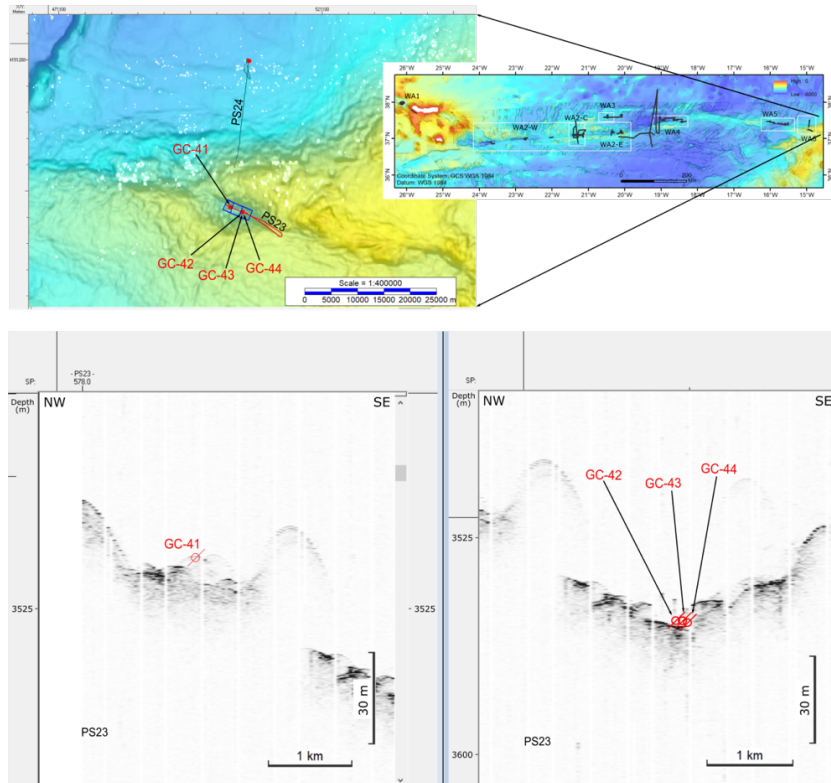
Fig. 5.1.17   Examples of Parasound profile PS 23 WA-6 and location of gravity cores (thin sediment cover).
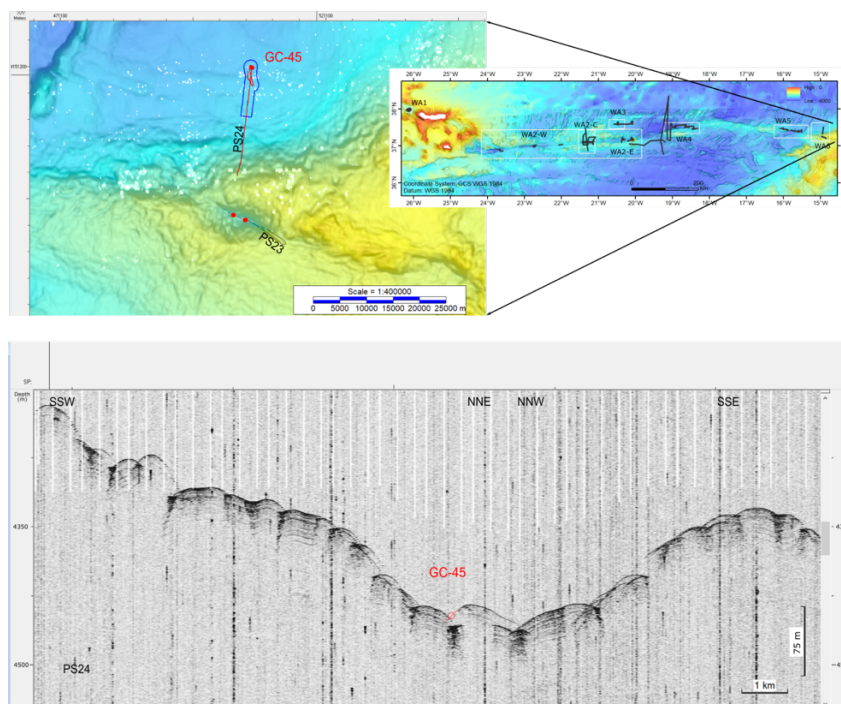
Fig. 5.1.18   Examples of Parasound profile PS 24 in WA-6 and location of gravity core GC-45. Note that the image includes a 180º turn.

5.2   Seafloor monitoring and water sampling

(M. Schmidt[1], T. Müller[1], S. Cherednichenko[1], A. Bodenbinder[1])

[1]GEOMAR

5.2.1   Methodology

A video-guided Water Sampler Rosette/CTD system (VCTD, Fig. 5.2.1) was used to study oceanographic characteristics of the water column and to monitor the seafloor for fluid release structures and chemical/physical bottom water anomalies. The Water Sampler frame was equipped with Niskin bottles (11x10 L) to take water samples at interesting spots. An HD-Video camera and light sources were attached to the lower part of the frame and are controlled by the telemetry deck unit via the 18 mm coaxial cable of winch 12 onboard RV Meteor (Fig. 5.2.1). The digital video and data telemetry system (Linke et al., 2015) providing real-time monitoring of the seafloor was also used to control the distance to the seafloor in "bottom view" mode. The VCTD rosette was equipped with additional sensors e.g. for dissolved gases, i.e. O_2, and CH_4, to monitor dissolved gas anomalies near the seafloor (Schmidt et al., 2015).

The SBE 9plus underwater unit was equipped with pressure sensors, 2 temperature sensors, 2 oxygen sensors and 2 conductivity sensors. Furthermore, an altimeter sensor measuring distance between VCTD and seafloor, and a turbidity sensor (Chelsea Nephelometer) measuring suspended particulates and colloids were attached. The SBE underwater unit and Niskin bottle carousel motor were powered via the winch's coaxial-cable by using the modem/power unit from SST (Linke et al., 2015). CTD data recording and triggering Niskin bottles were controlled with SEASAVE software (version 7.21) on an external laptop. CTD data were recorded with 24 Hz. GPS position data (DGPS 3050/1) was logged parallel to the CTD and Video data from NMEA-string of RV Meteor. Hydro-casts and hydrographic data from towed SBE-CTD were processed by using SBE software SBE7.22.1. Usually data files of 1 second bins and 1-meter bins were created from raw data files and exported to ASCII. CTD data is combined with data sets from external sensors by correlating with their UTC time stamps.

HydroCTM-CH_4 sensors
The membrane inlet methane sensor (CH4P-1019-001, KM Contros) had been mounted to the rosette frame replacing one Niskin bottle. The highly sensitive methane sensor was able to detect even smallest increases of dissolved CH4 above an average background level of 1-2 nM (Schmidt et al., 2013). The sensor was connected to 5V external sensor connector of the SBE CTD (A/D voltage channel 7) enabling online CH4-data visualisation during recording. The methane sensor was powered by three NiMH-rechargeable battery packs (24 V, 9 Ah, 6000 m rated), which were mounted to the rosette frame.

Deploying the Video-CTD
The VCTD system was towed by using winch 12 ("Schiebebalken") from the starboard side of RV Meteor and water depths of the device were controlled using rope length (DSHIP), pressure and altimeter readings. Fiering (lowering) and heaving of the VCTD was done at a rope speed of 0.5 m s^{-1}. Since the water depth for all stations was above 3000 meters, the transfer of the VCTD to and from the sea floor was in most cases > 2 hours. Once bottom sight was reached the ship moved with 0.5 kn along predefined transects. The observation times along the seafloor varied

between 70 min and 250 minutes. During upcast of the Video-CTD the winch was stopped for 10-20 minutes at 300 meters below sea level (mbsl) to allow decompression of the sensors.
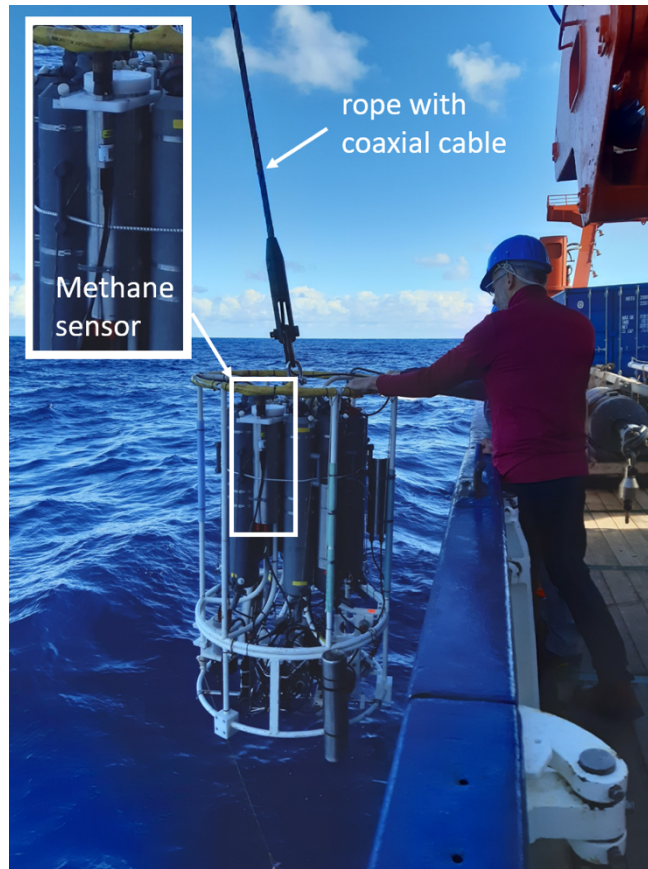
Fig. 5.2.1   Deploying the Video-CTD. Water sampler (11x10 L Niskin) rosette including SBE9plus CTD, O_2, turbidity (Chelsea), Methane (Contros), and altimeter sensors.

5.2.2   Recorded Video-CTD data sets

Towed Video-CTD measurements were performed at working areas 01, 02, 04 and 06 (Fig. 5.2.2, Table 5.2.1).

SBE software SBE7.22.1 uses for the computation of salinity, density, potential temperature, specific volume anomaly, and sound velocity formulas described in Fofonoff and Millard, 1983. The potential temperature of seawater is defined as "the temperature an element of seawater would have if raised adiabatically with no change in salinity to reference pressure" (Sea-Bird Electronics, Inc., 2017). It is calculated depending on salinity, temperature, pressure and reference pressure, where the Sea-Bird software uses a reference pressure of 0 decibars. A detailed derivation of the calculation can be found in Fofonoff and Millard (1983).

For each Video CTD-station the following sensor data were collected (and are provided as *.xlsx): Time (UTC), water depth (m), density (kg m^{-3}), temperature (°C), sound velocity (m s^{-1}), oxygen (μM/ L^{-1}), salinity, Latitude (°N), Longitude (°W), Pressure (db), Methane (ppm), turbidity (FTU), conductivity (S m^{-1}), potential temperature (°C).
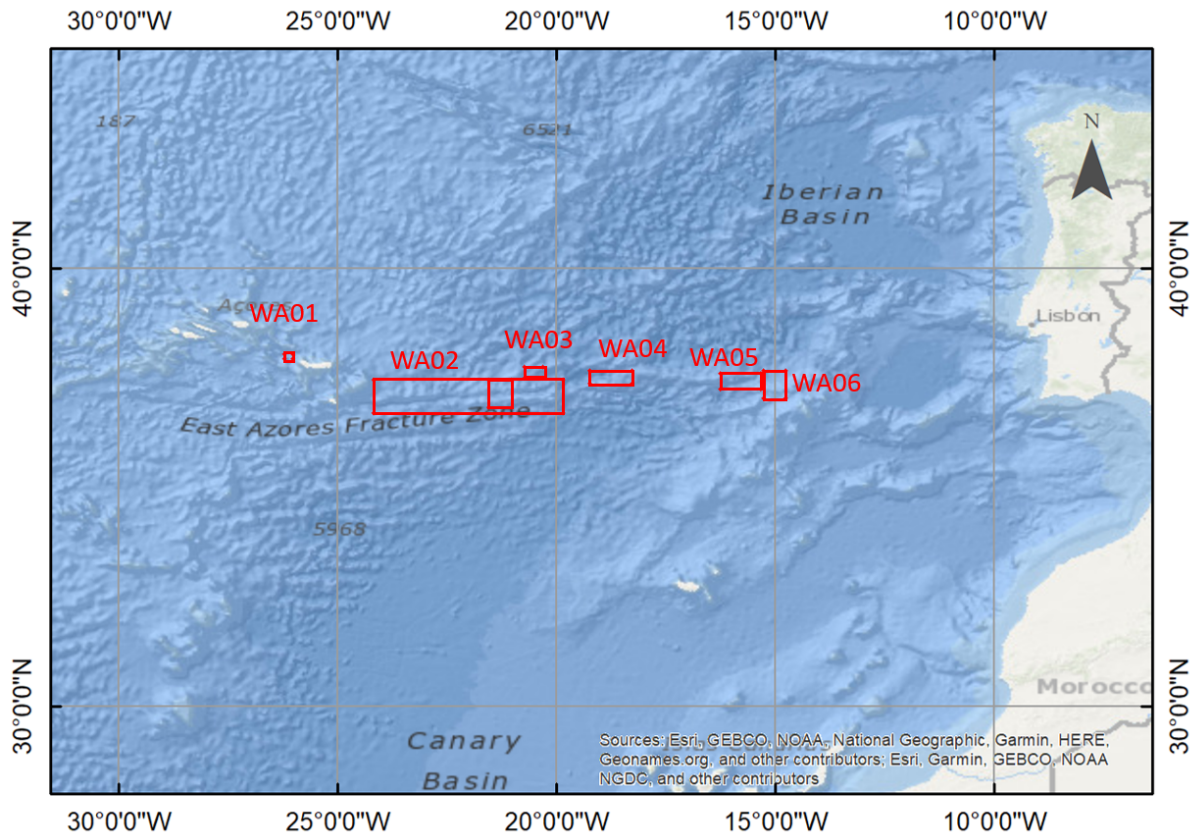
Fig. 5.2.2   Location of the working areas and stations where the Video-CTD was deployed.

Table 5.2.1   Overview of Video-CTD stations.

Station ID	Date / time (UTC)	Area	VCTD No.	Action	Latitude (N)	Longitude (W)	Water Depth (m)
M162-06	07.03.2020 / 19:06	WA01	VCTD01	in water	37°58.040′	26°05.250′	3153
M162-06	08.03.2020 / 03:53	WA01	VCTD01	on deck	37°95.888′	26°10.388′	3180
M162-11	10.03.2020 / 17:59	WA02	VCTD02	in water	37°19.658′	21°20.207′	4124
M162-11	11.03.2020 / 02:13	WA02	VCTD02	on deck	37°20.952′	21°20.324′	4120
M162-24	14.03.2020 / 19:14	WA02	VCTD03	in water	37°03.527′	21°18.733′	4185
M162-24	15.03.2020 / 01:57	WA02	VCTD03	on deck	37°05.121′	21°18.730′	4500
M162-26	15.03.2020 / 14:50	WA02	VCTD04	in water	37°04.540′	21°17.313′	4448
M162-26	16.03.2020 / 02:23	WA02	VCTD04	on deck	37°04.661′	21°18.848′	4540
M162-59	24.03.2020 / 08:58	WA04	VCTD05	in water	37°29.207′	18°40.285′	4718
M162-59	25.03.2020 / 08:58	WA04	VCTD05	on deck	37°30.310′	18°40.040′	4500
M162-60	25.03.2020 / 08:58	WA04	VCTD06	in water	37°27.866′	18°24.898′	4613
M162-60	25.03.2020 / 08:58	WA04	VCTD06	on deck	37°27.778′	18°25.838′	4650
M162-85	02.04.2020 / 05:52	WA06	VCTD07	in water	37°14.866′	14°54.947′	3515
M162-85	02.04.2020 / 11:14	WA06	VCTD07	on deck	37°14.765′	14°55.656′	3520

Niskin water sampling

Niskin water samplers triggered at selected spots at the seafloor were subsampled after retrieval on deck for various onshore laboratory analyses (Tab. 2). Major and trace element concentrations of seawater samples will be determined by using ICP-OES. Nutrients like nitrate and phosphate will be measured with an autoanalyser. Ion chromatography will be used to analyse chloride, iodine and sulphate content of the samples. Headspace gas sampling was performed by filling 120 ml glass vials, crimped with butyl-rubber stoppers, poisoning with HgCl2-solution and replacing 20 ml of water by helium gas. 10 ml of seawater was subsampled into plastic vials and stored at -

20°C for onshore nutrient analyses. DIC samples (8 ml of seawater) were stored in glass vials after poisoning with 30 microliters of saturated $HgCl_2$-solution. Subsamples for IC (1.8 ml), ICP-OES (3 ml, acidified with 30 microliter HNO3), and stable isotopes of water (~15 ml) were subsampled into plastic vials and stored at 4°C until onshore laboratory analysis.

Table 5.2.2   Niskin bottles sampled for onshore laboratory analyses.

Station	Date	Sampled Niskins (bottle no)	ICP-OES	IC	DIC	Nutrients	$\delta^{18}O/\delta D$-H_2O	Headspace gas
6VCTD1	07.03.2020-08.03.2020	1, 3, 7, 9, 11	x	x	x	x	x	x
11VCTD2	10.03.2020-11.03.2020	1, 2, 3	x	x	x	x	x	x
24VCTD3	14.03.2020-15.03.2020	1, 2, 3, 4, 5, 6, 7, 9, 10	x	x	x	x	x	x
26VCTD4	14.03.2020-15.03.2020	1, 2 ,3	x	x	x	x	x	x
59VCTD5	24.03.2020-25.03.2020	-	-	-	-	-	x	-
60VCTD6	25.03.2020	1, 2	x	x	x	x	x	x
85VCTD7	02.04.2020	1, 2, 3, 4, 6	x	x	x	x	x	x

5.2.3   Preliminary results

The first results for all stations are briefly described below. For station 6, the images are included in the text; for all other stations, the associated figures are in the appendix (section 12.2.).

Working area 01 - Station 6

Station 6 is located in working area 1. The observation of the seafloor started at 20:57 (UTC) when bottom sight was reached and continued for 4 hours. Seafloor depth at the beginning of the observation was around 3215 meters mbsl and 3180 mbsl when the survey was stopped (Fig. 5.2.3). The lowest sea depth at the profile was about 3110 mbsl, resulting in a maximum height difference of 115 meters. Temperature and potential temperature are not parallel, indicating that a correction for the adiabatic process has been made. The potential temperature along the bottom profile showed little variation and plots between 4.380 and 4.382°C.

The recorded vertical profile (upcast) data plotted in Fig. 5.2.4 shows the expected behaviour of Eastern North Atlantic Central Water for temperature, salinity and oxygen when compared to e.g. Liu and Tanhua (2019). Oxygen-rich deep Atlantic water is separated from intermediate and shallow water masses at about 1000 and 500 m, respectively. The measured methane data of deep water is slightly enriched by 1 ppm compared to surface water (Fig. 5.2.4). The calculated methane concentrations are ranging between 1.9 nM (surface water) and 4.4 nM (deep water).
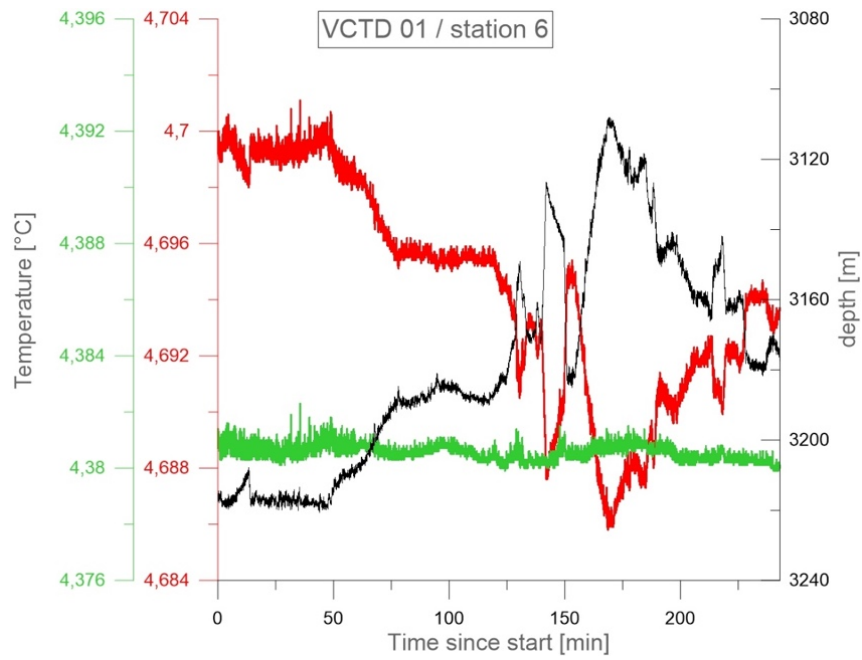
Fig. 5.2.3   VCTD01 data station 6 at bottom sight recorded between 07.03.2020 20:57:00 and 08.03.2020 01:00:00 along the predefined transect (Ship movement 0.5 kn). The green line represents calculated potential temperatures.
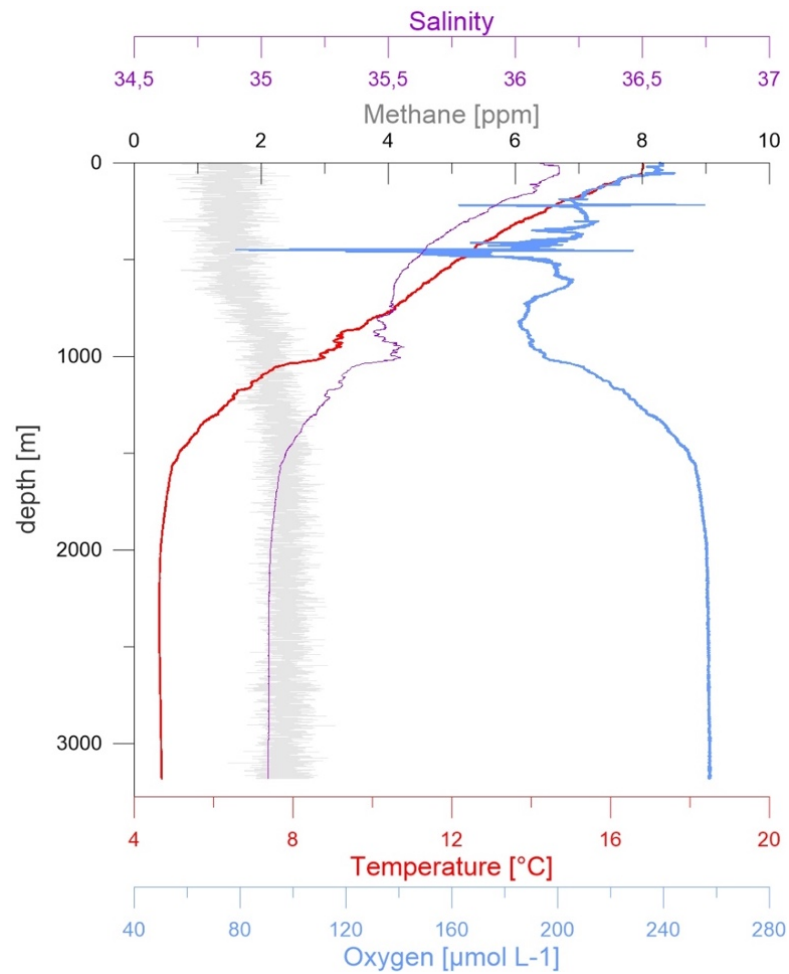
Fig. 5.2.4   VCTD01 data as upcast profile for Station 6.

In addition to the continuous video recordings, pictures at selected points have been taken. A selection of these is shown in Figure 5.2.5. Flat seabed in the trench filled with sediment and basalt rocks of the surrounding walls, partly colonised by cold water corals (upper part, Fig. 5.2.5) characterises the area. Numerous structures indicating bioactivity were seen at the seafloor of the trench (lower part, Fig. 5.2.5).
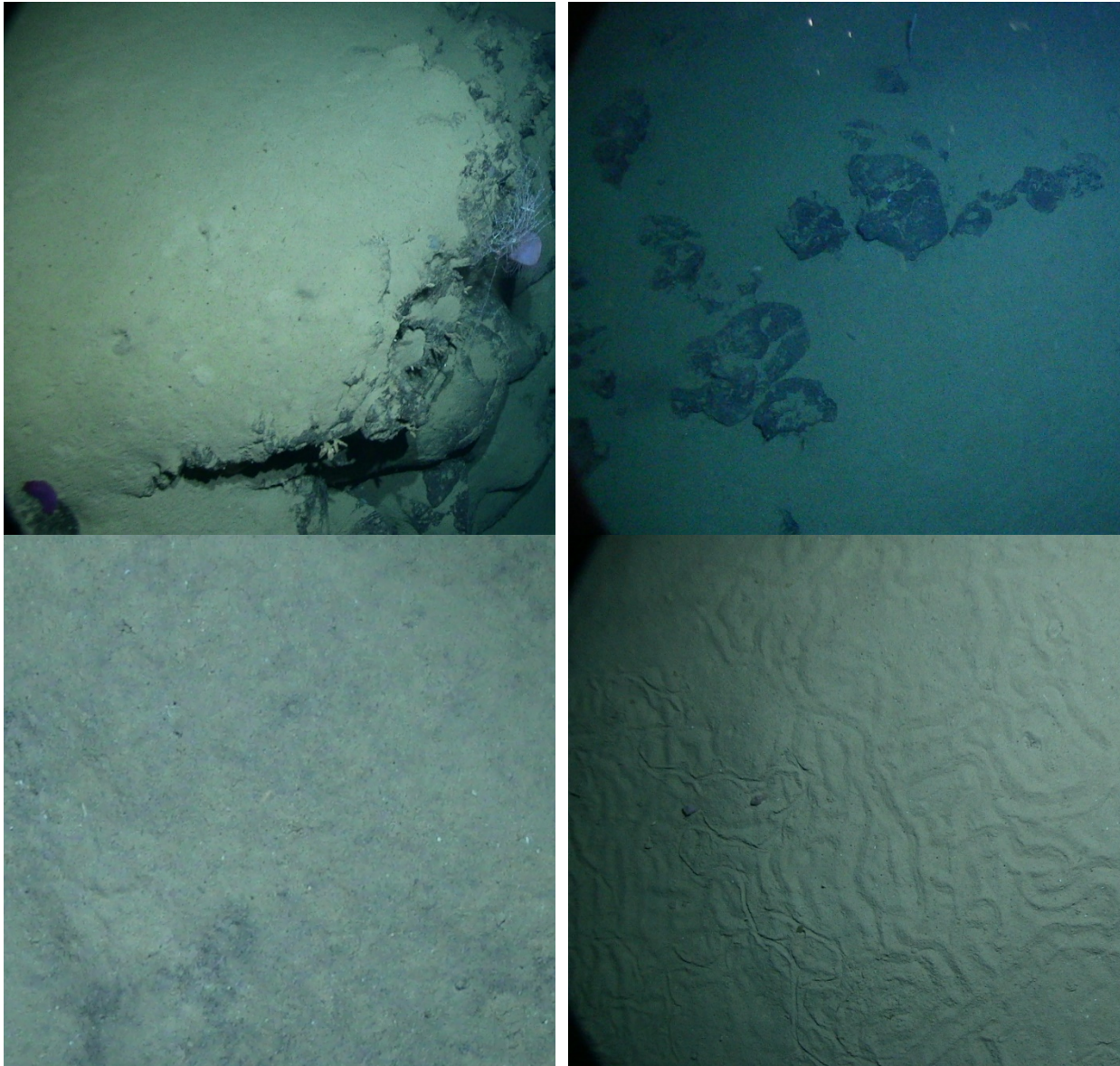
Fig. 5.2.5   Seafloor pictures taken along the transect of station 6. The upper pictures show steep walls of basalt formations covered partly by sediment and cold-water corals. The lower from the base of the trench show flat seabed of greyish sediment, mm-cm sized gravels, and numerous traces of benthic bioactivity like burrow openings and channels. The areas are about 2 by 2 meters.

Working area 02 - Station 11
Station 11 is located in working area 2. The observation of the seafloor started at 20:13 (UTC) in bottom view mode continuing until 22:51 on the predefined bottom track. Seafloor depth at the beginning of the observation was around 4124 mbsl and stayed almost constant at this level for the whole track (Fig. 12.1.1). The lowest water depth encountered during the track was 4114 mbsl, resulting in a maximum height difference of 10 meters. Temperature and potential temperature run parallel, the latter increases from 2.178°C at the start of the profile to 2.184 °C at the end.

In the vertical profile (upscale) for station 11 highest salinity and temperature are observed at the sea surface, while the oxygen maxima were detected at around 2000 mbsl (Fig. 12.2.2). The approximately 1.8 degrees colder bottom temperature compared to station 6, is attributed to the greater depth (4100 m station 11 to 3100 m at station 6). Methane corresponds to the background concentration of seawater masses as described before.

Working area 02 - Station 24

Station 24 is located in working area 2 und runs vertically to station 26. At station 24 the observation of the seafloor started at 19:25 (UTC) when bottom sight was reached and continued until 22:55 on the predefined profile. Seafloor depth at the beginning of the observation was with around 4200 mbsl at the highest level for that station (Fig. 12.2.3). Along the course the sea depth increased, with a maximum of 4550 mbsl inside the trench, resulting in in a maximum height difference of 350 meters. At the end of the course the sea depth was around 4500 mbsl. Temperature increases with increasing depth, but since this is not confirmed by the potential temperature this does not represent an actual temperature increase.

The vertical profile (upcast) confirms the oxygen maxima at around 2000 mbsl and the minima just above 1000 mbsl as observed at station 11 (Fig. 12.2.4). The bottom temperature is only slightly smaller compared to station 11 (2.14 to 2.18°C). Methane corresponds to the background concentration of seawater. The strong gradient of the seabed in the area of the trench, with abrupt edges and channel structures in which the sediments slides, are clearly visible in the pictures of the seafloor (Fig. 12.2.5). can also be seen.

Working area 02 - Station 26

Station 26 runs in east-west direction vertically to the course of station 24. At station 26 the observation of the seafloor started at 17:16 (UTC) when bottom sight was reached and continued until 20:57 on the predefined profile. Seafloor depth at the beginning of the observation was around 4400 mbsl. The profile started outside the trench but reached into it after approximately 100 minutes. From there the sea depth increased to 4570 mbsl at the end of the profile. As for station 24, the peak in the temperature at the greatest sea depth (inside the trench) is not confirmed by the potential temperature and therefore does not represent an actual temperature increase (Fig. 12.2.6).

The vertical profile for station 26 (Fig. 12.2.7) shows no significant differences of measured CTD parameters compared to the nearby station 24 (Fig. 12.2.5).

Working area 04 - Station 59

Station 59 is located in WA04 (Fig. 5.2.2). At station 59 the observation of the seafloor started at 20:04 (UTC) when bottom sight was reached and continued until 22:30 on the predefined profile. Seafloor depth at the beginning of the observation was around 4700 mbsl at the beginning of the observation and increased to around 4300 mbsl at the end of the station (Fig. 12.2.8). This means that there is a maximum height difference of 400 m for this station. As depth decreases over time a very slight increase in the potential temperature can be observed. The vertical CTD/O_2-profiles of station 59 (Fig. 12.2.9) are comparable to WA-2 hydrocast data (Fig. 12.2.7).

Indications of benthic bioturbation were observed along the track of station 59 (upper left in Annex, Fig 10). A large basalt block located on top of a small hill (extent and height could not be estimated) was also observed (Fig. 12.2.10). Probably due to the steep flanks, hardly any sediment has accumulated.

Working area 04 - Station 60

Station 60 is located in WA04 and almost as deep as station 60. The observation of the seafloor started at 07:10 (UTC) when bottom sight was reached and continued until 08:50 on the predefined profile. Seafloor depth at the beginning of the observation was around 4610 mebsl at the beginning of the observation and went down to 4670 mbsl after 45 minutes. The depth was almost constant at this level for the next 50 minutes and decreased to 4590 mbsl towards the end of the profile (Fig. 12.2.11). The potential temperature remains almost constant along the track. The vertical profile of station 60 is shown in Figure 12.2.12 in the Appendix. The seabed at station 60 shows relatively uniform sediment cover with no hard ground exposed (Fig. 12.2.13).

Working area 06 - Station 85

Station 85 is located in WA06. The average water depth of station 85 is between the water depths of the shallow station 6 (around 3200 mbsl) and all other stations (> 4000 mbsl). The observation of the seafloor started at 07:54 (UTC) when bottom sight was reached and continued until 09:06 on the predefined profile. Seafloor depth was around 3500 mbsl at the beginning of the observation and decreased to 3530 mbsl during the course of the profile (Fig. 12.2.14). Temperature and potential temperature run almost parallel and show a trend to lower values with increasing depth. The vertical data of the VCTD cast is and pictures from the seafloor are shown in the Appendix (Figs. 12.2.15-12.2.16).

Turbidity characteristics of hydrocasts

Figure 5.2.6 shows the turbidity for the vertical profile of station 59 as an example for all stations. Higher turbidity was observed at all stations in the upper 200 meters of the water column indicating highest abundancy of phyto- and zooplankton. No indications for particle plumes have been observed during towed VCTDs in bottom view mode, except when hitting the ground with the small weight hanging 1.5 m below the CTD/water sampler frame.
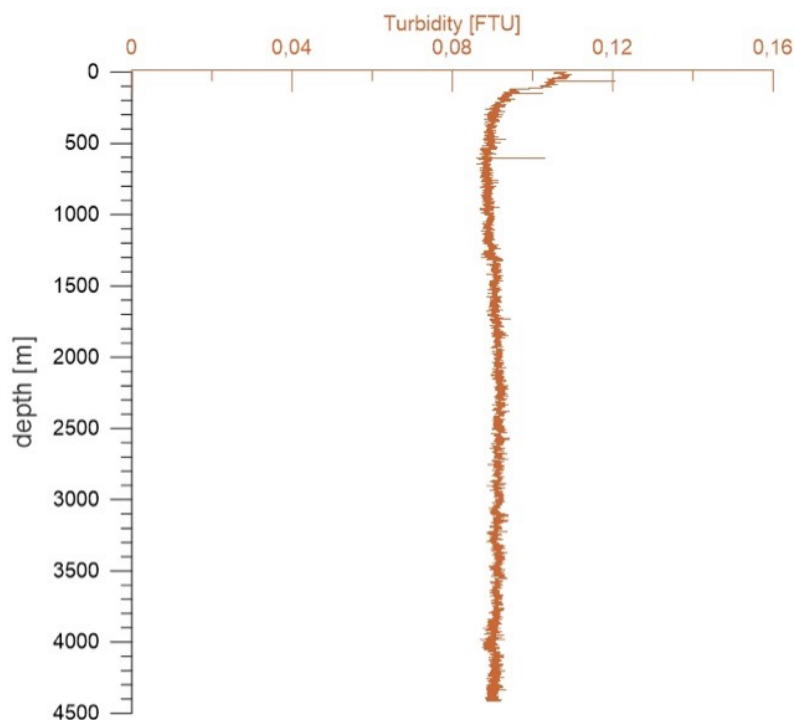
Fig. 5.2.6   VCTD05 data as vertical profile (upcast) showing turbidity and oxygen for Station 59.

Marine litter observations

Numerous spots at the seafloor contaminated by litter were observed during the Video-CTD monitoring tracks. Photos of plastic and glass bottles and plastic net are presented in Fig. 5.2.7. Detailed evaluation of recorded videos concerning marine litter will follow.
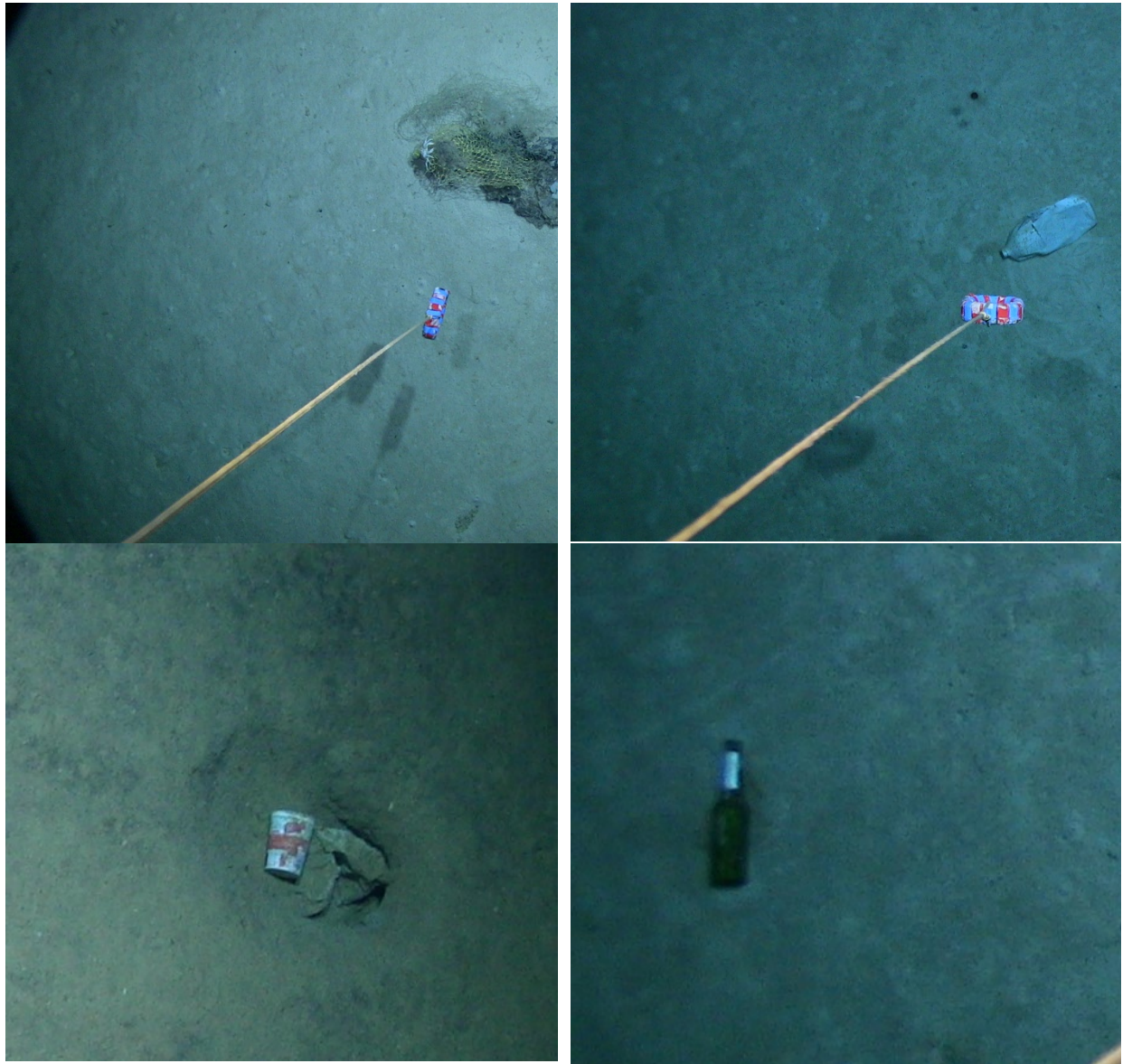
Fig. 5.2.7   Marine litter observed at the seafloor during VCTD observations. upper left: remains of a fish net; upper right: plastic bottle; lower left: yoghurt pot; lower right: glass bottle

5.3   Coring and Sedimentology

(P. Terrinha[1], P. Nogueira[2], L. Batista[1], L. Belosa[3], V. Liebetrau[4], A. Petersen[4])

[1]IPMA, [2]UÉvora, [3]CEED-UIO, [4]GEOMAR

The main aim of the sediment sampling on M162 was to find evidence for potential fluid migration pathways along the Gloria Fault. The positions of the sampling locations were carefully chosen based on multibeam and Parasound imaging. A total number of 3 deployments of the video-guided multicorer (VMUC) and 45 deployments of the gravity corer (GC) resulted in 39 successful recoveries (Table 5.3.1). An overview of all sampling stations is presented in Figure 5.3.1 (for more detailed maps cf. section 5.1).

5.3.1   Methods

The description of the gravity cores was done in each case immediately after the recovery of the core. The first samples were taken for DNA analysis, pore water, gas and biology. After this was completed, the already labelled cores were cut into two halves, archive and work. The archive half was photographed and then we proceeded to the detailed visual description followed by systematic profiling measurements of the magnetic susceptibility. Sediment description of the archive half sections included grain size, sedimentary fabric, colour, sedimentary structure, presence of fossils or fauna, disturbance and/or bioturbation, identification of paleo-redox fronts, authigenic minerals such as sulfides or carbonates. After description and core photos taken, both archive and work sections were packed and stored at 4°C in order to preserve sediment moisture and other chemical properties. In addition, measurements of thermal conductivity were carried out in the GC's by the heat flow group. For more information cf. section 5.7. The work half served for more phase-specific sub-sampling for further work in the onshore laboratories with regard to magnetic susceptibility, mineralogy and sedimentology.
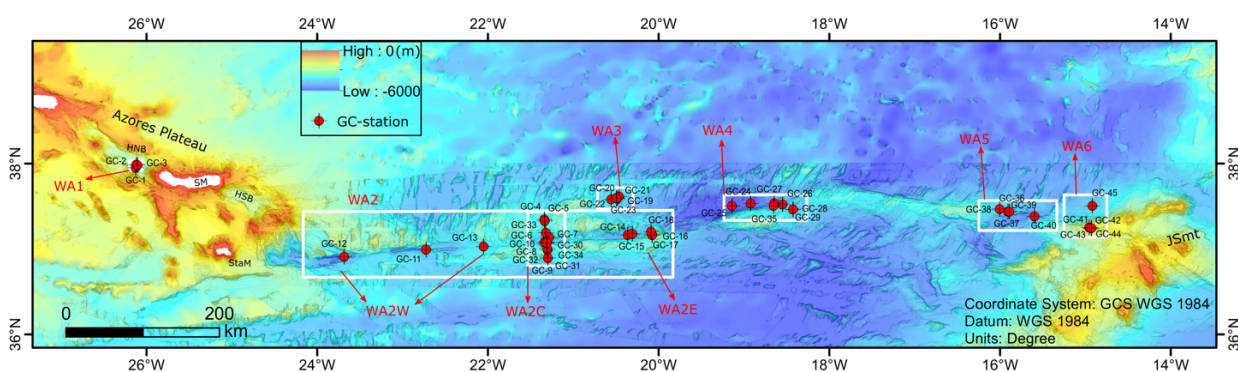
Fig. 5.3.1   Location of gravity cores.

Macroscopic Description

All cores were described visually and one log for each gravity core was produced. Additionally, the Munsell color description was registered for each part of the cores (cf. section 12.3). Examples of the magnetic susceptibility logging, core description, and photographs are shown in Figures 5.3.2-5.3.4. The remaining logs can be found in the appendix (section 12.3).

Magnetic susceptibility

The magnetic susceptibility was measured using a KT10 Magnetic Susceptibilimeter (courtesy of Dr. Helena Sant'Ovaia of the Univ. Porto, Earth Sciences Institute, Porto pole). The measurements

were generally made each 5 cm except when the core was very monotonous (each 10 cm) or when singular sedimentary horizons occurred in between each 5 cm mark. One magnetic susceptibility log was produced for each core as exemplified in Figure 5.3.2. The remaining logs are in appendix (section 12.3).

Tab. 5.3.1   List of gravity cores sampled on M162.

Date	Station N°	GC N°	Latitude N°	Longitude W°	Recovery (cm)
07.03.20	M162_3	GC-1	37°57.200	026°07.513	140
07.03.20	M162_4	GC-2	37°59.401	026°07.124	180
07.03.20	M162_5	GC-3	37°58.852	026°06.467	140
12.03.20	M162_15	GC-4	37°20.647	021°20.327	156
12.03.20	M162_16	GC-5	37°19.711	021°20.239	155
12.03.20	M162_17	GC-6	37°04.541	021°18.818	380
13.03.20	M162_19	GC-7	37°08.145	021°16.855	353
13.03.20	M162_20	GC-8	37°04.431	021°18.772	0
13.02.20	M162_21	GC-9	36°53.793	021°17.742	382
14.03.20	M162_23	GC-10	37°04.604	021°20.282	273
16.03.20	M162_29	GC-11	36°59.472	022°43.585	227
17.03.20	M162_32	GC-12	36°54.458	023°41.117	0
17.03.20	M162_33	GC-13	37°01.749	022°03.178	250
18.03.20	M162_35	GC-14	37°09.949	020°21.790	350
18.03.20	M162_36	GC-15	37°10.566	020°18.494	260
19.03.20	M162_39	GC-16	37°09.821	020°04.717	0
19.03.20	M162_40	GC-17	37°09.844	020°04.558	0
19.03.20	M162_41	GC-18	37°12.248	020°05.313	20
20.03.20	M162_43	GC-19	37°35.378	020°29.070	127
20.03.20	M162_44	GC-20	37°35.937	020°29.592	243
20.03.20	M162_45	GC-21	37°36.973	020°27.729	20
21.03.20	M162_47	GC-22	37°34.964	020°33.408	276
21.03.20	M162_48-	GC-23	37°35.766	020°29.531	109
23.03.20	M162_52	GC-24	37°32.176	018°55.391	0
23.03.20	M162_53	GC-25	37°30.396	019°08.508	0
24.03.20	M162_57	GC-26	37°31.462	018°32.801	449
24.03.20	M162_58	GC-27	37°32.138	018°38.737	276
25.03.20	M162_62	GC-28	37°27.796	018°25.486	423
26.03.20	M162_64	GC-29	37°27.804	018°25.437	484
27.03.20	M162_65	GC-30	37°04.758	021°18.743	246
27.03.20	M162_66	GC-31	36°59.253	021°18.182	251
27.03.20	M162_67	GC-32	37°00.520	021°18.260	293
28.03.20	M162_69	GC-33	37°11.478	021°19.411	163
28.03.20	M162_70	GC-34	37°04.286	021°18.703	136
29.03.20	M162_72	GC-35	37°30.418	018°39.282	193
30.03.20	M162_76	GC-36	37°26.365	015°54.463	40
30.03.20	M162_77	GC-37	37°26.182	015°53.518	140
30.03.20	M162_78	GC-38	37°27.993	016°00.397	270
01.04.20	M162_80	GC-39	37°26.226	015°53.515	40
01.04.20	M162_82	GC-40	37°23.140	015°35.754	484
02.04.20	M162_88	GC-41	37°15.262	014°57.488	60
03.04.20	M162_90	GC-42	37°14.755	014°55.966	126
03.04.20	M162_91	GC-43	37°14.754	014°55.968	126
03.04.20	M162_92	GC-44	37°14.753	014°55.967	128
03.04.20	M162_94	GC-45	37°30.358	014°55.108	300
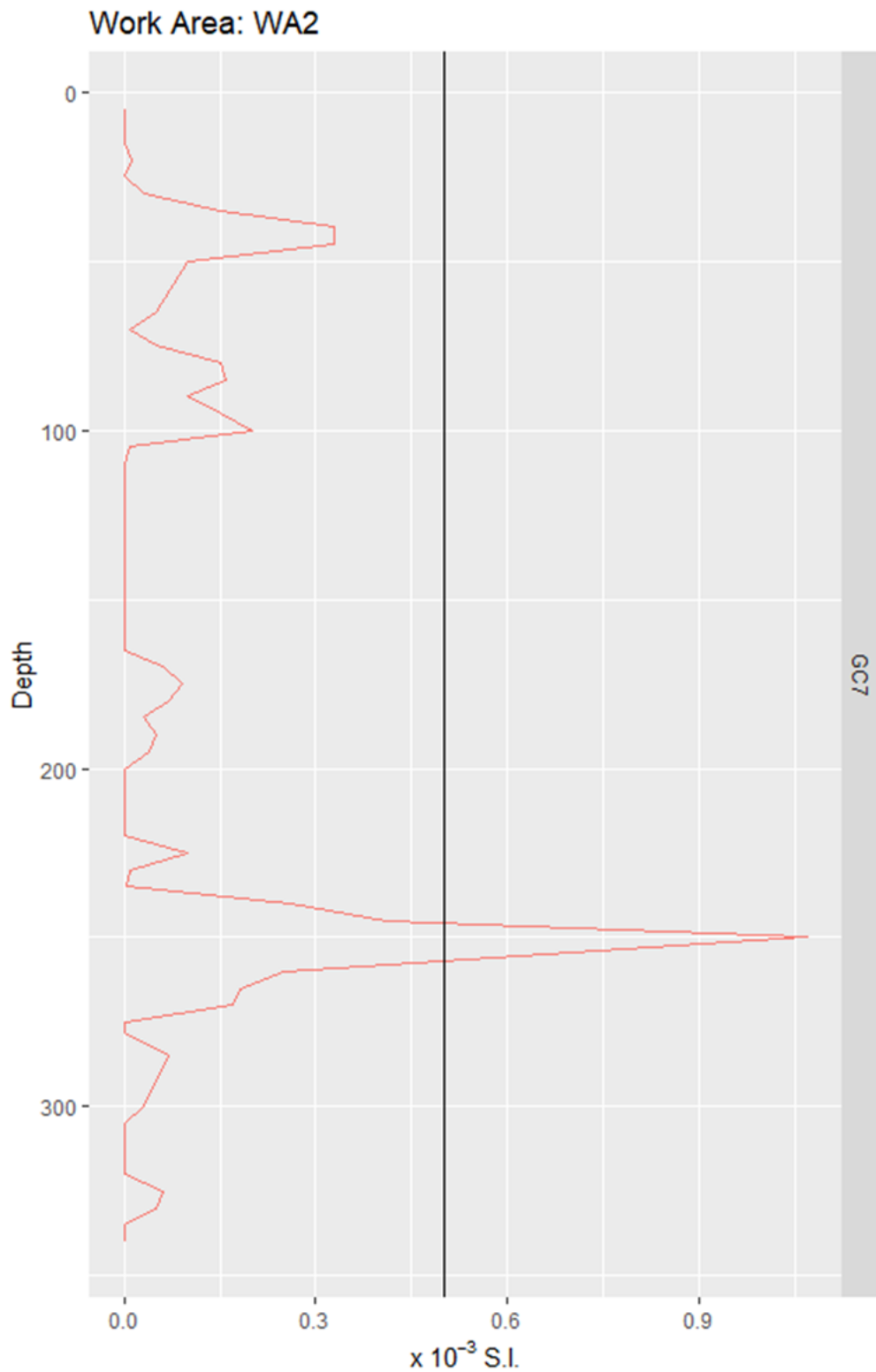
Fig. 5.3.2   Magnetic susceptibility plot for the Gravity Core 19-GC7. Note the coincidence of the large peak at 250 cm and the oxi-red spots in the visual description. The secondary peak at ~45 cm is close to the dark minerals event in the visual description.

GRAVITY CORE LOG   **M162**

Date: 2020/03/13 Hour: 10h32 Lat: 37º 8.353 N   Lon: 21º 16.375 W
Station: 19   WA- 2   GC- 7   Depth: 4491

Carbonaceous silt w/Foram. size > upwards

Very fine sand w/Foram. and dark minerals
Carbonaceous silt

Laminated layer
Very fine sand w/Foram. sparse lithoclasts
Carbonaceous silt
3x1 Mound
Very fine sand w/Foram.

Argilaceous silt w/Foram. small

Oxi-red spots

Argilaceous silt w/Foram. small w/igninbrite cobles

Oxi-red spots
Sand w/Foram.

Clay w/Foram. size of silt

Argilaceous silt w/Foram. dark clay matrix (O.M.?)

Argilaceous silt w/Foram. small w/igninbrite cobles
Foram. Sand w/ igninbrite size 1cm

Argilaceous silt w/Foram. small w/igninbrite cobles

Oxi-red spots
Silt w/Foram.

Argilaceous silt w/Foram.
silt mound w/Foram.

Vertical green tubes: nontronite? epigenetic epidote? zeolite?
1mm Foram. sand
Very fine sand w/dark minerals and clay matrix

Argilaceous silt w/Foram.

Very fine sand and silt w/ Foram.

Silt and clay

Fine bands of sand

Silt w/Foram.

Thining upwards
Erosive base
Sand channel
Foram.
Nodule
Volcanic pyroclast

Fig. 5.3.3   Example-Log of visual core description.

5.3.2   Preliminary Results

The recovery of the gravity cores varied between 0 and 449 cm. There is no correlation between water depth and length of recovery. Although the results are still preliminary non-recovery or poor recovery occurred in sites where the sub-bottom imaging of the sediment thickness was meagre or the sediments appeared deformed, disturbed or not well bedded. The visual macroscopic inspection of these cores allowed for identifying various types of sediment that can be described as follows:

- I) Pelagic sediments

These constitute the largest volume of sediments in the collected cores. They are made up of silt to clay fractions containing very fine-grained sand particles and foraminifera shells (forams). The finer fraction is rich in carbonate that probably results from dissolution of the forams. Layers of "foram sands" occur episodically. Volcanic clasts occur episodically within the pelagic sediments. These clasts are pumice, possibly resulting from distal eruptions that deposited by increasing their density after degassing.

- II) Mass transport deposits (MTD)

The MTDs in these cores are turbidites. They consist of upward fining sequences usually with an erosive base. The basal deposit is usually of fine to medium grain sand grain size fining upwards into the silt and clay pelagic sediments. The sandy fraction often consists of "foram sands" with detrital sandy particles of volcanic nature.

- III) Volcanoclastic sediments.

Horizons consisting of siliceous sands usually less than 2 cm of thickness occur episodically. Visual identification indicates that some of these horizons are repeated in various cores along the study area, suggesting a tele-volcanic origin. These horizons consist of fine to very fine-grained mono-mineralic sands. The main mineral constituent is, possibly, quartz. Dark minerals also occur as well as volcanic clasts up to 3 cm in diameter. These are pumice and these horizons always have magnetic susceptibility peaks.

Diagenetic effects could also be observed as described below.

- i) Black stains. These consist of alteration of organic matter, usually foraminifera or bioturbation parts of the sediments.
- ii) "leopard skin-like" pattern; probably the same process as the previous one but very pervasive. In some cores this pattern vanishes upwards suggesting reactions caused by upward migrating fluids (Fig. 5.3.5). Furthermore, this patchy colouring pattern is instable once the core is opened and in contact to ambient atmosphere.
- iii) light green horizons. These are generally of three types: i) restricted to approx. 1 cm thick bands that are of the same grain size of the enclosing sediment, ii) faint green tinted parts of the core that vanish vertically and can be up to approx. 10 cm of thickness; iii) discrete darker and more intense green spots either around detrital particles or bioturbation features. All these are highlighted in the logs and one possibility is that they consist of alteration of basic volcanic materials into nontronite.
- iv) light brown stains. These appear to be the result of oxidation. They can be discrete or distributed along large volumes of the cores.

Fig. 5.3.4   Gravity core GC-7. Top: Log description of gravity core GC-7. Bottom: photograph of GC-7.
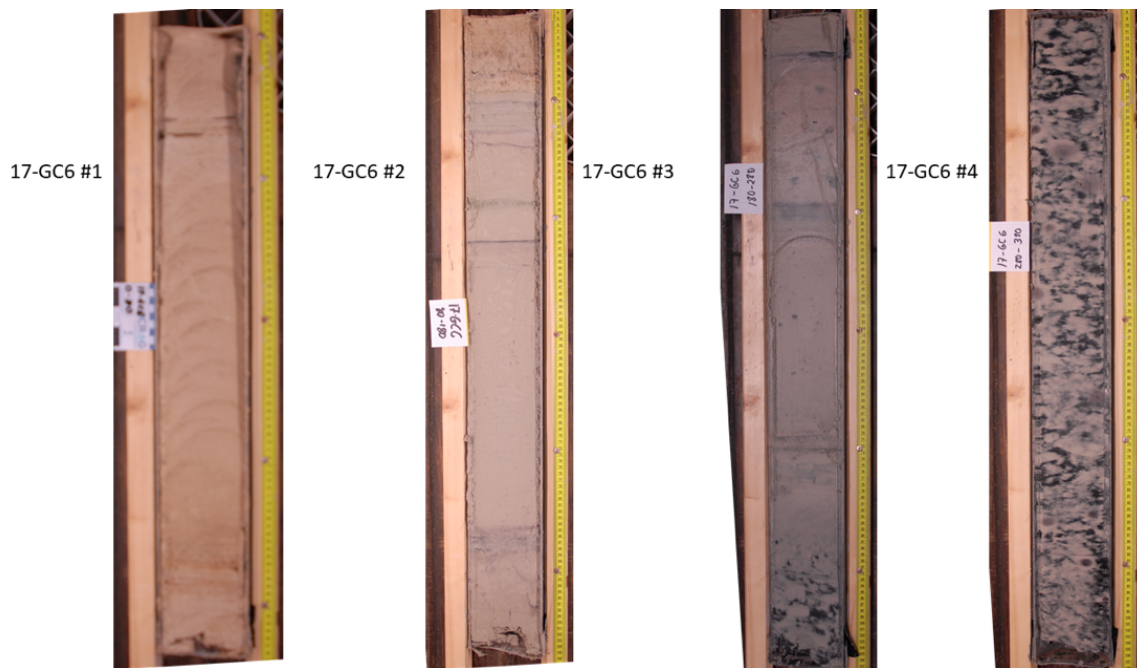
Fig. 5.3.5   Example of "leopard-like skin" pattern of black stains distribution. Note how the pattern vanishes upwards.

5.4   Meiofauna communities

(H. Adão[1], K. Sroczyńska[1])

[1]UÉvora

Investigating processes that drive species spatial distribution, biodiversity and interactions in deep-sea is essential to comprehend the ecosystem functioning of this least explore biome of Earth (Danovaro et al. 2017). In deep-water sediments, small organisms such as nematodes (meiofauna) are the dominant metazoans that feed on highly abundant microbes providing a link to support higher trophic levels (i.e. macrofauna and megafauna; Giere 2009; Danovaro et al. 2008; Brandt 2008). Therefore, understanding the factors that mediate the interactions between the microbes and nematodes and their concomitant diversity and abundance will determine the functioning of the entire deep-sea benthic trophic food web (Lohrer et al. 2004). Sediment microorganisms are the primary mediators of biogeochemical processes, including the processing of organic matter, with strong potential impact on sediment trophic conditions (Thakur and Geisen, 2019). We know that primary drivers of nematode distributional patterns in deep sea are likely mediated by the microbial communities and different sedimentary conditions (i.e. organic matter availability, oxygen concentration, sediment grain size; Moens et al. 2014). However, existing inconsistencies among different studies conducted at different regions suggest that other unknown biotic and abiotic processes are shaping the nematode distribution patterns (Rosli et al. 2018). Additionally, lack of data on the interactions between bacteria and nematodes in this ecosystem impede to establish a direct link between sediment biogeochemical conditions and nematodes diversity and abundance. Recent development of sequencing technologies and the applicability of DNA metabarcoding make possible to assess the sediment microbial biodiversity. By combining metagenomics with morphological approach this project aims to respond a question to what extent sedimentary biogeochemical conditions and microbial diversity shape the distribution of the benthic nematode communities on the abyssal plains along the Gloria Fault (North-West Atlantic). Our hypothesis assumes that the biogeochemical conditions of the sediment will strongly determine nematode abundance and diversity patterns. Additionally, we expect that these patterns will be also correlated with the microbial diversity and abundance. At last, this study will provide the first database of the spatial distribution patterns of benthic nematode communities and microbiome on the abyssal plains along the Gloria Fault, Mid-West Atlantic.

Specific Objectives are:

- to investigate large spatial and vertical distributional patterns of nematodes communities along Oceanic Plate boundary (Gloria Fault)
- to investigate the drivers of the nematode distributional patterns by simultaneous analysis of the geochemical composition of pore water (cf. section 5.6).
- to simultaneously analyse the microbial communities associated to sediments using metabarcoding approach (microbiology group)
- to establish the link between sedimentary conditions, microbial diversity and nematode communities along the Oceanic Plate boundary (Gloria Fault)

5.4.1   Methodology and sampling overview

Nematode community sampling from Gravity Cores (GC)

From each gravity core (GC) the first top 10 cm of sediment was collected for nematode community characterization. Collected 10 cm of sediment was sectioned vertically with the following divisions: 0-1 cm; 1-4 cm; 4-6 cm and 6-10 cm.

Each vertical sub-section was stored in pre-labelled 100 ml plastic container and immediately fixed with 70 % ethanol. Following fixation, the samples were sealed with laboratory parafilm and stored for further analysis in the NemaLab laboratory at the University of Évora, Portugal. Simultaneously the sample for grain size analysis is taken from each layer. Simultaneously the sample for grain size analysis is taken from each layer.

Nematode community sampling from Multicore (MUC)

Sampling of meiofauna obtained from MUC followed the similar procedure as the samples obtained from GC. First, the supernatant water was siphoned off the core. Secondly, the core was carefully sliced followed the above division: 0-1 cm; 1-4 cm, 4-6 and 6-10 cm. All the sediment slices were immediately stored in pre-labelled 250 ml plastic containers and fixed with 70 % ethanol for further analysis in the laboratory. Simultaneously the sample for grain size analysis is taken from each layer.

DNA sampling for microbial characterization from Gravity Core (GC)

From each top 10 cm of sediment, two replicate samples for DNA were taken. Samples were taken using plastic, sterilized syringe cut on the top. Two 5ml eppendorfs were filled with the sediment. Samples were immediately stored in liquid nitrogen container. As the first 20 cm of gravity core are highly mixed, DNA sample were taken without the distinction for separate sub-sections.

DNA sampling for microbial characterization from Multicore (MUC)

From each sediment slice, two replicate DNA samples were taken. Samples were taken using plastic, sterilized syringe cut on the top. Two 5ml eppendorfs per sliced sub-section were filled with the sediment and immediately stored in liquid nitrogen container. Simultaneously to nematode community sampling and DNA, the measurements for oxygen concentration and samples for fatty acids and pore water analysis were taken.

In total, 119 samples (26 for DNA and 88 for granulometry analysis; Table 5.4.1) from GCs and 23 samples (12 for DNA and 8 for granulometry analysis; Table 5.4.2) from MUCs were taken for meiofauna characterization.

Nematode-Bacteria community composition

During the campaign, in four cores (GC 10, 20, 32, 35) the presence of an ancient superficial layer of the sediment surface was identified below the present surface. The oxygen records demonstrated that these ancient layers still have high oxygen concentrations, similar to those found on the surface (cf. section 5.5). Due to high oxygen concentrations and presence of bacteria it was hypothesized that these ancient superficial layers might host unique nematode and bacterial assemblages. It created an opportunity to investigate nematode and bacteria interactions in the habitat that stayed separated from the superficial layers of the sediment for thousands of years and therefore was naturally cut off from predatory control and might have evolved its own nematode and bacterial communities' characteristics and specific bacteria-nematode interactions. For this reason, we

decided to additionally take nematode and DNA samples from these ancient layers. In total five samples for meiofauna and DNA from ancient layers were collected (Table 5.4.3).

Samples for nematode identification will be further analysed in the NemaLab, University of Évora, Portugal; Samples for bacterial community (DNA) will be analysed by the microbiology group from ETH Zürich, Switzerland and samples for granulometry analysis will be analysed at IPMA, Lisbon.

5.5   Microbiology

(C. Glombitza[1], J. Li[1], S. Arn[1])

[1]ETH-Zurich

5.5.1   Subsurface microbiology – study aim and expected outcome

The aim of microbiological research during expedition M162 and post-cruise research is to determine the abundance, community composition and activity of microbial communities in the deep sediments at the Gloria Fault and potential relations, adaptations and/or stimulations of the deep sedimentary biosphere related to fluid flow from the underlying oceanic crust and mantle.

Water-rock interactions such as serpentinization, generate hydrogen and small organic compounds, i.e. methane and small organic acids (Eickenbusch et al., 2019; Schrenk et al., 2013). These compounds are substantial components of serpentinizing fluids and can be transported into sediments overlying the crust and mantle when fluids intrude the sediments. Hydrogen and organic acids as well as methane are important substrates in microbial metabolisms (Adhikari et al., 2016; Glombitza et al., 2019; Nealson et al., 2005; Sørensen et al., 1981) and consequently fluid flow from the crust and mantle has the potential to feed and stimulate or alter the sedimentary microbial biosphere.

Additionally, microbial abundance, activity and community composition in the abyssal sediments at the North Atlantic are not known until today and consequently our findings will contribute to closing significant gaps in deep biosphere exploration.

5.5.2   Dissolved oxygen and hydrogen

Hydrogen Sampling

Samples for analysis of dissolved hydrogen were taken with 3-mL cut-off syringes from the bottom end of each Gravity Core (GC) section immediately after core sectioning or at a resolution of 1-2 cm from a Multi Corer (MUC). Two replicates of 3 cc sediment were taken with a syringe and placed inside 10-mL gals vial and completely filled with brine amended with sodium azide (38.5 mM) and sealed with a butyl rubber stopper and crimp cap avoiding any trapped air bubbles. The samples were used for gas chromatography measurements using the extraction method (Lin et al., 2012). Another set of two replicates of 3 cc sediment were placed in 10-mL gals vials, closed with a butyl rubber stopper and crimp cap, the headspace was flushed with N_2 for 2 min and the samples were subsequently incubated at near in-situ temperature (4°C, incubation method, (Hoehler et al., 1998; Lin et al., 2012).

Hydrogen Analysis by RCP GC

Extraction method: 2 mL of N_2 gas were added to the brine filled sample vials to form a headspace by replacing 2 mL of the brine and the samples were shaken vigorously on a vortex®. The headspace gas was analysed on board by gas chromatography.

Incubation method: Samples stored in N2-flushed glass vials where incubated at 4°C in a fridge at the on-board laboratory. Headspace was measured by gas chromatography on board the ship after 3 days and again after 10 days and after 21 days (mainly post cruise) to verify establishment of a steady-state condition in the vial. Gas chromatography with reduced compound detector (RCP GC): Hydrogen concentrations in the headspace of extraction and incubation vials were measured by a Peak Performer 1 GC (Peak Laboratories, USA) equipped with a reduced compound (RCP) detector. About 2 mL of a gas sample was injected manually in the GC equipped with a 1-mL sample loop. Column temperature was set to 105°C. The RCP detector consists of a HgO bed operated at 265°C at which HgO is reduced to Hg(g) by the reducing analyte and the amount of Hg(g) is quantified by adsorption of UV light inside a closed chamber. Calibration was done by a one-point calibration using a certified H2 standard (5.07 ppm in N_2, Linde).

Oxygen microsensor measurements

Dissolved oxygen was measured with a Clark-Type needle microsensor (OX-NP, Unisense, DK) and recorded with a Unisense Field Multimeter. Calibration was done by a two-point calibration with 100% and 0% air saturated water at approximate in-situ core temperature (i.e. 6°C) on a daily basis. The sensor needle was inserted through small holes drilled in the core liner immediately after core recovery and cutting into 1-m sections and subsequent microbiological sampling at fresh section cuts on board RV Meteor. Resolution of measurements was decided during measurements with the aim to generate best possible profiles and reached from 3-20 cm distance between subsequent measurements points.

5.5.3   Dissolved microbial metabolic intermediates in interstitial water (IW)

Interstitial water sampling

Interstitial water (IW) samples from GCs were obtained as shared samples with the on board geochemistry team recovered from pressing of 30-50 cc sediment under Ar gas stream at 4°C in the cold room. IW from MUC was sampled by cleaned Rhizon sampler (Seeberg-Elverfeldt et al., 2005) in 1 cm intervals at 4°C in the cold-room. Aliquot of 2 mL pore water was stored in pre-heated (5h, 450°C) 4-mL Zinser® glass vials for analysis of volatile fatty acids (VFAs) (Glombitza et al., 2019, 2015, 2014), another 5-mL aliquot was stored in acid-washed 10-mL glass vials, sealed with crimp-cap for analysis of methanol (Zhuang et al., 2014). All pore water samples were stored frozen at -80°C.

Dissolved metabolic intermediates: quantification and thermodynamic modelling

Dissolved microbial metabolic intermediates, i.e. volatile fatty acids (format, acetate, propionate, butyrate, valerate) and methanol will be quantified from the interstitial water. These compounds are primary products of organic matter degradation by hydrolysis and fermentation and at the same time act as substrates for terminal mineralization processes, such as nitrate, metal, and sulfate reduction or methanogenesis. Concentrations of these metabolic intermediates typically represent the equilibrium between production and consumption processes and determine the energy yield of the respective metabolic process and hence the metabolic energy yield. Determined concentrations will be used for calculating microbial metabolic rates and energy turnover in the sediments by calculating the Gibbs energy yield of the metabolic redox reaction under in-situ conditions and relating these to the determined substrate turnover rates (see section 4.2.).

Volatile fatty acid (VFA) concentrations in IW will be determined at ETH Zurich by a two-dimensional ion chromatography (2D IC) according to a previously published protocol (Glombitza et al., 2014).

Methanol concentrations in IW will be determined by gas chromatography in collaboration with Dr. Gunagchao Zhuang (Ocean University of China) according to a previously published protocol (Zhuang et al., 2014)

5.5.4   Microbial community composition, abundance and activity

Sampling

DNA samples: Samples for DNA analysis were taken with sterile cut-off syringes from the bottom of each section-end immediately after cutting (GC) or at a resolution of 1 - 2 cm depth (VMUC). VMUC samples were taken inside the cold room. We sampled two replicates of 4 cc, and stored them in cryovials frozen immediately at -178°C in a liquid nitrogen cooled dry-shipper.

Microbial activity assay samples: Samples for microbial activity measurements were sampled with cut-off syringes from the bottom of each section-end (GC) or at a resolution of 2 - 4 cm (MUC). MUC samples were collected inside the cold room. Eight replicates of 3 cc each where sampled from every section-end and placed in 20-mL pre-heated (450°C, 5 h) glass vial, sealed with a butyl rubber stopper and crimp-cap. The headspace was flushed with Nitrogen for about 2 min and the vials were then stored at near in-situ temperature (4°C) in the cold room. The eight replicates will be distributed for different activity assays (i.e. methanogenesis, sulfate reduction) as described below.

Backup samples: We sampled 30-50 cc sediment from the bottom of each section (GC) or at a resolution of 1 – 2 cm (MUC) with a clean spoon and stored them inside a sterile plastic bag (Whirlpack®) at -80°C. These samples will serve as back-up for DNA work in case of very low biomass content of the sediment and will further serve as back-up sample for additional chemical or biological analysis if needed during post cruise research.

In total we collected 1222 individual sediment samples for microbiological analysis and experiments and for hydrogen analysis by incubation and extraction methods (Supplementary Table WW – (Geochemistry and Microbiology Samples).

Microbiological analysis and experiments at ETH Zurich

Microbial community composition and abundance: We will determine the presence, abundance and composition of bacterial and archaeal communities in abyssal sediments of the North Atlantic which, to the best of our knowledge, have never been investigated before. We seek to reveal the relation between environmental (geochemical, sedimentological) and biological variables (syntrophic partner organisms) in controlling aerobic respiration as well as sulfate and methane-cycling and the microbial community structure. In addition, we will try to identify potential changes and adaptation of the microbial community to fluid flow from the underlying mantle. We will extract microbial DNA with a modular extraction protocol (Lever et al., 2015). Total bacterial and archaeal populations will be quantified by quantitative PCR (qPCR) of 16S rRNA genes. Total populations of methane-cycling archaea will be quantified by qPCR of methyl coenzyme M reductase (mcrA) genes. The zonation of methane-cycling archaeal communities and total microbial communities will be determined by next-generation sequencing (NGS) of PCR-amplified mcrA and 16S rRNA genes. All NGS will be done at the ETH Zurich's Genetic Diversity Center (GDC; www.gdc.ethz.ch) using a MiSeq Personal Sequencer (Illumina Inc.).

Anaerobic metabolic activity: We will use samples from anoxic sediment intervals to measure rates of anaerobic microbial metabolism, in particular of microbial sulfate reduction (SR) and methanogenesis (MG). This will provide insight into anaerobic microbial activity in abyssal sediments and may reveal potential changes in activity as a result of fluid flow from the underlying mantle and may reveal a potential stimulation by a supply of energetic substrates (e.g. H_2 or VFAs) generated by abiotic processes during mantle rock-water interactions (Eickenbusch et al., 2019; Russell et al., 2010). The eight replicates will be distributed to different activity assays with respect to information obtained from the IW chemical composition determined on board the ship. For example, samples from within the sulfate zone will be predominantly used for measurement of microbial SR rates whereas in low-sulfate sediments determination of microbial MG rates will be prioritized. Sediments will be incubated under in-situ temperatures with and without addition of potential electron donors (i.e. hydrogen, methane, acetate, and formate for SR and bicarbonate, methanol and hydrogen for MG). All incubations will be at least performed with two replicates. For SR, we will incubate samples with a trace amount of radio-labelled sulfate ($35SO_4{}^{2-}$), samples for MG rates will be incubated with trace amounts of radio-labelled bicarbonate and/or methanol ($H14CO_3{}^-$ and/or $14CH_3OH$). Turnover rates will be determined according to standard protocols (Beulig et al., 2018; Glombitza et al., 2016; Jørgensen, 1978; Kallmeyer et al., 2004) in the radio isotope laboratory at ETH Zurich (CH) and EAWAG Kastanienbaum (CH).

5.5.5   Onboard results

Dissolved oxygen

General Note: Uppermost data points (<30 cmbsf) obtained with the oxygen sensor should be considered with care and may represent an overestimation of the in-situ oxygen concentrations. Generally, equilibration to a stable value was significantly delayed at these sampling points which may result in overestimation. Additionally, the topmost parts of the gravity core were usually very soft and mixed with sea water, resulting in large void space inside the liner above the soft sediment and significant contamination from air should be expected following the time needed for core recovery, sectioning and microbiological sampling all of which occurred prior to the sensor measurements. Bottom water oxygen concentrations obtained during CTD survey may be considered to replace the topmost sensor measurements for a realistic profile.

Oxygen vs. depth profiles are shown in Figures 5.5.1-5.5.4 (cf. Tab. 12.5.1). Generally, sites at slightly higher elevations on ridges, hills or terraces had lower recovery due to thin sediment cover, and were usually oxygenated throughout the recovered sequence of approx. 1.4 m, i.e. sites M162-15 (GC04) and M162-16 (GC05). The very deep oxygen penetration found e.g. at sites M162-21 (GC09) and M162-29 (GC11) to 3.5 and 2.5 mbsf does not show the typical clear consumption trend but decreases rather linear with depth with broad scattering and may be related to fluid down-flow. Sites located inside deeper successions, i.e. sites M162-17 (GC06), M162-19 (GC07), M162-23 (GC10), M162-35 (GC14) and M162-62 (GC28) had higher sediment recovery during coring and oxygen profiles showed clear diagenetic consumption profile with oxygen penetration depth to around 1.00 to 1.50 mbsf and remained anoxic below.
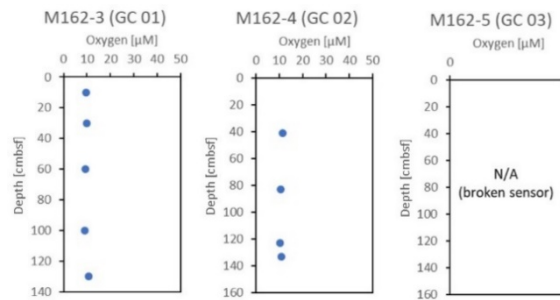
Fig. 5.5.1   Dissolved oxygen profiles in GC 1-3.
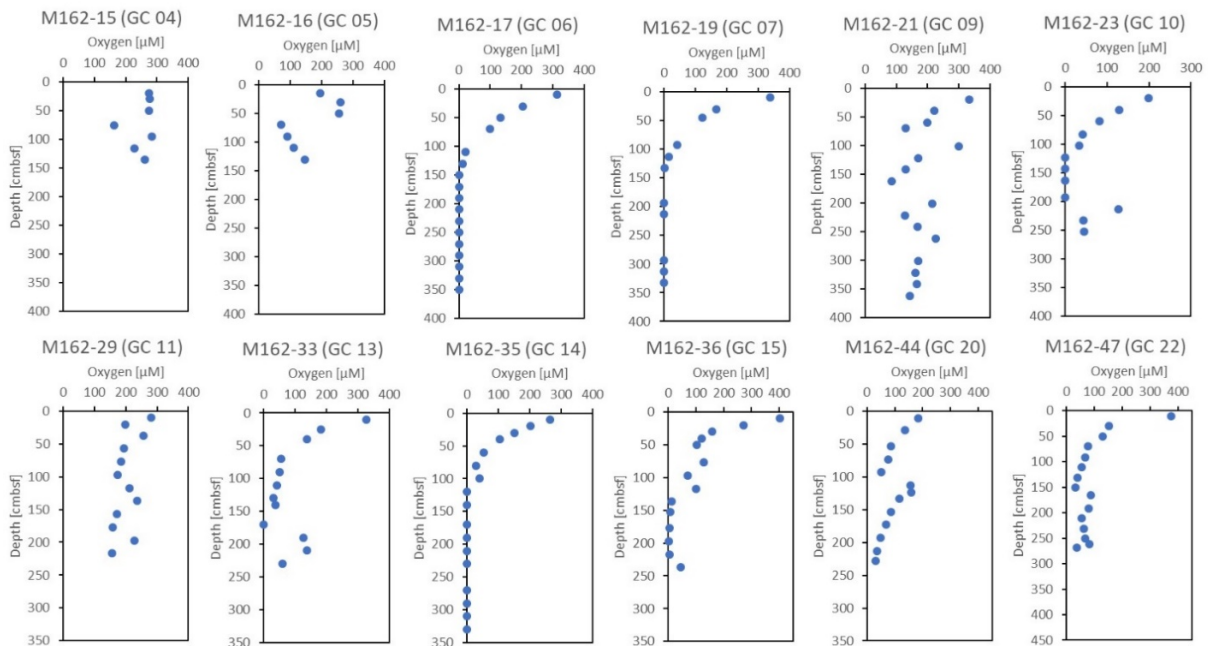
Fig. 5.5.2   Dissolved oxygen profiles in GC 4-22.
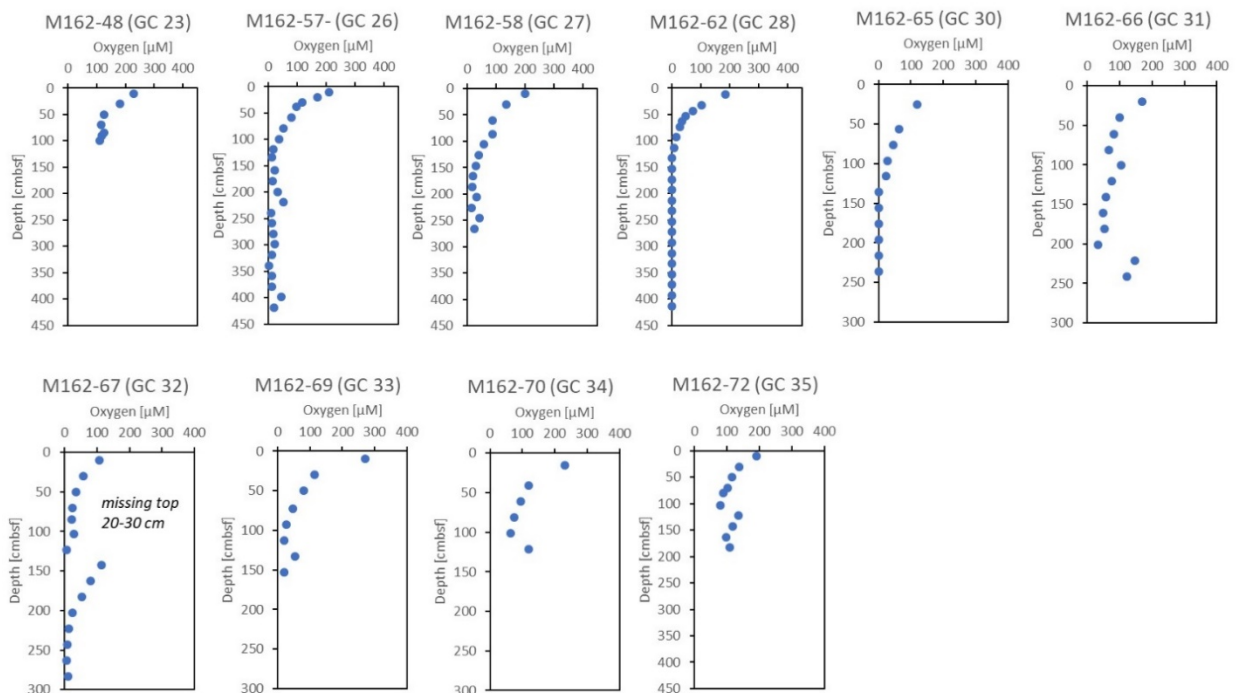
Fig. 5.5.3   Dissolved oxygen profiles in GC 23-35.

At sites M162-90 (GC 42) at 3546 m water depth and M162-92 (GC 43) at 3547 m water depth, oxygen was already depleted at 35 cmbsf which is the shallowest oxygen penetration depth observed during the cruise (Fig. 5.5.4), suggesting higher OM respiration rates. In contrast, at site M162-94 (GC45) oxygen is only gradually depleted and penetrates all the way down to the bottom of the core at 3 mbsf.
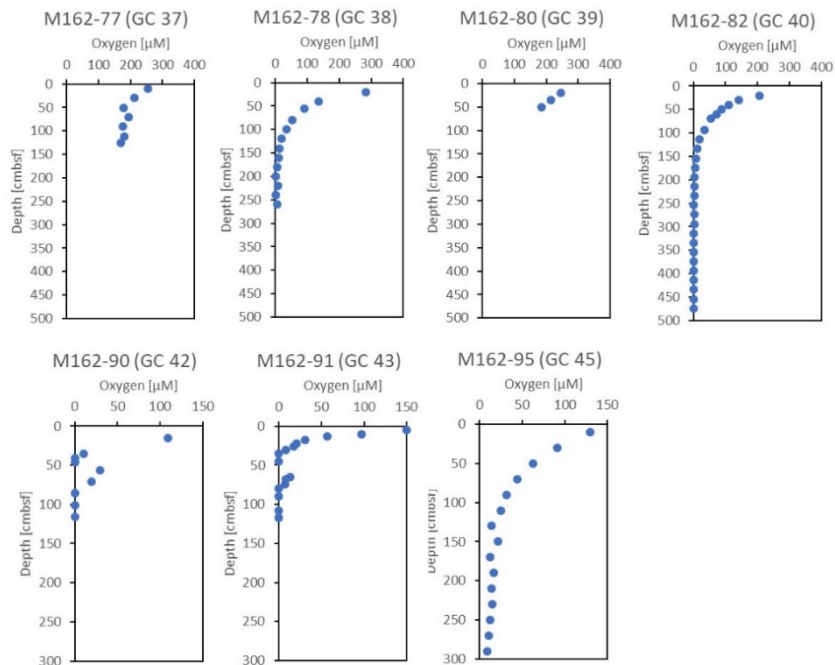
Fig. 5.5.4   Dissolved oxygen profiles in GC 37-45.

Dissolved hydrogen

Dissolved hydrogen concentrations were mostly below detection of the extraction method. Additionally, the extraction method revealed a significant high background from contamination by the butyl rubber stopper and is thus only applicable if hydrogen concentrations are comparably high, exceeding at least 50 nM. Thus, only result obtained by the incubation method will be considered.

The dissolved hydrogen concentration in the majority of recovered cores were almost always very low with values between the detection limit of the incubation method (ca. 0.05 nM) and 1 nM. A few exceptional cores had slightly elevated concentrations within the anoxic section of the cores. Because the incubations are not finished and equilibrium for most of the samples was not reached during the cruise, final hydrogen concentrations are not included in this report.

5.6   Pore water geochemistry

(M. Nuzzo[1], B. Domeyer[2], A. Bodenbinder[2], T. Schmidt[2], C. Hensen[2])

[1]IGI, [2]GEOMAR

5.6.1   Pore water sampling and analytical methods onboard

Sediment samples were taken from the gravity cores at depth intervals of up to 20 cm. The MUCs were stepwise extruded from the core liners and cut into 1 – 5 cm thick discs. Pore water recovery was realized in a cold room at 5 °C using a sediment squeezer at a pressure of 1 to 7 bar. The extruded pore water was filtered through 0.2 μm cellulose membrane filters. In addition to the

squeezing method, some cores were sampled by rhizons (Rhizosphere, The Netherlands) in order to minimize contamination with atmospheric oxygen during pore water extraction. About 5 cm^3 of wet sediment sample were stored for the determination of water content and porosity. Sediments remaining after pressure filtration (squeeze cakes) were stored for solid phase analyses in shore-based laboratories.

Analyses for ammonium (NH_4^+), phosphate (PO_4^{3-}) and silicate (SiO_4^{4-}) were carried out onboard using a Hitachi U2800A spectrophotometer. The respective chemical analytics follow standard procedures and are described in detail in Grasshoff et al. (1999) and on the GEOMAR webpage (www.geomar.de), respectively. Aliquots for NH_4^+ analyses were partly diluted prior to measurements in order to avoid interferences with HS^-. For the same purpose, aliquots for PO_4^{3-} and SiO_4^{4-} analyses were acidified and bubbled with argon for at least one hour. The total alkalinity (TA) of the pore water was determined by titration with 0.02 N HCl using the Tashiro indicator, a mixture of methyl red and methylene blue. The titration vessel was bubbled with argon to strip any CO_2 and H_2S produced during the titration. The pore water contents of chloride (Cl^-), bromide (Br^-) and sulfate (SO_4^{2-}) were determined by ion-chromatography (IC, Metrohm 761 Compact). The IAPSO seawater standard was used to check the reproducibility and accuracy of all chemical analyses.

In addition to the shipboard analyses, sub-samples were taken for shore-based analyses of major and minor cations (acidified with HNO_3), nitrate, iodide (IC) as well as for various isotope systems (cf. Tab. 12.6.1). Moreover, selected GCs were analysed for He isotopes ($^3He/^4He$) and other noble gases (see section 5.6.3).

Sediment samples were collected from GCs and MUCs for adsorbed hydrocarbon gas analyses and lipid biomarker studies at onshore labs (Tab. 12.6.1) in appendix). The samples for adsorbed hydrocarbon gases were stored in sealed plastic bags at 4°C for preservation. The samples for biomarker analyses were collected in aluminium foil or glass bottles and stored at -20°C.

5.6.2   Preliminary Results

Forty Gravity Cores (GCs) and three MUCs were successfully recovered in the M-162 survey area (with five failed GCs). A list of all the porewater samples collected for each coring station is provided in appendix in Table (cf. Tab. 12.6.1). While some measurements were performed onboard, most of the analyses will be made at onshore laboratories.

Overall, the porewater geochemistry profiles for the parameters measured onboard do not show indications for the vertical flow of deep-sourced fluids enriched in methane, but note that methane concentrations have not been measured onboard. Nevertheless, the oxygen concentration is seen to decrease to zero within the first 150 to 100 cm below the seafloor in about fifteen cores, seven of which being shown on Figure 5.6.1.

The oxygen penetration depth is often slightly shallower in the Eastern part of the survey area (WA4, WA5 and WA6) than in the western area (WA2-west and WA2-central). It is markedly shallower (~35 cmbsf) in GC43, which was cored in the easternmost WA6 (see Fig. 1). In the absence of Total Organic Carbon content (TOC) values for the sediments, it is at present unclear if oxygen is depleted due to sedimentary organic matter degradation or to reactions driven by the upward migration of anoxic fluids. Moreover, the results of the analyses due to be performed at onshore labs are required to identify if the porewater geochemical signals observed are caused by the advection of deep-sourced fluids and/or only by diagenetic sediment-fluid interactions.

The porewater alkalinity is low in all cores, and only increases with depth in core GC6 (WA-2) and very slightly in GC43 (WA6). In some cores collected in the westernmost part of the survey area, the alkalinity values sometimes actually decrease below seawater values across some intervals, as highlighted on Figure 5.6.1 for cores GC10 and GC13. The ammonium concentration values, which are overall low in the survey area, are seen to increase with depth to values of ~200 µM in GC6 and around100 µM in GC43, GC28 and GC14 (Fig. 5.6.1). Ammonium is a by-product of the degradation of organic matter due to diagenesis or to thermal degradation at temperatures higher than ~ 90°C. Again, it is not possible to assess which process might be involved until TOC and other analyses are completed onshore. The silica concentration profiles suggest that in most GCs, silica may at some depths be removed from the sediment into the porewater and at others be removed from the porewater into the sediment. In most GCs, the silica concentration gradient with depth is also relatively low, *i.e.* the downward increase in concentration below the seafloor takes place over a relatively large interval (Fig. 5.6.1).
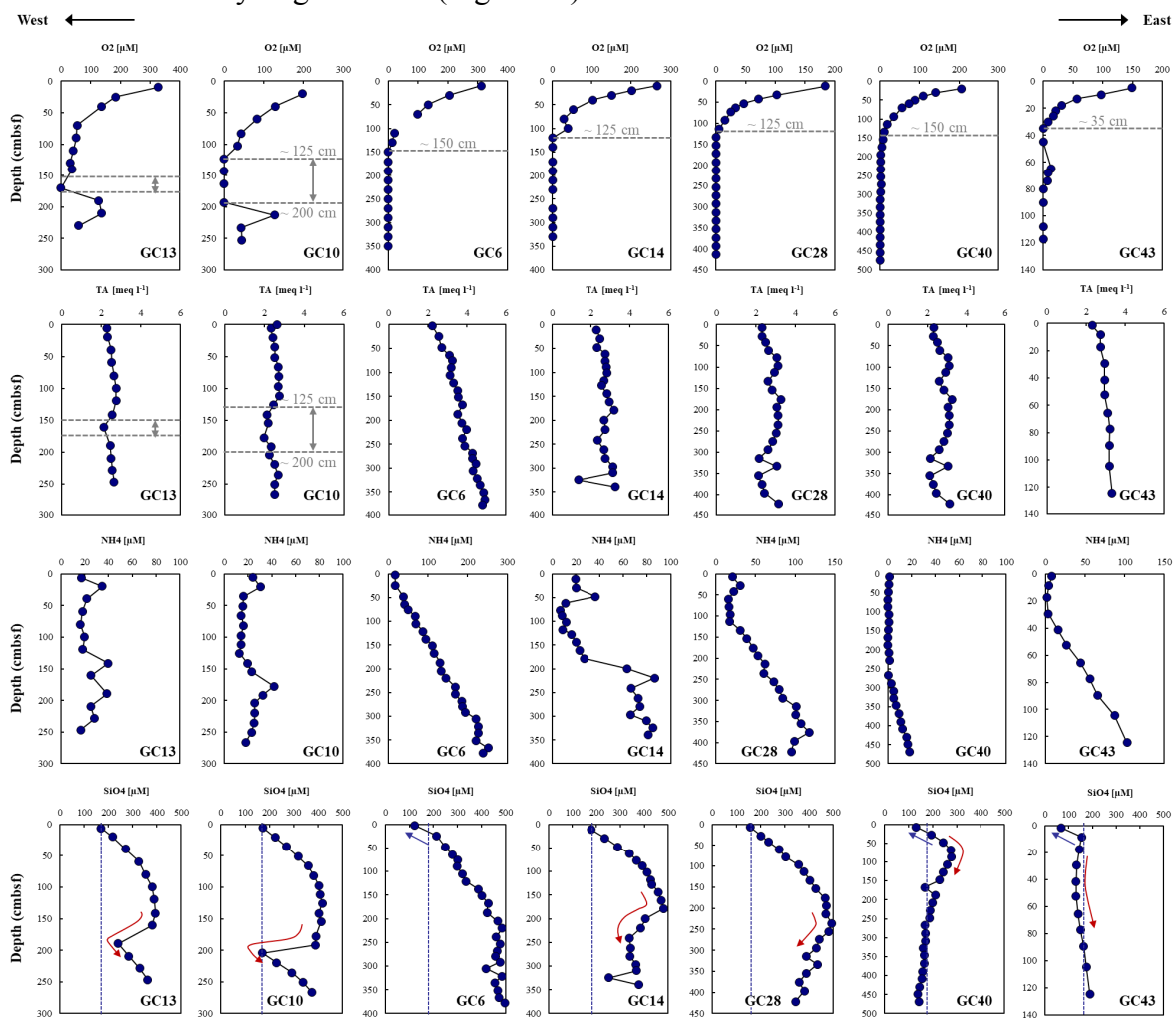
Fig. 5.6.1   Porewater concentration profiles of Oxygen (O_2), Total Alkalinity (TA), Ammonium (NH_4) and Silica (SiO_4), from top to bottom shown for seven cores located from West to East along the Gloria Fault.

As mentioned before, both sediment-porewater reactions or the upward flow of a deep-sourced fluid might be involved and the results from presently missing analyses are needed for further interpretations. In summary, the preliminary porewater geochemistry data suggest that upward-directed flow of deep-sourced fluid might eventually have taken place (or still occur) in the locations of GC6, GC43, GC28 and GC14 but further data are required to investigate this

hypothesis. The figures below show oxygen, silica and ammonium concentration profiles for GCs collected in the WA2-west (Fig. 5.6.2), WA2-central (Figs. 5.6.3, 5.6.4), WA3 (Fig. 5.6.5) and WA4 (Fig. 5.6.6) and in WA5 and WA6 (Fig. 5.6.7).
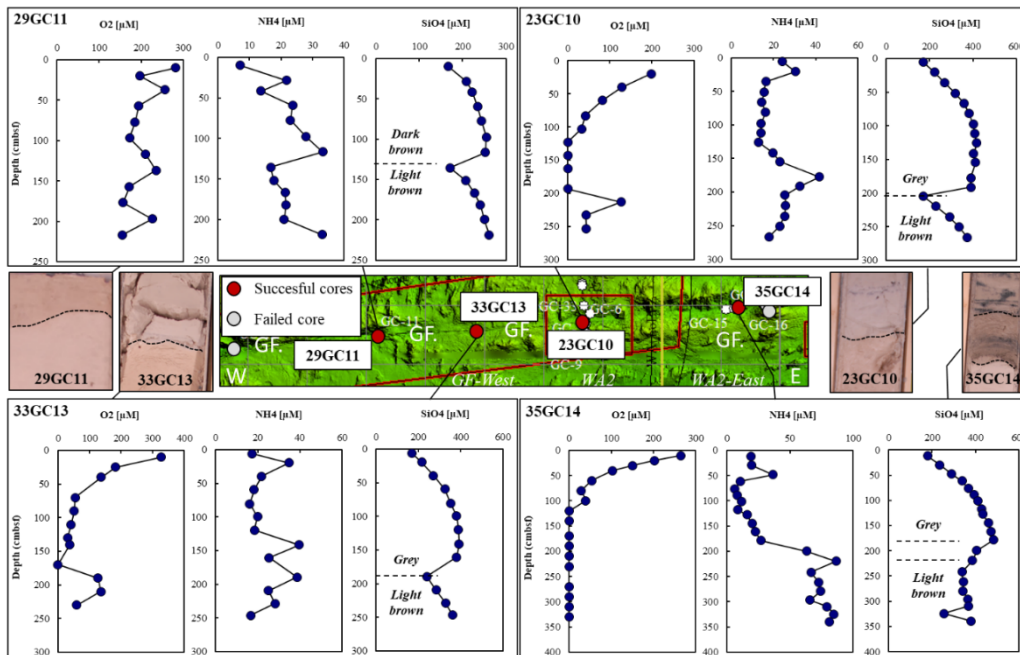
Fig. 5.6.2   Location and porewater concentration *versus* depth profiles for oxygen, ammonium and silica from WA2 west.
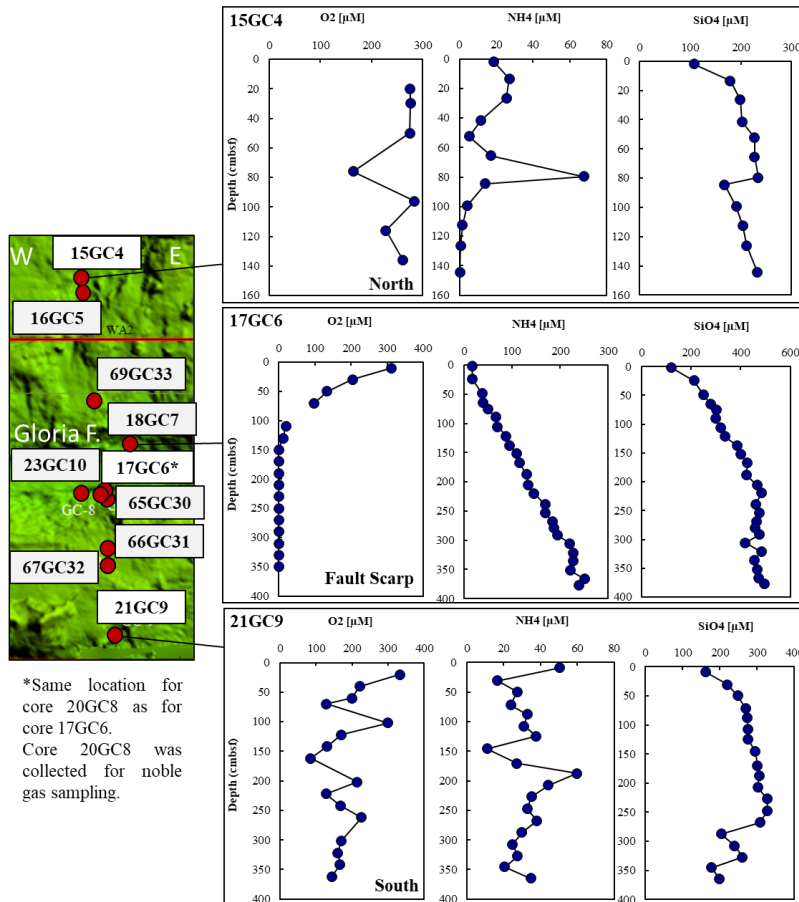
Fig. 5.6.3   Location and porewater concentration *versus* depth profiles for oxygen, ammonium and silica in WA2-central.

They highlight possible systematic changes in porewater composition from west to east. In WA2-west, markedly higher ammonium concentrations and slightly lower oxygen penetration depths are observed in GC14 as opposed to other cores in this segment of the fault (Fig. 5.6.2). In WA2-central, core GC6 located in the deepest part of the fault graben shows clearly distinct porewater profiles compared to sites located to the north or south of the fault (Fig. 5.6.3). The preliminary data are not sufficient to assess whether this may result from flow of deep-sourced fluids at the location of GC6, or from diagenetic reactions. However, it is noteworthy that the geochemical profiles obtained in cores GC30 and GC10 located very near GC6 are different (Fig. 5.6.4), even though the original sedimentological differences with GC6 might have been limited. Figure 5.6.4 additionally shows sulphate (SO_4) concentration profiles because GC6 is the only core in which a decrease in sulphate concentration has been observed in the M162 survey area.
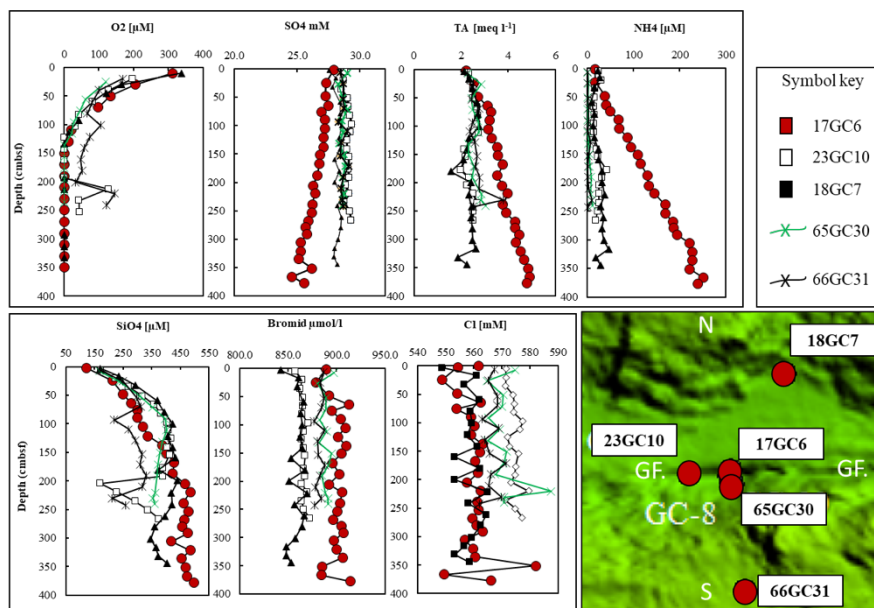
Fig. 5.6.4   Location and porewater concentration *versus* depth profiles for oxygen, ammonium, sulphate and silica in the central part of WA2-central around GC6.
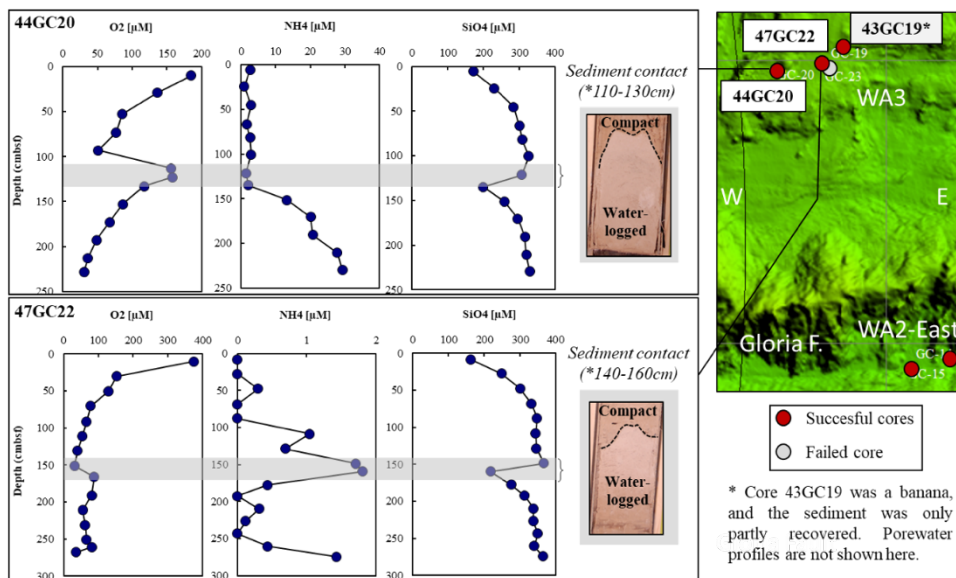
Fig. 5.6.5   Location and porewater concentration *versus* depth profiles for oxygen, ammonium and silica in WA3.

Three cores collected in WA-3 show a sharp contact between more compact and darker sediment (above) and water-logged lighter sediment (below) at depths of about 100 to 150 cmbsf. It coincides with clear variations in oxygen, silica and ammonium concentrations (Fig. 5.6.5) that probably exclude the hypothesis of a repeated sedimentary sequence due to coring issues. A similarly odd contact in core GC35 (WA-4) is thought to be a sampling artefact (Fig. 5.6.6). Note the higher ammonium concentrations in core GC28 compared to other cores retrieved in this area. In the easternmost study area of the Madeira Tore Rise, relatively high ammonium concentrations and low oxygen penetration depths are observed in core GC43 (Fig. 5.6.7).

* Porewater geochemistry profiles for core 58GC27 very similar to those of core 72GC35 (hence only the latter are shown here).
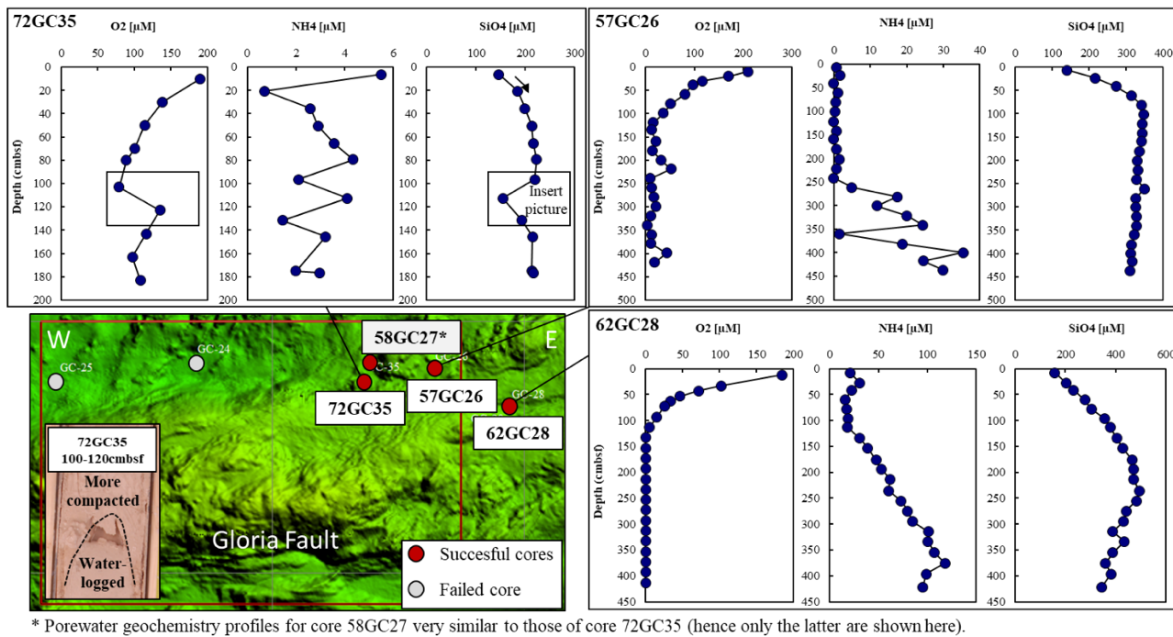
Fig. 5.6.6   Location and porewater concentration *versus* depth profiles for oxygen, ammonium and silica in WA4.

* Based on the sedimentology & porewater profiles, the core recovery is suspected to have been flawed, hence data for 77GC37 are not shown here.
** Porewater geochemical profiles for cores 90GC42 & 91GC43 are very similar and only data from the latter are shown here.
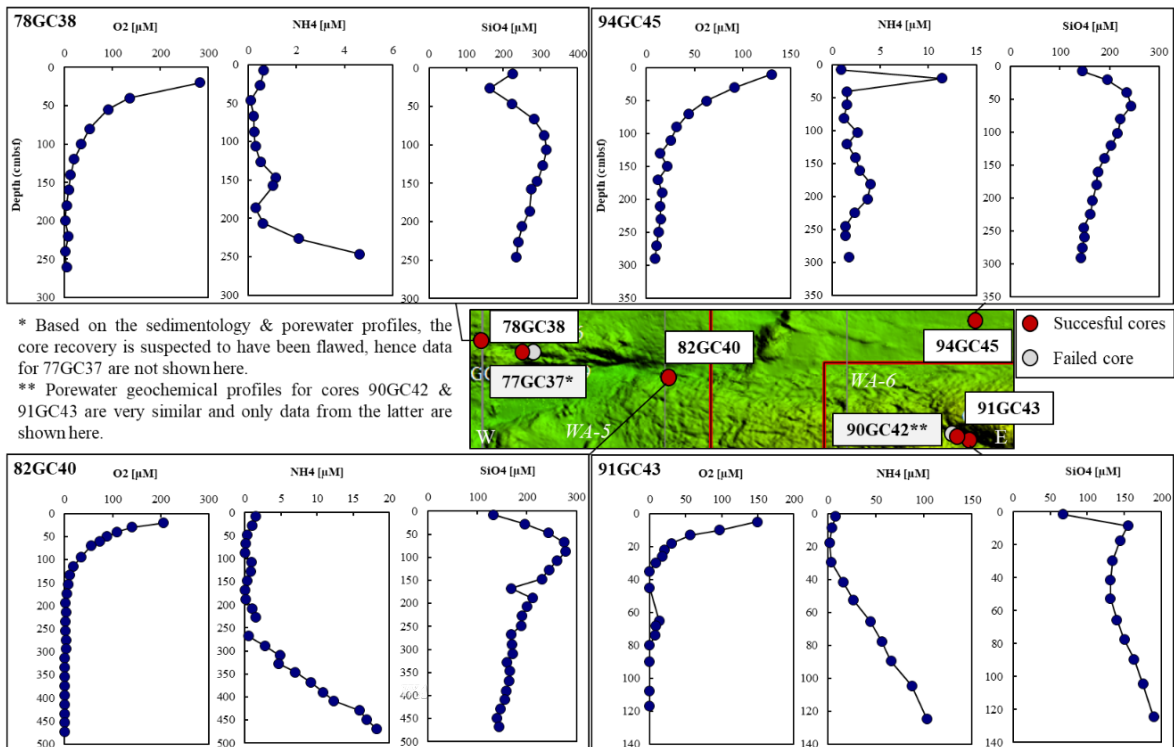
Fig. 5.6.7   Location and porewater concentration *versus* depth profiles for oxygen, ammonium and silica in WA5 and WA6.

5.6.3 Sampling for noble gas analysis

(U.W. Weber[1])

[1]Eawag, UIO

Noble gas concentrations and their isotopic ratios in sediment porewater are determined by the source of the components constituting the porewater. The components can be divided into three main reservoirs with distinctive signatures. Those reservoirs are the atmosphere, the crust and the mantle. Hence, determining the noble gases in sediment pore water and calculating the ratio of these components allows deriving the origin of a fluid mixture. The noble gas with the most distinctive isotopic ratio is helium, which is briefly discussed here in representation of the other analysed noble gases neon, argon, krypton and xenon: A low value of the ^{3}He/^{4}He ratio is typically associated to a crustal source (^{3}He/^{4}He$\approx$10^{-8}); ^{4}He has been accumulated radiogenically, originating from α-decay of uranium and thorium in the rocks or sediment. The ratio depends on accumulation rate and time and may therefore cover a certain range. A mantle-sourced gas has a relatively high, primordial, ^{3}He content and the value is ^{3}He/^{4}He$\approx$10^{-5}. The atmosphere currently has a value of ^{3}He/^{4}He$\approx$1.384·10^{-6}. A detailed overview and a description of secondary processes such as excess air or gas stripping can be found in Brennwald et al. (2013).

Sampling is conducted by extracting sediment with a squeezing setup from gravity core segments into copper tubes (Brennwald et al. 2003). The liners of the gravity cores were pre-drilled so that the sample containers (copper tubes) can be attached without opening the core. The 1-meter long segments of the retrieved core are then mounted into a press allowing to squeeze the sediments into the copper tubes (Fig. 5.6.8). After sufficient flushing of the container, the samples are clamped off airtight. Subsequently, the samples will be centrifuged to separate the fluid from the solid phase (Tomonaga et al. 2011). The part of the sample containing a couple of millilitres of pore water is clamped off again. Analyses of such pore water samples will be conducted with the mass spectrometer at the laboratories of ETH Zurich. A list of samples is included in Table 12.6.1 in the appendix.

Fig. 5.6.8   Sediment sampling from core segments for noble gas analysis used during M162.

5.6.4   Radon (^{222}Rn) Measurements

(V. Liebertrau[1])

[1]GEOMAR

On M162 ^{222}Rn pore water depth profiles of sediment cores recovered by gravity corer (GC) and video guided multi-corer (VMUC) as well as bottom waters (VMUC) and close to seafloor reaching water column profiles by video guided CTD rosette water sampler (VCTD) were performed in order to study gas transport through marine sediments of different geological and sedimentary settings. The goal of the study is to contribute to the determination of advection and diffusion rates in seepage and non-seepage site settings.

^{222}Rn is a member of the ^{238}U decay chain and directly produced by the decay of ^{226}Ra in the marine sediments, with the parent isotopes hosted in the particles and potentially dissolved in the pore water. The emanation of the decay product ^{222}Rn from the particles into the pore water and the gas transport processes may lead to an excess concentration and activity of ^{222}Rn with regard to the activity of dissolved parent isotope in the pore water. Because ^{238}U and ^{230}Th are enriched in sediments its production is depth dependent and increases as a function of the sedimentary height below the water column. The emanation of the decay product ^{222}Rn from the particles into the pore water and gas transport processes may lead to an excess concentration and activity of so-called unsupported ^{222}Rn with regard to the activity of dissolved parent isotope in the pore water. ^{222}Rn is an excellent tracer in order to determine diffusion and advection rates because as a radioactive noble gas it is chemically inert but decays away with a half-life of about 3.5 days (λ=0.0001374 1/min). Thus, the time dependent transport of ^{222}Rn can be simplified regarded as a function of time and sediment depth. Because of the short half-life it needs to be investigated directly on board of a ship in order to quantify the difference between the excess and supported fraction while performing liquid-scintillation- counting (LSC) analyses on mobile and sea-going devices (Purkl and Eisenhauer, 2004). The results from ^{222}Rn depth profile measurements can then be compared to other gases of interest (e.g. CH_4, He) and geochemical tracers supplied from the sediments to the water column.

Sediments for ^{222}Rn measurements were subsampled at different sediment depth and from different lithostratigraphic units from cores recovered by GC and VMUC. After gas-tight centrifuging a volumetrically quantified aliquot of the porewater is layered under a Rn susceptible liquid scintillation cocktail in a measurement vial and shaken vigorously for reproducible extraction yield. Whereas pore waters are providing sufficient signal already on 10 ml sample sizes, bottom water and water column samples are usually required in one-liter volumes. On this pure water sample the LSC cocktail is just added and after shaking and extraction procedures measured in the same LSC device as the porewater samples. After the on-board analyses for total ^{222}Rn content back-measurements after at least 3 weeks and usually performed in the land-based main facility are required to identify the amount of supported ^{222}Rn and therefore the amount in equilibrium dissolved parent isotope ^{226}Ra, a divalent cation. Rn samples taken for analysis are listed in Table 12.6.1. The counting device used on this cruise had to be calibrated and recalibrated before and after shipping. Furthermore, the back-measurements and additional extraction runs on the water samples will have to be performed before presenting final results for comparison with the independent geochemical and gas tracer.

5.7   Heat Flow

(N. Kaul[1], J.-N. Schmidt[1], N. Warnken[1])

[1]GeoB

5.7.1   Heat Probe system and deployment procedure

During this cruise we used the 6 m long Bremen heat flow probe also called Giant Heat Flow Probe (GHF). The heat probe is designed for operation in a pogo-style mode up to 6000 m water depth. The latest modification in 2020 is the possibility to divide the instrument into easy to transport sections. A 20' container is sufficient. Due to the 5.20 m operation-length of its temperature sensor string, undisturbed temperature gradients can be determined even where seasonal bottom water temperature variations are superimposed on the undisturbed temperature field in the sea floor.

The heat probe (Fig. 5.7.1) is constructed in the classical "violin bow" design (Hyndman et al., 1979; Hartmann and Villinger, 2002, Villinger et al., 2010), with 21 thermistors distributed over an active length of 5.2 m in 0.26 m intervals mounted inside an oil filled hydraulic tube (O.D. 14 mm) which is attached to the strength member (O.D. 130 mm). The sensor tube also contains a heater wire for the generation of high energy heat pulses, typically of 800 J/m. This enables *in situ* thermal conductivity measurements according to the pulsed needle probe method (Lister, 1979).

The data acquisition unit including power supply (Sea & Sun, Trappenkamp, Germany) is housed in a single titanium pressure case (110 mm O.D. x 300 mm) and mounted inside the probe's weight stand.
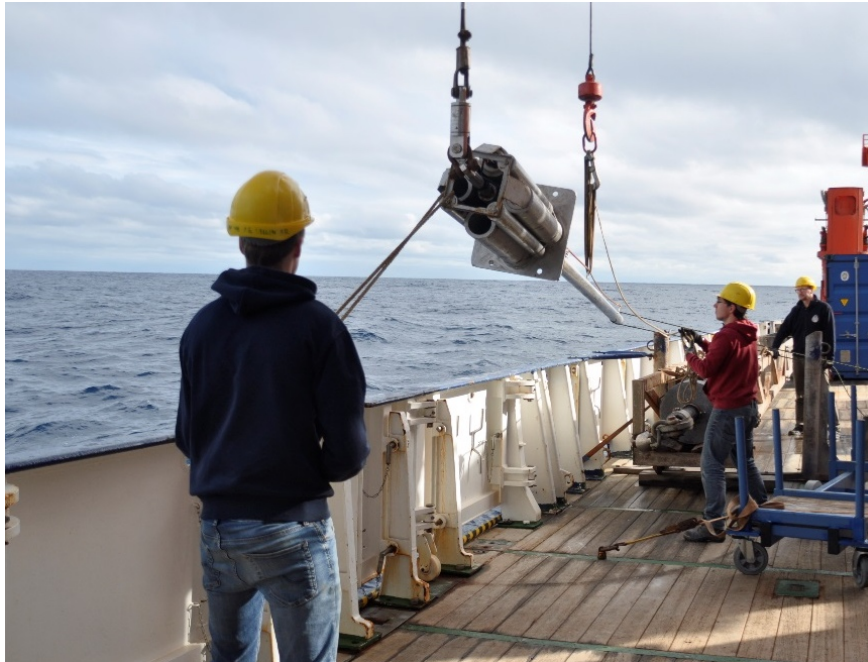
Fig. 5.7.1   Deployment of the heat probe, using the crane and a slip-hook.

A second pressure case houses the battery pack for heat pulses. For heat flow stations during this cruise, data acquisition unit #488 was used. The signal of the temperature sensors is measured with a resolution of 20-bit at a sample rate of 1 sec, resulting in a final temperature resolution of better than 1 mK at ambient seafloor temperatures. A calibrated PT-100 seawater sensor allows for calibration of the sensor string with reference to the deep water. Inclination and acceleration of the

probe is measured to monitor the penetration process into the sediment and potential disturbances during the actual measurement period. We used both wires (W11, 18 mm coring wire; W12, 18 mm coax) and operated in autonomous mode with internal data storage and automated heat pulse trigger at all times.

Winch speed for penetration of the heat probe is 1.0 to 1.2 m/s for maximum penetration into the sediment. Time to equilibrate to in situ temperatures is assumed to be 8 minutes; time for heat pulse decay observation takes another 8 minutes. We increased the maximum angle allowance for the heat pulse trigger to 11° because poor penetration due to a layer of foraminifer sand made a vertical penetration difficult. The mean duration of one measurement, including transit of approximately 0.5 km between waypoints, is about 1 h per single point of measurement. A USBL (iXblue Posidonia) transponder, mounted to the coring wire 50 meters above the instrument allowed to monitor the position of the heat probe at depth on many sites.

The retrieved temperature-time series from the heat probe are evaluated and reduced according to Villinger and Davis (1987). In this challenging environment, we could achieve a success rate of app. 40%, that is, we are confident in the resulting temperature gradients. Fig. 5.7.2 shows two examples of heat flow measurements made during M162.

a)   162 Station HF2002   Pen 04   10-Mar-2020 01:23:30
Latitude: 37 05.9052 Longitude: -21 18.8262 Water Depth: 4476.0 m

b)   M162 Station HF2017   Pen 01   03-Apr-2020 21:24:30
Latitude: 37 30.309 Longitude: -14 55.094 Water Depth: 4311.0 m
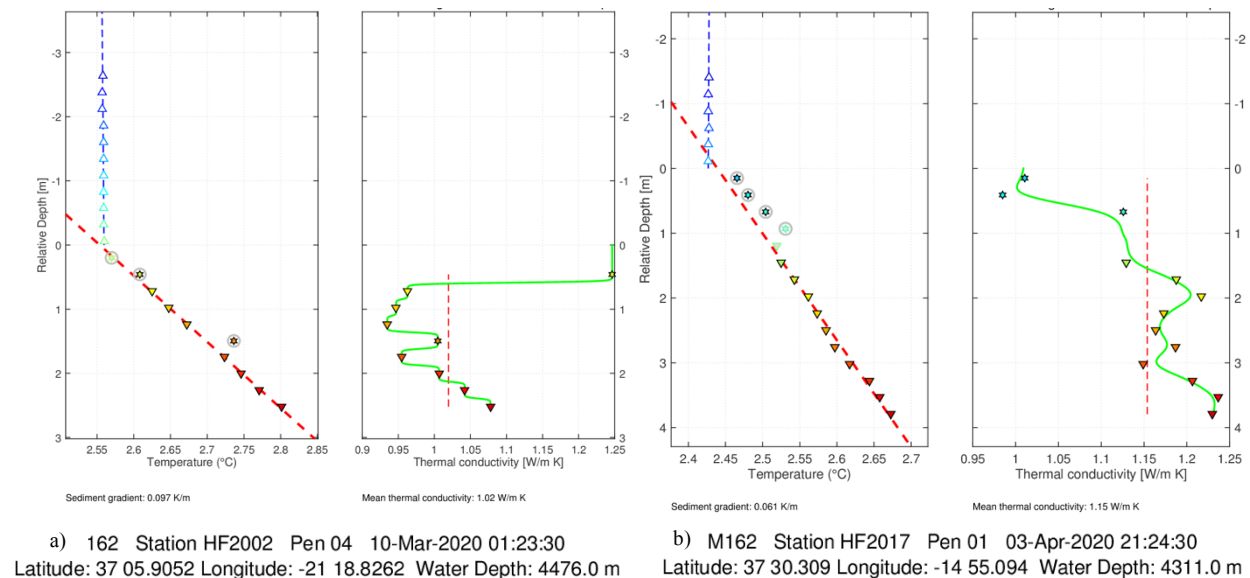
Fig. 5.7.2   Temperature gradient (dT/dz) and thermal conductivity (k) results of two representative sites. a) is located in the western area, b) in the most eastern working area. Penetration depths of 2.5 m and less are abundant; k-values above 1 W/m K are common.

5.7.2   Preliminary results

In total, a number of 106 positions were tested on 17 stations. A number of 67 sites gave reliable results, corresponding to a success rate of 63%. A location map of all stations is given in Fig. 5.7.3. The aim was to find hints for active fluid flow and indications for frictional heating due to dextral movement along this oceanic transform fault. On two occasions a positive correlation of faults, seen in the sediment echo sounder or in multichannel seismic data, could be confirmed.
A 53 km long south-north profile (Fig. 5.7.4) across the Gloria fault awaits further investigation. An age-jump of 15 − 20 Ma across the Gloria fault should result in an observable difference in crustal heat flow. Steep scarps may produce significant thermal refraction and may be responsible for rapid sedimentation.
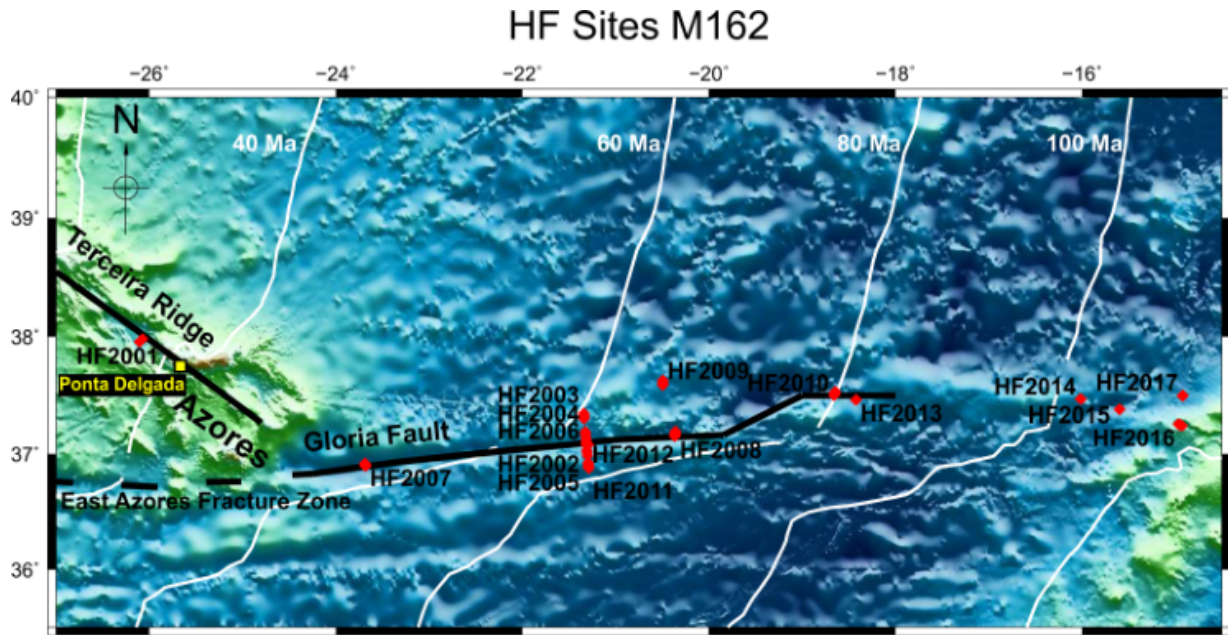
Fig. 5.7.3   Summary of all heat flow sites along the GLORIA fault on 40 – 110 Ma old crust. The major heat flow transect is a 53 km long south-north profile near 21°W. Bathymetry from GEBCO 2014, crustal ages according to Müller et al. (2008).
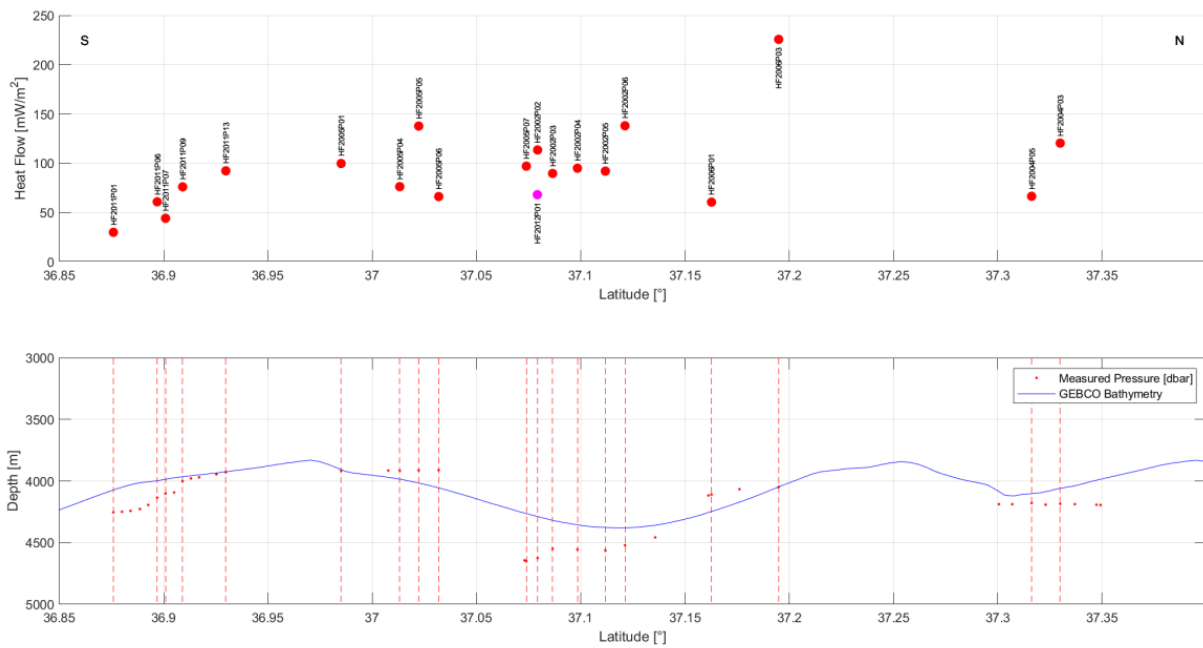
Fig. 5.7.4   Preliminary results of the south-north profile across GLORIA fault. Upper sketch shows those 40% of sites which gave reliable heat flow values on this profile; lower sketch displays bathymetry, blue line from GEBCO 2014, red dots calculated from the heat probe's pressure sensor.

6   Ship's Meteorological Station

(M. Stelzner[1])

[1]DWD

At 9am ships time on the 6th of March 2020, the research vessel (RV) Meteor left the port of Ponta Delgada/Azores. The first research area was located just west of the island Sao Miguel.

The weather situation was dominated by a high over the Azores at the start of the cruise, which slowly moved eastwards. The wind came from the south with 5 to 6 Bft. The significant wave height was approx. 3 m with a swell from northwest, resulting in crossing seas. As the high pressure receded, a cold front approached, originating from a low near Iceland. This was followed by an extensive expanding high. The wind blew only with a maximum of 4 Bft from south to southwest. In addition, the significant wave height calmed to 2m.

In the morning of the 8th of March 2020, the research work in the first area concluded and the one-day transit to the second working area at 37°N 20°W commenced with nearly unchanged weather conditions. On the 10th of March 2020, a secondary swell from southeast reached the cruising area. At the same time, the high moved eastwards, followed by two fronts from the northwest, which crossed the cruising area on 11th and 12th of March 2020. After the passing of the two frontal systems, a high-pressure system again developed north of the Azores, with winds veering to northeast 5 Bft. Due to the superposition of two swell fields from southeast and northwest and the increasing wind sea, the sea state temporarily increased to 3m on the 13th of March 2020. Another front moved across the cruising area on 15th of March 2020, again followed by a high, but this time its centre lay directly over the working area. The wind decreased to less than 4 Bft, at times even weakly circulating and the significant wave height decreased to 1m.

Unfortunately, this was the proverbial "calm before the storm": On the 18th of March 2020, an Atlantic low moved towards Biscay. Blocked by a heavy storm depression further north and a high over Europe, this low could only move southwards, so that its centre passed the research area. On the 21st and 22nd March 2020, a strong wind with mean wind speeds 7 to 8 Bft, in gusts up to 10 Bft from the northwest, passed the research area. Due to the long fetch, a developed sea with significant wave height up to 5m in the morning of the 22nd of March 2020 occurred; single waves reached even greater heights. The poor weather condition enforced a temporarily halt of research work on cruise M162 to await better weather conditions. On the 23rd of March 2020, the depression moved on a south-easterly track towards Africa.

As in the weeks before, a weather situation dominated by high-pressure built up. The north-westerly wind decreased to 3-4 Bft and gradually veered north. The significant wave height also decreased to 1.5 to 2m, combined with a dominating swell component from northwest. This weather remained for a whole week.

On the 30th of March 2020 a depression approached from northwest while RV Meteor was operating in its third research area at 15°W. This time the centre moved directly over RV Meteor. The wind veered first southeast, later south to southwest, and increased again 6 to 7 Bft. In addition, the significant wave height reached another peak of 4-5m on the 31st of March 2020. The low continued eastward towards Portugal over the course of the first days of April. Another depression followed seamlessly, changing its eastward track once passed the Azores towards northeast. As a result, the southerly wind remained at 6 to 7 Bft throughout early April, and the significant wave height decreased only slightly to 3 to 2.5 m.

On the 4th of April 2020, RV Meteor finished the scheduled research work. Due to the worldwide outbreak of the CoVID19, the follow-up expedition M163 was cancelled without replacement, so that RV Meteor made transit via Lisbon to Emden in Germany. In the morning of the 5th of April 2020, RV Meteor reached the anchorage in Lisbon to drop off the Portuguese participants. At the same time, a high-pressure area spread again in the region of Portugal and the Bay of Biscay. The wind finally decreased to less than 4 Bft, the significant wave height to less than 2m. Simultaneously, the stabilizing air stratification led to a significant increase in humidity, so that RV Meteor was wrapped in mist on the 6th and 7th of April 2020.

Following the disembarkation of the Portuguese scientists on the morning of the 5th of April 2020, the transit to Emden, Germany began. RV Meteor was almost the entire transit back under the influence of a very slowly eastward shifting high. In this calm weather situation, RV Meteor crossed the Bay of Biscay and the English Channel. In contrast to the past two weeks, which were quite rough, the return journey was dominated by weak easterly winds and a significant wave height of 1.5m, reducing to less than 1m.

At midday on the 10th of April 2020, RV Meteor reached the mouth of the river Ems and 4 hours later M162 ended in the port of Emden.

7 Station List M162

7.1 Overall Station List

Date UTC	St. No. M162	Gear Station Meteor	Gear No.	Begin	Start Sci. Program	End Sci. Program	End	Duration hh:mm	Latitude N°	Longitude W°	Latitude N°	Longitude W°	Water depth (m)	Comment	Recovery (cm)	Area
					Time (UTC)				Begin / on seafloor		End / off seafloor					
06.03.20	1	M162_1-1_MB_PS	MB/PS-1	13:00	13:00	19:30	19:30	07:30	37°55.801	026°06.147	37°57.912	026°04.523	3212			WA1/ south Hirondelle Basin
06.03.20	2	M162_2-1 HF	HF-1	21:10	22:05	06:37	07:43	10:33	37°58.907	026°04.227	37°57.363	026°06.505	3193	HF2001		WA1/ south Hirondelle Basin
06.03.20	2.1	M162_2-1 HF	HF-1	-	22:05	22:21	-	00:16	37°58.880	026°04.224	37°58.880	026°04.224	3194	HF2001P01		WA1/ south Hirondelle Basin
06.03.20	2.2	M162_2-1 HF	HF-1	-	23:03	23:19	-	00:16	37°58.721	026°04.459	37°58.721	026°04.459	3217	HF2001P02		WA1/ south Hirondelle Basin
07.03.20	2.3	M162_2-1 HF	HF-1	-	00:03	00:19	-	00:16	37°58.560	026°04.710	37°58.560	026°04.707	3218	HF2001P03		WA1/ south Hirondelle Basin
07.03.20	2.4	M162_2-1 HF	HF-1	-	01:02	01:10	-	00:08	37°58.411	026°04.947	37°58.411	026°04.947	3219	HF2001P04		WA1/ south Hirondelle Basin
07.03.20	2.5	M162_2-1 HF	HF-1	-	01:49	02:05	-	00:16	37°58.250	026°05.181	37°58.251	026°05.184	3219	HF2001P05		WA1/ south Hirondelle Basin
07.03.20	2.6	M162_2-1 HF	HF-1	-	02:45	02:53	-	00:08	37°58.087	026°05.422	37°58.086	026°05.420	3219	HF2001P06		WA1/ south Hirondelle Basin
07.03.20	2.7	M162_2-1 HF	HF-1	-	03:26	03:42	-	00:16	37°57.986	026°05.586	37°57.987	026°05.588	3201	HF2001P07		WA1/ south Hirondelle Basin
07.03.20	2.8	M162_2-1 HF	HF-1	-	04:21	04:28	-	00:07	37°57.831	026°05.769	37°57.831	026°05.797	3197	HF2001P08		WA1/ south Hirondelle Basin
07.03.20	2.9	M162_2-1 HF	HF-1	-	05:04	05:20	-	00:16	37°57.687	026°06.047	37°57.687	026°06.047	3205	HF2001P09		WA1/ south Hirondelle Basin
07.03.20	2.10	M162_2-1 HF	HF-1	-	06:21	06:37	-	00:16	37°57.362	026°06.505	37°57.363	026°06.505	3225	HF2001P10		WA1/ south Hirondelle Basin
07.03.20	3	M162_3-1 GC	GC-1	08:44	09:55	09:57	10:50	02:06	37°57.200	026°07.513	37°57.198	026°07.513	3228		0-140	WA1/ south Hirondelle Basin
07.03.20	4	M162_4-1 GC	GC-2	11:46	12:34	12:36	13:27	01:41	37°59.401	026°07.124	37°59.400	026°07.124	3218		0-180	WA1/ south Hirondelle Basin
07.03.20	5	M162_5-1 GC	GC-3	14:05	14:51	14:53	15:59	01:54	37°58.852	026°06.467	37°58.858	026°06.488	3215		0-140	WA1/ south Hirondelle Basin
07.03.20	6	M162_6-1 CTD	V-CTD-1	19:00	21:00	01:04	03:55	08:55	37°58.048	026°05.252	37°57.533	026°06.234	3219	Video record		WA1/ south Hirondelle Basin
08.03.20	7	M162_7-1 TVMUC	V-MUC-1	08:12	09:27	12:11	13:31	05:19	37°58.048	026°05.320	37°58.480	026°06.433	3203	Video record, 2 cores	0-6/ 0-18	WA1/ south Hirondelle Basin
09.03.20	8	M162_8-1 MB_PS	MB/PS-2	11:26	11:26	18:55	18:55	07:29	37°28.698	021°21.120	36°52.640	021°17.196	4213			WA2/ central
09.03.20	9	M162_9-1 HF	HF-2	20:35	21:49	08:26	09:28	12:53	37°04.363	021°18.709	37°09.673	021°19.164	4515	HF2002		WA2/ central Graben
09.03.20	9.1	M162_9-1 HF	HF-2	-	21:49	21:57	-	00:08	37°04.382	021°18.727	37°04.382	021°18.726	4498	HF2002P01		WA2/ central Graben
09.03.20	9.2	M162_9-1 HF	HF-2	-	22:48	23:05	-	00:17	37°04.755	021°18.736	37°04.760	021°18.737	4521	HF2002P02		WA2/ central Graben
09.03.20	9.3	M162_9-1 HF	HF-2	-	23:59	00:16	-	00:17	37°05.187	021°18.783	37°05.187	021°18.782	4477	HF2002P03		WA2/ central Graben
10.03.20	9.4	M162_9-1 HF	HF-2	-	01:23	01:39	-	00:16	37°05.905	021°18.826	37°05.905	021°18.826	4481	HF2002P04		WA2/ central Graben
10.03.20	9.5	M162_9-1 HF	HF-2	-	02:51	02:59	-	00:08	37°06.711	021°18.875	37°06.711	021°18.873	4491	HF2002P05		WA2/ central Graben
10.03.20	9.6	M162_9-1 HF	HF-2	-	04:04	04:19	-	00:15	37°07.271	021°18.935	37°07.271	021°18.935	4444	HF2002P06		WA2/ central Graben
10.03.20	9.7	M162_9-1 HF	HF-2	-	05:51	05:59	-	00:08	37°08.141	021°18.990	37°08.141	021°18.987	4388	Posidonia not working		WA2/ central Graben
10.03.20	9.8	M162_9-1 HF	HF-2	-	08:10	08:26	-	00:16	37°09.673	021°19.169	37°09.673	021°19.167	4050	Posidonia not working		WA2/ central Graben
10.03.20	10	M162_10-1 TVMUC	V-MUC-2	10:40	12:20	15:59	17:09	06:29	37°18.246	021°20.076	37°19.659	021°20.209	4126	Video record, 5 cores	3x0-6 / 2x0-9	WA2/ central, basin at north side of WA2
10.03.20	11	M162_11-1 CTD	V-CTD-2	17:46	20:13	22:55	02:15	08:31	37°19.658	021°20.207	37°20.952	021°20.324	4124	Video record		WA2/ central, basin at north side of WA2

Date UTC	St. No. M162	Gear Station Meteor	Gear No.	Time (UTC) Begin	Start Sci. Program	End Sci. Program	End	Duration hh:mm	Begin / on seafloor Latitude N°	Longitude W°	End / off seafloor Latitude N°	Longitude W°	Water depth (m)	Comment	Recovery (cm)	Area
11.03.20	12	M162_12-1 HF	HF-3	02:33	03:38	03:46	08:38	06:05	37°20.953	021°20.324	37°20.849	021°20.292	4127	HF2003		WA2/ central, basin at north side of WA2
11.03.20	12.1	M162_12-1 HF	HF-3	-	03:38	03:46	-	00:08	37°20.952	021°20.326	37°20.952	021°20.326	4126	HF-survey stopped, winch failure		WA2/ central, basin at north side of WA2
11.03.20	13	M162_13-1 MB_PS	MB/PS-3	10:05	10:05	19:36	19:36	09:31	37°15.802	021°24.936	37°09.349	021°08.778	3910	16:45-16:56 sounding interrupted, dolphins close to the ship		WA2/ central Graben
11.03.20	14	M162_14-1 HF	HF-4	21:40	23:05	07:21	08:50	11:10	37°20.846	021°20.286	37°18.029	021°20.331	4124	HF2004		WA2/ central, basin at north side of WA2
11.03.20	14.1	M162_14-1 HF	HF-4	-	23:05	23:12	-	00:07	37°20.847	021°20.284	37°20.847	021°20.284	4124	HF2004P01		WA2/ central, basin at north side of WA2
12.03.20	14.2	M162_14-1 HF	HF-4	-	00:39	00:56	-	00:17	37°20.212	021°20.245	37°20.212	021°20.245	4121	HF2004P02		WA2/ central, basin at north side of WA2
12.03.20	14.3	M162_14-1 HF	HF-4	-	02:16	02:24	-	00:08	37°19.790	021°20.206	37°19.788	021°20.207	4125	HF2004P03		WA2/ central, basin at north side of WA2
12.03.20	14.4	M162_14-1 HF	HF-4	-	03:21	03:37	-	00:16	37°19.375	021°20.178	37°19.376	021°20.176	4120	HF2004P04		WA2/ central, basin at north side of WA2
12.03.20	14.5	M162_14-1 HF	HF-4	-	04:26	04:42	-	00:16	37°18.972	021°20.146	37°18.971	021°20.145	4120	HF2004P05		WA2/ central, basin at north side of WA2
12.03.20	14.6	M162_14-1 HF	HF-4	-	05:45	06:02	-	00:17	37°18.415	021°20.083	37°18.416	021°20.082	4123	HF2004P06		WA2/ central, basin at north side of WA2
12.03.20	14.7	M162_14-1 HF	HF-4	-	07:04	07:21	-	00:17	37°18.031	021°20.330	37°18.031	021°20.329	4118	HF2004P07		WA2/ central, basin at north side of WA2
12.03.20	15	M162_15-1 GC	GC-4	11:07	12:17	12:19	13:31	02:24	37°20.647	021°20.327	37°20.611	021°20.362	4127	Posidonia	0-156	WA2/ central, basin at north side of WA2
12.03.20	16	M162_16-1 GC	GC-5	14:09	15:17	15:20	16:40	02:31	37°19.711	021°20.239	37°19.711	021°20.239	4126	Posidonia	0-155	WA2/ central, basin at north side of WA2
12.03.20	17	M162_17-1 GC	GC-6	18:34	19:52	19:54	21:23	02:49	37°04.541	021°18.818	37°04.444	021°18.736	4575		0-380	WA2/ central Graben
12.03.20	18	M162_18-1 MB_PS	MB/PS-4	22:28	22:28	07:12	07:12	08:44	37°06.417	021°21.886	37°05.244	021°25.764	4439			WA2/ central
13.03.20	19	M162_19-1 GC	GC-7	09:15	10:32	10:34	12:14	02:59	37°08.145	021°16.855	37°08.146	021°16.861	4491	Posidonia	0-353	WA2/ central, north
13.03.20	20	M162_20-1 GC	GC-8	13:09	14:26	14:28	15:48	02:39	37°04.431	021°18.772	37°04.446	021°18.743	4576		void	WA2/ central Graben
13.02.20	21	M162_21-1 GC	GC-9	17:24	18:32	18:34	19:49	02:04	36°53.793	021°17.742	36°53.782	021°17.719	4018		0-382	WA2/ central, south
13.03.20	22	M162_22-1 HF	HF-5	21:55	23:05	09:18	10:45	12:50	36°59.108	021°18.082	37°04.435	021°18.721	3861	HF2005		WA2/ central, south
13.03.20	22.1	M162_22-1 HF	HF-5	-	23:05	23:14	-	00:09	36°59.107	021°18.085	36°59.107	021°18.083	3862	HF2005P01		WA2/ central, south
14.03.20	22.2	M162_22-1 HF	HF-5	-	00:47	01:04	-	00:17	37°00.146	021°18.221	37°00.146	021°18.220	3844	HF2005P02		WA2/ central, south
14.03.20	22.3	M162_22-1 HF	HF-5	-	01:43	01:59	-	00:16	37°00.469	021°18.260	37°00.469	021°18.262	3861	HF2005P03		WA2/ central, south
14.03.20	22.4	M162_22-1 HF	HF-5	-	02:41	02:49	-	00:08	37°00.790	021°18.318	37°00.790	021°18.319	3860	HF2005P04		WA2/ central, south
14.03.20	22.5	M162_22-1 HF	HF-5	-	03:45	04:01	-	00:16	37°01.337	021°18.391	37°01.338	021°18.390	3857	HF2005P05		WA2/ central, south
14.03.20	22.6	M162_22-1 HF	HF-5	-	05:03	05:11	-	00:08	37°01.914	021°18.464	37°01.914	021°18.466	3858	HF2005P06		WA2/ central, south
14.03.20	22.7	M162_22-1 HF	HF-5	-	09:02	09:18	-	00:16	37°04.436	021°18.719	37°04.435	021°18.435	4517	HF2005P07		WA2/ central, south
14.03.20	23	M162_23-1 GC	GC-10	11:36	12:50	12:52	14:19	02:43	37°04.604	021°20.282	37°04.592	021°20.269	4513		0-273	WA2/ central Graben
14.03.20	24	M162_24-1 CTD	V-CTD-3	16:27	19:25	23:19	01:59	09:32	37°03.525	021°18.734	37°05.121	021°18.729	4186			WA2/ central, north
15.03.20	25	M162_25-1 HF	HF-6	03:10	04:20	07:46	09:05	05:55	37°09.764	021°19.221	37°11.696	021°19.443	4051	HF2006		WA2/ central, north

Date UTC	St. No. M162	Gear Station Meteor	Gear No.	Begin	Start Sci. Program	End Sci. Program	End	Duration hh:mm	Latitude N°	Longitude W°	Latitude N°	Longitude W°	Water depth (m)	Comment	Recovery (cm)	Area
					Time (UTC)				Begin / on seafloor		End / off seafloor					
15.03.20	25.1	M162_25-1 HF	HF-6	-	04:20	04:37	-	00:17	37°09.763	021°19.242	37°09.763	021°19.243	4051	HF2006P01		WA2/ central, north
15.03.20	25.2	M162_25-1 HF	HF-6	-	05:47	05:55	-	00:08	37°10.568	021°19.332	37°10.566	021°19.332	4000	HF2006P02		WA2/ central, north
15.03.20	25.3	M162_25-1 HF	HF-6	-	07:29	07:46	-	00:17	37°11.697	021°19.443	37°11.697	021°19.444	3993	HF2006P03		WA2/ central, north
15.03.20	26-1	M162_26-1 CTD	V-CTD-4-1	10:33	-	-	13:38	03:05	37°04.589	021°17.312	37°04.591	021°17.313	4443	CTD system failure		WA2/ central
15.03.20	26-2	M162_26-2 CTD	V-CTD-4-2	14:43	17:16	21:04	02:25	11:42	37°04.590	021°17.314	37°04.571	021°18.809	4443	T2-sensor not connected		WA2/ central
16.03.20	27	M162_27-1 MB_PS	MB/PS-5	05:46	05:46	06:25	06:25	00:39	37°02.343	022°00.351	37°01.725	022°04.225	4136			WA2/ west
16.03.20	28	M162_28-1 MB_PS	MB/PS-6	09:13	09:13	11:32	11:32	02:19	37°01.201	022°40.491	37°01.325	022°44.197	4521			WA2/ west
16.03.20	29	M162_29-1 GC	GC-11	12:25	13:44	13:45	15:14	02:49	36°59.472	022°43.585	36°59.473	022°43.583	4887		0-227	WA2/ west
16.03.20	30	M162_30-1 MB_PS	MB/PS-7	19:29	19:29	22:12	22:12	02:43	36°52.036	023°34.956	36°54.506	023°39.403	4407	data storage problems		WA2/ west
16.03.20	31	M162_31-1 HF	HF-7	22:46	00:08	05:49	07:20	08:36	36°53.700	023°40.867	36°55.267	023°41.233	4787	HF2007		WA2/ west
17.03.20	31.1	M162_31-1 HF	HF-7	-	00:08	00:24	-	00:16	36°53.700	023°40.867	36°53.700	023°40.867	4787	HF2007P01		WA2/ west
17.03.20	31.2	M162_31-1 HF	HF-7	-	01:02	01:10	-	00:08	36°53.938	023°40.925	36°53.938	023°40.925	4814	HF2007P02		WA2/ west
17.03.20	31.3	M162_31-1 HF	HF-7	-	01:47	02:04	-	00:17	36°54.177	023°40.982	36°54.177	023°40.982	4814	HF2007P03		WA2/ west
17.03.20	31.4	M162_31-1 HF	HF-7	-	02:49	03:05	-	00:16	36°54.479	023°41.042	36°54.479	023°41.042	4917	HF2007P04		WA2/ west
17.03.20	31.5	M162_31-1 HF	HF-7	-	03:39	03:56	-	00:17	36°54.727	023°41.133	36°54.727	023°41.133	4816	HF2007P05		WA2/ west
17.03.20	31.6	M162_31-1 HF	HF-7	-	04:43	04:51	-	00:08	36°55.023	023°41.171	36°55.023	023°41.171	4733	HF2007P06		WA2/ west
17.03.20	31.7	M162_31-1 HF	HF-7	-	05:33	05:49	-	00:16	36°55.322	023°41.231	36°55.322	023°41.230	4696	HF2007P07		WA2/ west
17.03.20	32	M162_32-1 GC	GC-12	07:41	09:06	09:07	10:29	02:48	36°54.458	023°41.117	36°54.459	023°41.116	4916		void	WA2/ west
17.03.20	33	M162_33-1 GC	GC-13	19:21	20:32	20:33	22:01	02:40	37°01.749	022°03.178	37°01.749	022°03.169	4250		0-250	WA2/ west
18.03.20	34	M162_34-1 MB_PS	MB/PS-8	07:53	07:53	11:21	11:21	03:28	37°05.480	020°22.702	37°09.856	020°23.178	4092			WA2/ east
18.03.20	35	M162_35-1 GC	GC-14	12:13	13:33	13:34	15:27	03:14	37°09.949	020°21.790	37°09.976	020°21.854	4740		0-350	WA2/ east
18.03.20	36	M162_36-1 GC	GC-15	16:07	17:28	17:29	18:57	02:50	37°10.566	020°18.494	37°10.547	020°18.503	4745		0-260	WA2/ east
18.03.20	37	M162_37-1 HF	HF-8	19:40	21:05	06:12	07:43	12:03	37°09.008	020°21.931	37°11.807	020°21.475	4661	HF2008		WA2/ east
18.03.20	37.1	M162_37-1 HF	HF-8	-	21:05	21:21	-	00:16	37°09.025	020°21.934	37°09.025	020°21.934	4661	HF2008P01		WA2/ east
18.03.20	37.2	M162_37-1 HF	HF-8	-	21:57	22:05	-	00:08	37°09.280	020°21.895	37°09.279	020°21.891	4700	HF2008P02		WA2/ east
18.03.20	37.3	M162_37-1 HF	HF-8	-	22:40	22:48	-	00:08	37°09.536	020°21.857	37°09.535	020°21.853	4725	HF2008P03		WA2/ east
18.03.20	37.4	M162_37-1 HF	HF-8	-	23:23	23:41	-	00:18	37°09.774	020°21.812	37°09.773	020°21.813	4745	HF2008P04		WA2/ east
19.03.20	37.5	M162_37-1 HF	HF-8	-	00:18	00:36	-	00:18	37°10.032	020°21.778	37°10.031	020°21.777	4545	HF2008P05		WA2/ east
19.03.20	37.6	M162_37-1 HF	HF-8	-	01:10	01:18	-	00:08	37°10.303	020°21.739	37°10.303	020°21.738	4748	HF2008P06		WA2/ east
19.03.20	37.7	M162_37-1 HF	HF-8	-	01:52	02:10	-	00:18	37°10.549	020°21.703	37°10.549	020°21.706	4746	HF2008P07		WA2/ east
19.03.20	37.8	M162_37-1 HF	HF-8	-	02:43	02:51	-	00:08	37°10.810	020°21.662	37°10.810	020°21.663	4745	HF2008P08		WA2/ east
19.03.20	37.9	M162_37-1 HF	HF-8	-	03:28	03:44	-	00:16	37°11.062	020°21.623	37°11.060	020°21.625	4745	HF2008P09		WA2/ east
19.03.20	37.10	M162_37-1 HF	HF-8	-	04:23	04:31	-	00:08	37°11.323	020°21.578	37°11.322	020°21.578	4745	HF2008P10		WA2/ east
19.03.20	37.11	M162_37-1 HF	HF-8	-	05:08	05:25	-	00:17	37°11.567	020°21.543	37°11.565	020°21.540	4739	HF2008P11		WA2/ east

Date UTC	St. No. M162	Gear Station Meteor	Gear No.	Time (UTC) Begin	Start Sci. Program	End Sci. Program	End	Duration hh:mm	Begin / on seafloor Latitude N°	Longitude W°	End / off seafloor Latitude N°	Longitude W°	Water depth (m)	Comment	Recovery (cm)	Area
19.03.20	37.12	M162_37-1 HF	HF-8	-	06:03	06:12	-	00:09	37°11.824	020°21.502	37°11.822	020°21.500	4735	HF2008P12		WA2/ east
19.03.20	38	M162_38-1 MB_PS	MB/PS-9	08:58	08:58	12:30	12:30	03:32	37°08.513	020°11.726	37°11.388	020°07.718	4360			WA2/ east
19.03.20	39	M162_39-1 GC	GC-16	13:10	14:00	14:01	14:57	01:47	37°09.821	020°04.717	37°09.832	020°04.721	3001	piece of rock in cc	0-0	WA2/ east
19.03.20	40	M162_40-1 GC	GC-17	15:21	16:13	16:14	17:09	01:48	37°09.844	020°04.558	37°09.845	020°04.561	3057	no no recovery	0-0	WA2/ east
19.03.20	41	M162_41-1 GC	GC-18	17:53	18:57	18:58	20:05	02:13	37°12.248	020°05.313	37°12.291	020°05.310	3833	only core catcher filled	0-20	WA2/ east
20.03.20	42	M162_42-1 MB_PS	MB/PS-10	00:00	00:00	09:21	09:21	09:21	37°35.024	020°04.626	37°34.501	020°27.999	4732			WA3
20.03.20	43	M162_43-1 GC	GC-19	10:25	11:34	11:35	12:58	02:33	37°35.378	020°29.070	37°35.381	020°29.068	4184	Core barrel bent at 1,5 m	0-127	WA3
20.03.20	44	M162_44-1 GC	GC-20	13:25	14:37	14:38	15:53	02:28	37°35.937	020°29.592	37°35.406	020°29.622	4188		0-243	WA3
20.03.20	45	M162_45-1 GC	GC-21	16:33	17:46	17:47	19:05	02:32	37°36.973	020°27.729	37°36.999	020°27.740	4117	only cc filled	0-20	WA3
20.03.20	46	M162_46-1 HF	HF-9	19:56	21:09	06:14	07:42	11:46	37°35.158	020°29.600	37°38.403	020°29.556	4187	HF2009		WA3
20.03.20	46.1	M162_46-1 HF	HF-9	-	21:09	21:25	-	00:16	37°35.208	020°29.597	37°35.209	020°29.593	4187	HF2009P01		WA3
20.03.20	46.2	M162_46-1 HF	HF-9	-	21:56	22:05	-	00:09	37°35.441	020°29.586	37°35.441	020°29.584	4188	HF2009P02		WA3
20.03.20	46.3	M162_46-1 HF	HF-9	-	22:38	22:53	-	00:15	37°35.670	020°29.584	37°35.669	020°29.587	4188	HF2009P03		WA3
20.03.20	46.4	M162_46-1 HF	HF-9	-	23:21	23:29	-	00:08	37°35.760	020°29.558	37°35.759	020°29.558	4188	HF2009P04		WA3
20.03.20	46.5	M162_46-1 HF	HF-9	-	23:52	00:00	-	00:08	37°35.852	020°29.582	37°35.852	020°29.581	4187	HF2009P05		WA3
21.03.20	46.6	M162_46-1 HF	HF-9	-	00:39	00:56	-	00:17	37°36.111	020°29.576	37°36.112	020°29.575	4189	HF2009P06		WA3
21.03.20	46.7	M162_46-1 HF	HF-9	-	01:35	01:54	-	00:19	37°36.365	020°29.570	37°36.365	020°29.568	4191	HF2009P07		WA3
21.03.20	46.8	M162_46-1 HF	HF-9	-	02:34	02:42	-	00:08	37°36.631	020°29.562	37°36.631	020°29.562	4191	HF2009P08		WA3
21.03.20	46.9	M162_46-1 HF	HF-9	-	03:41	03:59	-	00:18	37°37.137	020°29.551	37°37.137	020°29.547	4165	HF2009P09		WA3
21.03.20	46.10	M162_46-1 HF	HF-9	-	04:55	05:11	-	00:16	37°37.535	020°29.553	37°37.536	020°29.552	4167	HF2009P10		WA3
21.03.20	46.11	M162_46-1 HF	HF-9	-	06:06	06:14	-	00:08	37°38.034	020°29.550	37°38.035	020°29.550	4149	HF2009P11		WA3
21.03.20	47	M162_47-1 GC	GC-22	08:42	09:51	09:52	11:04	02:22	37°34.964	020°33.408	37°34.990	020°33.470	4159		0-276	WA3
21.03.20	48	M162_48-1 GC	GC-23	11:34	12:55	12:56	14:14	02:40	37°35.766	020°29.531	37°35.726	020°29.454	4188		0-109	WA3
22.03.20	49	M162_49-1 MB_PS	MB/PS-11	01:33	01:33	02:45	02:45	01:12	36°46.578	019°14.462	36°50.074	019°15.354	5160			WA4
23.03.20	50	M162_50-1 MB_PS	MB/PS-12	04:43	04:43	09:11	09:11	04:28	37°09.488	019°03.307	37°36.421	019°02.749	4886			WA4
23.03.20	51	M162_51-1 MB_PS	MB/PS-13	10:16	10:16	13:13	13:13	02:57	37°29.988	018°59.030	37°31.669	018°56.699	5451			WA4
23.03.20	52	M162_52-1 GC	GC-24	13:59	15:31	15:32	17:11	03:12	37°32.176	018°55.391	37°32.174	018°55.390	5659	no recovery	0-0	WA4
23.03.20	53	M162_53-1 GC	GC-25	18:24	19:57	19:58	21:43	03:19	37°30.396	019°08.508	37°30.444	019°08.515	5665	no recovery	0-0	WA4
24.03.20	54	M162_54-1 MB_PS	MB/PS-14	01:10	01:10	03:36	03:36	02:26	37°33.772	018°38.080	37°32.229	018°38.159	4867			WA4
24.03.20	55	M162_55-1 MB_PS	MB/PS-15	04:14	04:14	05:15	05:15	01:01	37°30.225	018°33.687	37°31.451	018°34.263	4642			WA4
24.03.20	56	M162_56-1 MB_PS	MB/PS-16	06:23	06:23	07:20	07:20	00:57	37°31.715	018°25.172	37°26.844	018°25.880	4414			WA4
24.03.20	57	M162_57-1 GC	GC-26	08:35	09:56	09:57	11:21	02:46	37°31.462	018°32.801	37°31.498	018°32.948	4658		0-449	WA4

Date UTC	St. No. M162	Gear Station Meteor	Gear No.	Time (UTC)					Begin / on seafloor		End / off seafloor		Water depth (m)	Comment	Recovery (cm)	Area
				Begin	Start Sci. Program	End Sci. Program	End	Duration hh:mm	Latitude N°	Longitude W°	Latitude N°	Longitude W°				
24.03.20	58	M162_58-1 GC	GC-27	12:09	13:31	13:32	14:58	02:49	37°32.138	018°38.737	37°32.120	018°38.694	4846		0-276	WA4
24.03.20	59	M162_59-1 CTD	V-CTD-5	17:13	20:04	22:21	02:47	09:34	37°29.207	018°40.285	37°30.310	018°40.040	4708	posidonia from 20:06		WA4
25.03.20	60	M162_60-1 CTD	V-CTD-6	04:15	07:10	08:48	12:25	08:10	37°27.866	018°24.898	37°27.778	018°25.838	4613	Posidonia 04:27 ; 08:44		WA4
25.03.20	61	M162_61-1 MB_PS	MB/PS-17	13:14	13:14	14:30	14:30	01:16	37°27.736	018°28.029	37°28.511	018°20.153	4383			WA4
25.03.20	62	M162_62-1 GC	GC-28	15:39	16:54	16:55	18:14	02:35	37°27.796	018°25.486	37°27.795	018°25.487	4672		0-423	WA4
25.03.20	63	M162_63-1 HF	HF-10	20:10	21:32	07:06	08:29	12:19	37°32.220	018°38.650	37°29.755	018°40.352	4844	HF2010		WA4
25.03.20	63.1	M162_63-1 HF	HF-10	-	21:32	21:48	-	00:16	37°32.220	018°38.651	37°32.220	018°38.651	4844	HF2010P11 (P01)		WA4
25.03.20	63.2	M162_63-1 HF	HF-10	-	22:47	22:56	-	00:09	37°31.912	018°38.698	37°31.914	018°38.697	4843	HF2010P10 (P02)		WA4
25.03.20	63.3	M162_63-1 HF	HF-10	-	23:46	00:02	-	00:16	37°31.673	018°38.821	37°31.672	018°38.816	4833	HF2010P09 (P03)		WA4
26.03.20	63.4	M162_63-1 HF	HF-10	-	00:53	01:01	-	00:08	37°31.439	018°38.879	37°31.441	018°38.880	4836	HF2010P08 (P04)		WA4
26.03.20	63.5	M162_63-1 HF	HF-10	-	01:53	02:10	-	00:17	37°31.201	018°39.010	37°31.200	018°39.009	4838	HF2010P07 (P05)		WA4
26.03.20	63.6	M162_63-1 HF	HF-10	-	03:07	03:16	-	00:09	37°30.901	018°39.133	37°30.898	018°39.133	4828	HF2010P06 (P06)		WA4
26.03.20	63.7	M162_63-1 HF	HF-10	-	04:03	04:21	-	00:18	37°30.660	018°39.192	37°30.661	018°39.188	4818	HF2010P05 (P07)		WA4
26.03.20	63.8	M162_63-1 HF	HF-10	-	05:06	05:14	-	00:08	37°30.414	018°39.308	37°30.415	018°39.306	4821	HF2010P04 (P08)		WA4
26.03.20	63.9	M162_63-1 HF	HF-10	-	06:02	06:09	-	00:07	37°30.117	018°39.434	37°30.117	018°39.429	4799	HF2010P03 (P09)		WA4
26.03.20	63.10	M162_63-1 HF	HF-10	-	06:47	07:06	-	00:19	37°29.996	018°39.490	37°29.995	018°39.491	4816	HF2010P02 (P10)		WA4
26.03.20	64	M162_64-1 GC	GC-29	10:53	12:12	12:13	13:36	02:43	37°27.804	018°25.437	37°27.765	018°25.650	4673		0-484	WA4
27.03.20	65	M162_65-1 GC	GC-30	06:59	08:19	08:20	09:41	02:42	37°04.758	021°18.743	37°04.758	021°18.745	4512		0-246	WA2/ central Graben
27.03.20	66	M162_66-1 GC	GC-31	10:48	11:55	11:56	13:08	02:20	36°59.253	021°18.182	36°59.244	021°18.104	3863		0-251	WA2/ central, south
27.03.20	67	M162_67-1 GC	GC-32	13:33	14:40	14:41	15:55	02:22	37°00.520	021°18.260	37°00.479	021°18.267	3861		0-293	WA2/ central, south
27.03.20	68	M162_68-1 HF	HF-11	17:19	18:32	05:04	06:20	13:01	36°52.554	021°17.202	36°55.789	021°17.626	4187	HF2011		WA2/ central, south
27.03.20	68.1	M162_68-1 HF	HF-11	-	18:32	18:48	-	00:16	36°52.553	021°17.192	36°52.553	021°17.192	4187	HF2011P11 (P01)		WA2/ central, south
27.03.20	68.2	M162_68-1 HF	HF-11	-	19:23	19:31	-	00:08	36°52.798	021°17.223	36°52.798	021°17.222	4172	HF2011P10 (P02)		WA2/ central, south
27.03.20	68.3	M162_68-1 HF	HF-11	-	20:10	20:25	-	00:15	36°53.044	021°17.257	36°53.045	021°17.255	4166	HF2011P09 (P03)		WA2/ central, south
27.03.20	68.4	M162_68-1 HF	HF-11	-	21:04	21:12	-	00:08	36°53.317	021°17.292	36°53.317	021°17.293	4181	HF2011P08 (P04)		WA2/ central, south
27.03.20	68.5	M162_68-1 HF	HF-11	-	21:50	21:57	-	00:07	36°53.558	021°17.323	36°53.559	021°17.323	4141	HF2011P07 (P05)		WA2/ central, south
27.03.20	68.6	M162_68-1 HF	HF-11	-	22:36	22:53	-	00:17	36°53.814	021°17.357	36°53.814	021°17.357	4054	HF2011P06 (P06)		WA2/ central, south
27.03.20	68.7	M162_68-1 HF	HF-11	-	23:33	23:51	-	00:18	36°54.052	021°17.393	36°54.052	021°17.392	4046	HF2011P05 (P07)		WA2/ central, south
28.03.20	68.8	M162_68-1 HF	HF-11	-	00:26	00:42	-	00:16	36°54.303	021°17.425	36°54.302	021°17.425	3970	HF2011P04 (P08)		WA2/ central, south

Date UTC	St. No. M162	Gear Station Meteor	Gear No.	Begin	Start Sci. Program	End Sci. Program	End	Duration hh:mm	Latitude N°	Longitude W°	Latitude N°	Longitude W°	Water depth (m)	Comment	Recovery (cm)	Area
28.03.20	68.9	M162_68-1 HF	HF-11	-	01:18	01:25	-	00:07	36°54.544	021°17.457	36°54.544	021°17.458	3935	HF2011P03 (P09)		WA2/ central, south
28.03.20	68.10	M162_68-1 HF	HF-11	-	01:59	02:06	-	00:07	36°54.785	021°17.495	36°54.785	021°17.494	3901	HF2011P02 (P10)		WA2/ central, south
28.03.20	68.11	M162_68-1 HF	HF-11	-	02:44	03:00	-	00:16	36°55.022	021°17.525	36°55.022	021°17.526	3909	HF2011P01 (P11)		WA2/ central, south
28.03.20	68.12	M162_68-1 HF	HF-11	-	03:54	04:12	-	00:18	36°55.516	021°17.590	36°55.515	021°17.591	3879	HF2011P00 (P12)		WA2/ central, south
28.03.20	68.13	M162_68-1 HF	HF-11	-	04:56	05:04	-	00:08	36°55.789	021°17.627	36°55.789	021°17.627	3870	HF2011P(-1) (P13)		WA2/ central, south
28.03.20	69	M162_69-1 GC	GC-33	08:20	09:30	09:31	10:43	02:23	37°11.478	021°19.411	37°11.479	021°19.411	3992		0-163	WA2/ central, north
28.03.20	70	M162_70-1 GC	GC-34	12:21	13:37	13:38	14:59	02:38	37°04.286	021°18.703	37°04.286	021°18.702	4417		0-136	WA2/ central Graben
28.03.20	71	M162_71-1 HF	HF-12	15:38	17:02	19:57	21:23	05:45	37°04.752	021°18.345	37°04.678	021°17.267	4477	HF2012		WA2/ central Graben
28.03.20	71.1	M162_71-1 HF	HF-12	-	17:02	17:18	-	00:16	37°04.752	021°18.345	37°04.752	021°18.347	4477	HF2012P01		WA2/ central Graben
28.03.20	71.2	M162_71-1 HF	HF-12	-	17:58	18:06	-	00:08	37°04.606	021°17.988	37°04.606	021°17.987	4486	HF2012P02		WA2/ central Graben
28.03.20	71.3	M162_71-1 HF	HF-12	-	18:50	19:06	-	00:16	37°04.678	021°17.626	37°04.680	021°17.630	4462	HF2012P03		WA2/ central Graben
28.03.20	71.4	M162_71-1 HF	HF-12	-	19:49	19:57	-	00:08	37°04.680	021°17.271	37°04.678	021°17.267	4475	HF2012P04		WA2/ central Graben
29.03.20	72	M162_72-1 GC	GC-35	09:54	11:17	11:18	12:45	02:51	37°30.418	018°39.282	37°30.420	018°39.293	4807		0-193	WA4
29.03.20	73	M162_73-1 HF	HF-13	14:14	15:35	17:50	19:22	05:08	37°27.802	018°25.649	37°27.815	018°25.015	4672	HF2013		WA4
29.03.20	73.1	M162_73-1 HF	HF-13	-	15:35	15:52	-	00:17	37°28.793	018°25.671	37°28.793	018°25.671	4672	HF2013P01		WA4
29.03.20	73.2	M162_73-1 HF	HF-13	-	16:39	16:55	-	00:16	37°27.813	018°25.345	37°27.814	018°25.348	4676	HF2013P02		WA4
29.03.20	73.3	M162_73-1 HF	HF-13	-	17:33	17:50	-	00:17	37°27.812	018°25.015	37°27.812	018°25.017	4633	HF2013P03		WA4
30.03.20	74	M162_74-1 MB_PS	MB/PS-18	06:04	06:04	07:38	07:38	01:34	37°28.306	016°04.775	37°27.346	016°00.848	4251			WA5
30.03.20	75	M162_75-1 MB_PS	MB/PS-19	08:13	08:13	09:53	09:53	01:40	37°27.085	015°56.115	37°27.174	015°54.459	4456			WA5
30.03.20	76	M162_76-1 GC	GC-36	10:53	12:12	12:13	13:35	02:42	37°26.365	015°54.463	37°26.360	015°54.467	4566	Only pore water samples	0-40	WA5/ west
30.03.20	77	M162_77-1 GC	GC-37	13:51	15:10	15:11	16:32	02:41	37°26.182	015°53.518	37°26.312	015°53.496	4547		0-140	WA5/ west
30.03.20	78	M162_78-1 GC	GC-38	17:28	18:44	18:45	20:05	02:37	37°27.993	016°00.397	37°28.072	016°00.395	4383		0-270	WA5/ west
31.03.20	79	M162_79-1 HF	HF-14	19:03	20:19	23:07	00:35	05:32	37°28.189	016°00.453	37°28.316	016°01.242	4383	HF2014		WA5/ west
31.03.20	79.1	M162_79-1 HF	HF-14	-	20:19	20:36	-	00:17	37°28.186	016°00.450	37°28.188	016°00.452	4383	HF2014P01		WA5/ west
31.03.20	79.2	M162_79-1 HF	HF-14	-	21:34	21:49	-	00:15	37°28.248	016°00.844	37°28.248	016°00.842	4369	HF2014P02		WA5/ west
31.03.20	79.3	M162_79-1 HF	HF-14	-	22:51	23:07	-	00:16	37°28.316	016°01.242	37°28.316	016°01.241	4341	HF2014P03		WA5/ west
01.04.20	80	M162_80-1 GC	GC-39	05:58	07:18	07:19	08:43	02:45	37°26.226	015°53.515	37°26.206	015°53.491	4546	Only pore water samples	0-40	WA5/ west
01.04.20	81	M162_81-1 MB_PS	MB/PS-20	10:12	10:12	12:23	12:23	02:11	37°24.178	015°41.282	37°22.224	015°35.909	5264			WA5
01.04.20	82	M162_82-1 GC	GC-40	12:46	14:14	14:15	15:45	02:59	37°23.140	015°35.754	37°23.172	015°35.813	5054		0-484	WA5/ east
01.04.20	83	M162_83-1 MB_PS	MB/PS-21	16:14	16:14	17:49	17:49	01:35	37°24.480	015°35.553	37°22.538	015°30.724	5080			WA5
01.04.20	84	M162_84-1 HF	HF-15	18:55	20:25	23:45	01:42	06:47	37°22.742	015°35.887	37°23.169	015°35.810	4941	HF2015		WA5/ east
01.04.20	84.1	M162_84-1 HF	HF-15	-	20:25	20:42	-	00:17	37°22.741	015°35.883	37°22.742	015°35.885	4941	HF2015P01, winch probl.		WA5/ east

Date UTC	St. No. M162	Gear Station Meteor	Gear No.	Begin	Start Sci. Program	End Sci. Program	End	Duration hh:mm	Latitude N°	Longitude W°	Latitude N°	Longitude W°	Water depth (m)	Comment	Recovery (cm)	Area
					Time (UTC)				Begin / on seafloor		End / off seafloor					
01.04.20	84.2	M162_84-1 HF	HF-15	-	22:19	22:37	-	00:18	37°23.004	015°35.860	37°23.003	015°35.861	5021	HF2015P02, winch probl.		WA5/ east
01.04.20	84.3	M162_84-1 HF	HF-15	-	23:26	23:45	-	00:19	37°23.169	015°35.808	37°23.168	015°35.807	5055	HF2015P03, winch probl.		WA5/ east
02.04.20	85	M162_85-1 CTD	V-CTD-7	05:45	07:54	09:06	11:14	05:29	37°14.477	014°54.947	37°14.765	014°55.658	3515	camera start 07:54, posidonia start 07:59		WA6
02.04.20	86	M162_86-1 TVMUC	V-MUC-3	11:48	13:03	13:05	14:22	02:34	37°14.765	014°55.655	37°14.764	014°55.656	3537	recovery 4 tubes, 1x4 cm, 1x6 cm, 2x10 cm	~ sum of 30 cm	WA6
02.04.20	87	M162_87-1 MB_PS	MB/PS-22	15:10	15:10	16:28	16:28	01:18	37°12.665	014°51.046	37°15.545	014°58.201	2600			WA6
02.04.20	88	M162_88-1 GC	GC-41	17:12	18:14	18:15	19:15	02:03	37°15.262	014°57.488	37°15.273	014°57.463	3509	core barrel bent	~60	WA6
02.04.20	89	M162_89-1 HF	HF-16	20:10	21:14	01:20	02:35	06:25	37°14.551	014°55.346	37°15.170	014°57.138	3533	HF2016		WA6
02.04.20	89.1	M162_89-1 HF	HF-16	-	21:14	21:29	-	00:15	37°14.552	014°55.345	37°14.552	014°55.345	3533	HF2016P01		WA6
02.04.20	89.2	M162_89-1 HF	HF-16	-	22:35	22:42	-	00:07	37°14.747	014°55.893	37°14.746	014°55.893	3546	HF2016P02		WA6
02.04.20	89.3	M162_89-1 HF	HF-16	-	23:50	23:57	-	00:07	37°14.952	014°56.499	37°14.952	014°56.498	3534	HF2016P03		WA6
03.04.20	89.4	M162_89-1 HF	HF-16	-	01:04	01:20	-	00:16	37°15.169	014°57.136	37°15.169	014°57.138	3508	HF2016P04		WA6
03.04.20	90	M162_90-1 GC	GC-42	05:58	07:01	07:02	08:15	02:17	37°14.755	014°55.966	37°14.754	014°55.967	3547		0-126	WA6
03.04.20	91	M162_91-1 GC	GC-43	08:25	09:27	09:28	10:38	02:13	37°14.754	014°55.968	37°14.755	014°55.967	3547		0-126	WA6
03.04.20	92	M162_92-1 GC	GC-44	10:47	11:48	11:49	12:55	02:08	37°14.753	014°55.967	37°14.755	014°55.964	3547		0-128	WA6
03.04.20	93	M162_93-1 MB_PS	MB/PS-23	14:02	14:02	15:46	15:46	01:44	37°21.745	014°56.318	37°30.465	014°55.065	3770			WA6/ north
03.04.20	94	M162_94-1 GC	GC-45	17:03	18:14	18:15	19:35	02:32	37°30.358	014°55.108	37°30.312	014°55.092	4460		0-300	WA6/ north
03.04.20	95	M162_95-1 HF	HF-17	20:05	21:24	01:17	02:40	06:35	37°30.308	014°55.094	37°29.751	014°55.178	4460	HF2017		WA6/ north
03.04.20	95.1	M162_95-1 HF	HF-17	-	21:24	21:40	-	00:16	37°30.310	014°55.092	37°30.309	014°55.094	4460	HF2017P01		WA6/ north
03.04.20	95.2	M162_95-1 HF	HF-17	-	22:14	22:21	-	00:07	37°30.210	014°55.113	37°30.210	014°55.115	4455	HF2017P02		WA6/ north
03.04.20	95.3	M162_95-1 HF	HF-17	-	23:00	23:16	-	00:16	37°30.098	014°55.131	37°30.097	014°55.130	4448	HF2017P03		WA6/ north
03.04.20	95.4	M162_95-1 HF	HF-17	-	23:49	23:56	-	00:07	37°29.977	014°55.142	37°29.974	014°55.144	4438	HF2017P04		WA6/ north
04.04.20	95.5	M162_95-1 HF	HF-17	-	00:24	00:32	-	00:08	37°29.864	014°55.159	37°29.865	014°55.153	4440	HF2017P05		WA6/ north
04.04.20	95.6	M162_95-1 HF	HF-17	-	01:01	01:17	-	00:16	37°29.747	014°55.176	37°29.746	014°55.179	4419	HF2017P06		WA6/ north

8   Data and Sample Storage and Availability

Meta-data and data of onboard surveys, measurements, and samples collected on M162 "Gloria Flow" will be stored and maintained in a web-based multi-user system. In a first phase, only multibeam bathymetry (raw) data and meta-data will be available to the public. After a proprietary time of two years the data management team at GEOMAR will publish these data by dissemination to national and international data archives, i.e. the data will be submitted to PANGAEA no later than April, 2022. Digital object identifiers (DOIs) are automatically assigned to data sets archived in the PANGAEA Open Access library making them publically retrievable, citable and reusable for the future. All metadata are available publically via the following link pointing at the GEOMAR portal (https://portal.geomar.de/metadata/leg/show/351718). The majority of data and samples are hosted at GEOMAR. A brief overview of types of data/samples, responsible scientists, and host institutes are given below and in Table 8.1.

Hydrocoustics: Shipboard hydroacoustic surveys were coordinated by Dr. P. Terrinha (LNEG) Bathymetric and sub-bottom profiling data (Parasound) are hosted at GEOMAR. Raw data can be accessed through Dr. C. Hensen (GEOMAR).

CTD: Raw and processed CTD data are hosted at GEOMAR and can be accessed through Dr. M. Schmidt (GEOMAR).

Sediments: Sediment cores and samples are stored at GEOMAR and IPMA. Information and data can be obtained through Dr. C. Hensen, Dr. P. Terrinha, and Dr. P. Nogueira.

Pore water data: Pore water geochemical data can be accessed through Dr. C. Hensen. Biomarker samples are stored at GEOMAR and will be analysed by Dr. M. Nuzzo.

Microbiology: Microbiological data can be accessed through Dr. C. Glombitza (ETH Zurich). Samples are stored at ETH Zurich.

Biology: Biological samples for analysis of faunal assemblages are hosted at Universidade de Évora. The samples are currently being analysed for meiofauna by Dr H. Adão (Universidade de Évora).

Heat flow: Heat flow data recorded on M162 are stored at PANGAEA and can be accessed through Dr. N. Kaul (Bremen University).

Tab. 8.1   Data storage and availability

Type	Data base	Available Date	Free access Date	Contact E-Mail
Hydroacoustics	OSIS	October 2020	April 2022	chensen@geomar.de, pedro.terrinha@ipma.pt
CTD, ADCP (raw data)	OSIS	October 2020	April 2022	mschmidt@geomar.de
CTD (gas conc.)	OSIS, PANGAEA	January 2021	April 2025	mschmidt@geomar.de
Heat flow	PANGAEA	October 2020	April 2025	nkaul@uni-bremen.de
Pore water data	OSIS, PANGAEA	January 2021	April 2025	chensen@geomar.de
Sediment composition	OSIS, PANGAEA	June 2021	April 2025	chensen@geomar.de, pedro.terrinha@ipma.pt
Organic geochemistry	OSIS	June 2021	April 2025	mschmidt@geomar.de
Microbiology	PANGAEA	December 2021	April 2025	clemens.glombitza@usys.ethz.ch
Faunal assemblages	PANGAEA	December 2021	April 2025	hadao@uevora.pt

9   Acknowledgements

10   References

Adhikari, R.R., Glombitza, C., Nickel, J.C., Anderson, C.H., Dunlea, A.G., Spivack, A.J., Murray, R.W., D'Hondt, S., Kallmeyer, J. (2016). Hydrogen Utilization Potential in Subsurface Sediments. Front. Microbiol. 7, 8. https://doi.org/10.3389/fmicb.2016.00008

Batista, L., Hübscher, C., Terrinha, P., Matias, L., Afilhado, A., and Lüdmann, T. (2017). Crustal structure of the Eurasia–Africa plate boundary across the Gloria Fault, North Atlantic Ocean: Geophysical Journal International, v. 209, no. 2, p. 713-729.

Beulig, F., Røy, H., Glombitza, C., Jørgensen, B.B. (2018). Control on rate and pathway of anaerobic organic carbon degradation in the seabed. Proc. Natl. Acad. Sci. 115, 367–372, https://doi.org/10.1073/pnas.1715789115

Brandt, A. (2008). Deep-sea ecology: infectious impact on ecosystem function. Current Biology 18: 1104-1106.

Brennwald M.S., Vogel N., Scheidegger Y., Tomonaga Y., Livingstone D.M., Kipfer R., Noble Gases as Environmental Tracers in Sediment Porewaters and Stalagmite Fluid Inclusions in P. Burnard (ed.), The Noble Gases as Geochemical Tracers (2013), Advances in Isotope Geochemistry.

Brennwald M.S., Hofer M., Peeters F., Aeschbach-Hertig W., Strassmann K., Kipfer R., Imboden D.M. (2003). Analysis of dissolved noble gases in the pore water of lacustrine sediments. Limnol Oceanogr Methods 1:51–62.

Buforn, E., Udias, A., Colombàs, M.A. (1988). Seismicity, source mechanisms and tectonics of the Azores-Gibraltar plate boundary, Tectonophysics,152, 89–118.

Bullard, E. (1954). The Flow of Heat through the Floor of the Atlantic Ocean. Proceedings of the Royal Society A: Mathematical, Physical and Engineering Sciences 222 (1150), 408–429.

Danovaro, R., Corinaldesi, C., Dell'Anno, A., Snelgrove, Paul V.R. (2017). The deep-sea under global change. Current Biology 27, R431–R510

Danovaro, R., Gambi, C., Lampadariou, N., Tselepides, A. (2008). Deep-sea nematode biodiversity in the Mediterranean basin: testing for longitudinal, bathymetric and energetic gradients. Ecography 31: 231–244. https://doi.org/10.1111/j.0906-7590.2008.5484.x

Duarte, J. C., Rosas, F. M., Terrinha, P., Gutscher, M.-A., Malavieille, J., Silva, S., Matias, L. (2011). Thrust-wrench interference tectonics in the Gulf of Cadiz (Africa-Iberia plate boundary in the North-East Atlantic): Insights from analog models. Marine Geology, 289 (1—4), p. 135-149.

Duarte, J. C., Rosas, F. M., Terrinha, P., Schellart, W. P., Boutelier, D., Gutscher, M.-A., Ribeiro, A. (2013). Are subduction zones invading the Atlantic? Evidence from the southwest Iberia margin. Geology 41 (8), 839-842.

Eickenbusch, P., Takai, K., Sissman, O., Suzuki, S., Menzies, C., Sakai, S., Sansjofre, P., Tasumi, E., Bernasconi, S.M., Glombitza, C., Jørgensen, B.B., Morono, Y., Lever, M.A.

(2019). Origin of Short-Chain Organic Acids in Serpentinite Mud Volcanoes of the Mariana Convergent Margin. Front. Microbiol. 10, https://doi.org/10.3389/fmicb.2019.01729

Fofonoff, N.P. and Millard Jr, R.C. (1983). Algorithms for Computation of Fundamental Properties of Seawater. Endorsed by Unesco/SCOR/ICES/IAPSO Joint Panel on Oceanographic Tables and Standards and SCOR Working Group 51. Unesco Technical Papers in Marine Science, No. 44.

Giere O. (2009). Meiobenthology. The microscopicmotile fauna of aquatic sediments. Springer-Verlag, Berlin

Glombitza, C., Adhikari, R.R., Riedinger, N., Gilhooly III, W.P., Hinrichs, K.-U., Inagaki, F. (2016). Microbial sulfate reduction potential in coal-bearing sediments down to∼ 2.5 km below the seafloor off Shimokita Peninsula, Japan. Front. Microbiol. 7, 157n6.

Glombitza, C., Egger, M., Røy, H., Jørgensen, B.B. (2019). Controls on volatile fatty acid concentrations in marine sediments (Baltic Sea). Geochim. Cosmochim. Acta 258, 226–241. https://doi.org/10.1016/j.gca.2019.05.038

Glombitza, C., Jaussi, M., Røy, H., Seidenkrantz, M.-S., Lomstein, B.A., Jørgensen, B.B. (2015). Formate, acetate, and propionate as substrates for sulfate reduction in sub-arctic sediments of Southwest Greenland. Front. Microbiol. 6, 846.

Glombitza, C., Pedersen, J., Røy, H., Jørgensen, B.B. (2014). Direct analysis of volatile fatty acids in marine sediment porewater by two-dimensional ion chromatography-mass spectrometry. Limnol. Oceanogr. Methods 12, 455–468.

Harris, R.N., Fisher, A.T., Chapman, D.S. (2004). Fluid flow through seamounts and implications for global mass fluxes. Geology 32 (8), 725–728.

Hartmann, A., Villinger, H. (2002). Inversion of marine heat flow measurements by expansion of the temperature decay function. Geophysical Journal International 148 (3), 628–636.

Hensen, C., Duarte, J.C., Vannucchi, P., Mazzini, A., Lever, M.A., Terrinha, P., Géli, L., Henry, P., Villinger, H., Morgan, J., Schmidt, M., Gutscher, M.-A., Bartolome, R., Tomonaga, Y., Polonia, A., Gràcia, E., Tinivella, U., Lupi, M., Çağatay, M. N., Elvert, M., Sakellariou, D., Matias, L., Kipfer, R., Karageorgis, A. P., Ruffine, L., Liebetrau, V., Pierre, C., Schmidt, C., Batista, L., Gasperini, L., Burwicz, E., Neres, M., and Nuzzo, M., (2019). Marine Transform Faults and Fracture Zones: A Joint Perspective Integrating Seismicity, Fluid Flow and Life: Frontiers in Earth Science, v. 7, no. 39.

Hensen, C., Scholz, F., Nuzzo, M., Valadares, V., Gràcia, E., Terrinha, P., Liebetrau, V., Kaul, N., Silva, S., Martínez-Loriente, S., Bartolome, R., Piñero, E., Magalhães, V.H., Schmidt, M., Weise, S.M., Cunha, M., Hilario, A., Perea, H., Rovelli, L., Lackschewitz, K. (2015). Strike-slip faults mediate the rise of crustal-derived fluids and mud volcanism in the deep sea. Geology, doi:10.1130/G36359.1

Hoehler, T.M., Alperin, M.J., Albert, D.B., Martens, C.S. (1998). Thermodynamic control on hydrogen concentrations in anoxic sediments. Geochim. Cosmochim. Acta 62, 1745–1756. https://doi.org/10.1016/S0016-7037(98)00106-9.

Hyndman, R., Davis, E., Wright, J. (1979). The measurements of marine geothermal heat flow by a multipenetration probe with digital acoustic telemetry and insitu thermal conductivity. Marine Geophysical Researches 4 (2), 181–205.

Jørgensen, B.B. (1978). A comparison of methods for the quantification of bacterial sulfate reduction in coastal marine sediments. Geomicrobiol. J. 1, 11–27. https://doi.org/10.1080/01490457809377721.

Kallmeyer, J., Ferdelman, T.G., Weber, A., Fossing, H., Jørgensen, B.B. (2004). A cold chromium distillation procedure for radiolabeled sulfide applied to sulfate reduction measurements. Limnol. Oceanogr. Methods 2, 171–180. https://doi.org/10.4319/lom.2004.2.171.

Krüger, F., Dahm, T., Hannemann, K. (2020). Mapping of Eastern North Atlantic Ocean seismicity from Po/So observations at a mid-aperture seismological broad-band deep sea array. Geophysical Journal International 221 (2), 1055-1080.

Lever, M.A., Torti, A., Eickenbusch, P., Michaud, A.B., Šantl-Temkiv, T., Jørgensen, B.B. (2015). A modular method for the extraction of DNA and RNA, and the separation of DNA pools from diverse environmental sample types. Front. Microbiol. 6. https://doi.org/10.3389/fmicb.2015.00476.

Lin, Y.-S., Heuer, V.B., Goldhammer, T., Kellermann, M.Y., Zabel, M., Hinrichs, K.-U. (2012). Towards constraining H2 concentration in subseafloor sediment: A proposal for combined analysis by two distinct approaches. Geochim. Cosmochim. Acta 77, 186–201, https://doi.org/10.1016/j.gca.2011.11.008

Linke P., Schmidt M., Rohleder M., Al-Barakati A., Al-Farawati R. (2015). Novel online digital video and high-speed data broadcasting via standard coaxial cable onboard marine operating vessels. Marine Technology Society Journal 49(1), 7-18.

Lister, C.R.B. (1979). The pulse-probe method of conductivity measurement. Geophys. J. R. Astr. Soc. 57, 451–461.

Liu, M., & Tanhua, T. (2019). Characteristics of Water Masses in the Atlantic Ocean based on GLODAPv2 data. Ocean Science Discussions, 1-43.

Lohrer, A.M., Thrush, F.S., Gibbs, M.M. (2004). Bioturbators enhance ecosystem function through complex biogeochemical interactions. Nature 431: 1092-1095.

Moens, T., et al. (2014). Ecology of free-living marine nematodes. In: Schmidt-Rhaesa A (ed) Volume 2 Nematoda. De Gruyter, Berlin, Boston, pp 109–152.

Müller, R.D. et al. (2008). Age, spreading rates and spreading asymmetry oft he world's ocean crust. Geochem. Geophys. Geosyst., 9, Q04007, doi:10.1029/2007GC001743

Nealson, K.H., Inagaki, F., Takai, K. (2005). Hydrogen-driven subsurface lithoautotrophic microbial ecosystems (SLiMEs): do they exist and why should we care? Trends Microbiol. 13, 405–410, https://doi.org/10.1016/j.tim.2005.07.010.

Neres, M., Carafa, M.M.C., Fernandes; R., Matias, L., Duarte, J.C., Barba; S., Terrinha, P. (2016). Lithospheric deformation in the Africa–Iberia Plate Boundary: improved neotectonic modeling testing a basal-driven Alboran plate. Journal of Geophysical Research - Solid Earth. AGU, 10.1002/2016JB013012

Purkl S., Eisenhauer A. (2004). Determination of radium isotopes and 222Rn in a groundwater affected coastal area of the Baltic Sea and the underlying sub-sea floor aquifer. Marine Chemistry, 87, 137-149.

Rosli, N., Leduc, D., Rowden, A.A., Probert, P.K. (2018). Review of recent trends in ecological studies of deep-sea meiofauna, with focus on patterns and processes at small to regional spatial scales. Marine Biodiversity 48: 13-34.

Russell, M.J., Hall, A.J., Martin, W. (2010). Serpentinization as a source of energy at the origin of life. Geobiology 8, 355–371. https://doi.org/10.1111/j.1472-4669.2010.00249.x.

Schmidt, C., Hensen, C., Wallmann, K, Liebetrau, V., Tatzel, M., Schurr, S.L., Kutterolf, S., Haffert, L., Geilert, S., Hübscher, C., Lebas, E., Heuser, A., Schmidt, M., Strauss, H., Vogl, J., Hansteen, Thor H. (2019). Origin of High Mg and SO$_4$ Fluids in Sediments of the Terceira Rift, Azores-Indications for Caminite Dissolution in a Waning Hydrothermal System. Geochemistry, Geophysics, Geosystems, 20(12), 6078-6094, https://doi.org/10.1029/2019GC008525

Schmidt M., Linke P., Esser D. (2013). Recent development in IR-sensor technology for monitoring subsea methane discharge. Marine Technology Society Journal 47(3), 27-35.

Schrenk, M.O., Brazelton, W.J., Lang, S.Q. (2013). Serpentinization, Carbon, and Deep Life. Rev. Mineral. Geochem. 75, 575–606. https://doi.org/10.2138/rmg.2013.75.18.

Sea-Bird Electronics, Inc. (2017). Seasoft V2: Seasave V7 CTD Real-Time Data Acquisition Software for Windows. Retrieved from https://www.seabird.com/profiling/sbe-911plus-ctd/family-downloads?productCategoryId=54627473769.

Seeberg-Elverfeldt, J., Schlüter, M., Feseker, T., Kölling, M. (2005). Rhizon sampling of porewaters near the sediment-water interface of aquatic systems. Limnol. Oceanogr. Methods 3, 361–371. https://doi.org/10.4319/lom.2005.3.361.

Sørensen, J., Christensen, D., Jørgensen, B.B. (1981). Volatile Fatty Acids and Hydrogen as Substrates for Sulfate-Reducing Bacteria in Anaerobic Marine Sediment. Appl. Environ. Microbiol. 42, 5–11.

Terrinha, P., Matias, L., Vicente, J., Duarte, J., Luis, J., Pinheiro, L., Lourenco, N., Diez, S., Rosas, F., Magalhaes, V., Valadares, V., Zitellini, N., Roque, C., and Victor, L. M. (2009). Morphotectonics and strain partitioning at the Iberian-Africa plate boundary from multibeam and seismic reflection data. Marine Geology 267 (3-4), 156-174.

Thakur, M.P. and Geisen, S. (2019). Trophic regulations of the soil microbiome. Trends in Microbiology 27(9), 771-780.

Tomonaga, Y., Brennwald, M.S., Kipfer, R. (2011). An improved method for the analysis of dissolved noble gases in the porewater of unconsolidated sediments. Limnol. Oceanogr. Methods 2, 42-49.

Villinger, H., Davis, E. E. (1987). A New Reduction Algorithm for Marine Heat Flow Measurements. Journal of Geophysical Research 92 (B12), 12846–12856.

Villinger, H., Trehu, A.M., Grevemeyer, I. (2010). Seafloor marine heat flux measurements and estimation of heat flux from seismic observations of bottom simulating reflectors, In: Geophysical Characterization of Gas Hydrates special volume, ISBN (13) 9181560802181, Society of Exploration Geophysicists, 279-298, 2010.

Zhuang, G.-C., Lin, Y.-S., Elvert, M., Heuer, V.B., Hinrichs, K.-U. (2014). Gas chromatographic analysis of methanol and ethanol in marine sediment pore waters: Validation and implementation of three pretreatment techniques. Mar. Chem. 160, 82–90. https://doi.org/10.1016/j.marchem.2014.01.011

Zitellini, N., Gràcia, E., Matias, L., Terrinha, P., Abreu, M. A., DeAlteriis, G., Henriet, J. P., Dañobeitia, J. J., Masson, D. G., Mulder, T., Ramella, R., Somoza, L., and Diez, S. (2009). The quest for the Africa-Eurasia plate boundary west of the Strait of Gibraltar. Earth and Planetary Science Letters 280 (1-4), 13-50.

11   Abbreviations

Not applicable

12   Appendices

12.1   Appendix 1 - Parasound profiles
12.2   Appendix 2 - VCTD-graphs and -photos
12.3   Appendix 3 - Visual descriptions, photos, and magnetic susceptibility of GCs
12.4   Appendix 4 - Meiofauna samples
12.5   Appendix 5 - Pore water oxygen measurements
12.6   Appendix 6 - Pore water and sediment samples for geochemical analyses
12.7   Appendix 7 - Heat flow measurements

12.1   Appendix 1 – Parasound profiles
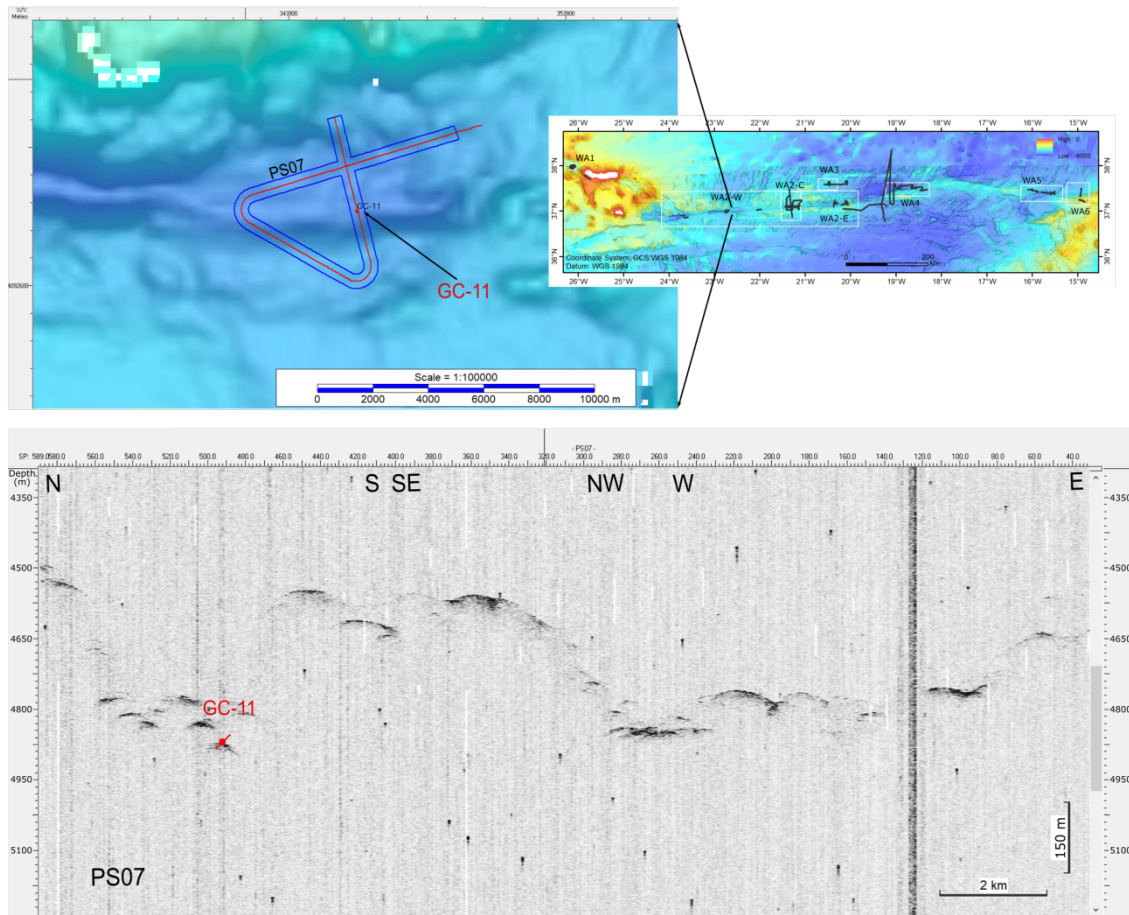
Fig. 12.1.1   Section of Parasound profile PS07 (GC-11), sub working area WA2-W.
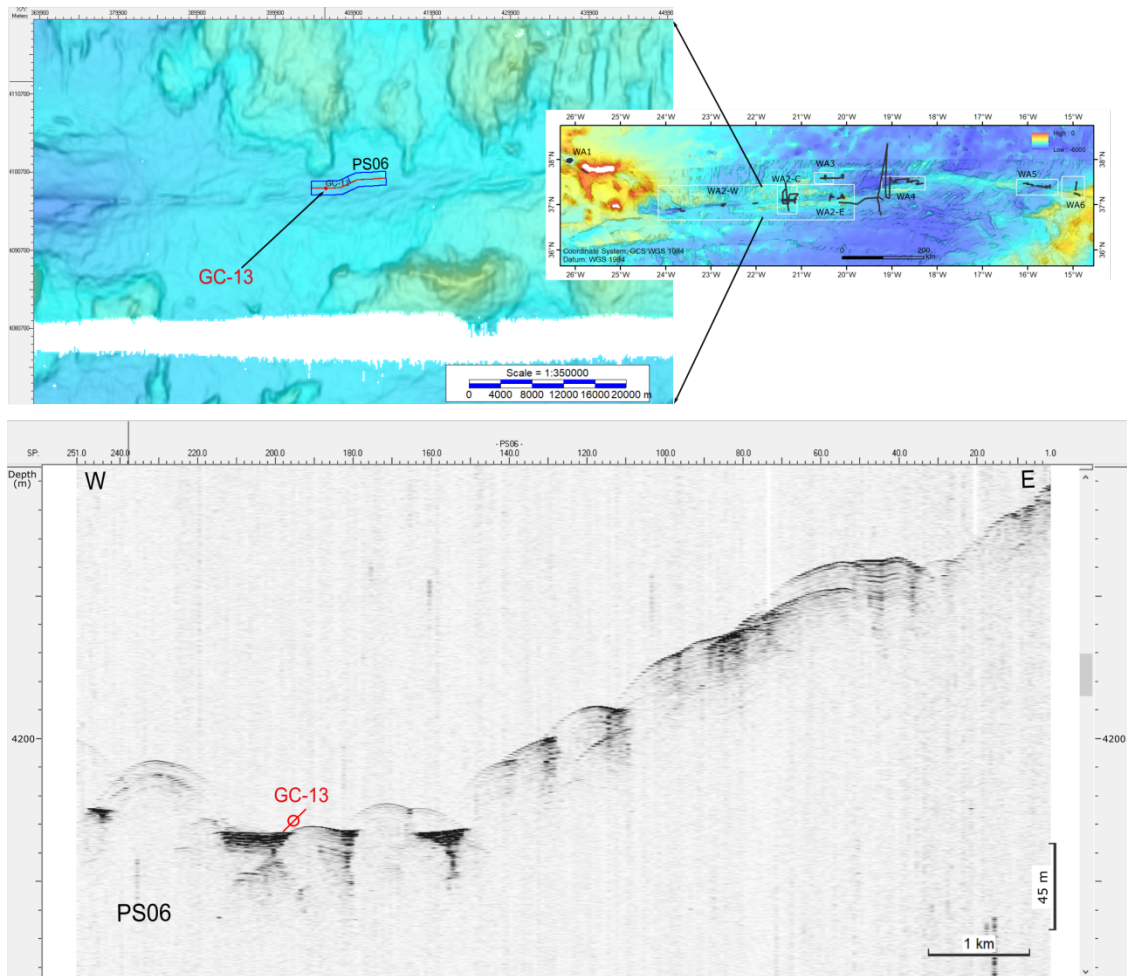
Fig. 12.1.2   Section of Parasound profile PS06 (GC-13), sub working area WA2-W.
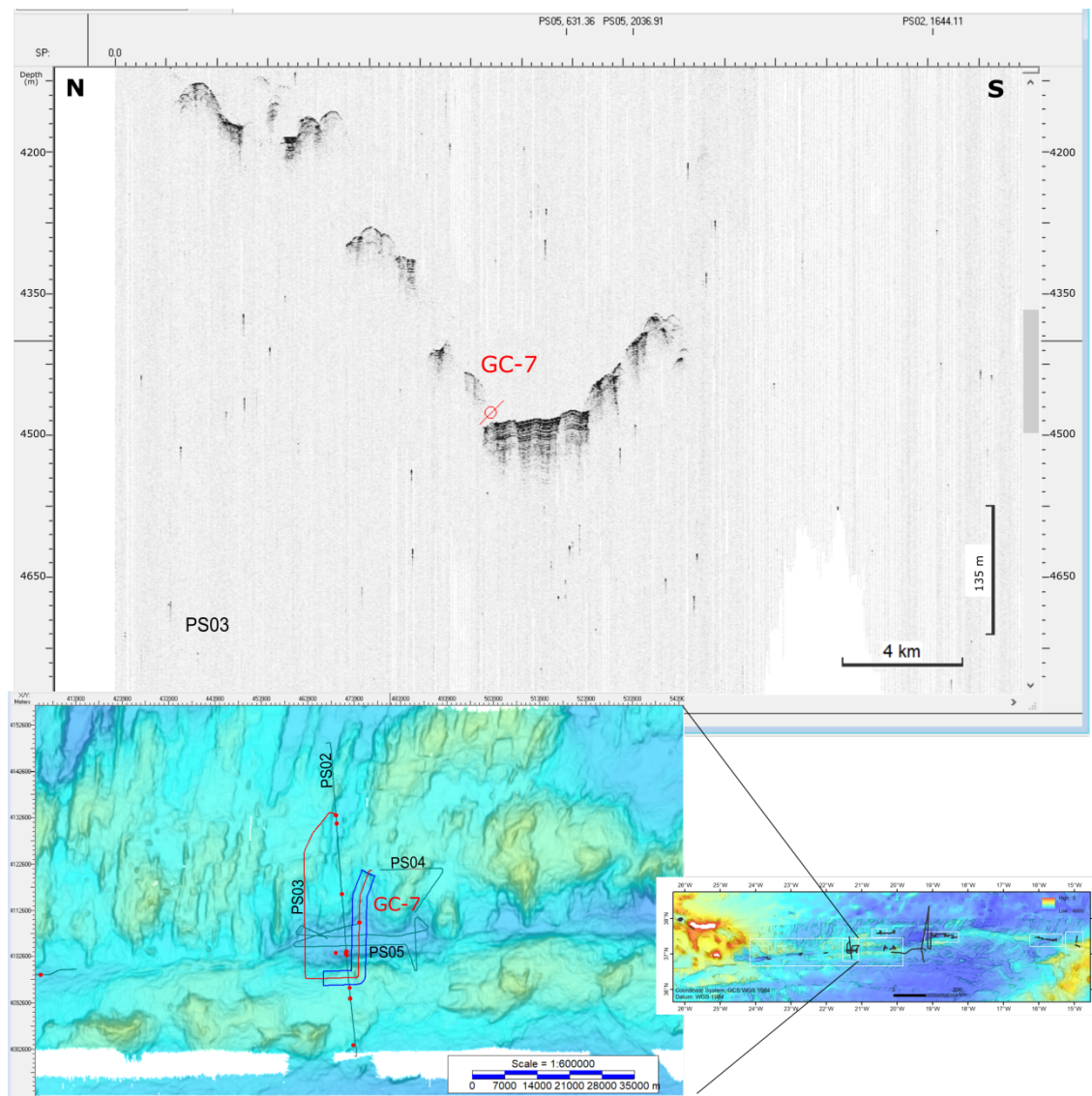
Fig. 12.1.3   Parasound profile PS03 and location of gravity core GC-7 within and across the GF M87 Basin.
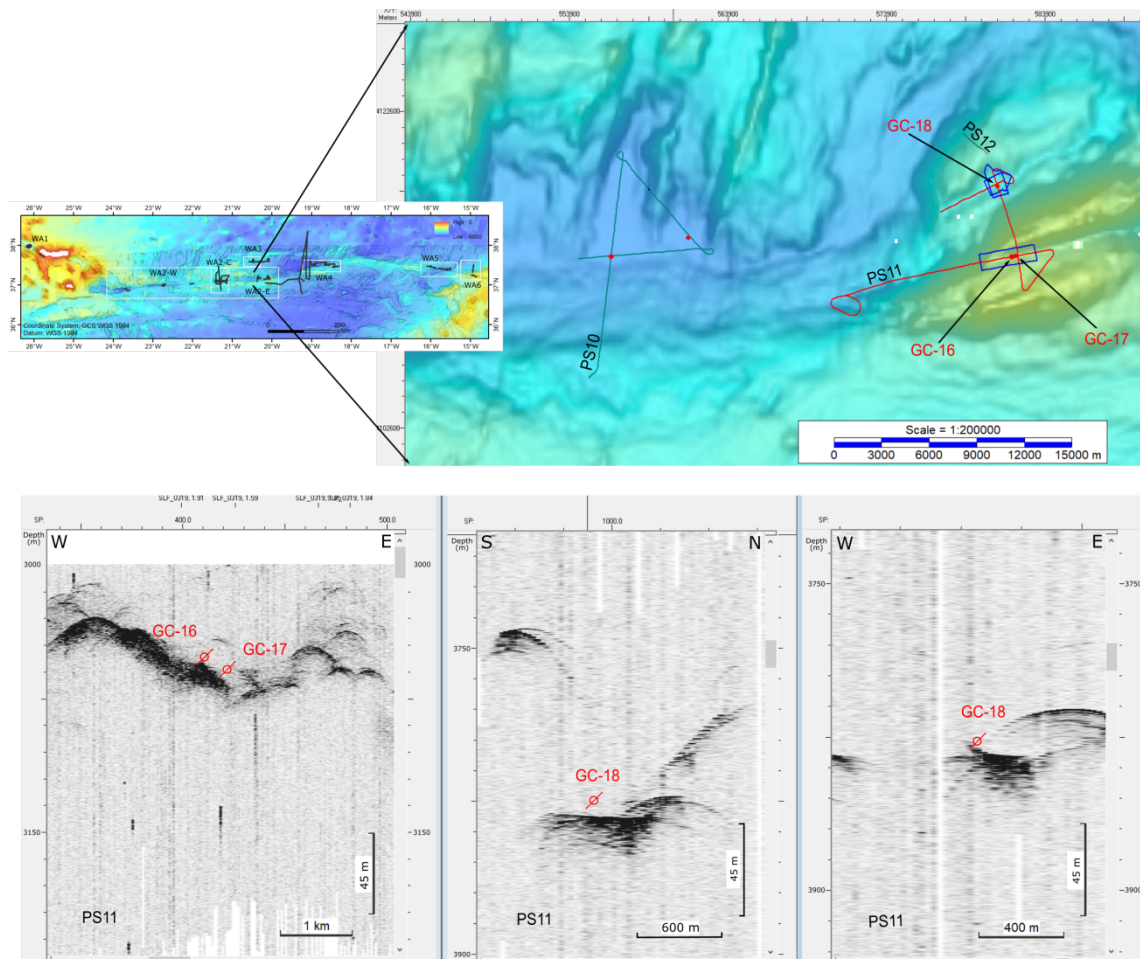
Fig. 12.1.4   Parasound profile PS11 with superimposed location of gravity cores GCs 16-18. No sedimentary cover is observed in the profiles. GC-16 and GC-17 did not recover sediments.
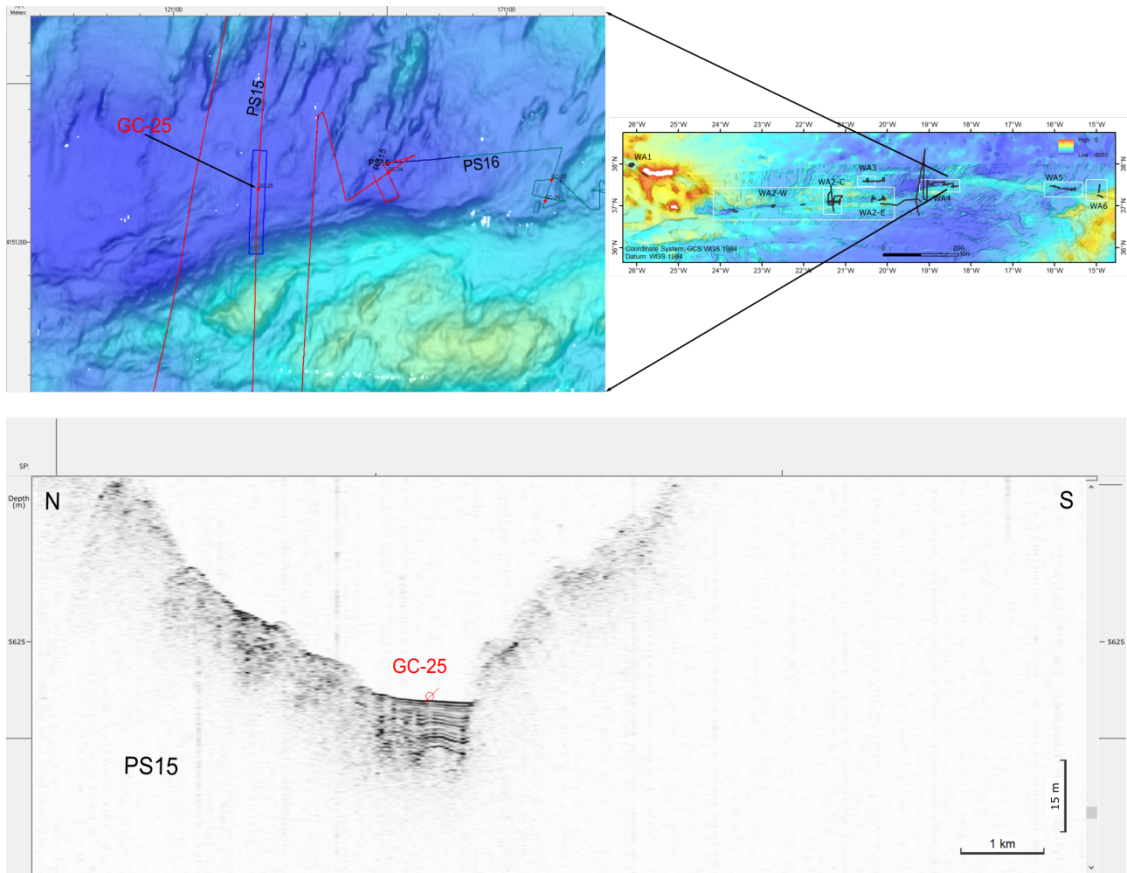
Fig. 12.1.5   Section of Parasound profile PS15 and location of gravity core GC25 in WA-4.
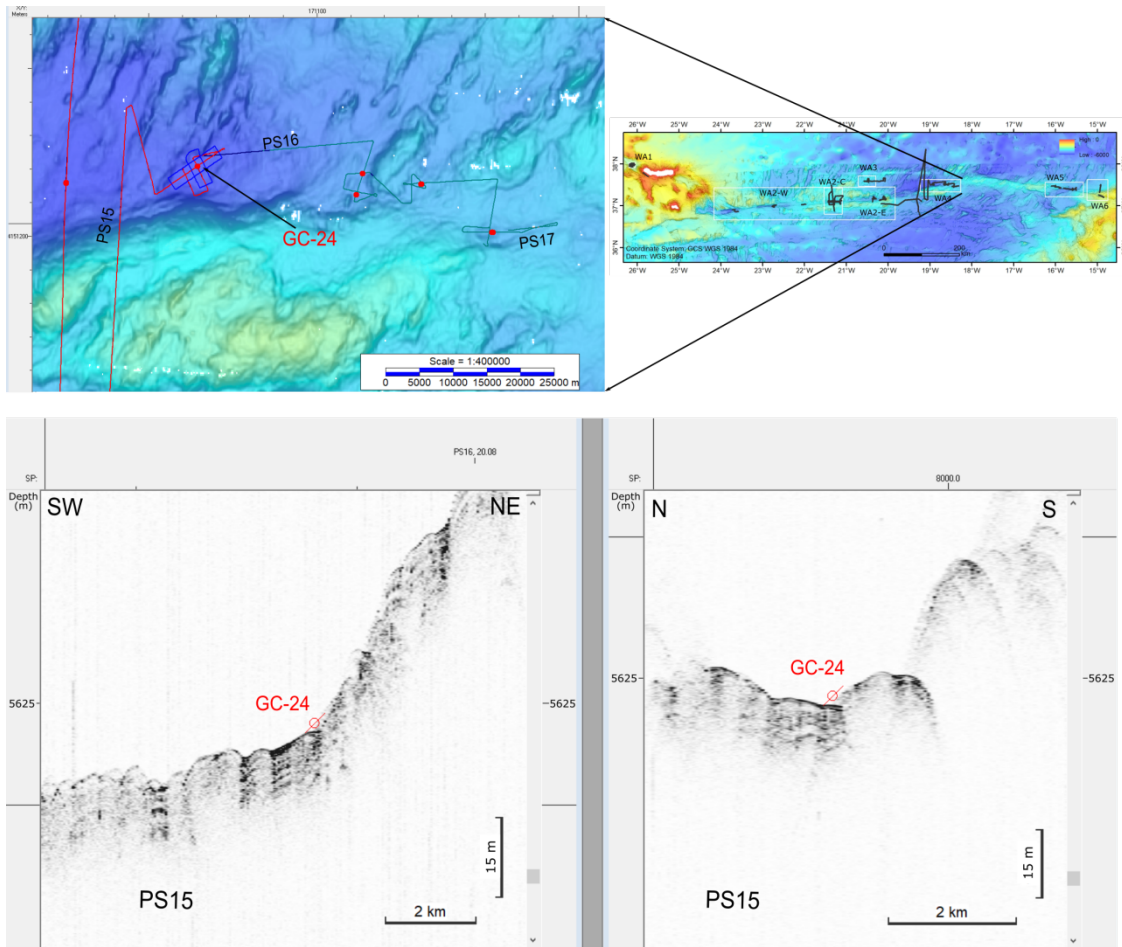
Fig. 12.1.6   Sections of Parasound profile PS15 and location of gravity core GC24 in WA-4.
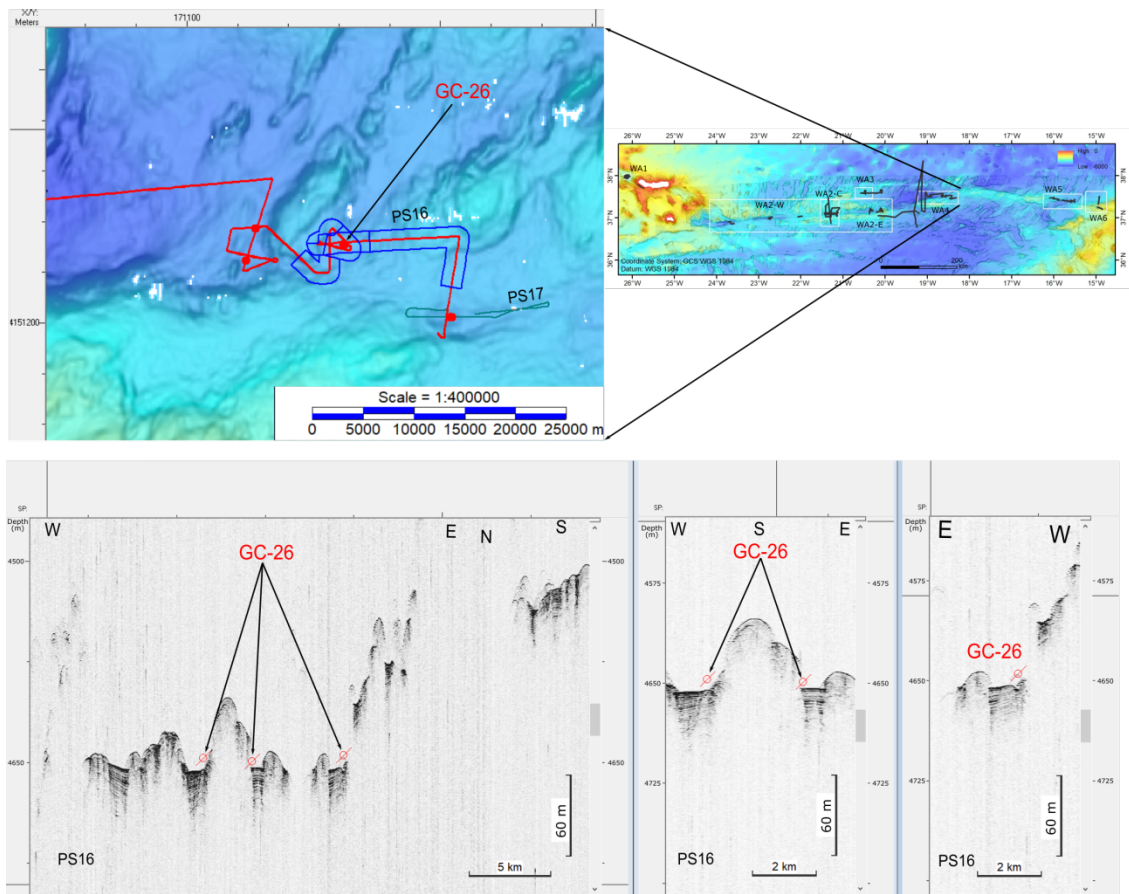
Fig. 12.1.7   Sections of Parasound profile PS16 and location of gravity core GC26 in WA-4.
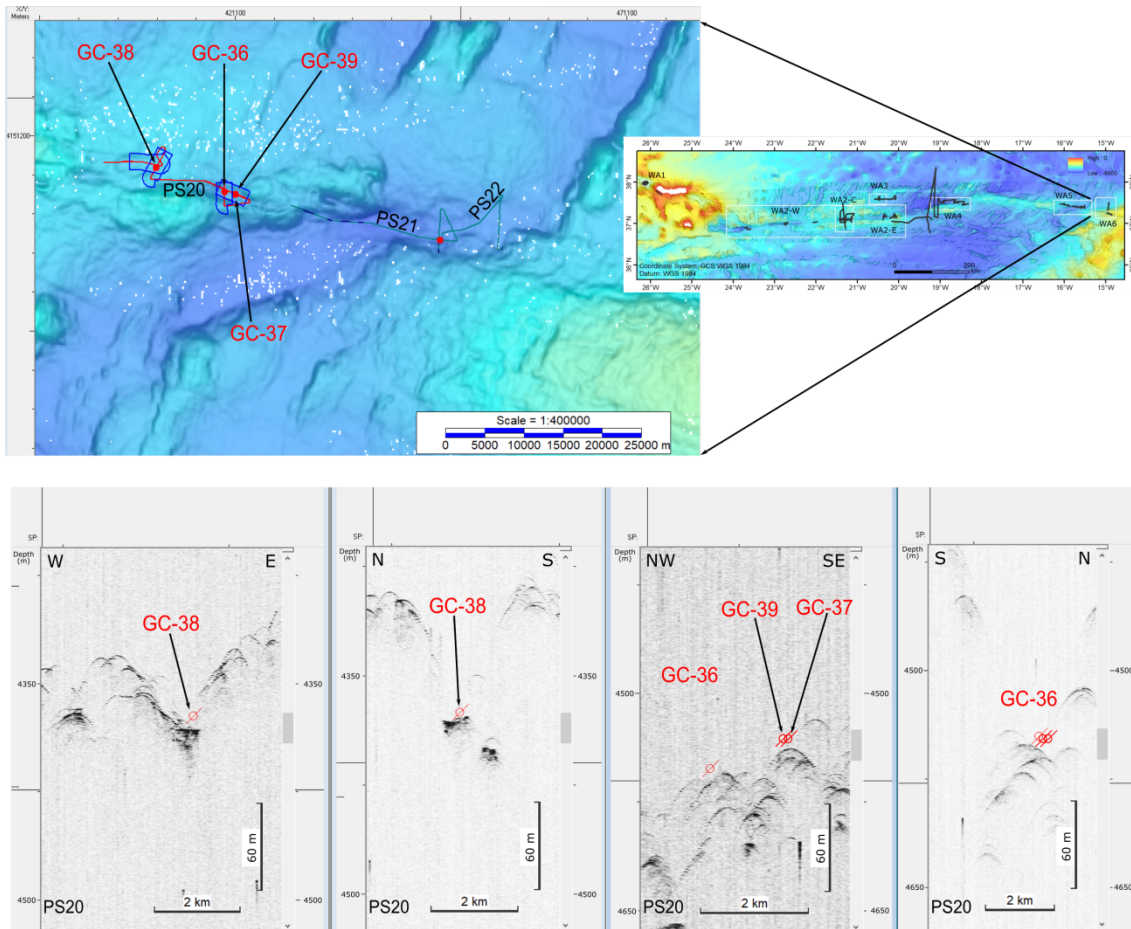
Fig. 12.1.8   Examples of Parasound profile PS 20 in WA-5.

12.2   Appendix 2 – VCTD-graphs and -photos

Working area 02 - Station 11
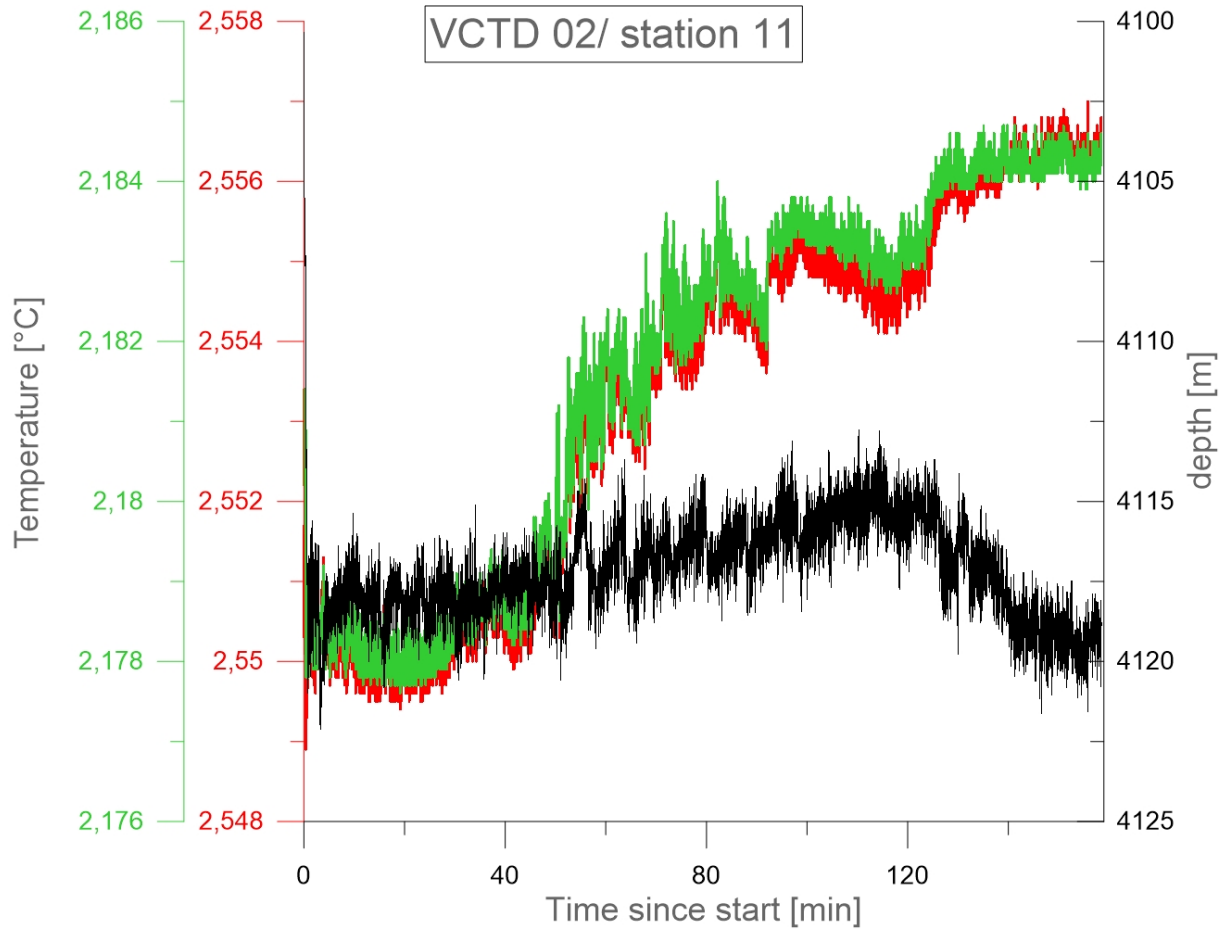
Fig. 12.2.1   VCTD02 data station 11 at bottom sight recorded between 10.03.2020 20:13:00 and 10.03.2020 22:51:00 along the predefined transect (Ship movement 0.5 kn).
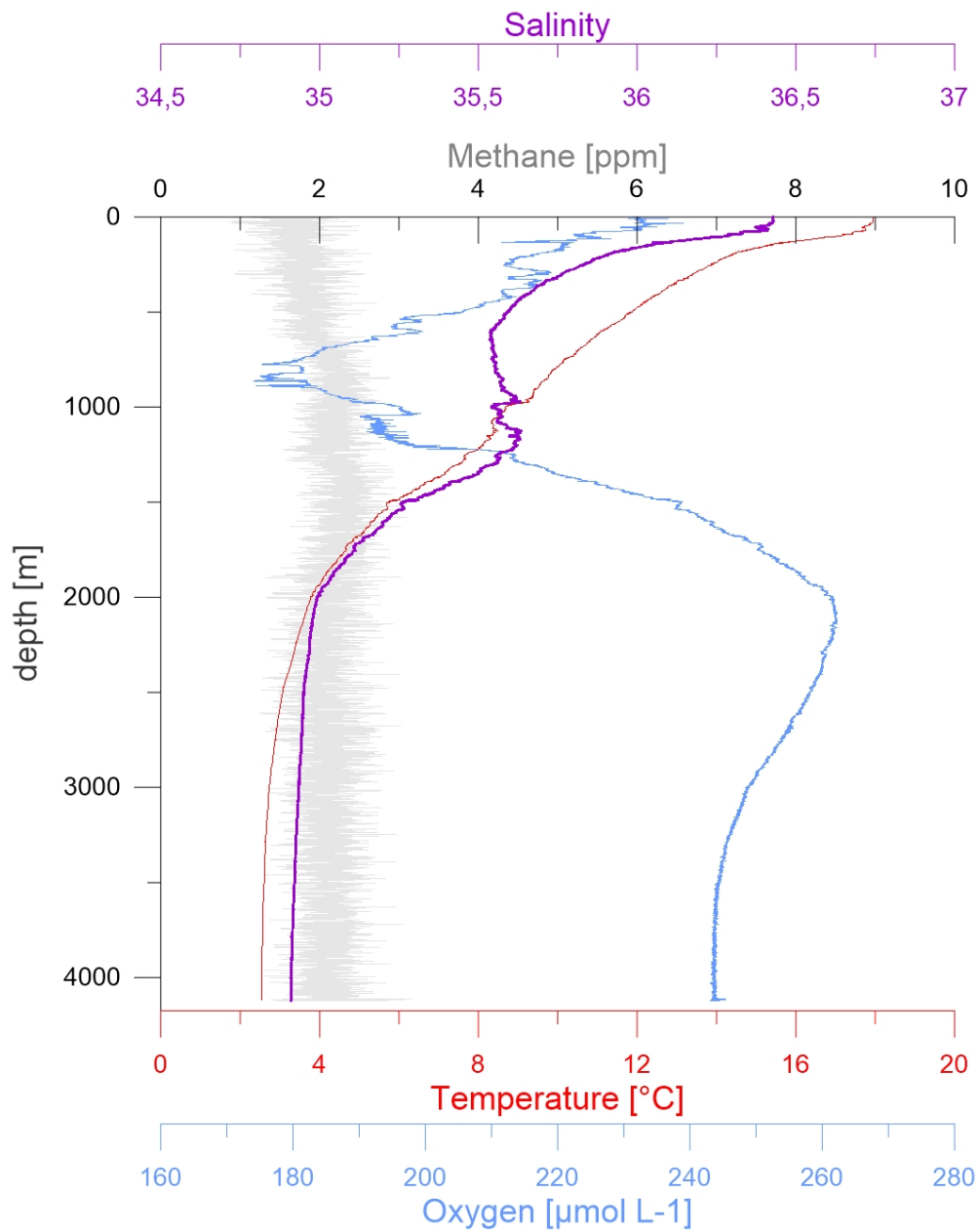
Fig. 12.2.2   VCTD02 data as vertical profile (upcast) profile for Station 11.

Working area 02 - Station 24
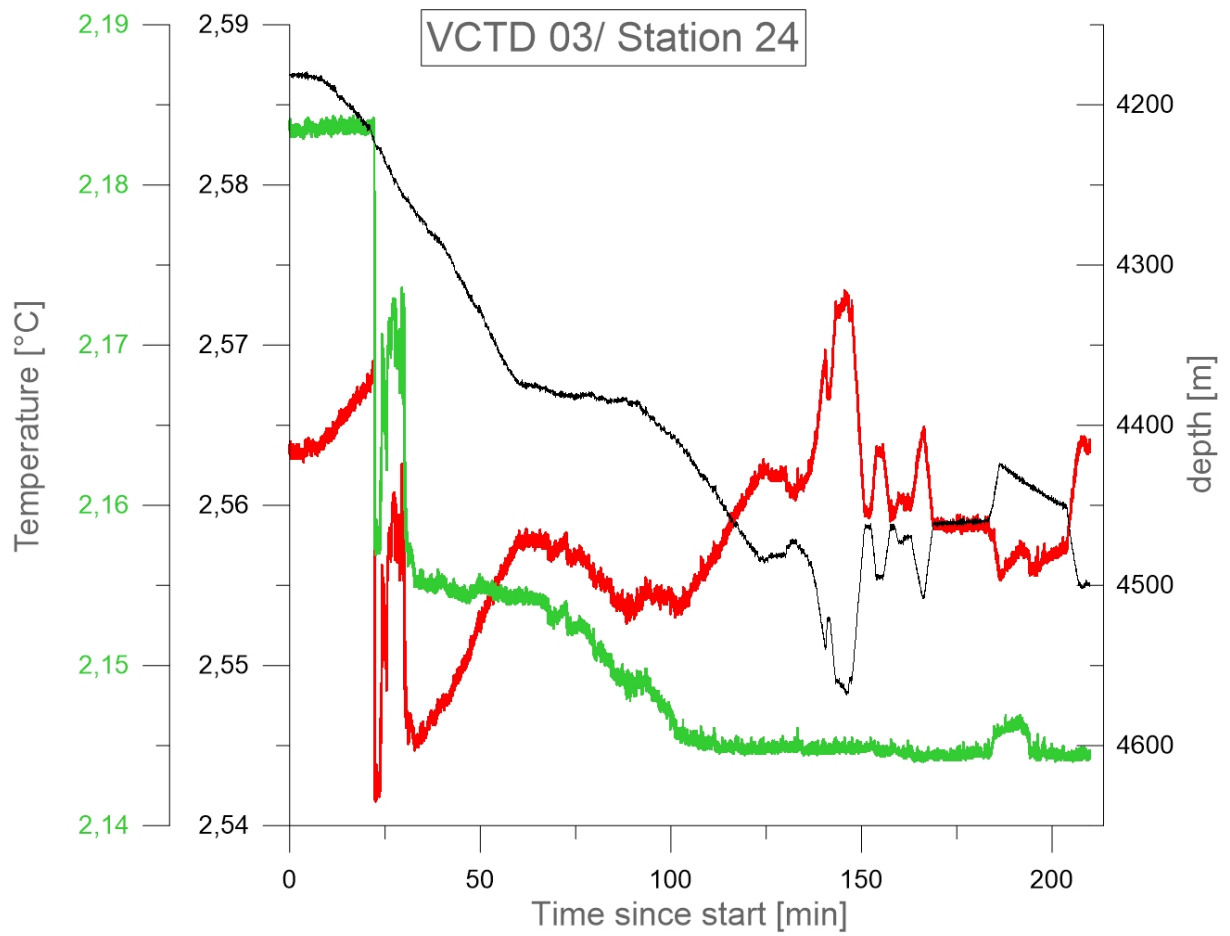
Fig. 12.2.3   VCTD03 data station 24 at bottom sight recorded between 14.03.2020 19:25:00 and 14.03.2020 22:55:00 along the predefined transect (Ship movement 0.5 kn). Potential temperature is marked by the green line.
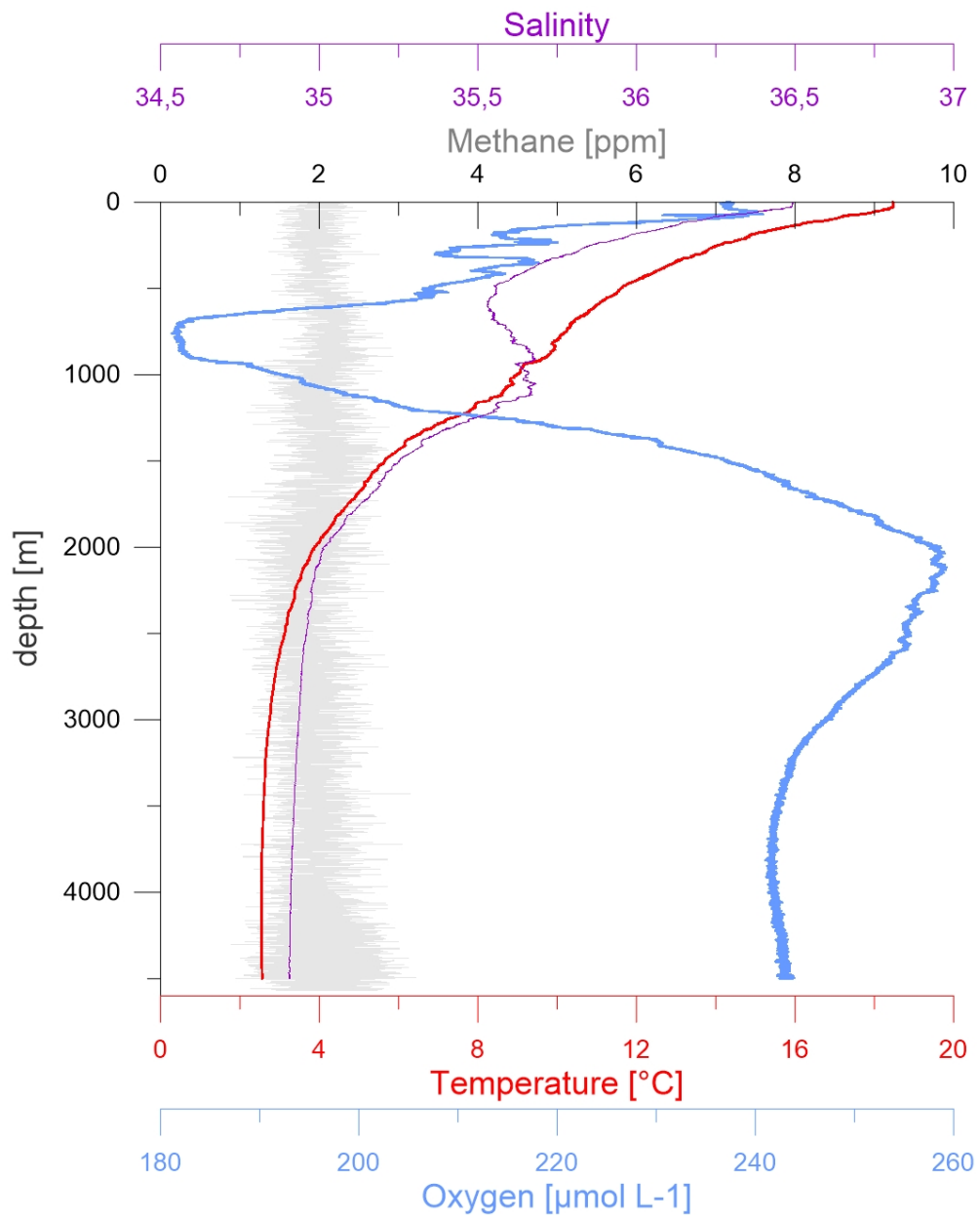
Fig. 12.2.4   VCTD03 data as vertical (upcast) profile for Station 24.
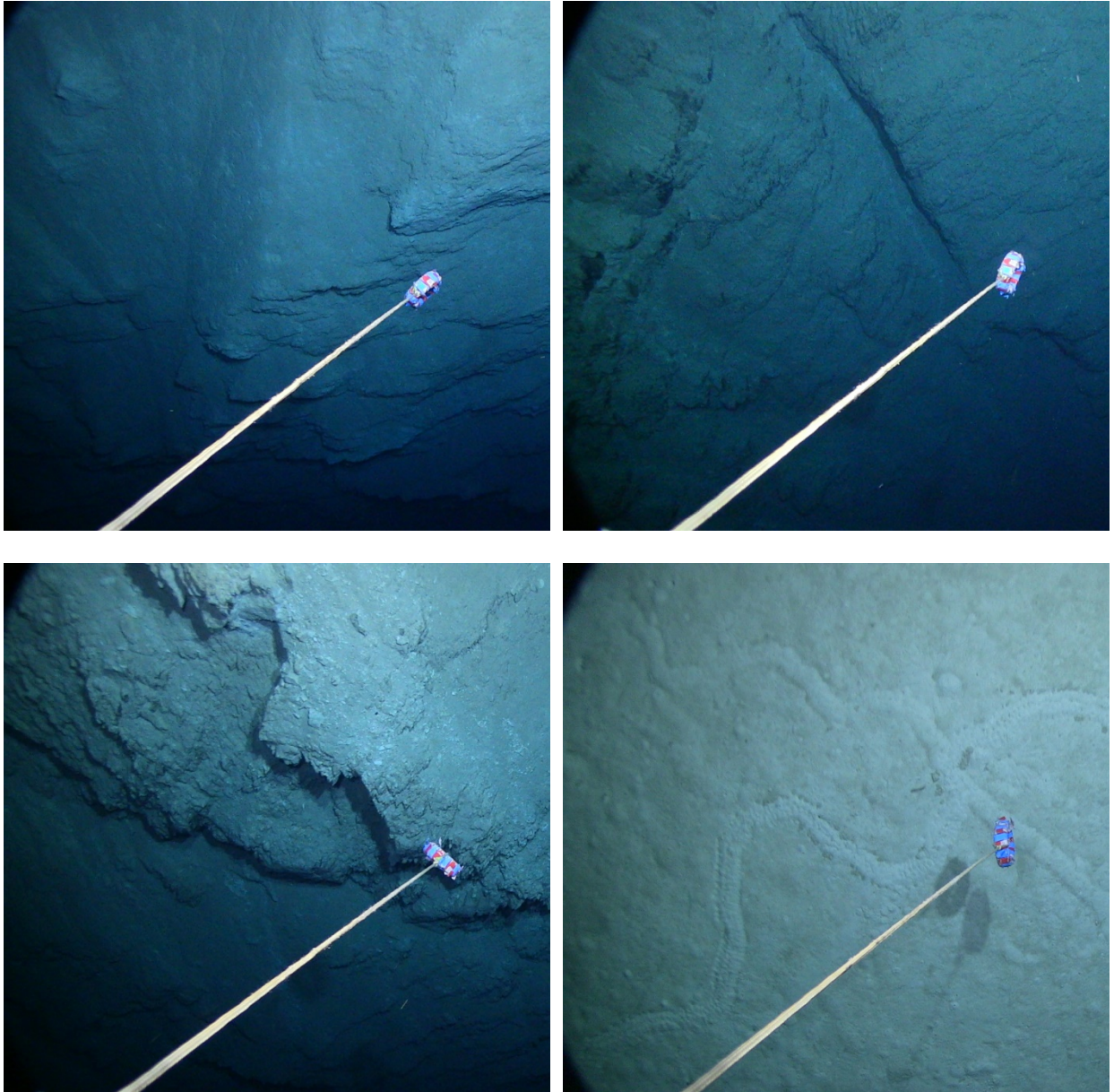
Fig. 12.2.5   Sharp edges and erosional structures of a basaltic wall where the terrain drops sharply. Tubular sedimentary features at the base of the trench indicating bioturbation (bottom right). A scale reference can be made using the weight length (12 cm) and the rope length (1.5 meter).

Working area 02 - Station 26
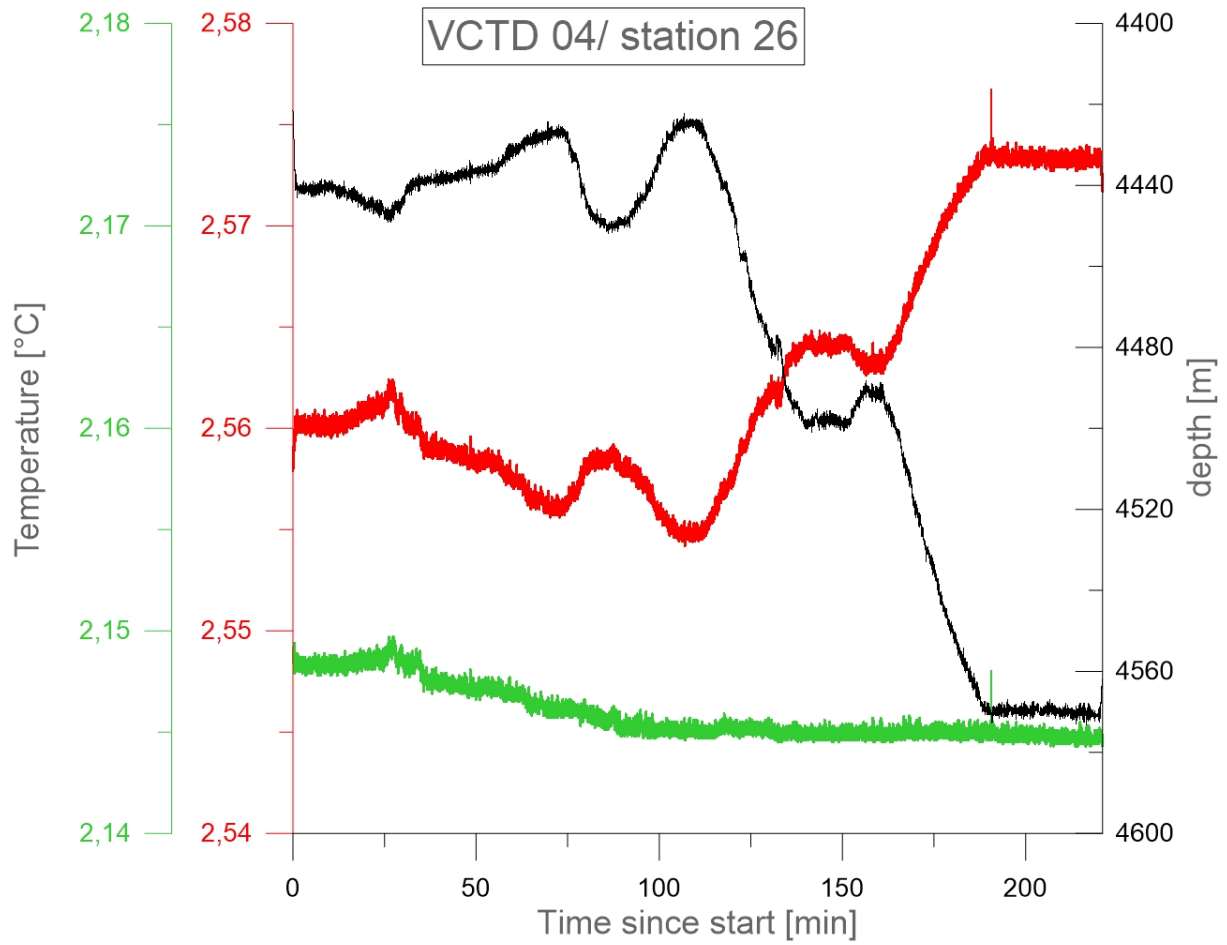
Fig. 12.2.6   VCTD04 data of station 26 at bottom view, recorded between 15.03.2020 17:16:00 and 15.03.2020 20:57:00 along the predefined transect (Ship movement of ~0.5 kn).
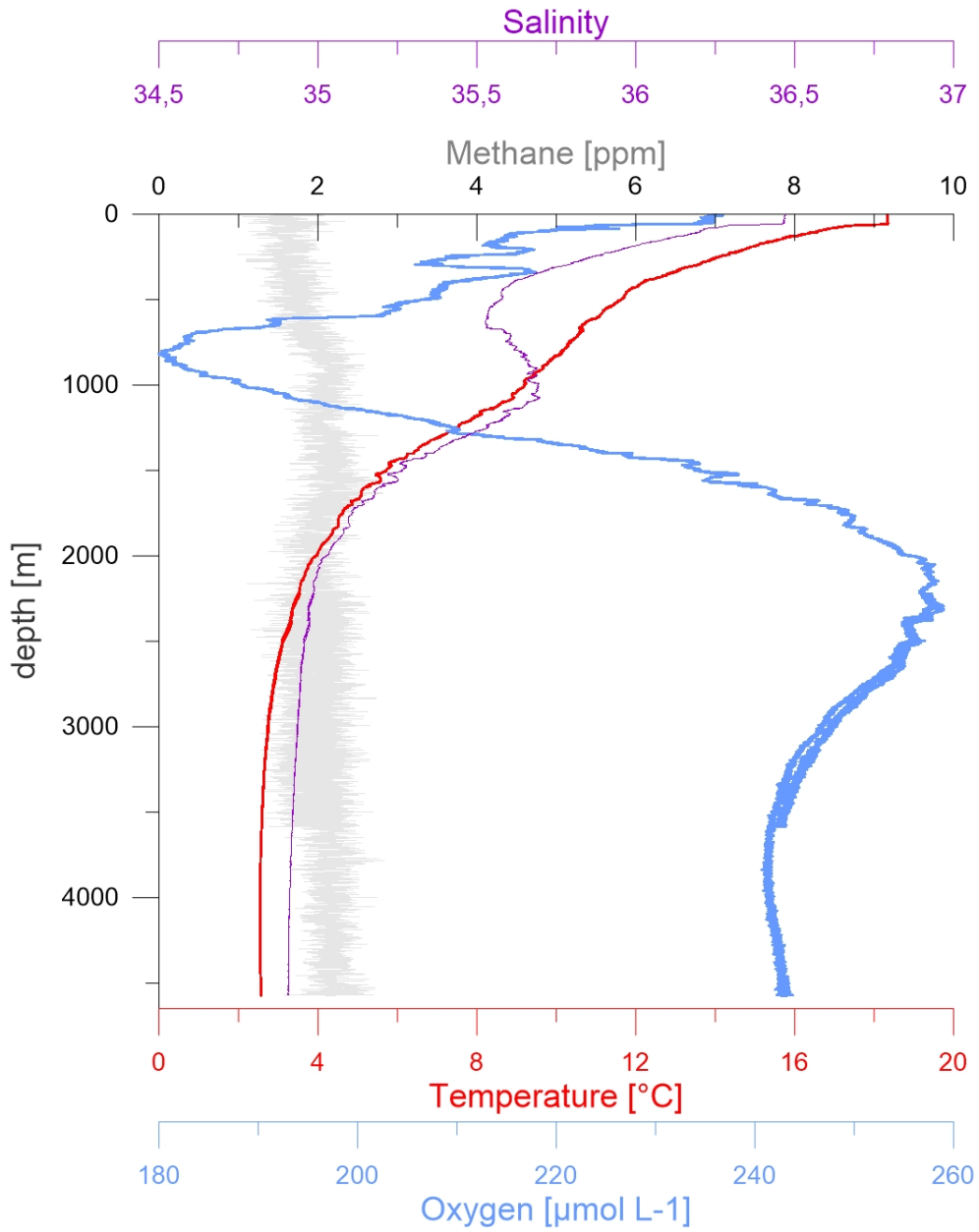
Fig. 12.2.7   VCTD04 data for the vertical (upcast) profile for Station 26.

Working area 04 - Station 59
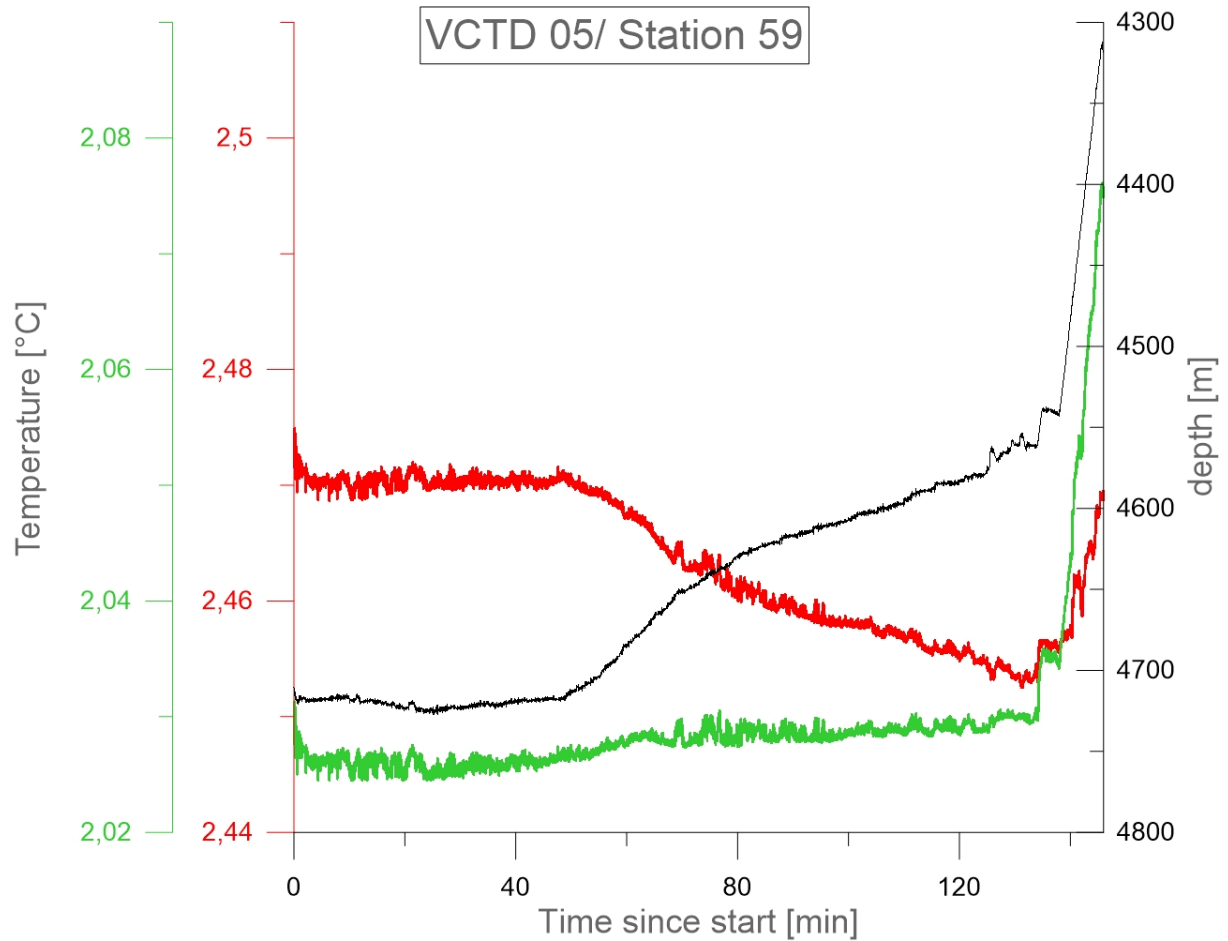
Fig. 12.2.8   VCTD05 data station 59 at bottom sight recorded between 24.03.2020 20:04:00 and 24.03.2020 22:30:00 along the predefined transect (Ship movement 0.5 kn).
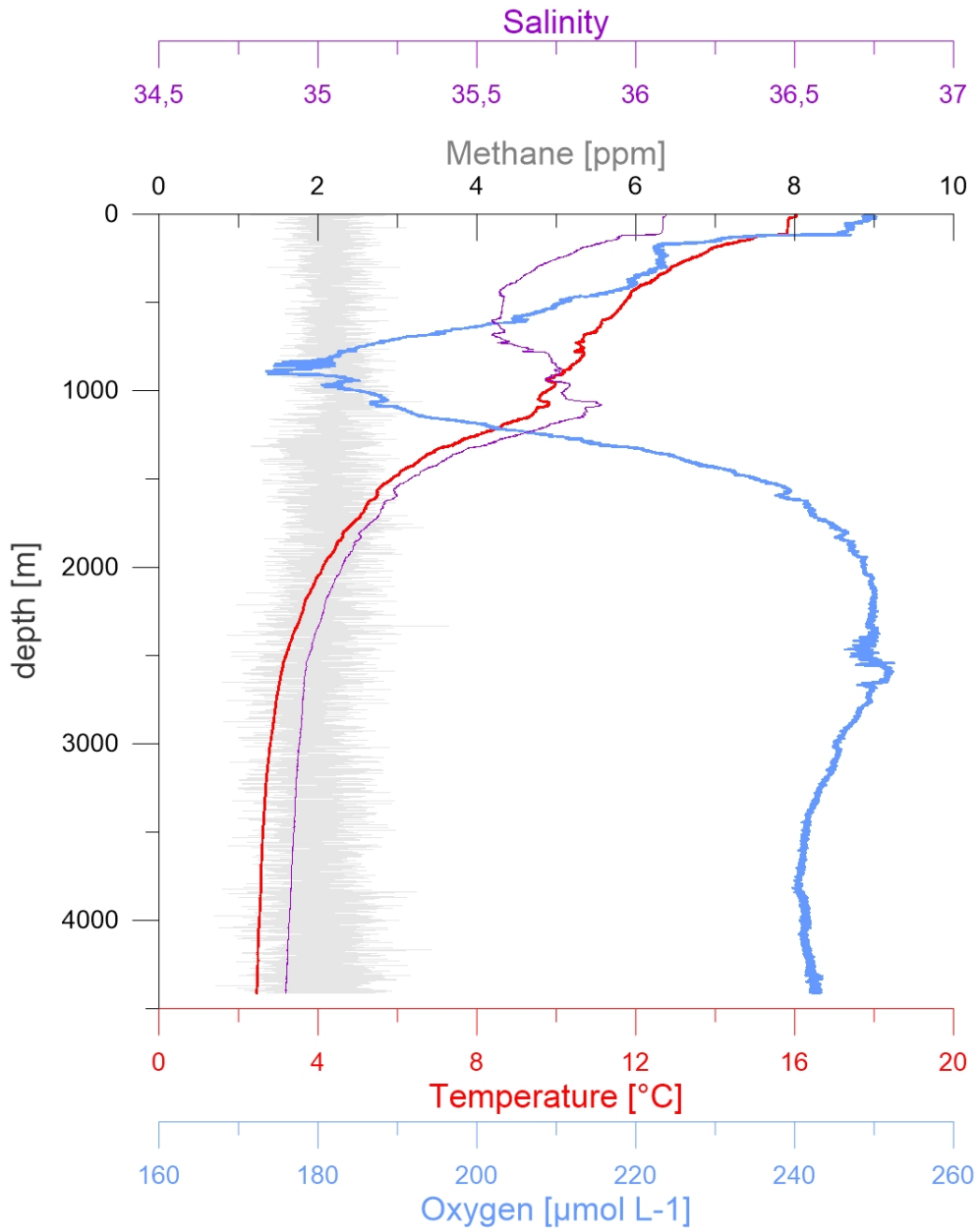
Fig. 12.2.9   VCTD05 data vertical (upcast) profile for Station 59.
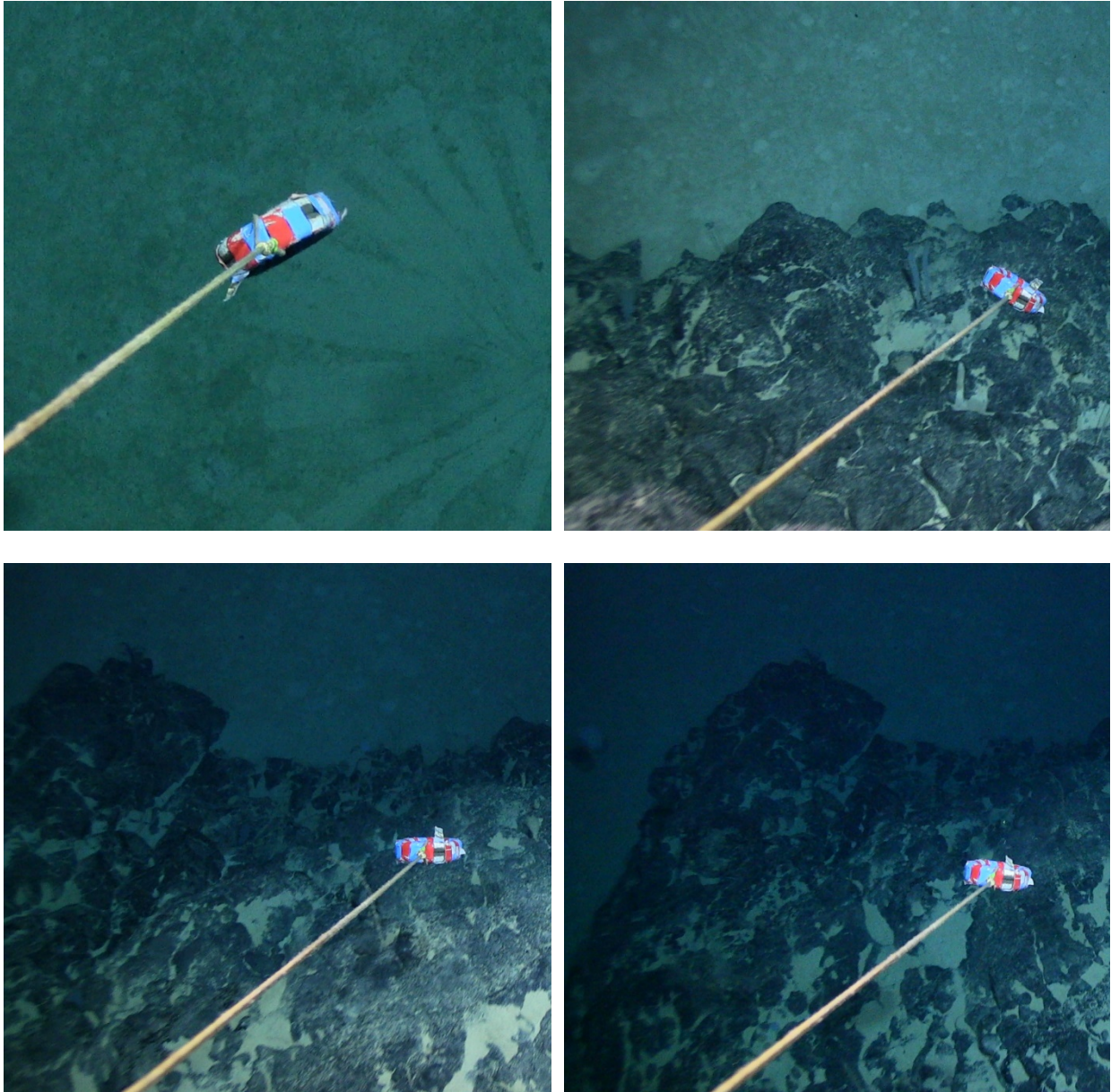
Fig. 12.2.10 Seafloor pictures taken along the transect of station 59. Fan structure indicating bioactivity (upper left). Large towering basalt block with hardly any sediment cover.

Working area 04 - Station 60
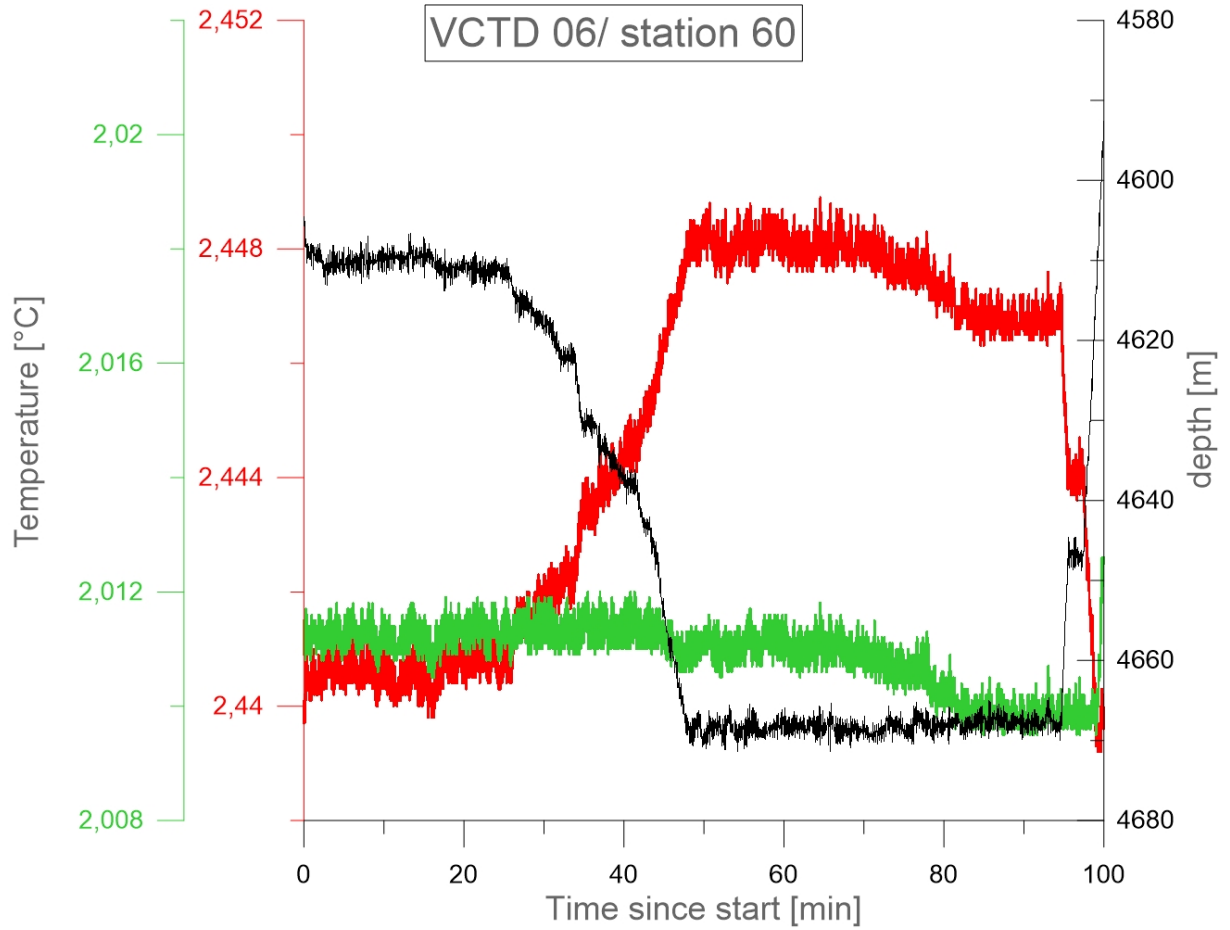
Fig. 12.2.11   VCTD06 data station 60 at bottom sight recorded between 25.03.2020 07:10:00 and 25.03.2020 08:50:00 along the predefined transect (Ship movement 0.5 kn).
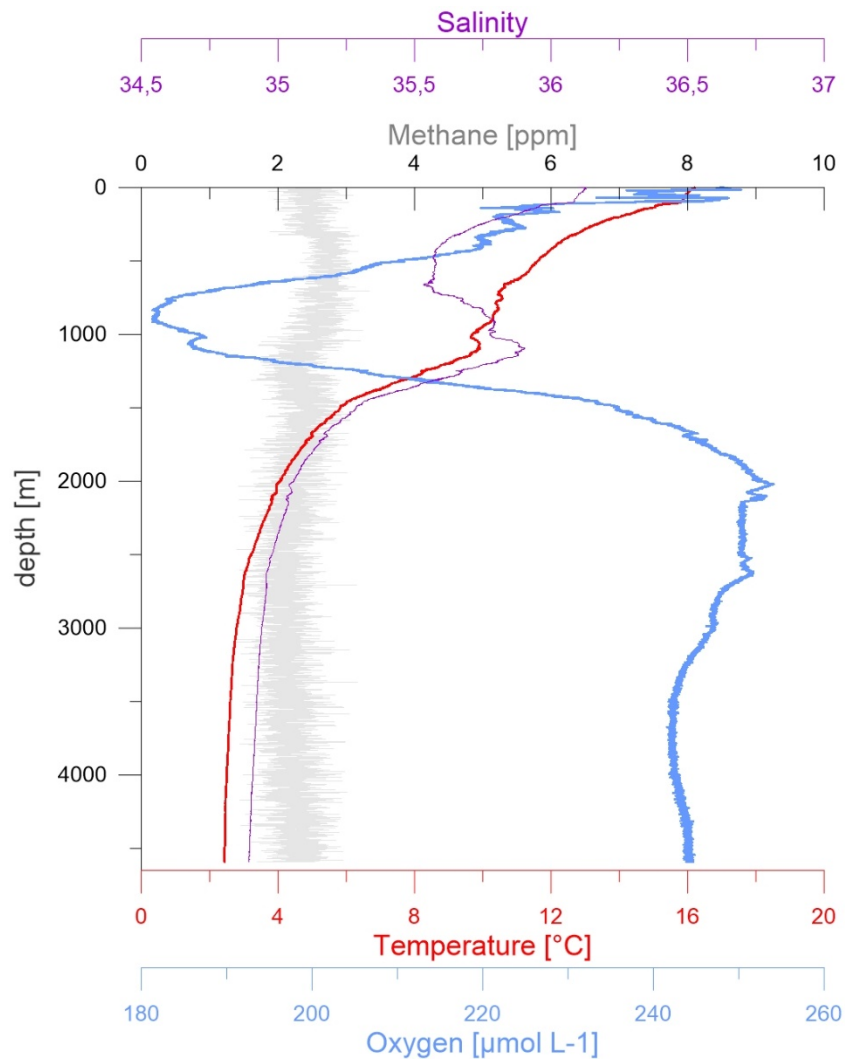
Fig. 12.2.12   VCTD06 data as vertical (upcast) profile for Station 60.
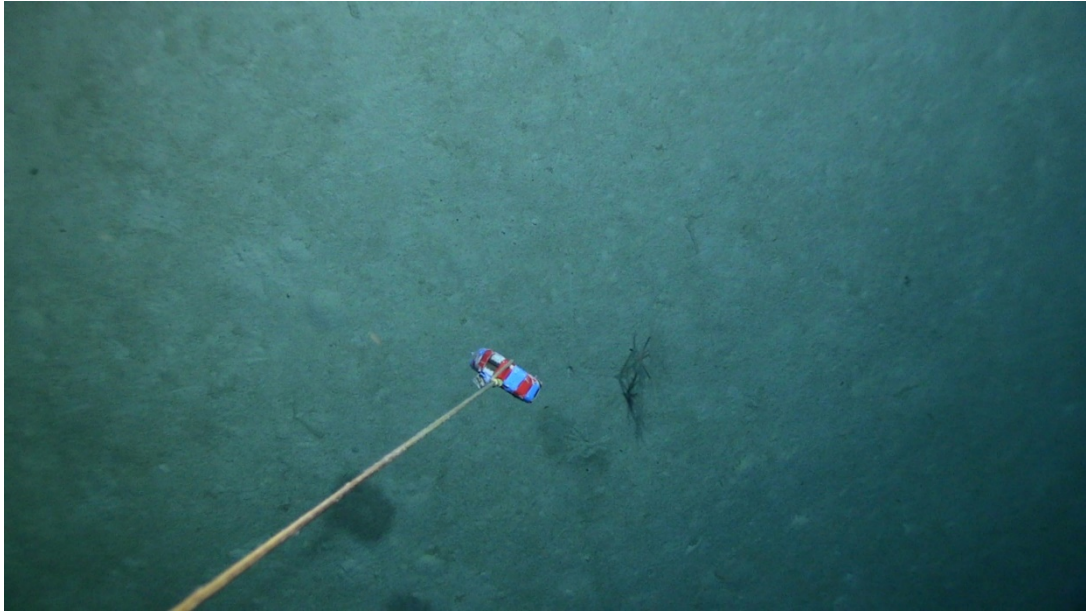
Fig. 12.2.13 Flat seabed with uniform sediment cover at station 60.

Working area 05 - Station 85
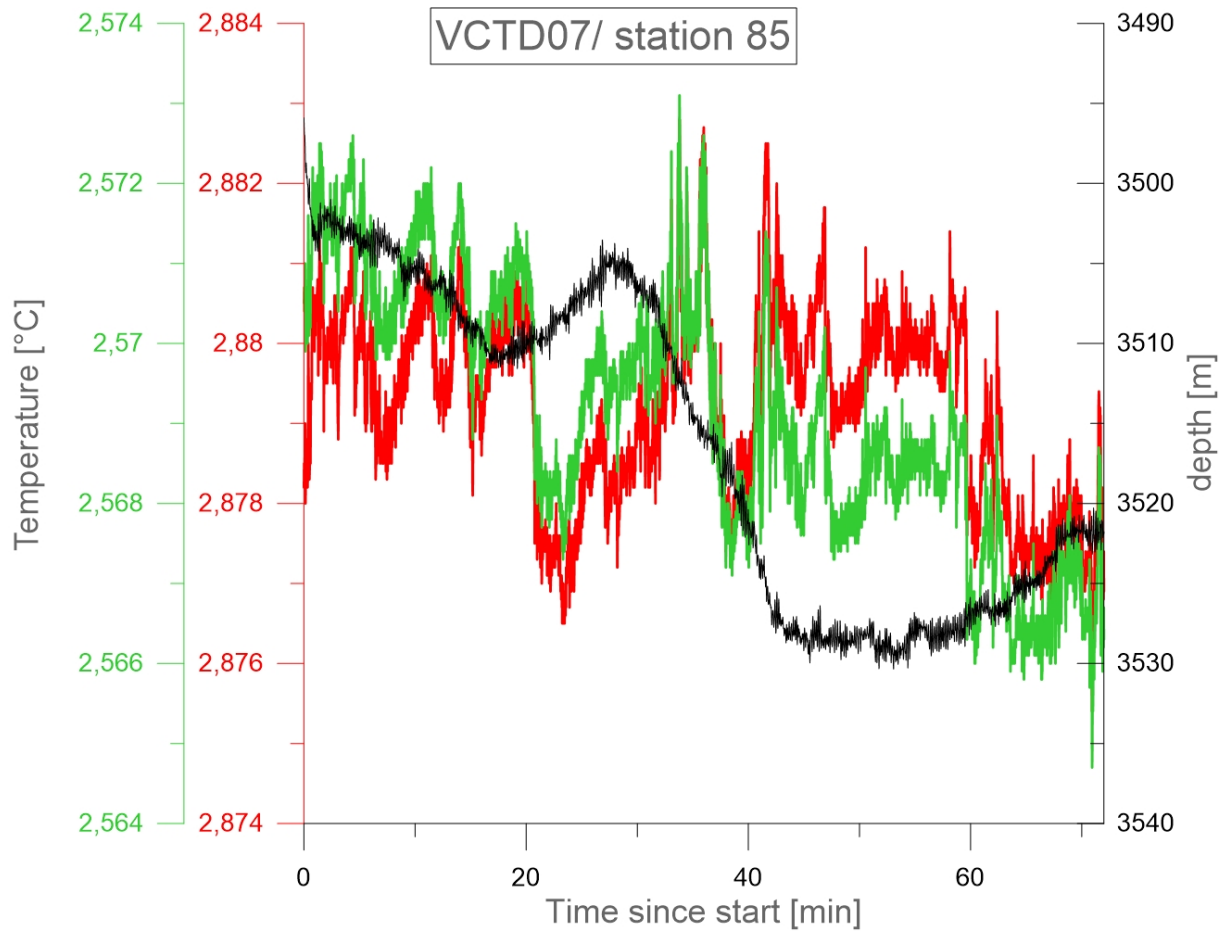
Fig. 12.2.14 VCTD07 data station 85 at bottom sight recorded between 02.04.2020 07:54:00 and 02.04.2020 09:06:00 along the predefined transect (Ship movement 0.5 kn).
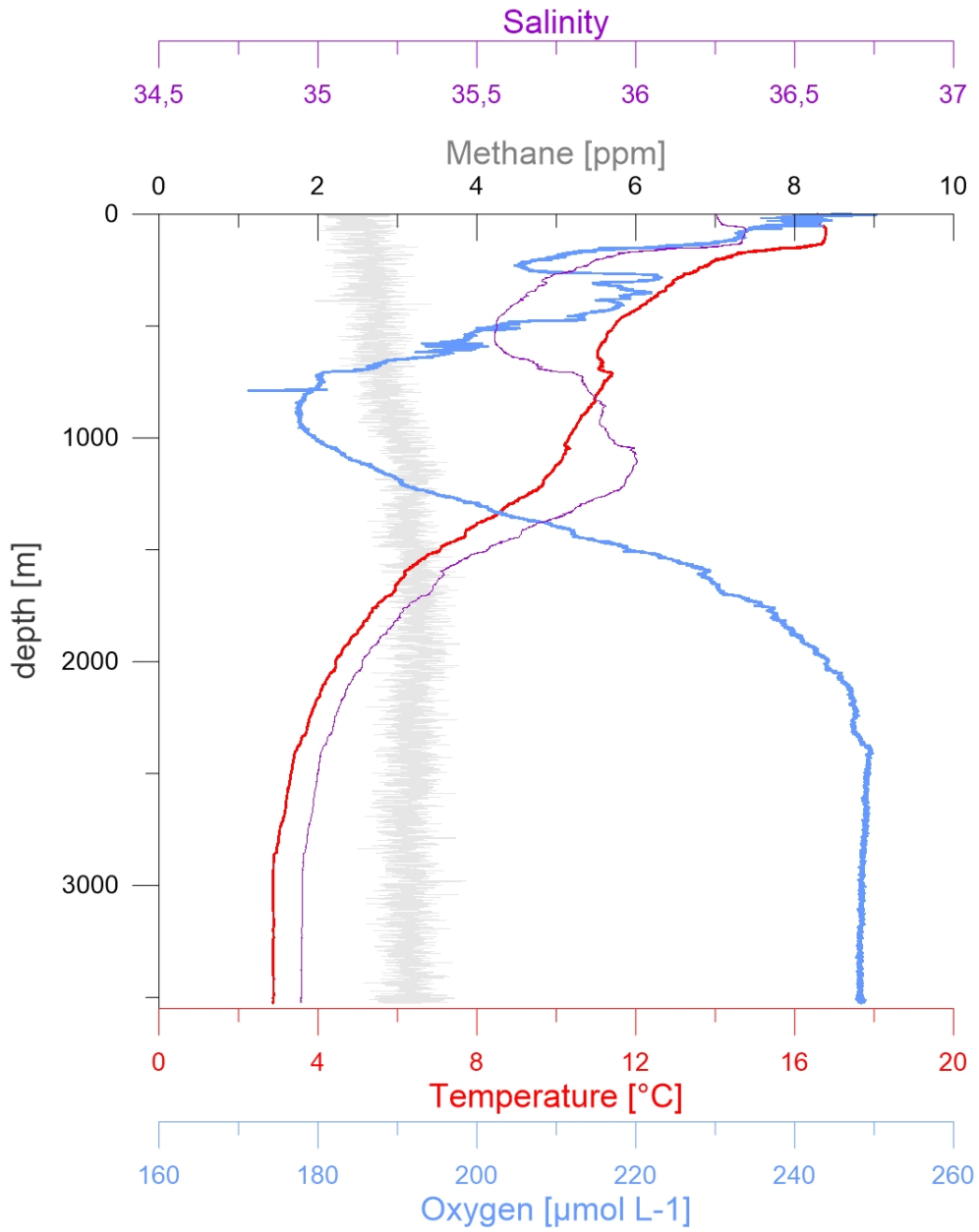
Fig. 12.2.15 VCTD07 data as vertical profile (upcast) for Station 85.
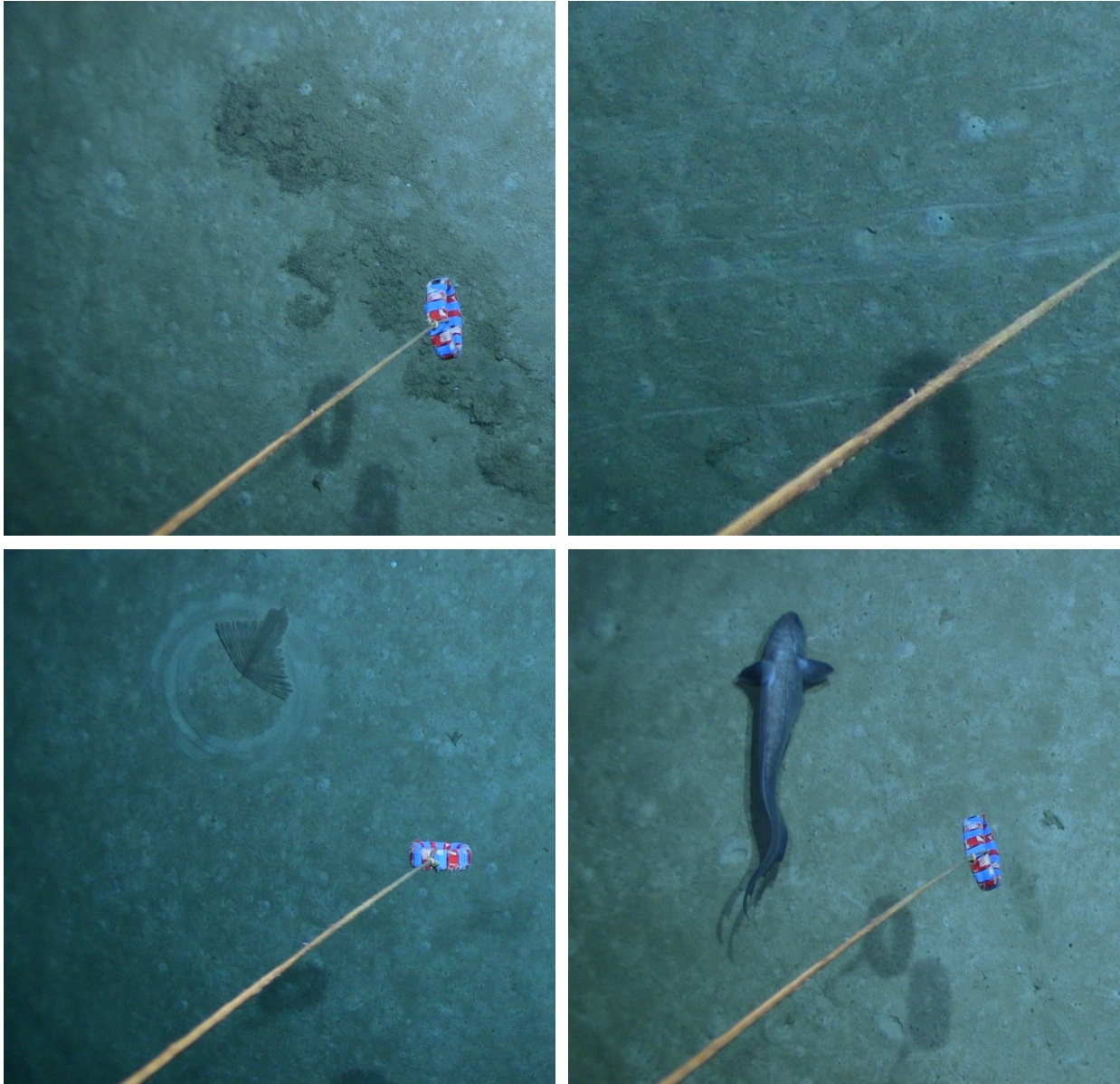
Fig. 12.2.16 Pictures of the seabed along station 85. Strongest benthic activity observed during towed M162-VCTD stations.

12.3   Appendix 3 – Visual descriptions, photos, and magnetic susceptibility of GCs
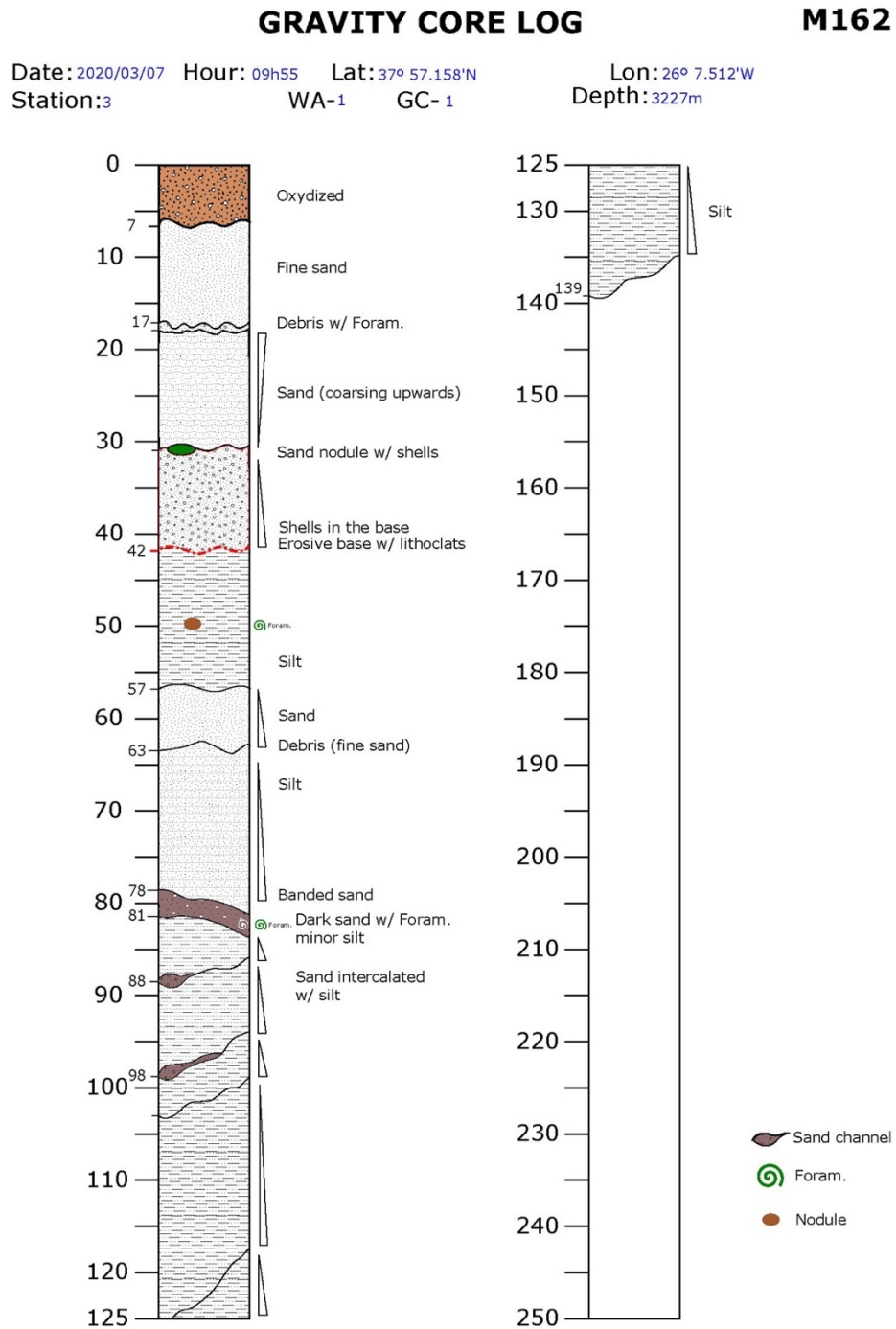
Fig. 12.3.1   Core description of GC-1.

3-GC1#1
(0-40cm)

3-GC1#2
(40-140cm)

Fig. 12.3.2   Core photo GC-1.
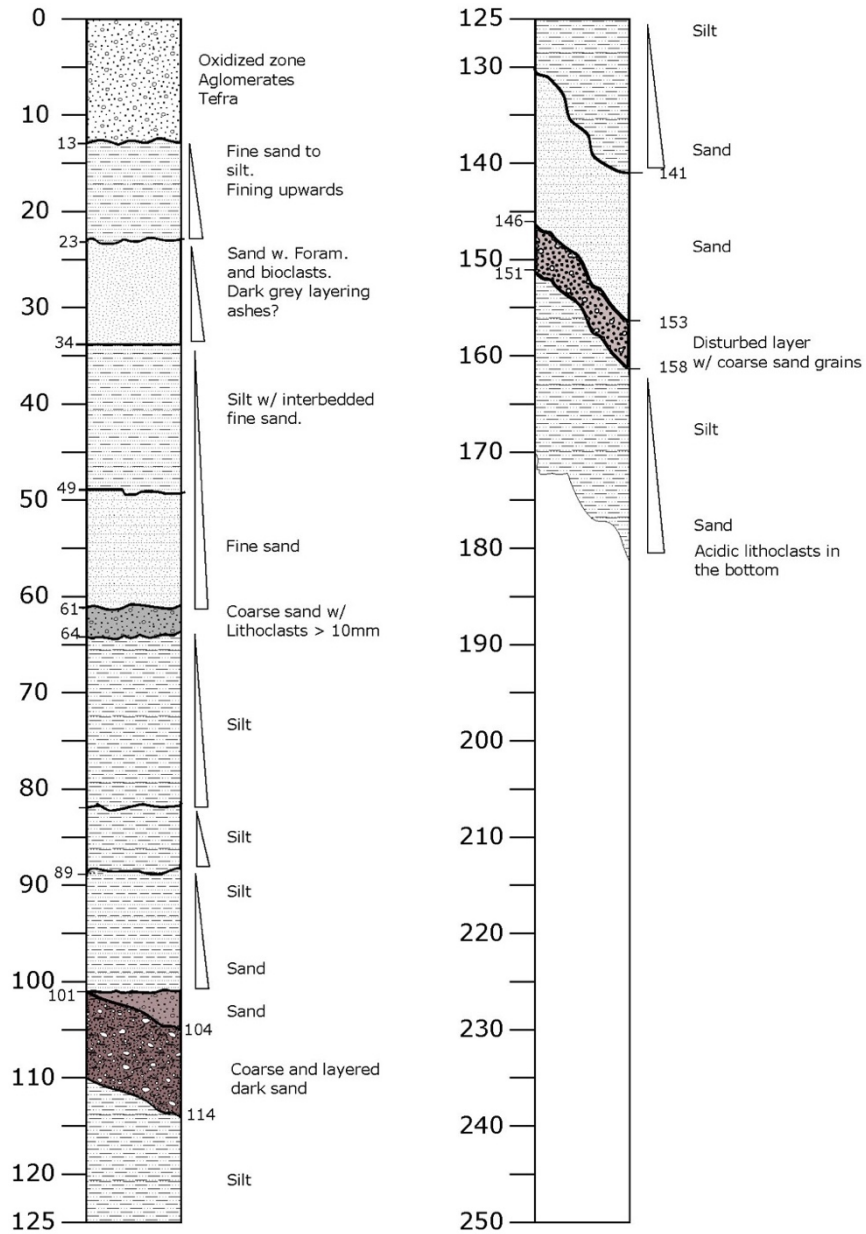
Fig. 12.3.3 Core description of GC-2.

4-GC2#1
(0 – 80cm)

4-GC2#2
(80-180cm)

Fig. 12.3.4   Core photo of GC-2.
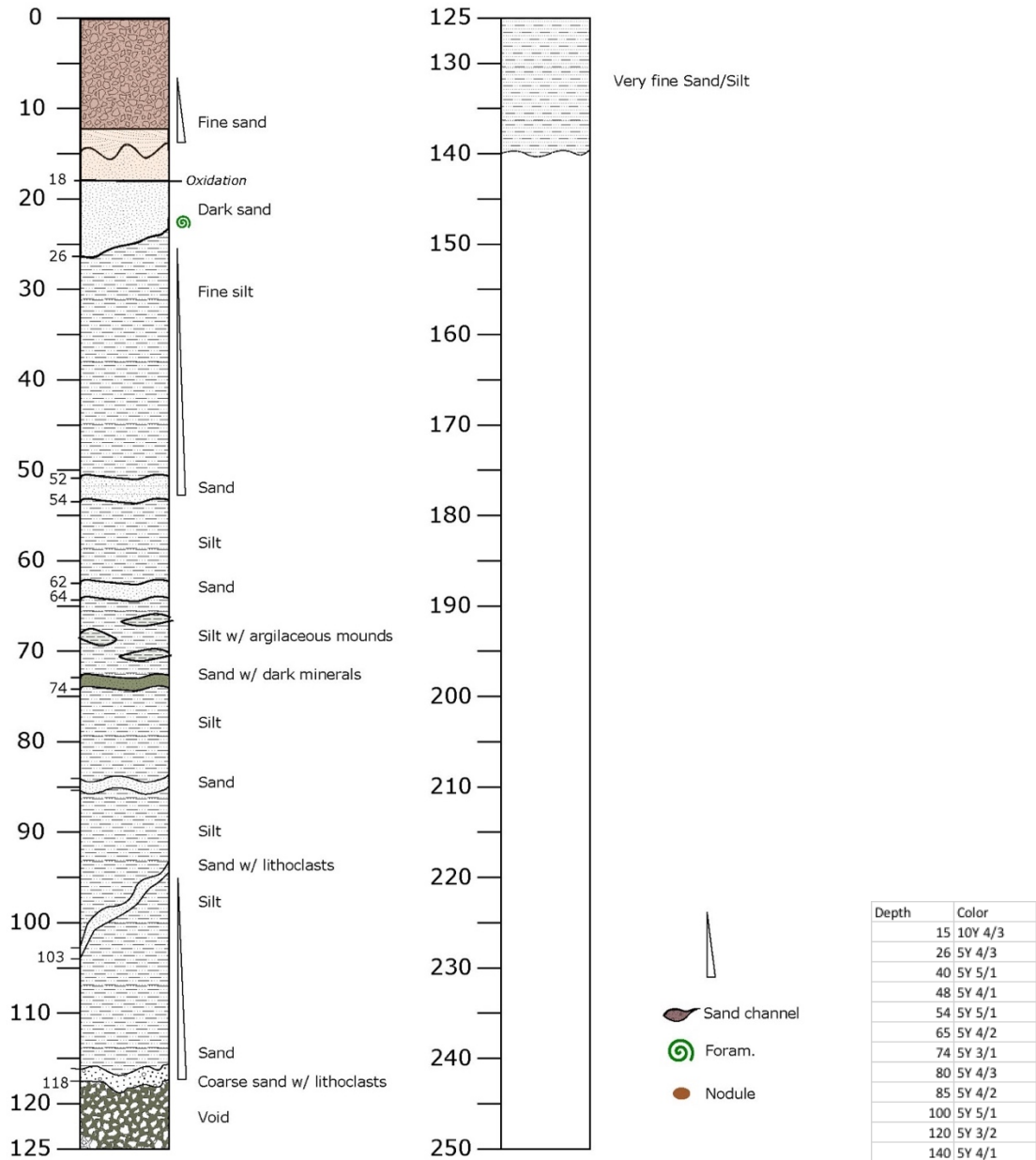
Fig. 12.3.5   Core description GC-3 with Munsell colour code.

5-GC3 #1
(0 – 40cm)

5-GC3 #2
(40 - 140cm)

Fig. 12.3.6   Core photo of GC-3.

GRAVITY CORE LOG   **M162**

Date: 2020/03/12 Hour: 12h19 Lat: 37º 20.632 N   Lon: 21º 20.238 W
Station: 15   WA- 2   GC- 4   Depth: 4126

Carbonate silt

Ooze w/ Foram.
Biosandstone

volcanic particles diminish
to the top

Ooze silt w/ Foram
Foram. size of fine sand

Piroclast size 1cm
Ooze Foram. w/ dark
minerals

Very fine sand w/Foram

Volcanic ash?

Ooze w/Foram size
fine sand/silt

Ooze fine sand

Silt
Silt w/some Foram.
Bioturbated and w/ volcanic
lithoclasts
Fine sand (ooze) darker in the
top silty clay w/Foram.

Clay w/Foram.

Ooze w/ coarse Foram.

Ooze fine sand/silt w/pyroclast
of felsic rocks size 1cm aprox.

Volcanic ash w/ dark lithoclast

Ooze w/ volcanic clasts

Fine sand / silt

Volcanic ash?

Fine ooze

Fine sand

Depth	Color
8	10Y 7/2
20	10Y 7/2
30	10Y 6/2
36	10Y 5/2
41	10Y 6/2
46	2.5Y 6/2
60	10Y 6/2
65	10Y 7/2
80	10Y 8/2
90	10Y 7/2
107	10Y 7/2
118	10Y 6/2
125	2.5Y 6/2
130	2.5Y 4/2
136	10Y 7/2
140	10Y 6/2
147	10Y 6/4

Sand channel

Foram.

Nodule

Volcanic pyroclast

Fig. 12.3.7   Core description GC-4 with Munsell colour code.

15-GC4 #1
(0 – 56cm)

15-GC4 #2
(56 – 156cm)

Fig. 12.3.8   Core photo of GC-4.
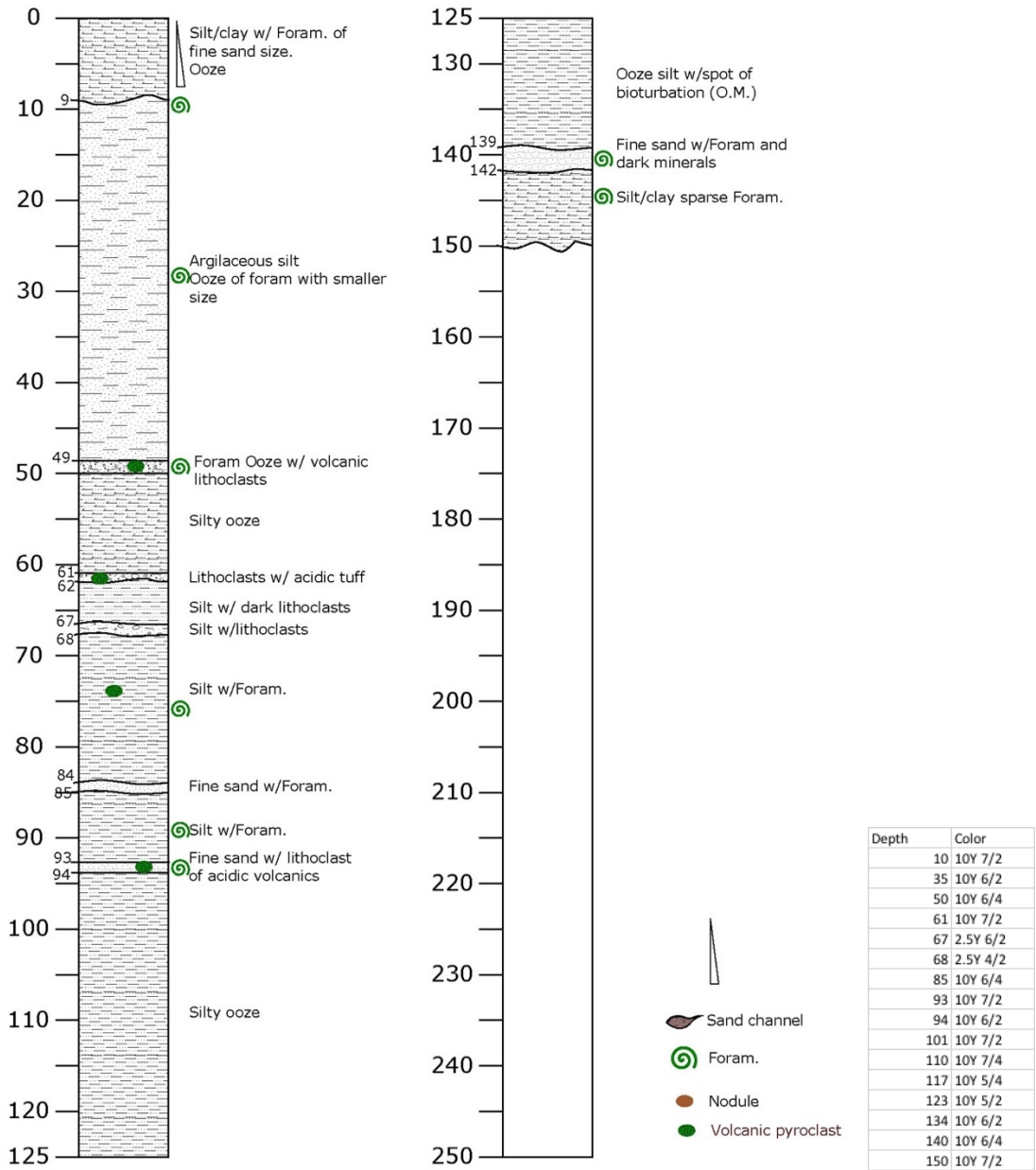
Fig. 12.3.9　Core description GC-5 with Munsell colour code.

16-GC5 #1
(0 – 55cm)

16-GC5 #2
(55 – 155cm)

Fig. 12.3.10   Core photo of GC-5.

GRAVITY CORE LOG **M162**

Date: 2020/03/12 Hour: 19h52 Lat: 37º 4.444 N Lon: 21º 18.736 W
Station: 17 WA- 2 GC- 6 Depth: 4575

Carbonate silt w/ Foram.

Sand w/ Foram.

Silt/clay w/ carboantes and Form.

Black mineral layering pyrite? O.M.?

Silt/clay w/ carboantes and Form.

Black mineral band pyrite? O.M.?

Red clay band

Silt/clay w/ carbonates and Form.

Fine sand w/ dark lithoclasts and Foram.

Fine sand w/ dark lithoclasts and Foram.

Silt/clay w/ carbonates and Form.

Fine sand w/ dark lithoclasts and Foram.

Silt/clay w/ carbonates and Form.

This unit presents a patchy fabric with black patchs in the silty matrix.
Some nodules appear.

Thining upwards
Erosive base
Sand channel
Foram.
Nodule
Volcanic pyroclast

Depth	Color
14	10Y 7/2
17	10Y 7/4
44	10Y 7/2
67	10Y 6/4
74	10Y 5/4
86	10Y 6/4
93	10Y 6/2
96	10Y 6/2
97	5Y 7/2
98	5GY 6/2
102	5Y 6/2
103	5Y 5/2
104	5Y 6/2
112.5	5Y 6/2
113.5	5GY 5/2
119	5Y 6/2
119.5	N 4/0
163	5Y 5/0
164	N 4/0
167	5Y 5/0
185	5Y 6/0
186	N 4/0
200	5Y 5/0
208	5Y 6/0
211	5GY 5/2
214	5GY 6/2
243	5Y 6/0
246	5Y 5/0
247	5Y 6/0
250	5GY 5/2
262	5Y 6/0
380	5Y 5/0

Fig. 12.3.11 Core description GC-6 with Munsell colour code.

17-GC6 #1 (0 – 80cm)

17-GC6 #2 (80 – 180cm)

17-GC6 #3 (180 – 280cm)

17-GC6 #4 (280 – 380cm)
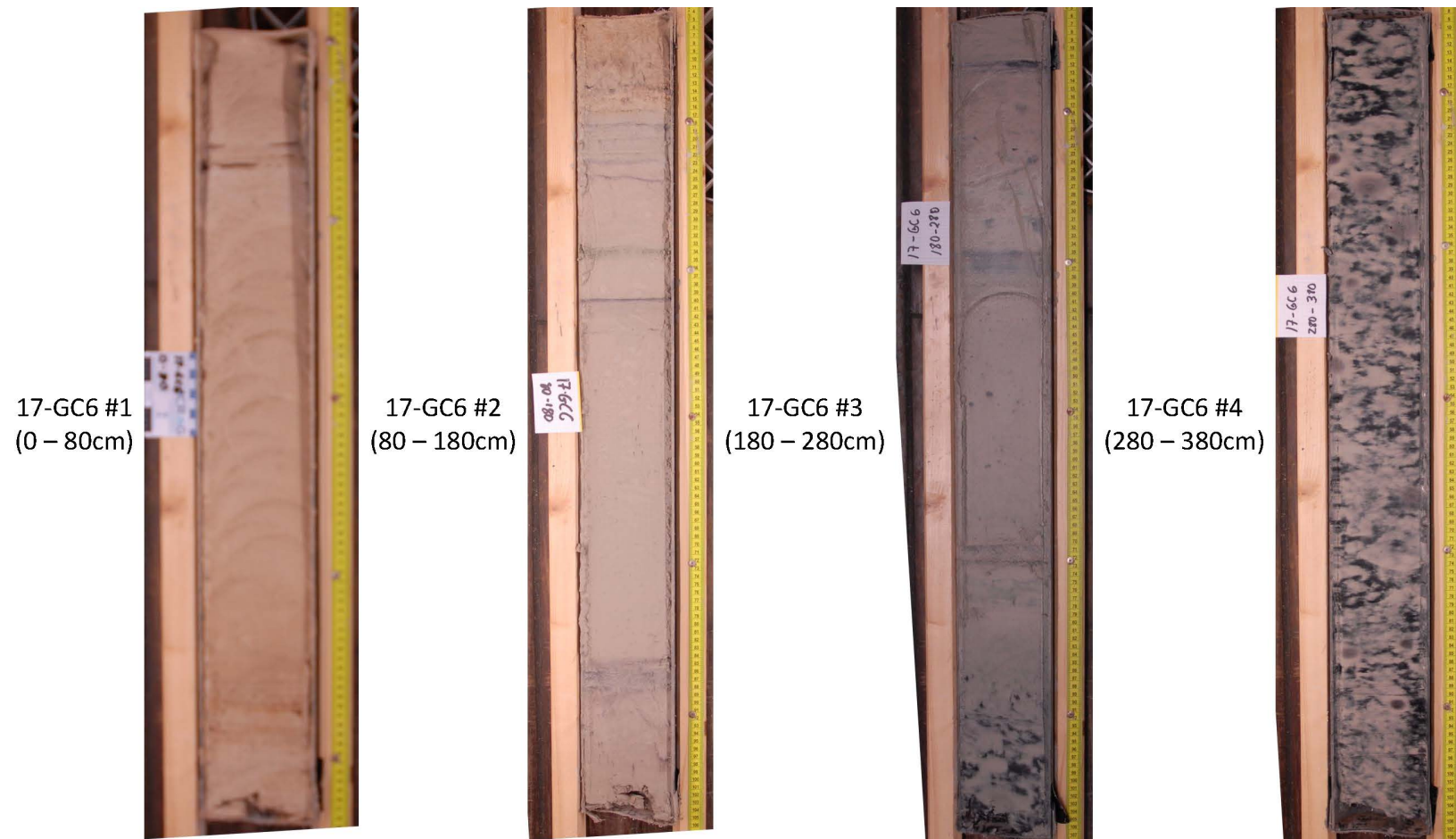
Fig. 12.3.12 Core photo of GC-6.

Fig. 12.3.13 Core description GC-7 with Munsell colour code.

19-GC7#1
(0 – 53cm)

19-GC7#2
(53 – 153cm)

19-GC7#3
(153 – 253cm)

19-GC7#4
(253 – 353cm)
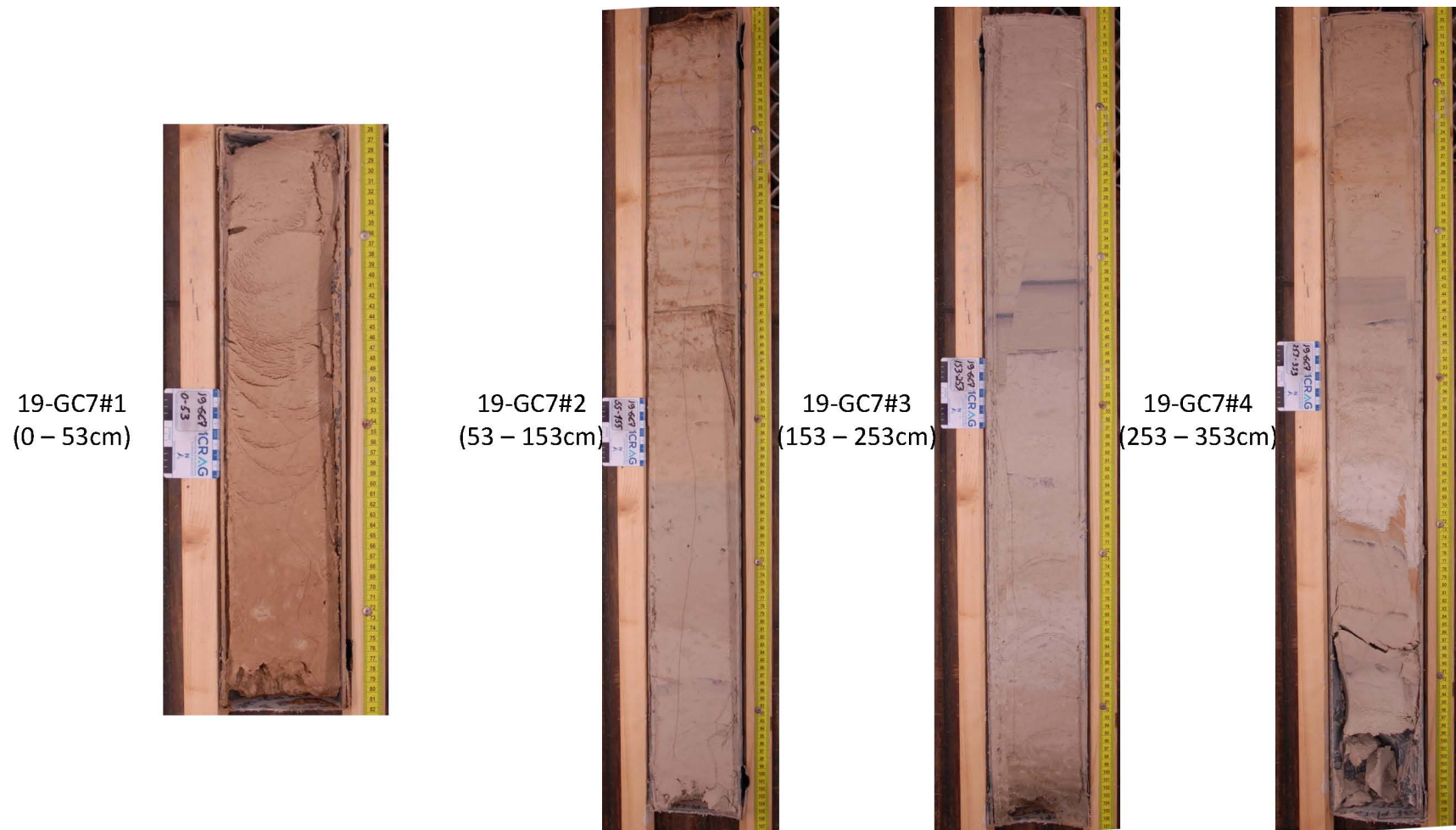
Fig. 12.3.14 Core photo of GC-7.

GRAVITY CORE LOG   M162

Date: 2020/03/13 Hour: 18h32 Lat: 36º 53.797 N   Lon: 21º 117.667 W

Station: 21   WA- 2   GC- 9   Depth: 4027

Fine sand w/Foram.

Silt

Fine sand
Fine sand w/Foram and dark lithoclasts

Spots w/dark minerals

Silt

Fine sand w/ bolders of felsic volcanics

Clay silt

Silt w/Foram size fine sand

Silt w/Foram. size fine sand

Clay w/Foram.

Silt w/Foram.

Sand w/Foram and dark minerals
Silt w/Foram and dark minerals
Silt/clay

Clay w/Foram

Silt/clay

Thining upwards

Erosive base

Sand channel

Foram.

Nodule

Volcanic pyroclast

Depth	Color
25	10Y 7/3
30	10Y 6/4
37	10Y 5/4
64	10Y 6/4
66	10Y 4/2
72	10Y 5/4
97	10Y 6/3
116	10Y 7/3
140	10Y 6/3
160	10Y 5/3
170	10Y 4/3
180	10Y 5/3
195	10Y 6/3
223	10Y 7/3
235	10Y 5/4
257	10Y 6/3
263	10Y 7/3
304	10Y 5/3
312	10Y 5/4
316	10Y 5/3
320	10Y 5/2
326	10Y 7/2
345	10Y 6/2
358	10Y 5/2
382	10Y 6/3

Fig. 12.3.15 Core description GC-9 with Munsell colour code.

21-GC9#1
(0 – 82cm)

21-GC9#2
(82 – 182cm)

21-GC9#3
(182 - 282cm)

21-GC9#4
(282 – 382cm)

Fig. 12.3.16   Core photo of GC-9.
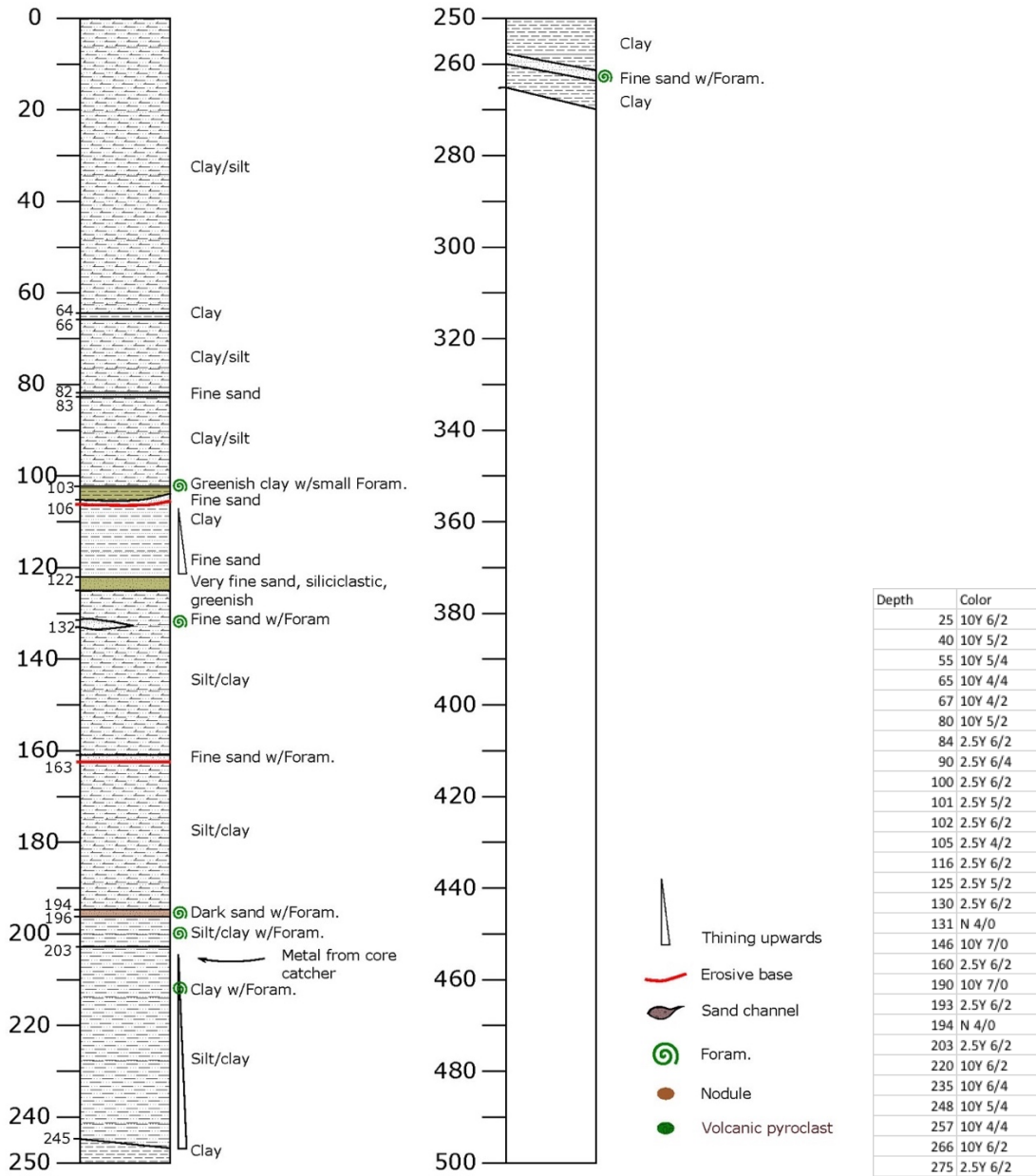
Fig. 12.3.17 Core description GC-10 with Munsell colour code.

23-GC10#1
(0 – 73cm)
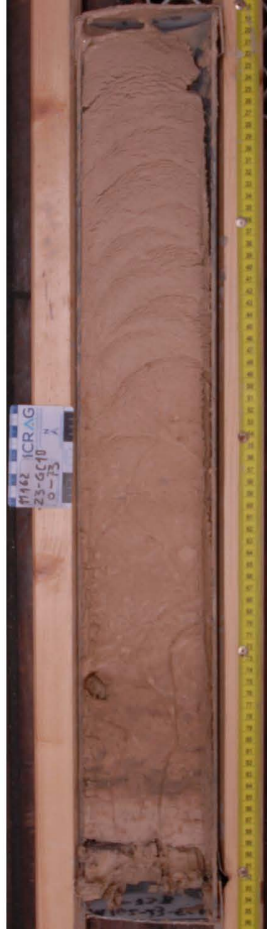
23-GC10#2
(73 – 173cm)
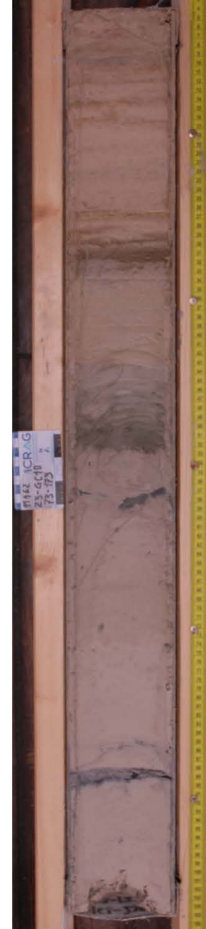
23-GC10#3
(173 - 273cm)

Fig. 12.3.18 Core photo of GC-10.

GRAVITY CORE LOG   **M162**

Date: 2020/03/16 Hour: 13h44 Lat: 36º 59.475 N
Station: 29   WA- 3 GC- 11   Lon: 22º 43.583 W
                                       Depth: 4887

Silt w/Forams

Felsic pyroclast w/ biotite

Clay w/Silt

Silt w/Forams (dark)

Silt w/Forams (light)

Silt w/Forams (light)

Clay w/Silt

Silt w/Clay

Foram Sand

Clay + Silt

Bioturbation

Mafic lithic minerals

Black streaks,
pyrite or organic matter

Thining upwards

Erosive base

Sand channel

Foram.

Nodule

Volcanic pyroclast

27	10Y 6/2
53	10Y 6/3
57	10Y 7/1
64	10Y 6/3
80	10Y 5/3
116	10Y 7/2
130	10Y 5/2
190	10Y 6/2
192	10Y 5/2
194	10Y 6/4
213	10Y 5/2
225	10Y 6/2

Fig. 12.3.19 Core description GC-11 with Munsell colour code.

29-GC11#1
(0 – 27cm)
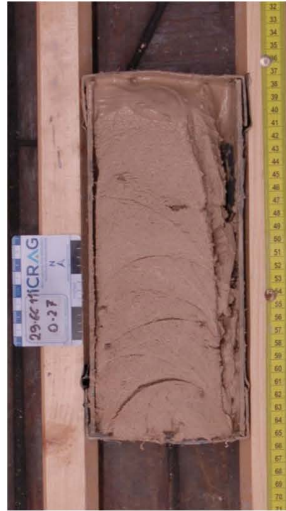
29-GC11#2
(27 – 127cm)

29-GC11#3
(127 – 227cm)

Fig. 12.3.20 Core photo of GC-11.

GRAVITY CORE LOG   **M162**

Date: 2020/03/17 Hour: 20h33 Lat: 37º 1.752 N   Lon: 22º 3.168 W
Station: 33   WA- 2   GC- 13   Depth: 4250
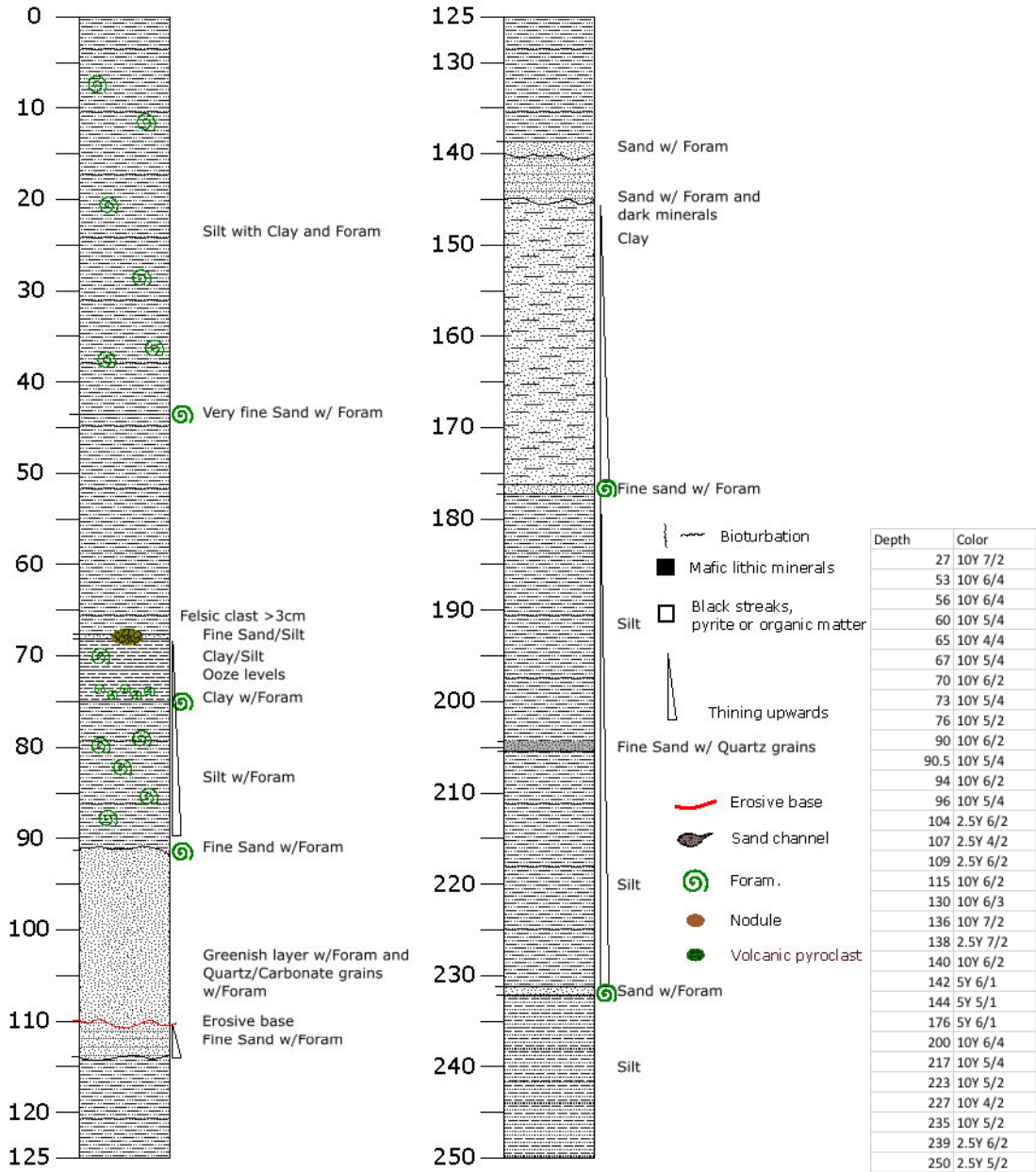
Fig. 12.3.21 Core description GC-13 with Munsell colour code.

33-GC13#1
(0 – 50cm)

33-GC13#2
(50 – 150cm)

33-GC13#3
(150 – 250cm)

Fig. 12.3.22 Core photo of GC-13.

Fig. 12.3.23 Core description GC-14 with Munsell colour code.
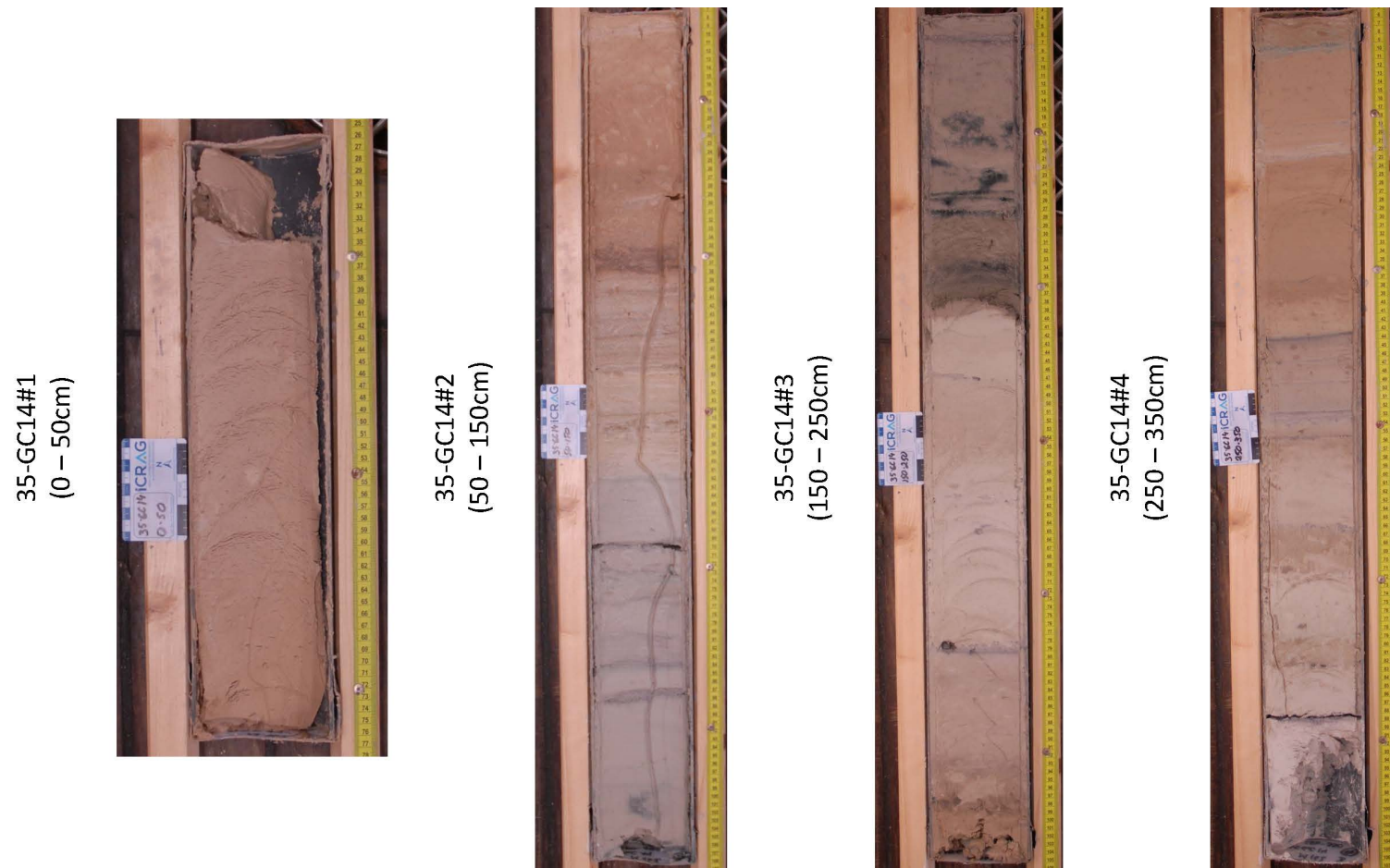
Fig. 12.3.24   Core photo of GC-14.

Fig. 12.3.25 Core description GC-15 with Munsell colour code.

36-GC15#1
(0 – 67cm)

3-GC15#2
(67 – 167cm)
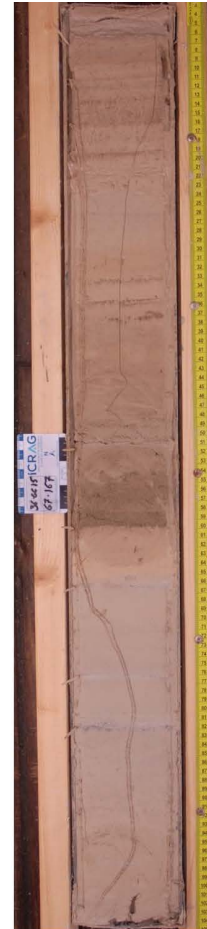
36-GC15#3
(167 – 267cm)

Fig. 12.3.26 Core photo of GC-15.

Fig. 12.3.27 Core description GC-19 with Munsell colour code.

43-GC19#1
(0 – 27cm)

43-GC19#2
(27 – 127cm)

Fig. 12.3.28   Core photo of GC-19.

GRAVITY CORE LOG   M162

Date: 2020/03/20 Hour: 13h25 Lat: 37°35.937 N
Station: 44   WA- 3   GC- 20
Lon: 20°29.592 W
Depth: 4188
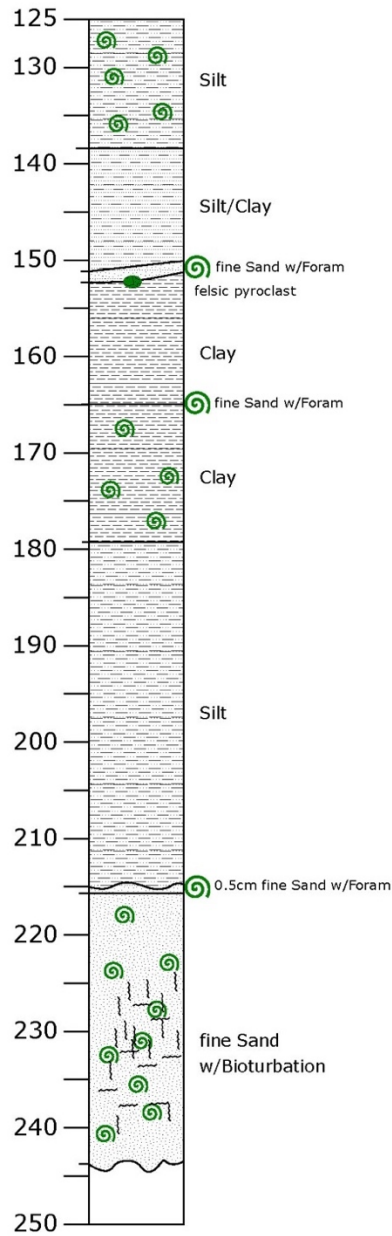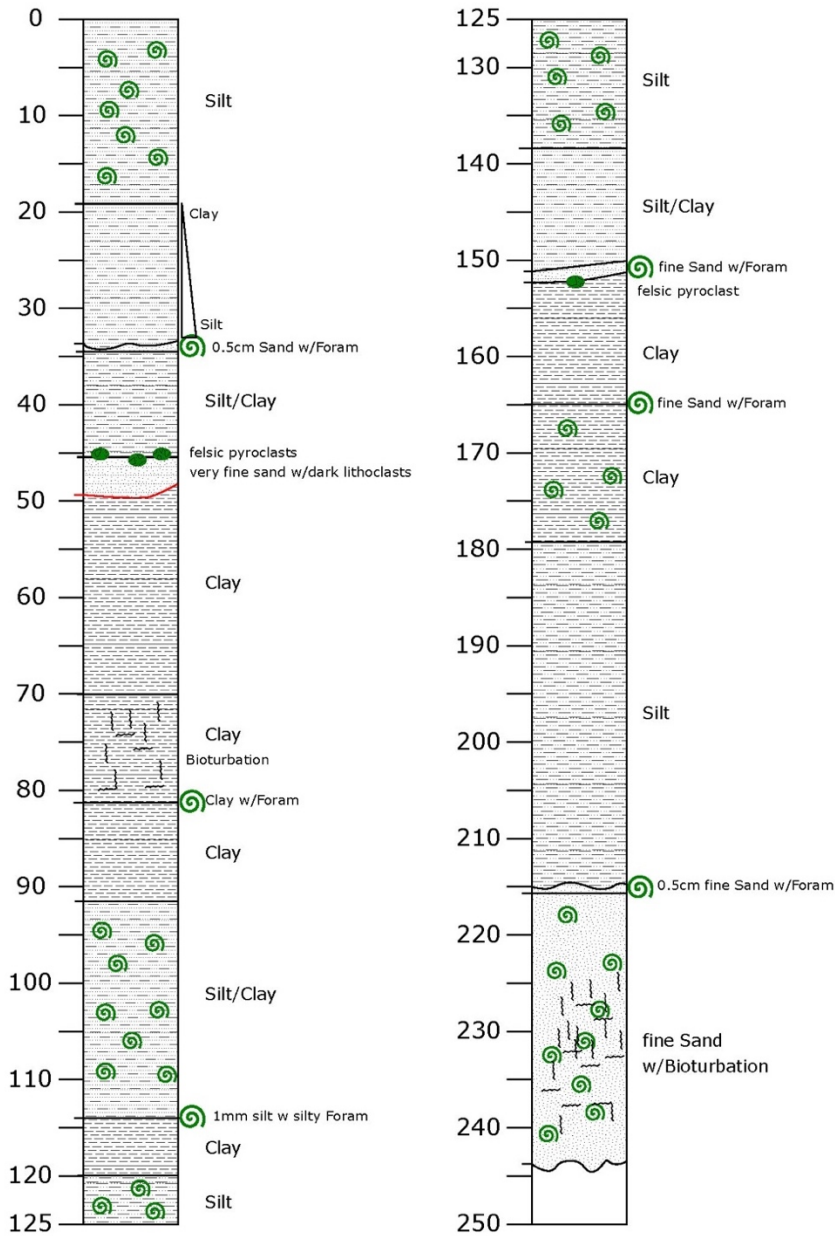
Depth	Color
24	10Y 7/2
36	10Y 5/4
40	10Y 7/2
48	10Y 5/3
50	10Y 5/2
65	10Y 5/3
101	10Y 5/2
108	10Y 6/3
121	10Y 5/3
141	10Y 7/2
151	10Y 5/2
161	10Y 6/3
167	10Y 5/3
181	10Y 5/4
225	10Y 6/3
243	10Y 5/3

Silt

Clay

Silt

0.5cm Sand w/Foram

Silt/Clay

felsic pyroclasts
very fine sand w/dark lithoclasts

Clay

Clay
Bioturbation

Clay w/Foram

Clay

Silt/Clay

1mm silt w silty Foram

Clay

Silt

Silt

Silt/Clay

fine Sand w/Foram
felsic pyroclast

Clay

fine Sand w/Foram

Clay

Silt

0.5cm fine Sand w/Foram

fine Sand
w/Bioturbation

Fig. 12.3.29 Core description GC-20 with Munsell colour code.

44-GC20#1
(0 – 19cm)

44-GC20#2
(19 – 43cmcm)

44-GC20#3
(43 – 143cm)

44-GC20#4
(143 – 243cm)
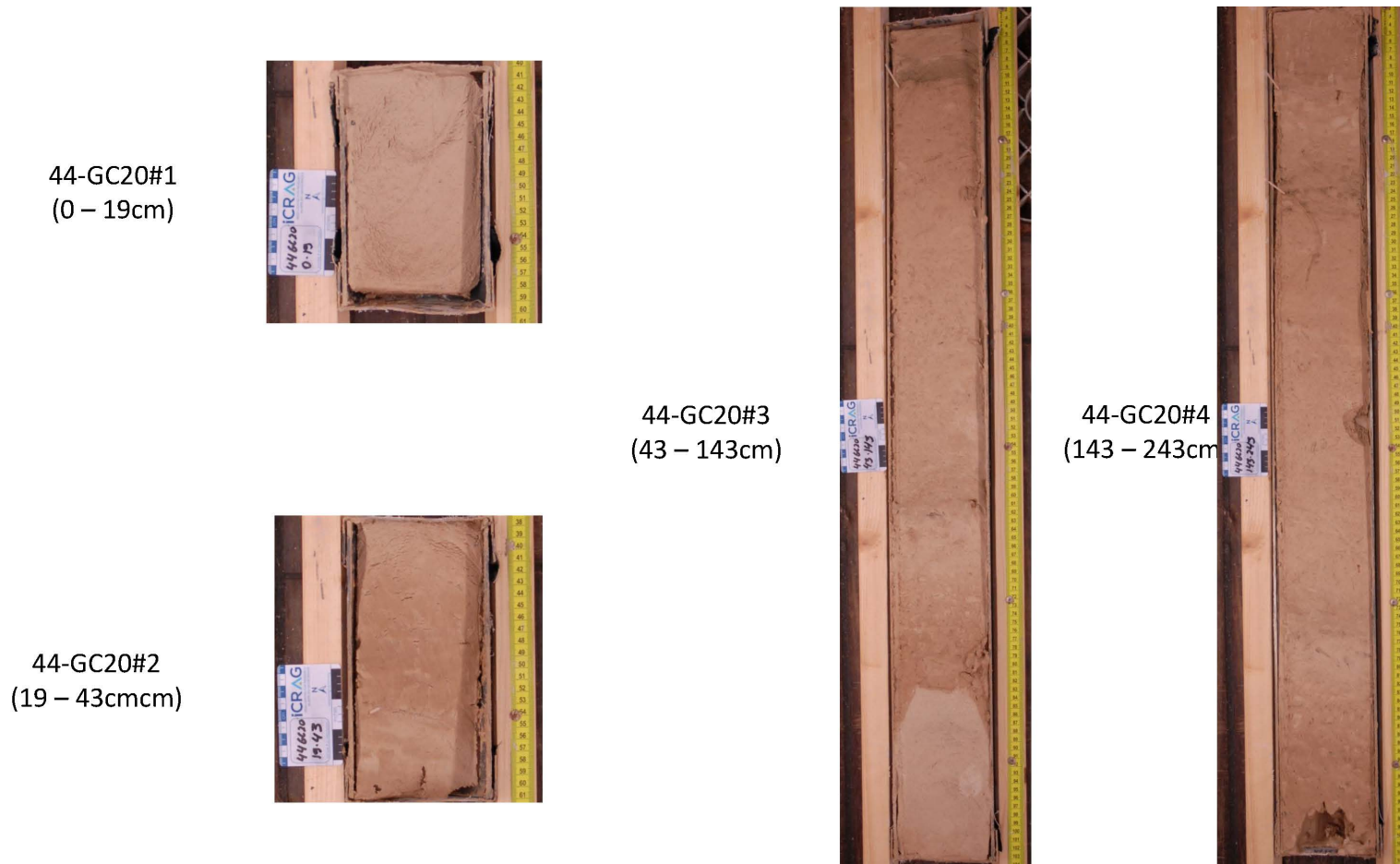
Fig. 12.3.30 Core photo of GC-20.
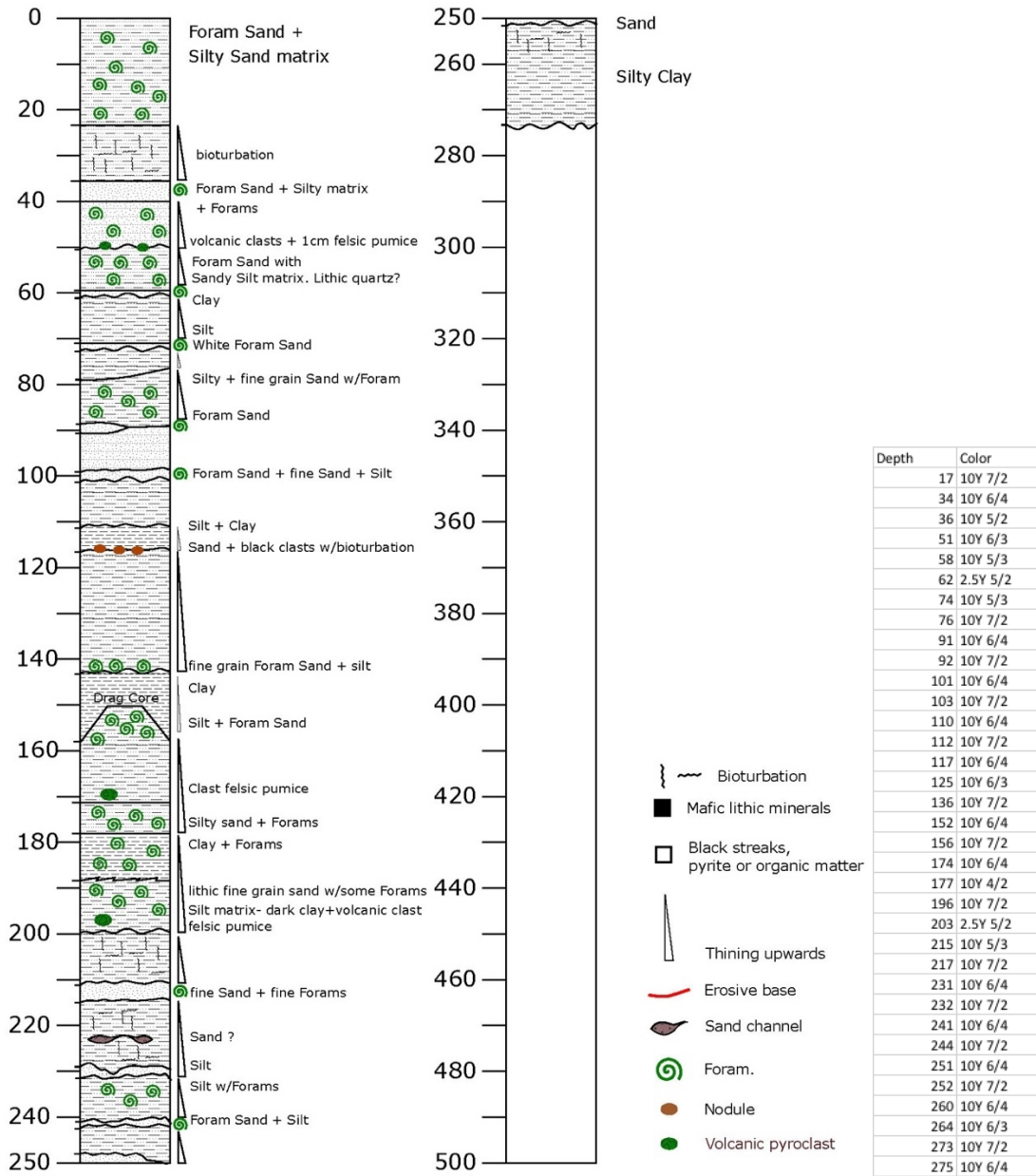
Fig. 12.3.31 Core description GC-22 with Munsell colour code.

47-GC22#1
(0 – 81cm)

47-GC21#2
(81 – 181cm)

47-GC21#3
(181 – 281cm)
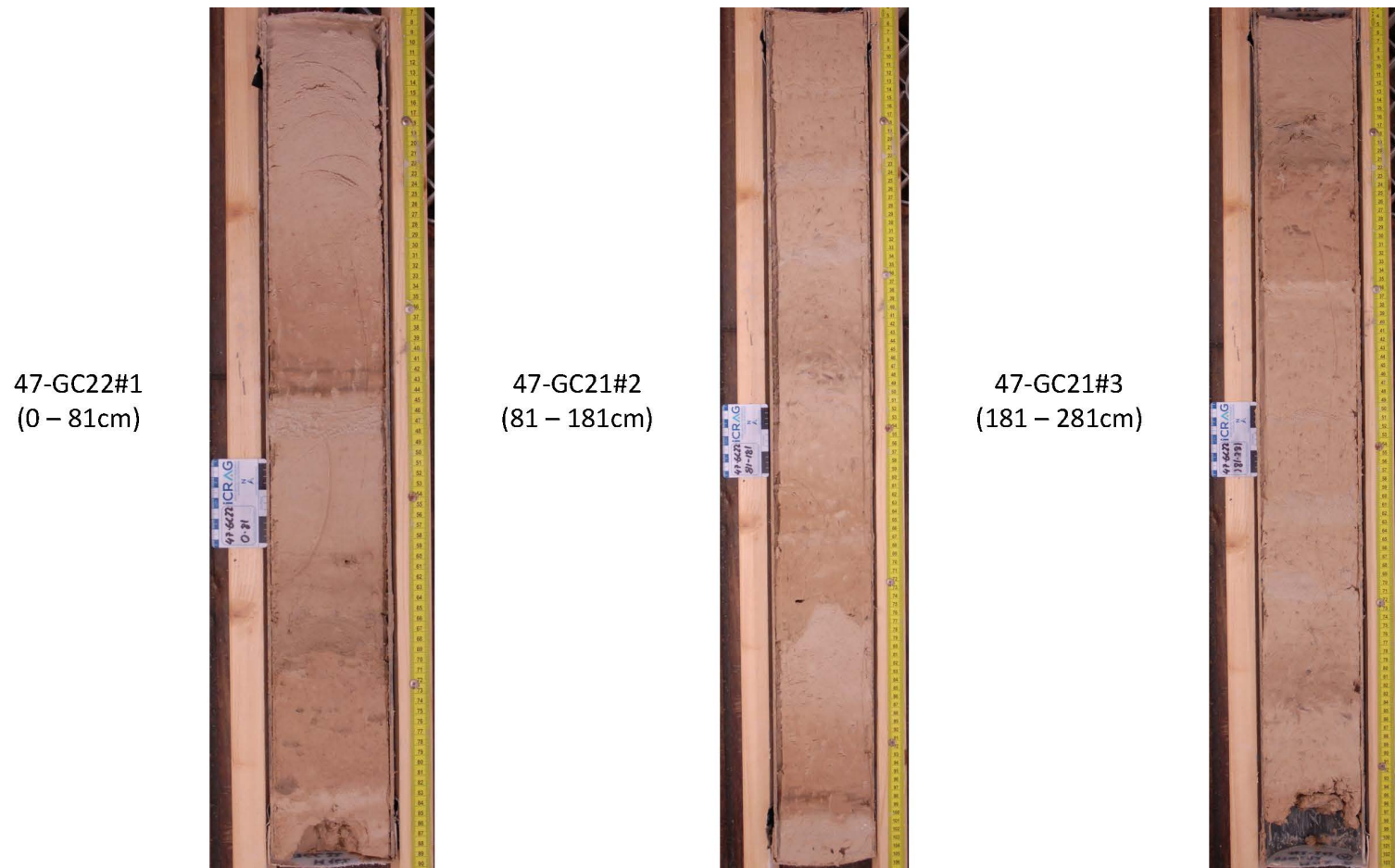
Fig. 12.3.32 Core photo of GC-22.

GRAVITY CORE LOG   **M162**

Date: 2020/03/21 Hour: 12h55 Lat: 37º 35.759 N   Lon: 20º 29.575 W
Station: 48   WA- 4   GC- 23   Depth: 4188

Silt w/Forams

bioturbation

fine Sand w/Foram Silty matrix
bioturbation
Silty Clay

Very fine silica Sand w/ black elements

Clay w/Sand podcasts

Clay w/scattered Forams

volcanic clast felsic pumice

bioturbation w/ fine black sand pyrite

volcanic clast felsic pumice

Bioturbation
Mafic lithic minerals
Black streaks, pyrite or organic matter
Thining upwards
Erosive base
Sand channel
Foram.
Nodule
Volcanic pyroclast

Depth	Color
23	10Y 7/2
31	10Y 6/3
35	10Y 7/3
40	10Y 6/3
43	2.5Y 5/2
56	10Y 6/3
84	10Y 7/3
90	10Y 5/3
106	10Y 6/3

Fig. 12.3.33 Core description GC-23 with Munsell colour code.

48-GC23#1
(0 – 108cm)

Fig. 12.3.34   Core photo of GC-23.
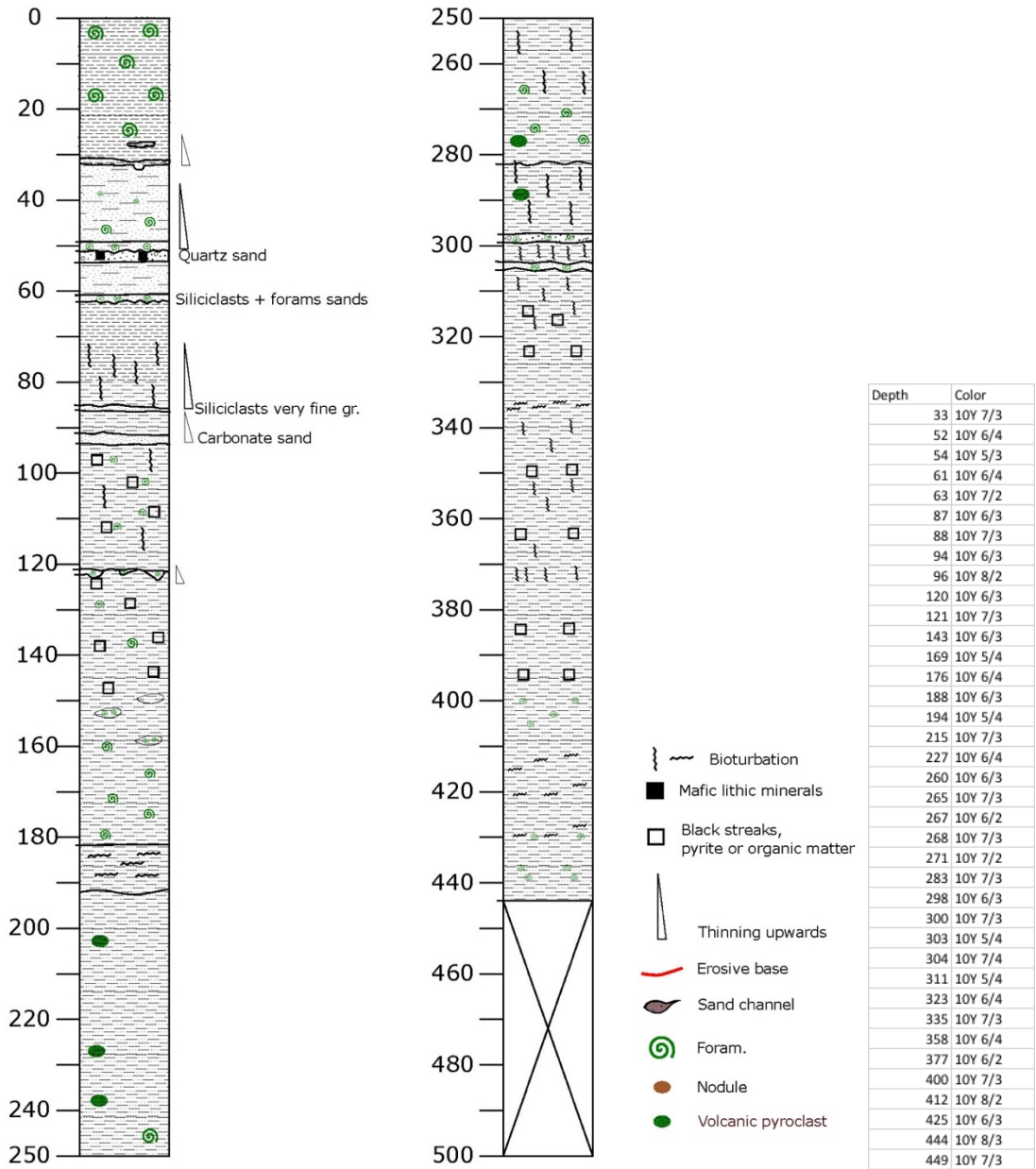
Fig. 12.3.35 Core description GC-26 with Munsell colour code.
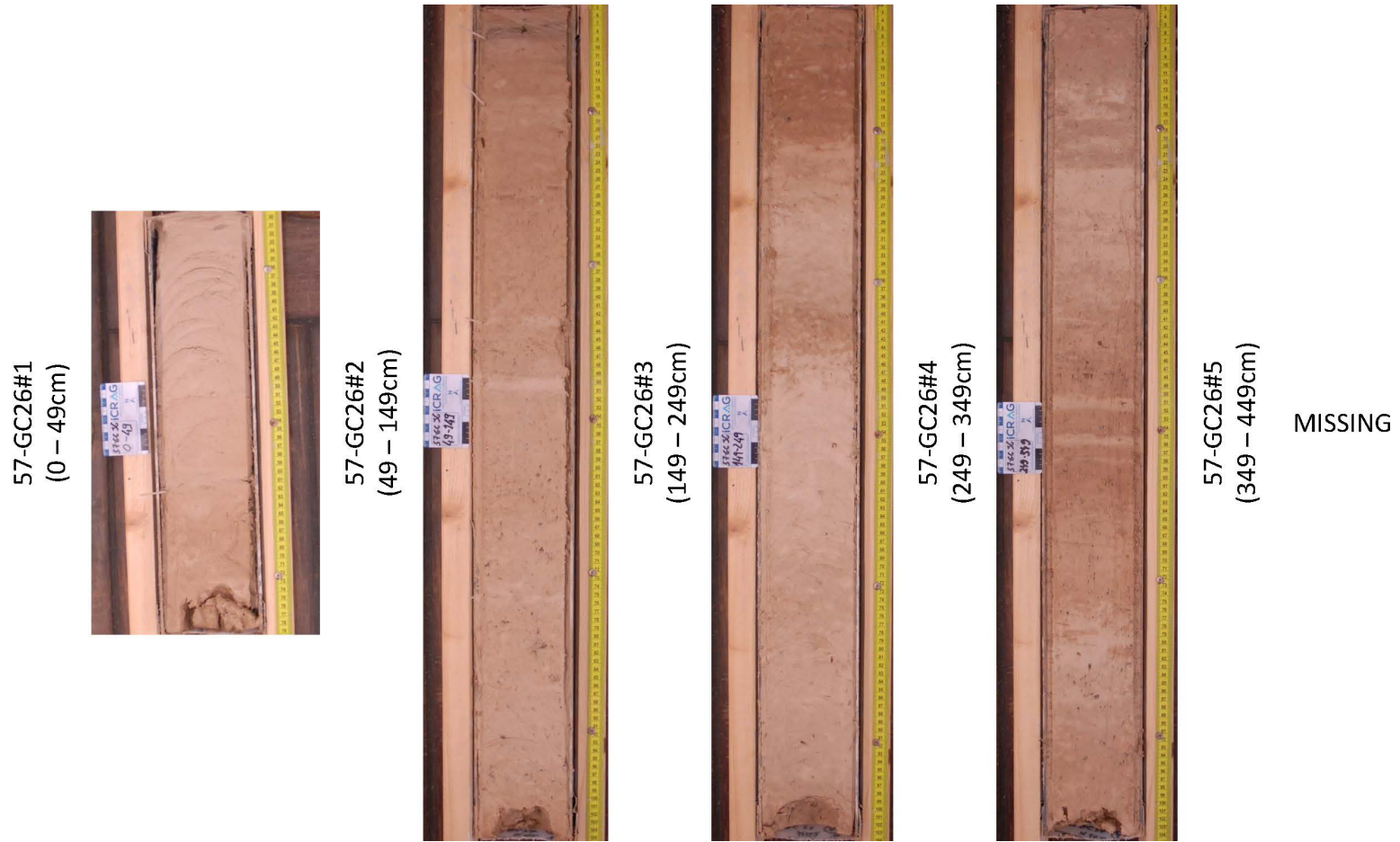
Fig. 12.3.36   Core photo of GC-26.

GRAVITY CORE LOG   **M162**

Date: 2020/03/24 Hour: 13h31 Lat: 37º 32.120N
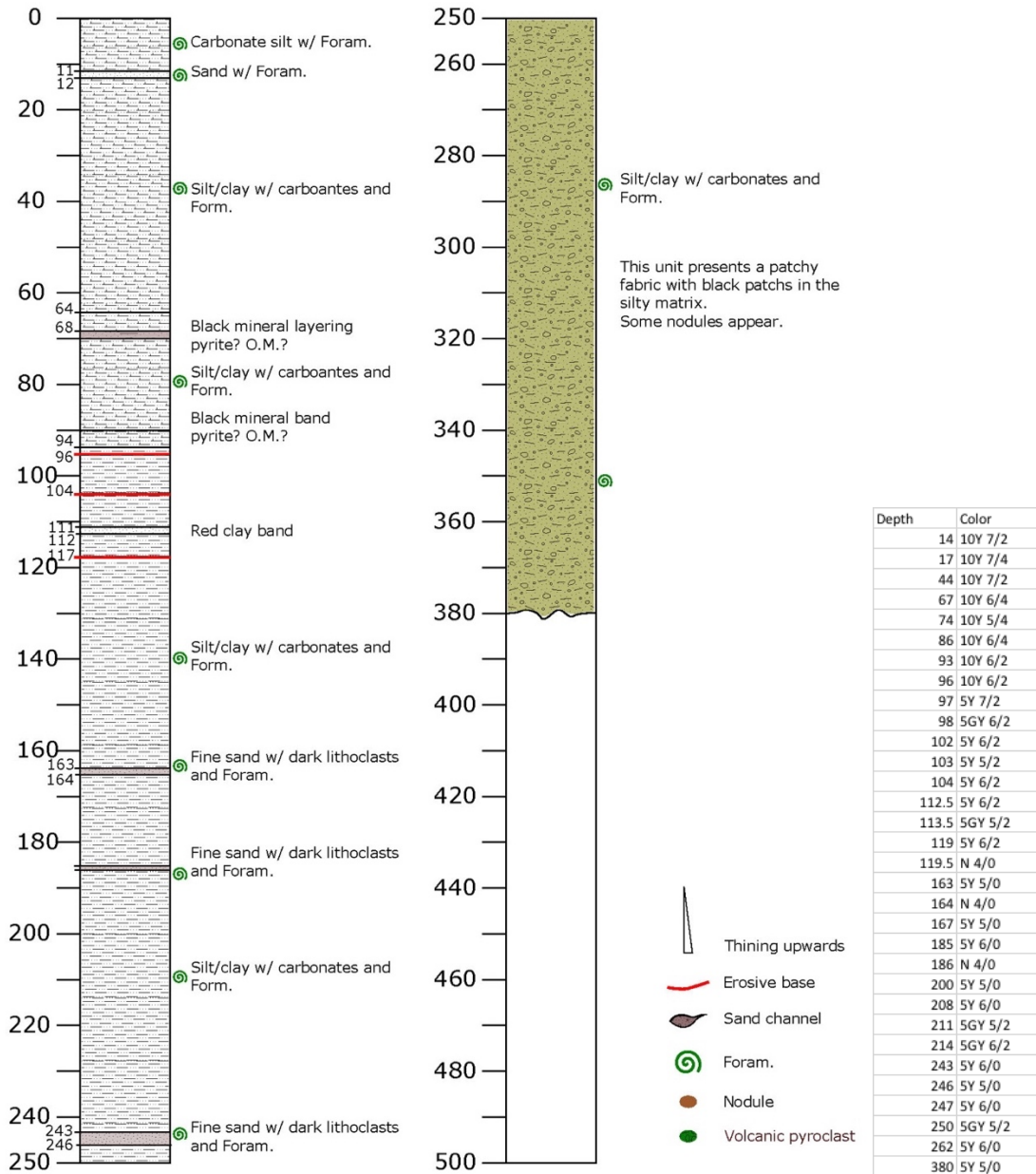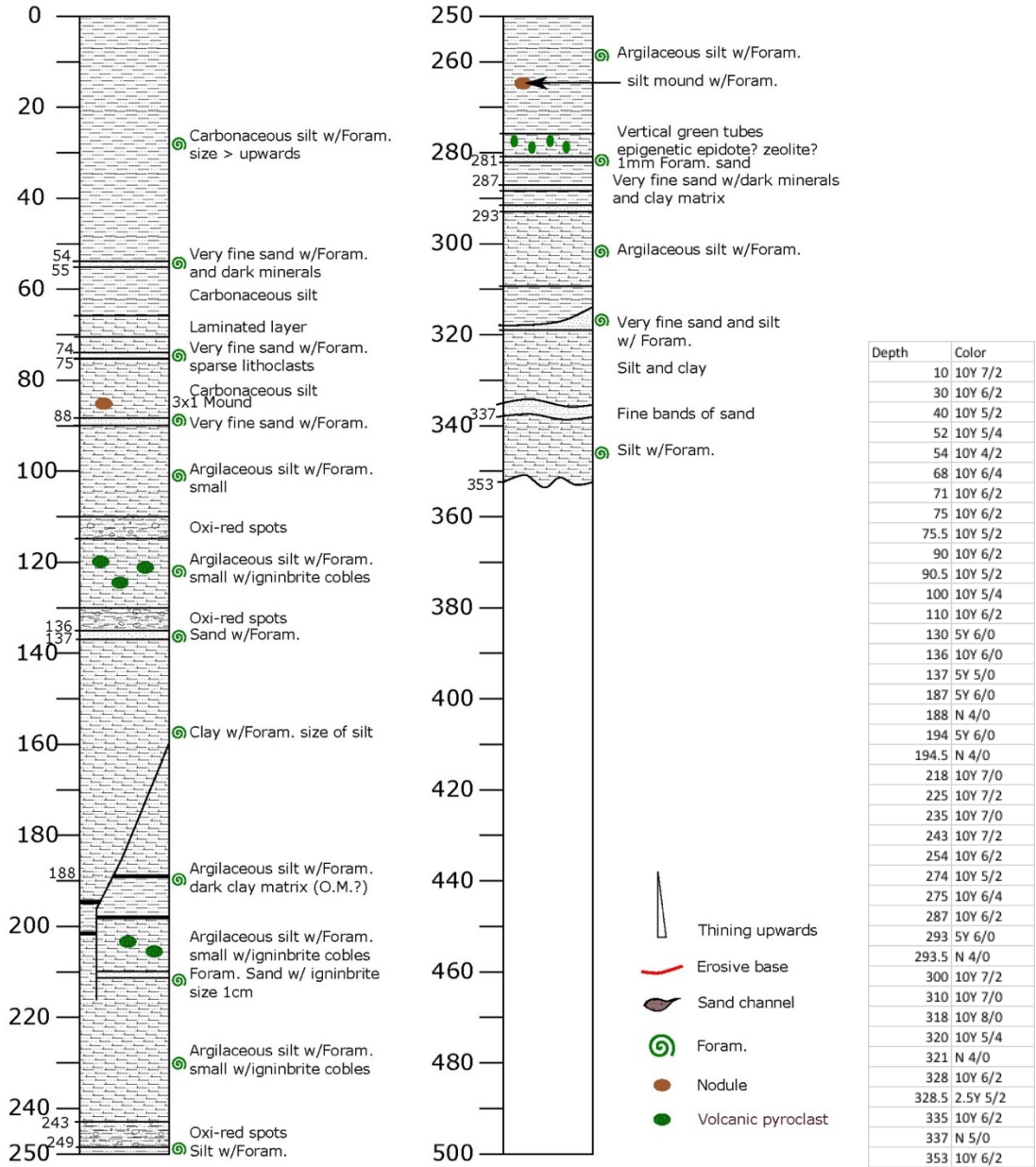Station: 58   WA- 3/4   GC- 27   Lon: 18º 38.693 W
Depth: 4846 m

Depth	Color
25	10Y 7/3
36	10Y 6/3
38	10Y 6/2
48	10Y 6/3
50	2.5Y 5/2
58	10Y 6/3
63	10Y 7/3
75	10Y 6/3
97	10Y 7/3
100	10Y 6/3
112	10Y 7/1
116	10Y 6/2
119	10Y 6/3
160	10Y 7/3
171	10Y 6/3
185	10Y 8/2
197	10Y 5/4
207	10Y 6/3
215	10Y 7/3
235	10Y 6/3
247	10Y 7/3
251	10Y 8/3
262	10Y 7/3
270	10Y 6/3
276	10Y 7/3

Legend:
- Bioturbation
- Lithic quartz, very fine
- Organic matter and/or pyrite
- Thining upwards
- Sand channel
- Foram.
- Nodule
- Volcanic pyroclast

Fig. 12.3.37 Core description GC-27 with Munsell colour code.

58-GC27#1
(0 – 76cm)

58-GC27#2
(76 – 176cm)
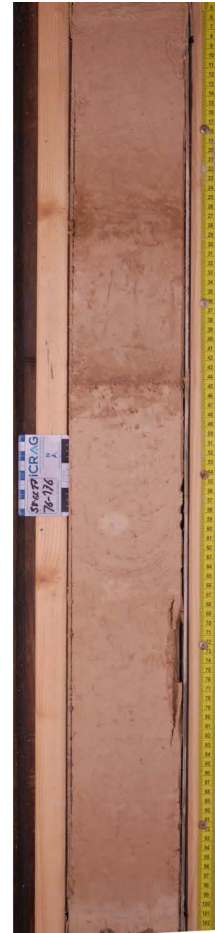
58-GC27#3
(176 – 276cm)

Fig. 12.3.38   Core photo of GC-27.
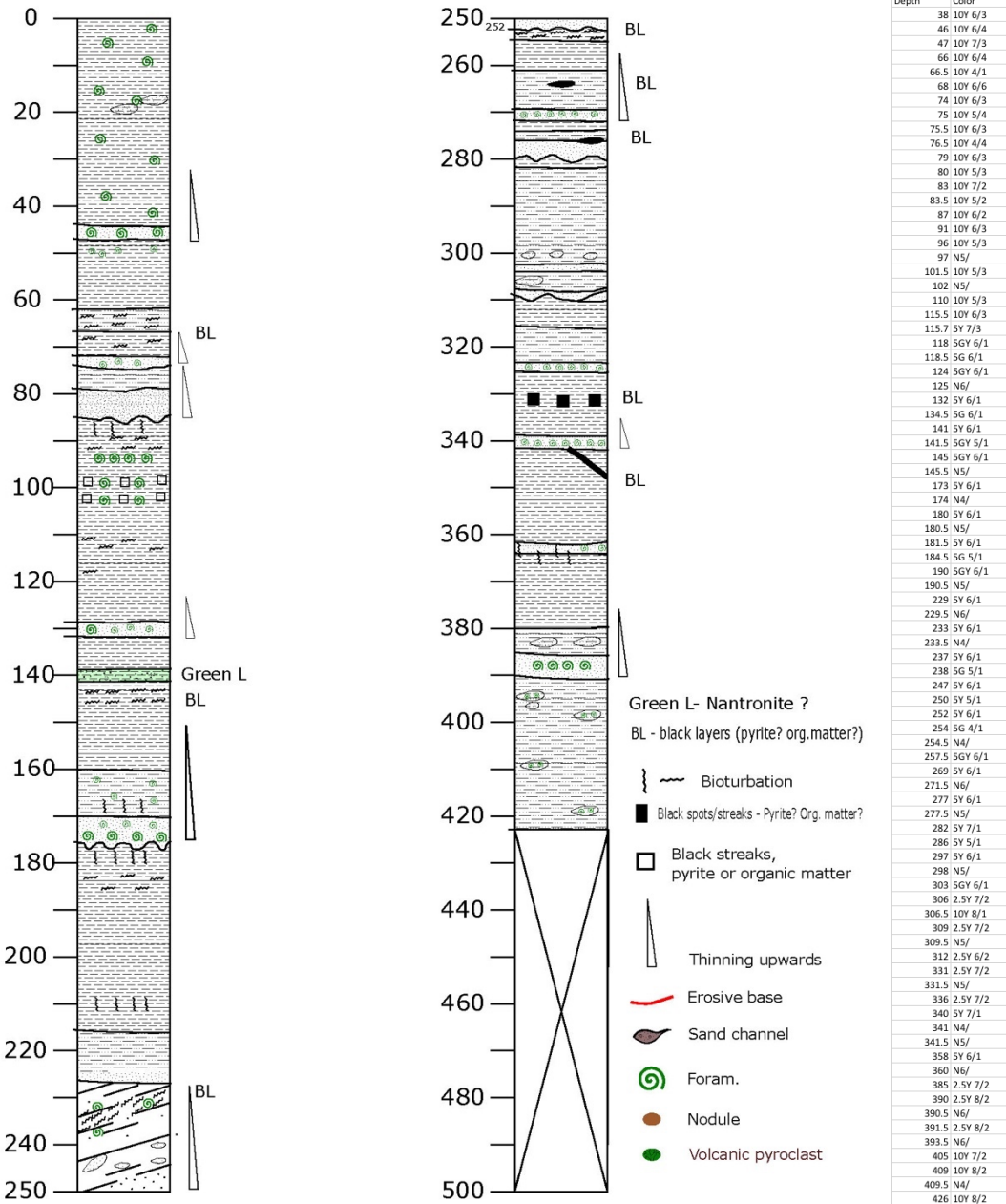
Fig. 12.3.39 Core description GC-28 with Munsell colour code.
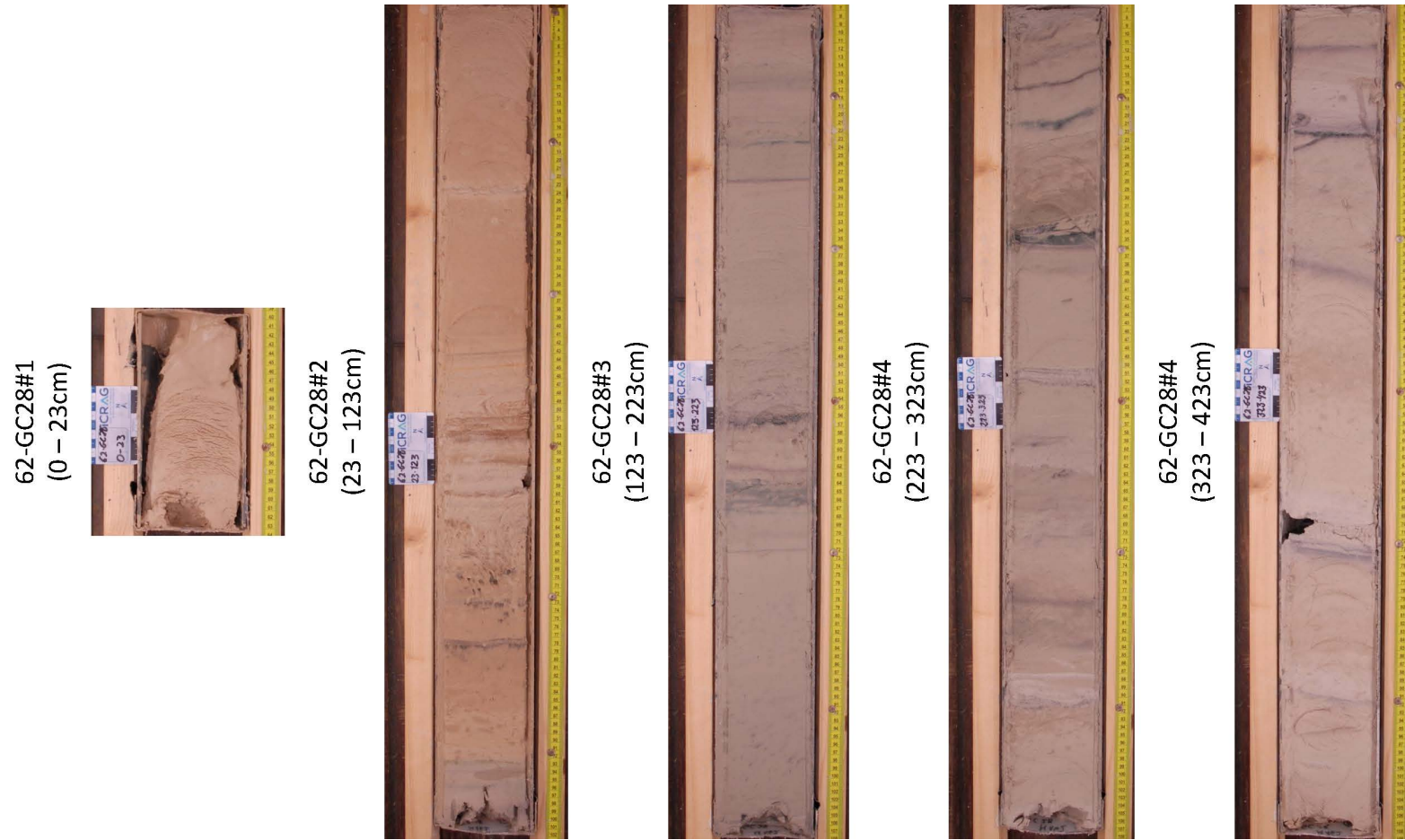
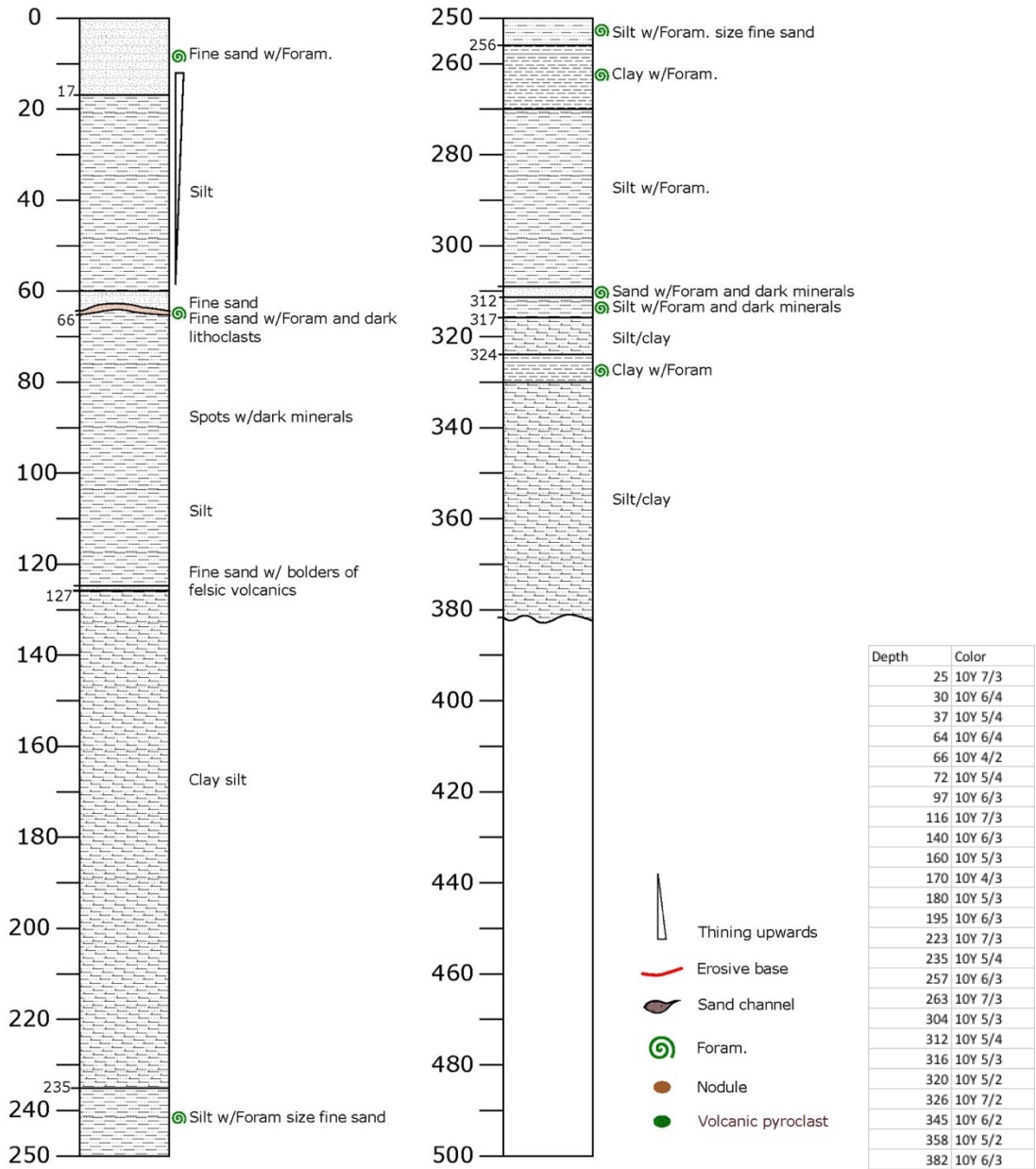**Fig. 12.3.40**   Core photo of GC-28.
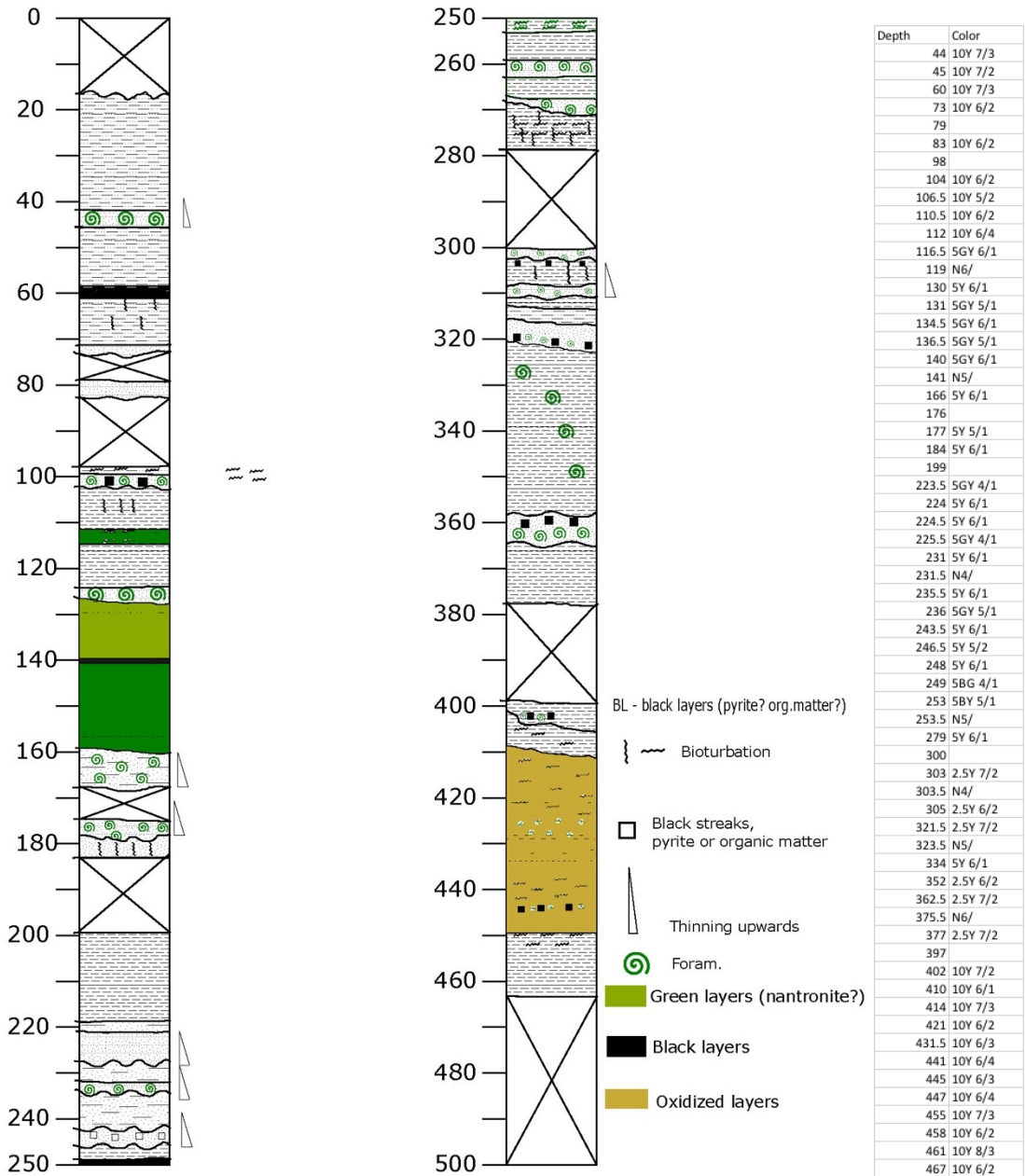
Fig. 12.3.41 Core description GC-29 with Munsell colour code.
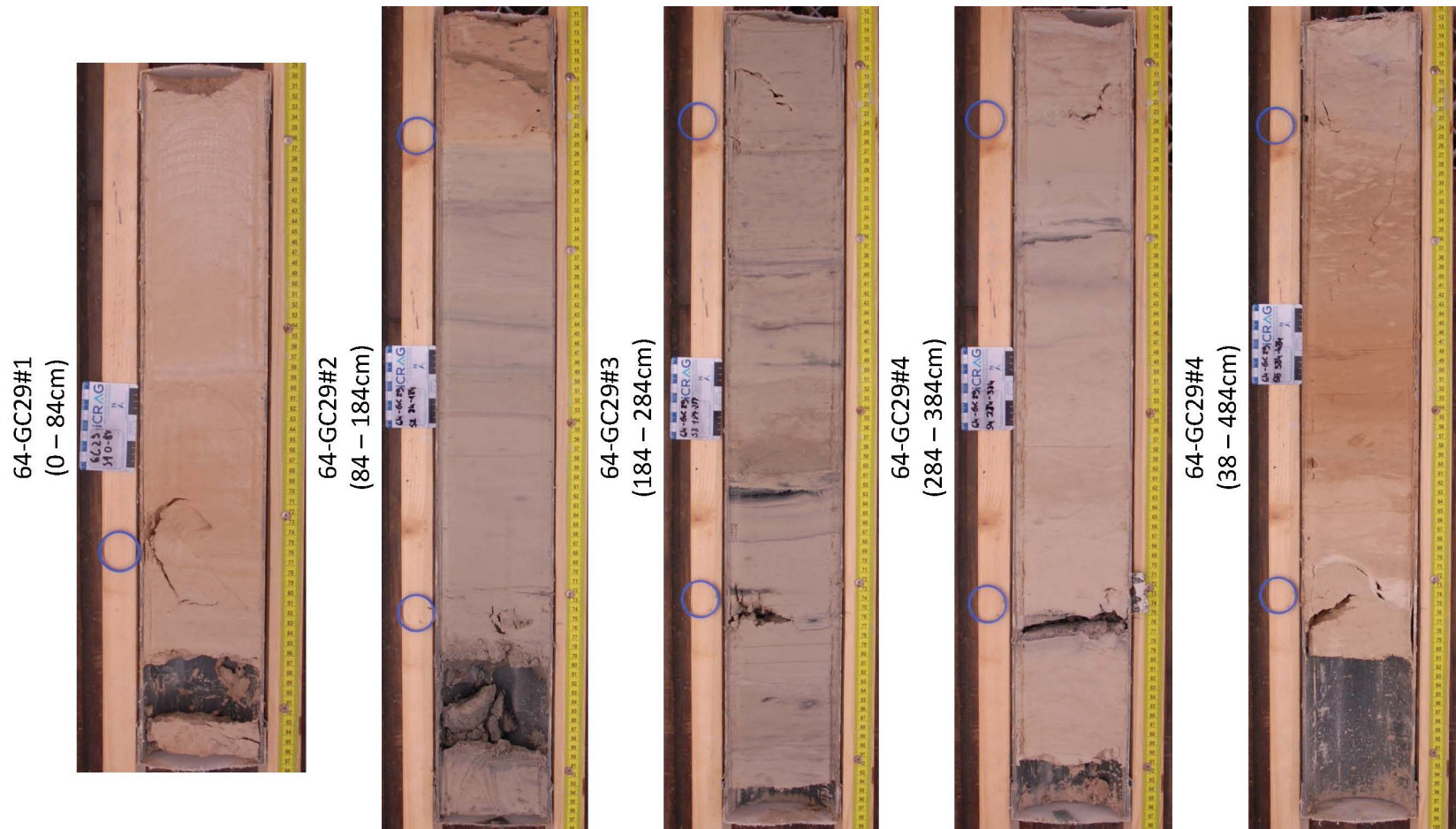
Fig. 12.3.42   Core photo of GC-29.

GRAVITY CORE LOG   **M162**

Date: 2020/03/27 Hour: 08h19   Lat: 37º 4,757 N   Lon: 21º 18.741 W
Station: 65   WA- 2   GC- 30   Depth: 4527 m

Depth	Color
9	10Y 7/3
29	10Y 6/4
55	10Y 5/4
58.5	10Y 4/4
60	10Y 6/4
61.5	10Y 5/4
67	10Y 6/4
72.5	10Y 6/3
80	10Y 5/3
84	2.5Y 4/3
86.5	10Y 6/3
90	10Y 7/3
92	2.5Y 6/2
117	10Y 7/2
132.5	2.5Y 7/2
165	10Y 7/2
171	5Y 6/2
189	10Y 7/2
201.5	10Y 7/2
205	10Y 6/3
206	10Y 7/2
215	10Y 6/3
225	10Y 7/3
229	10Y 6/3
231	10Y 6/2
247	10Y 7/2
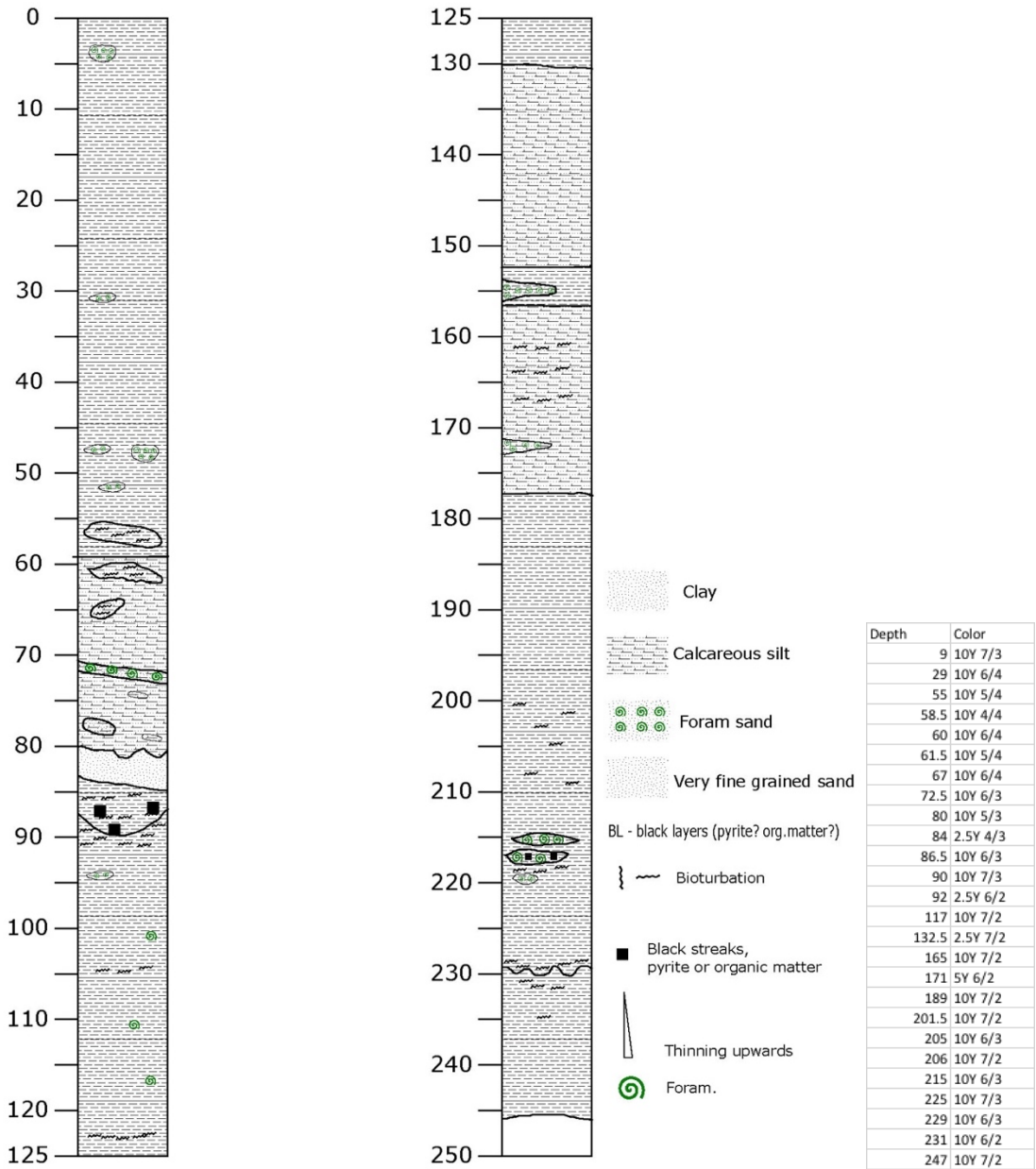
Fig. 12.3.43 Core description GC-30 with Munsell colour code.

65-GC30#1
(0 – 46cm)

65-GC30#2
(46 – 146cm)

65-GC30#3
146 – 246cm)

Fig. 12.3.44   Core photo of GC-30.
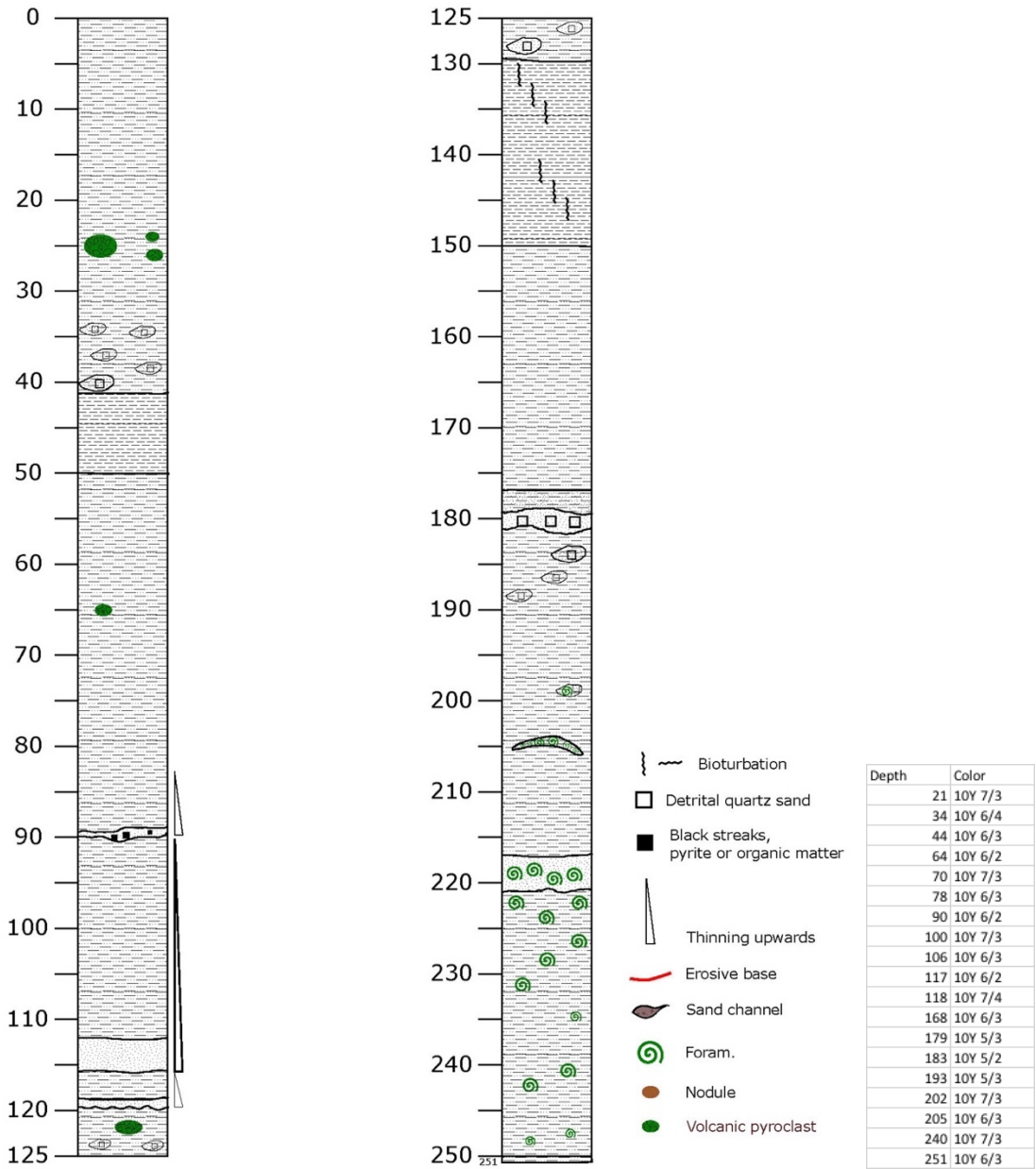
Fig. 12.3.45 Core description GC-31 with Munsell colour code.

66-GC31#1
(0 – 51cm)

66-GC31#2
(51 – 151cm)

66-GC31#3
(151 – 251cm)
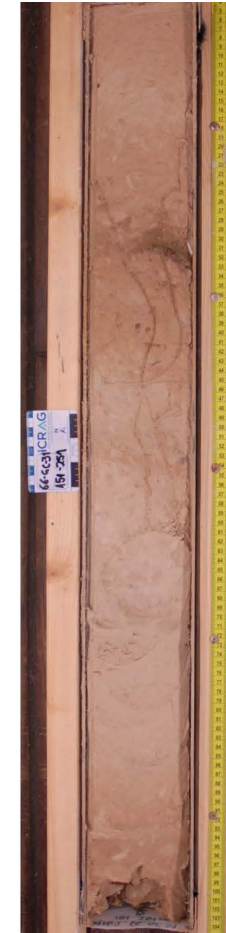
Fig. 12.3.46　　　Core photo of GC-31.
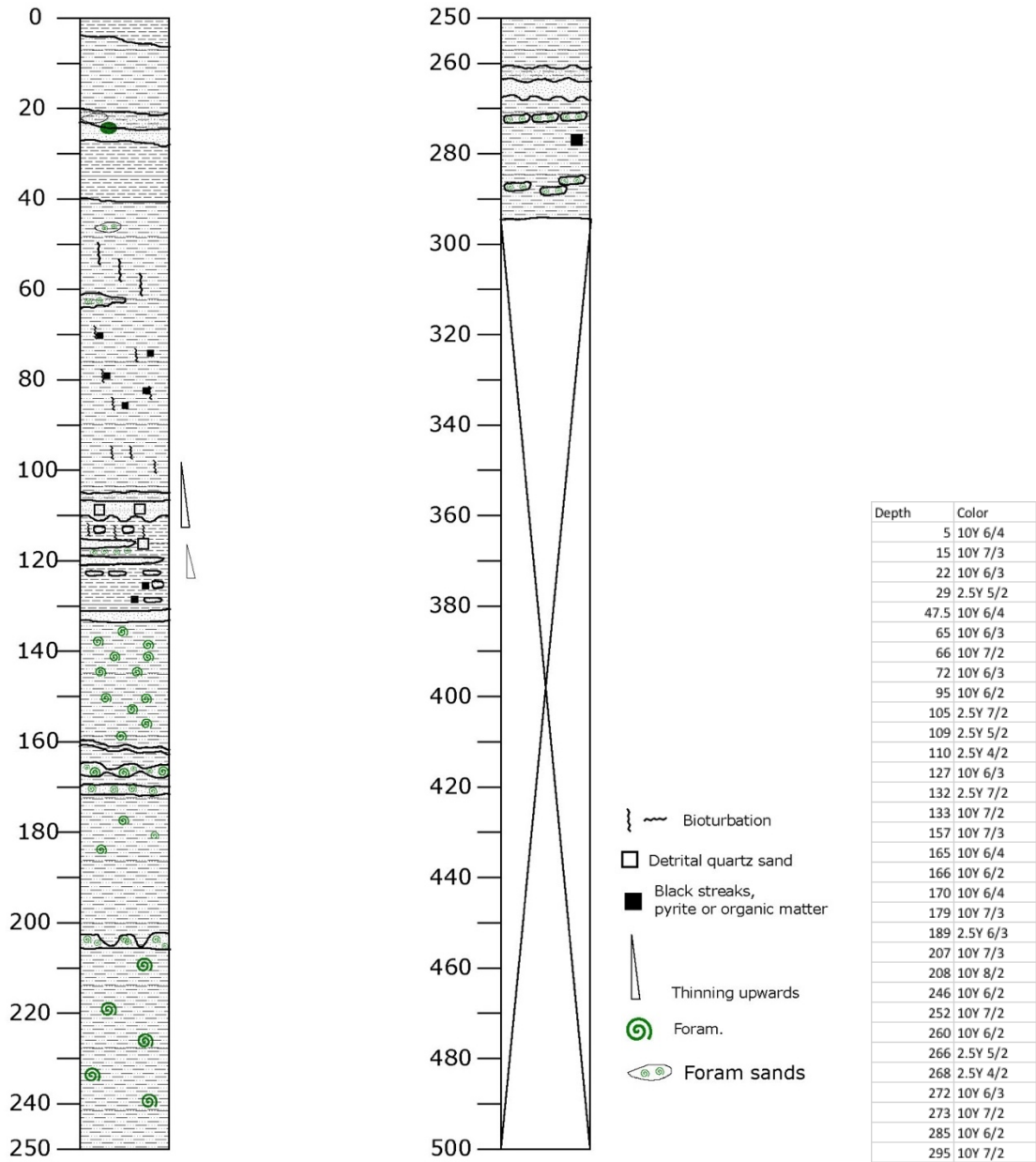
Fig. 12.3.47 Core description GC-32 with Munsell colour code.

67-GC32#1
(0 – 93cm)

67-GC32#2
(93 – 193cm)

67-GC32#3
(193 – 293cm)

Fig. 12.3.48   Core photo of GC-32.
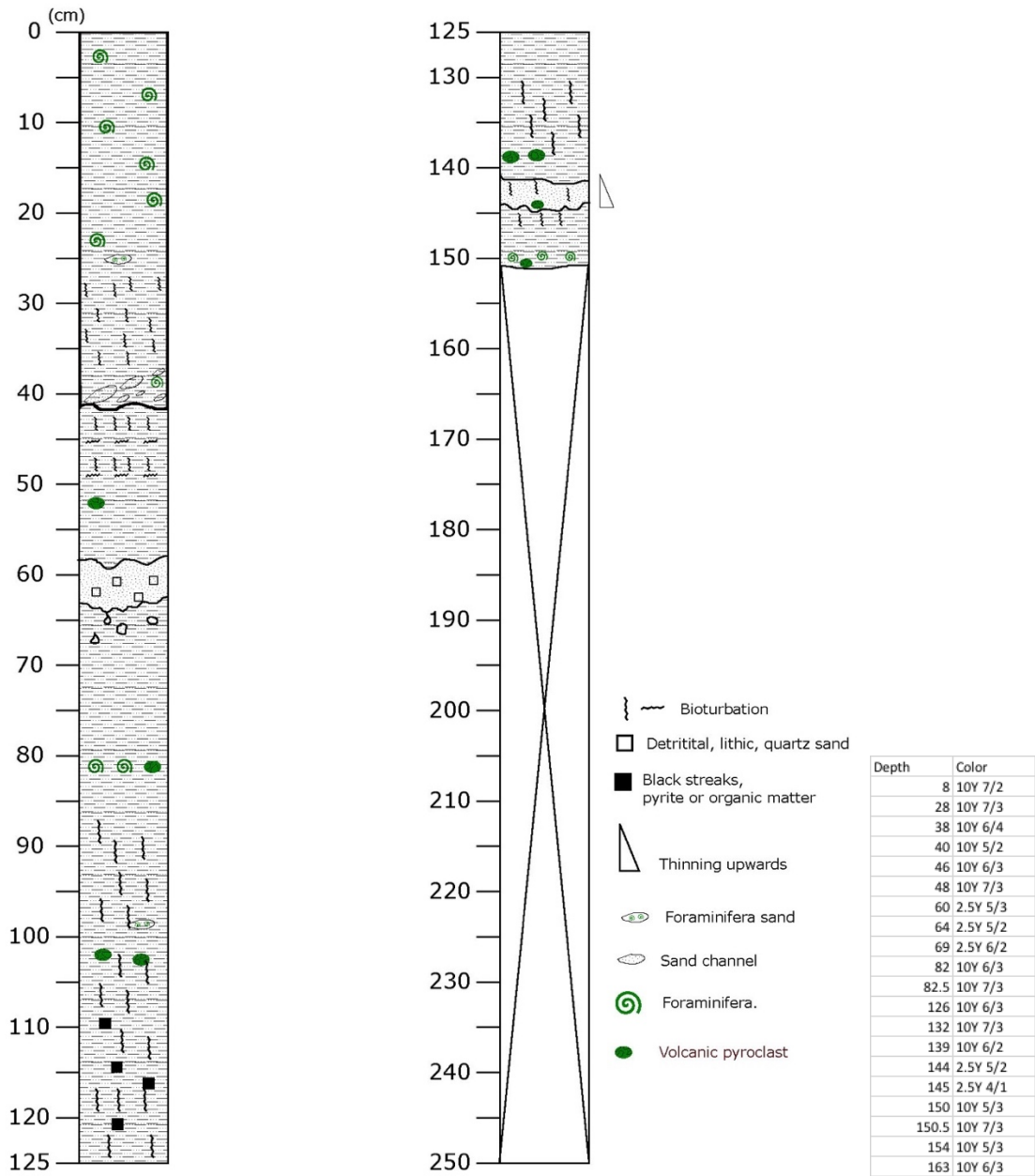
Fig. 12.3.49 Core description GC-33 with Munsell colour code.
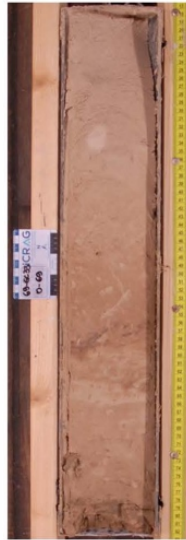
Fig. 12.3.50   Core photo of GC-33.
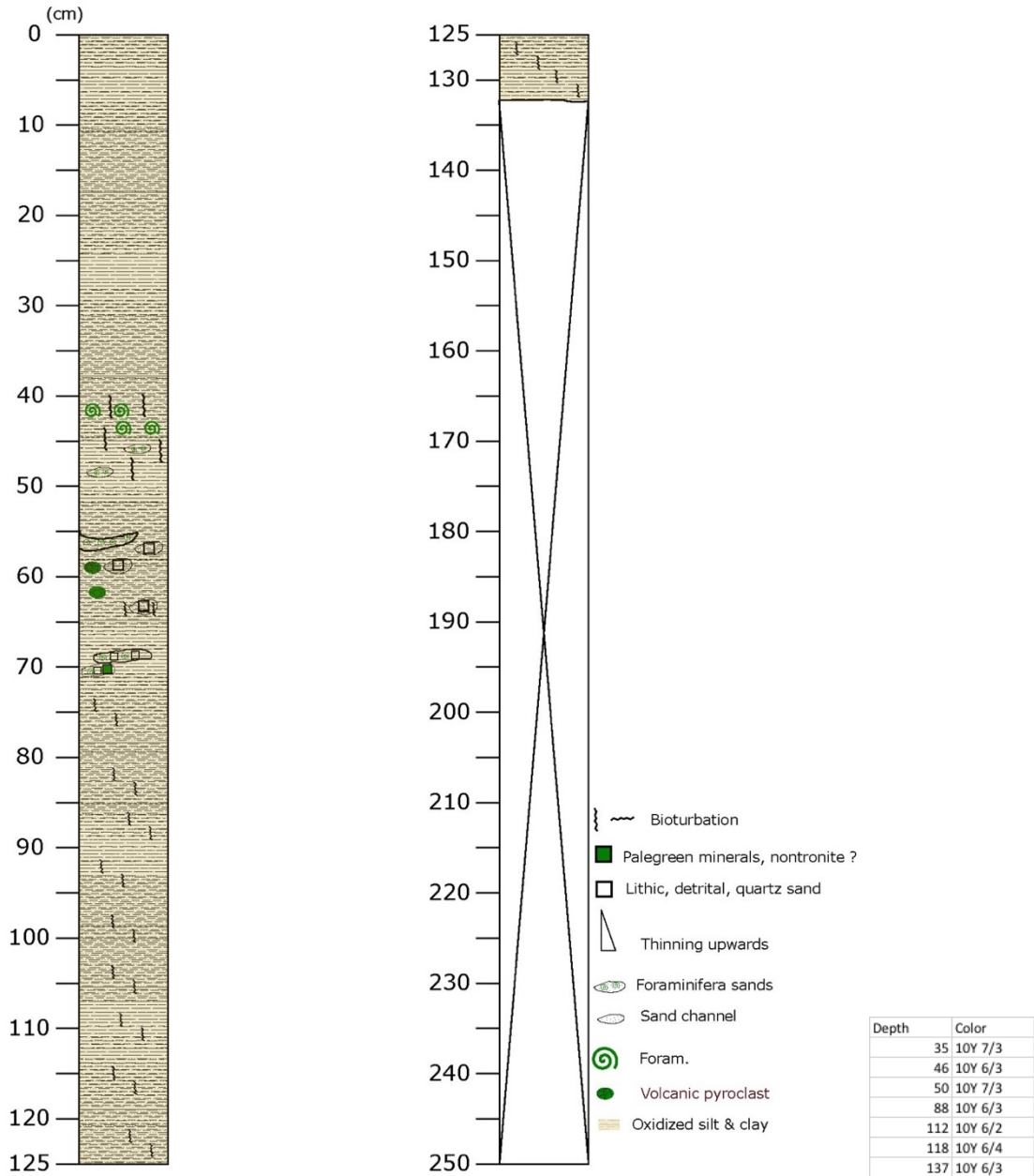
Fig. 12.3.51 Core description GC-34 with Munsell colour code.

70-GC34#1
(0 – 31cm)
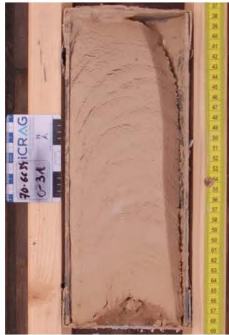
70-GC34#2
(31 – 136cm)

Fig. 12.3.52   Core photo of GC-34.

GRAVITY CORE LOG   **M162**

Date: 2020/03/29   Hour: 11h17   Lat: 37º 30.418 N   Lon: 18º 39.291 W
Station: 72   WA-   GC- 35   Depth: 4810 m

Uncompacted mud slice
Foram.
Volcanic pyroclast

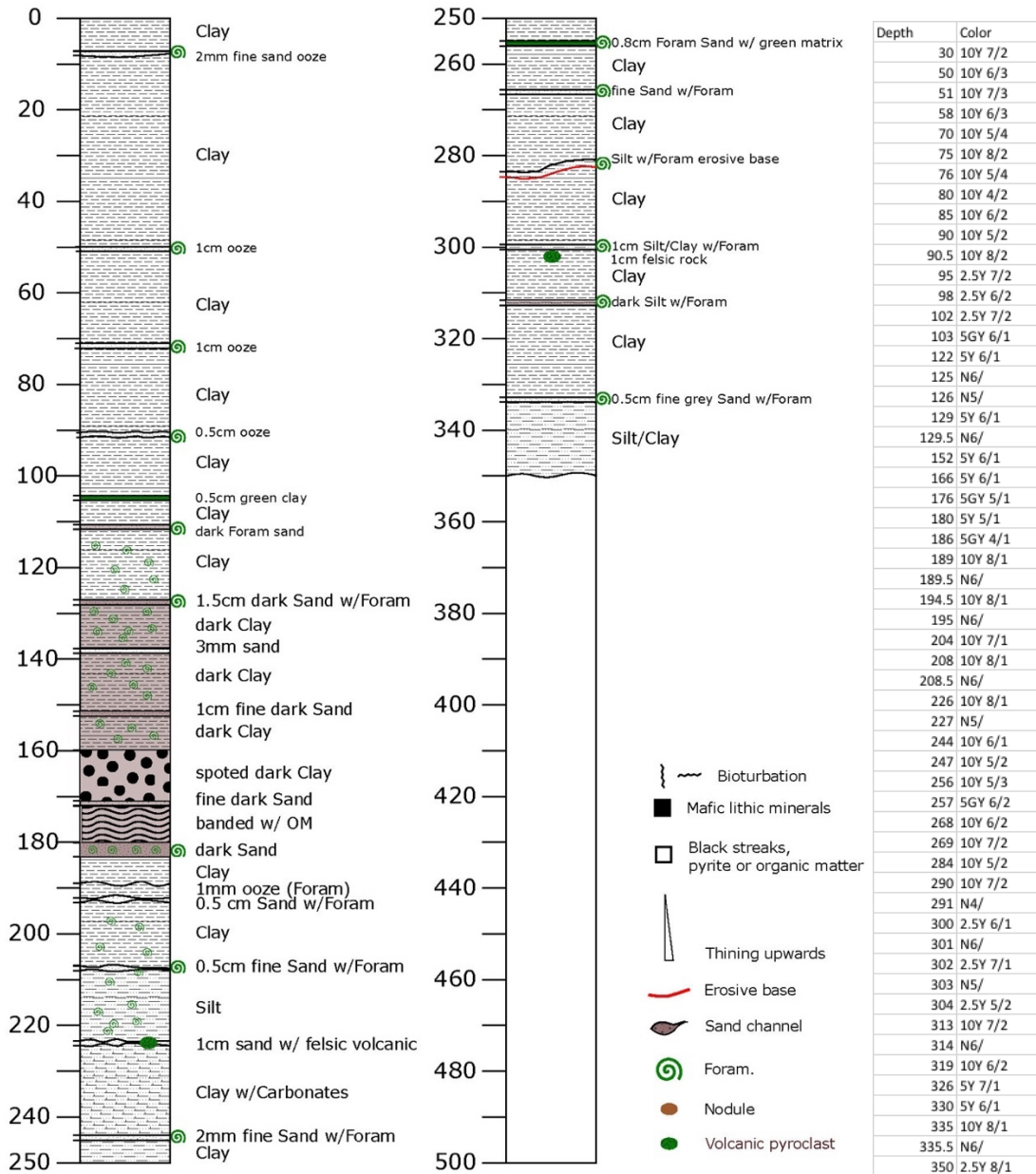| Depth	Color
14	10Y 7/3
23	10Y 6/4
35	10Y 6/3
40	10Y 7/3
50	10Y 6/3
78	10Y 7/3
99	10Y 5/4
112	10Y 7/3
129	10Y 7/2
144	10Y 6/3
150	10Y 6/2
157	10Y 6/3
193	10Y 6/2
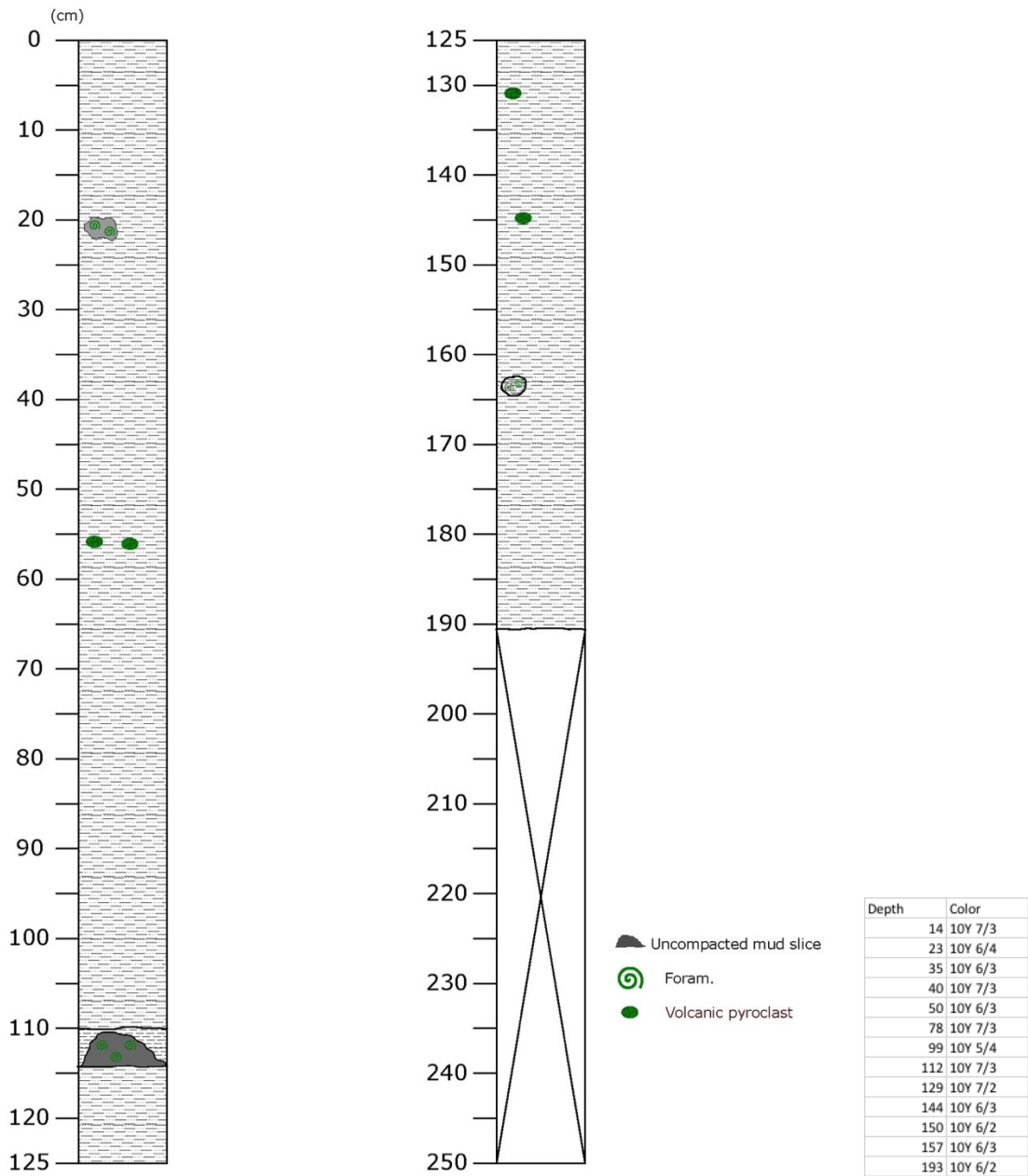
Fig. 12.3.53 Core description GC-35 with Munsell colour code.

72-GC35#1
(0 – 93cm)

72-GC35#2
(93 – 193cm)

Fig. 12.3.54   Core photo of GC-35.
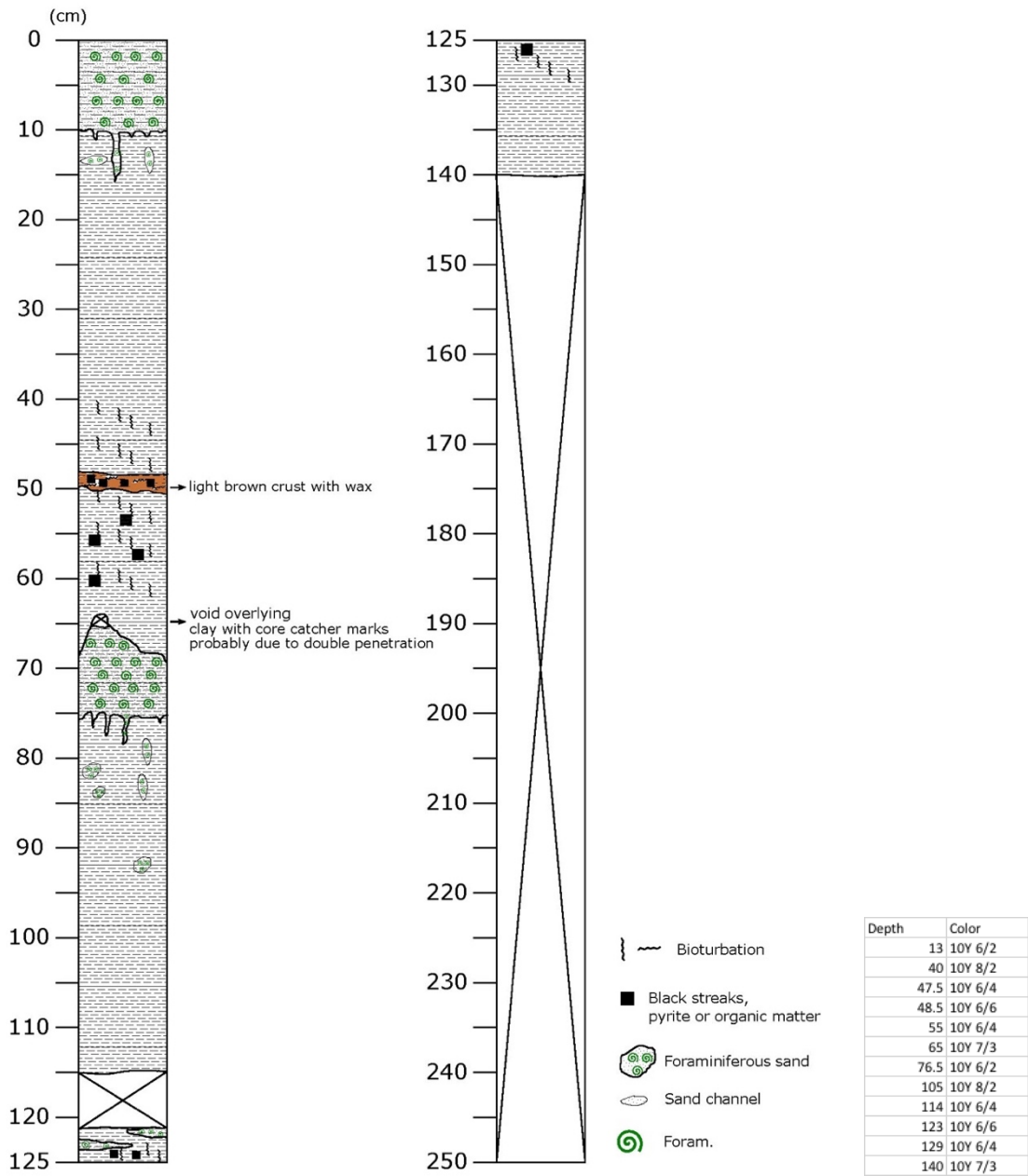
Fig. 12.3.55 Core description GC-37 with Munsell colour code.

77-GC37#1
(0 – 40cm)

77-GC37#2
(40 – 140cm)

Fig. 12.3.56   Core photo of GC-37.
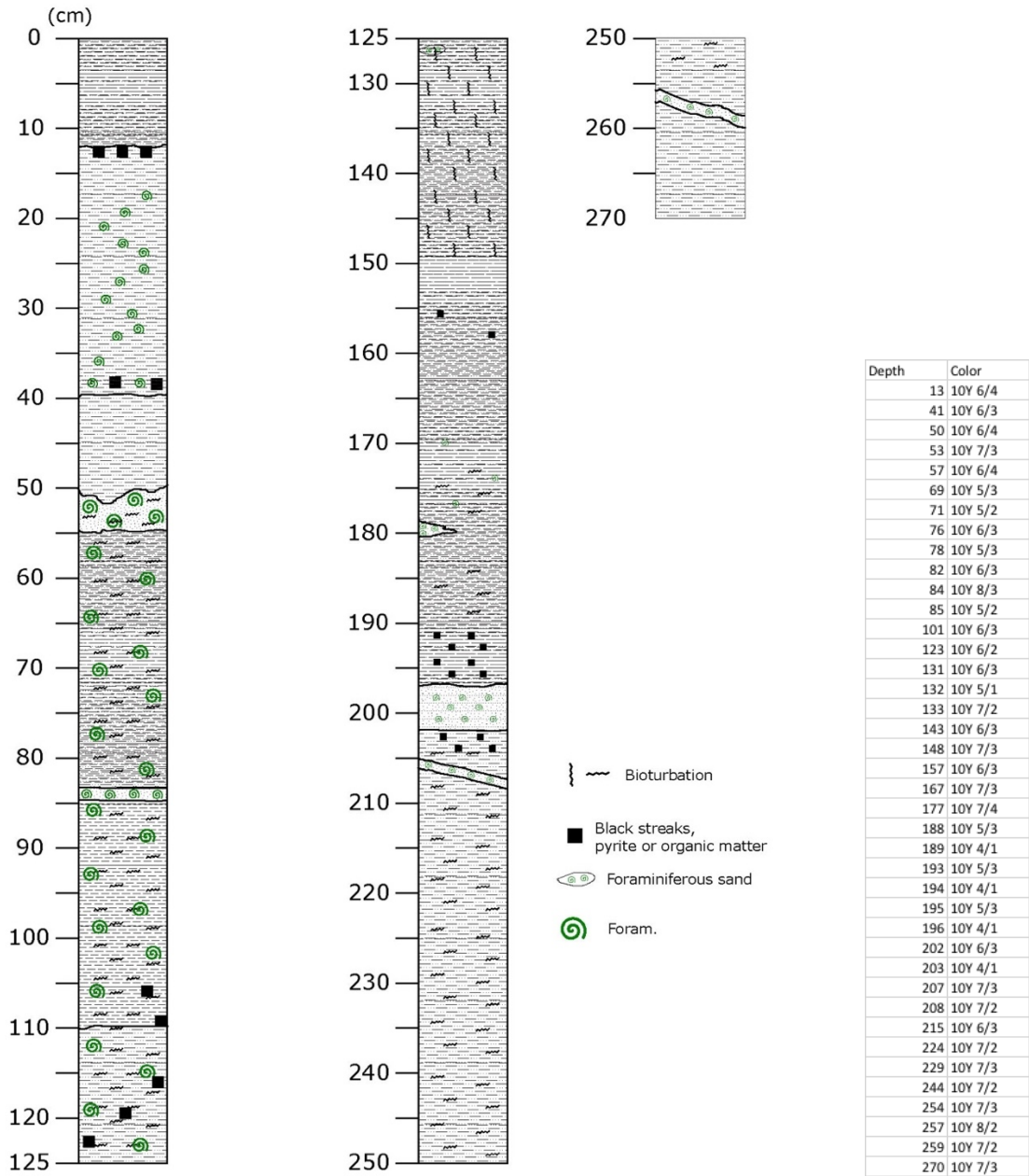
Fig. 12.3.57 Core description GC-38 with Munsell colour code.

78-GC38#1
(0 – 70cm)

78-GC38#2
(70 – 170cm)

78-GC38#3
(170 – 270cm)

Fig. 12.3.58   Core photo of GC-38.
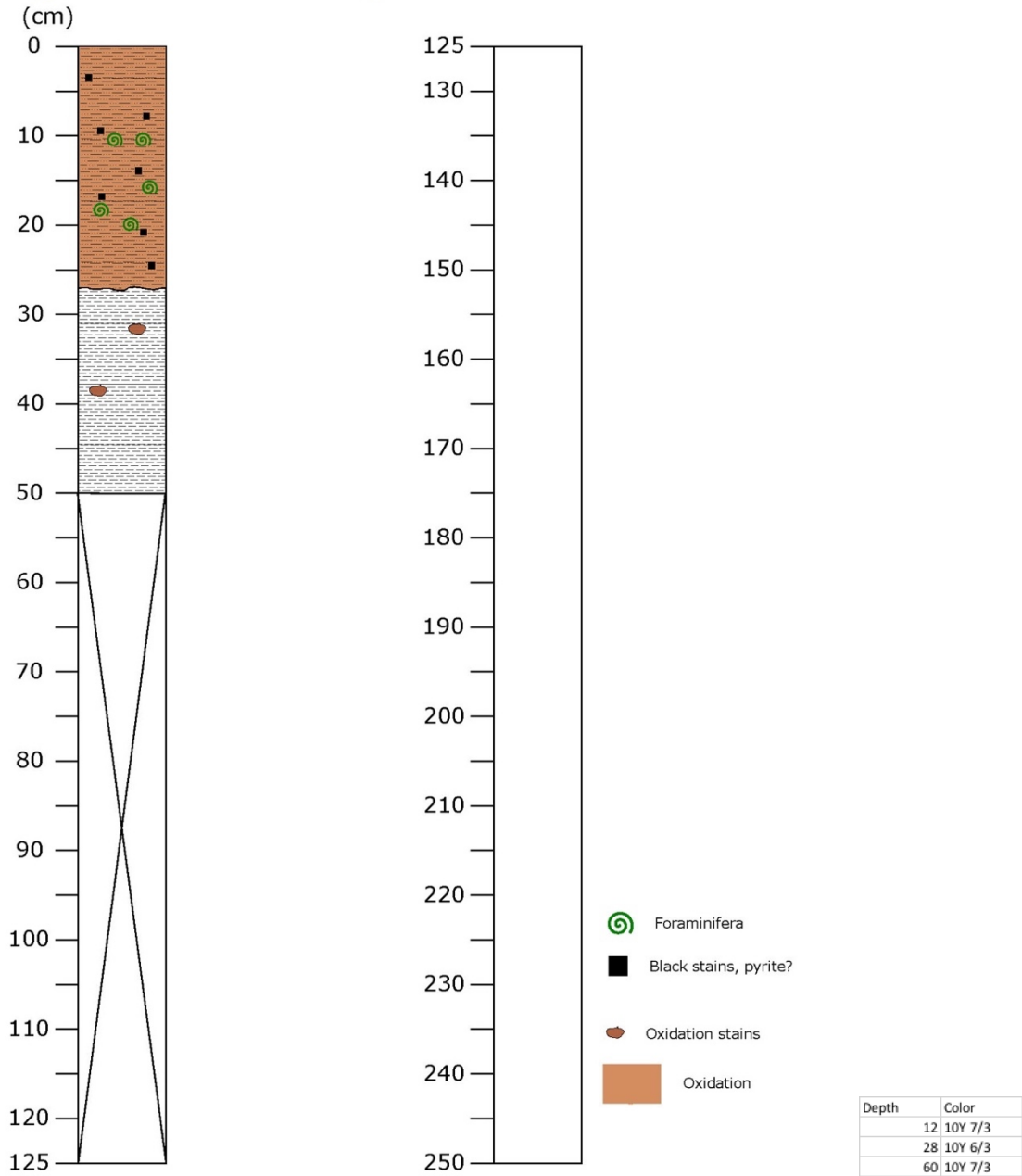
Fig. 12.3.59 Core description GC-39 with Munsell colour code.
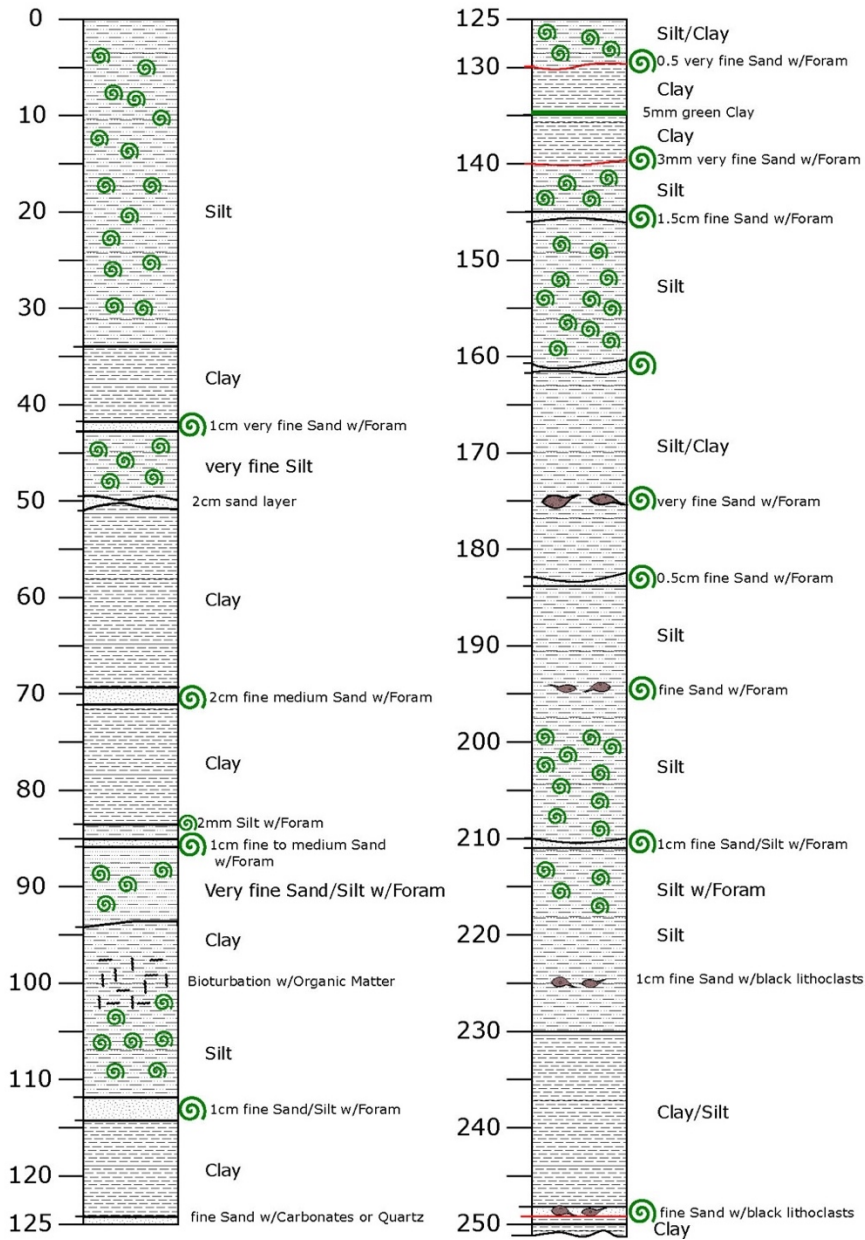
80-GC39#1
(10 – 60cm)

Fig. 12.3.60   Core photo of GC-39.

GRAVITY CORE LOG   **M162**

Date: 2020/04/01 Hour: 14h14 Lat: 37º 23.173 N   Lon: 21º 15.814 W
Station: 82   WA- 5   GC- 40   Depth: 5055 m

Depth	Color
34	10Y 6/3
50	10Y 6/4
57	10Y 6/3
59	10Y 5/3
63	10Y 5/4
66	10Y 6/2
72	10Y 6/4
75	10Y 7/3
110	10Y 6/4
116	10Y 5/4
138	10Y 6/4
141	10Y 6/3
143	10Y 7/3
154	10Y 6/3
162	10Y 4/4
164	10Y 5/2
166	10Y 5/6
170	10Y 4/4
171	10Y 5/4
173	10Y 4/4
179	10Y 6/4
181	10Y 5/4
191	10Y 6/3
209	10Y 7/3
215	10Y 6/4
260	10Y 8/3
265	10Y 6/3
298	10Y 8/3
302	10Y 7/3
303	10Y 8/3
305	10Y 7/3
307	10Y 8/3
326	10Y 6/3
330	10Y 8/3
333	2.5Y 5/2
333.5	10Y 8/3
338.5	2.5Y 6/2
344	10Y 6/3
353	2.5Y 5/2
358	10Y 6/3
359	10Y 6/3
361	2.5Y 5/2
363	10Y 6/3
365	2.5Y 5/2
384	10Y 5/3
394	10Y 6/3
401	10Y 5/3
404	10Y 6/3
408	10Y 5/3
413	10Y 6/3
414	10Y 8/3
422	10Y 7/3
432	10Y 6/3
435	10Y 6/4
435.5	10Y 7/3
438	10Y 6/4
439	10Y 6/2
455.5	10Y 6/3
457	10Y 6/2
461	10Y 6/3
463	10Y 7/3
465	10Y 6/2
470	10Y 6/3
478	10Y 5/3
490	10Y 7/3

Legend:
} ～ Bioturbation
▬ Black streaks, pyrite or organic matter
△ Thinning upwards
◌ Foraminifera sands
◉ Foraminifera

Fig. 12.3.61 Core description GC-40 with Munsell colour code.

Fig. 12.3.62 Core photo of GC-40.
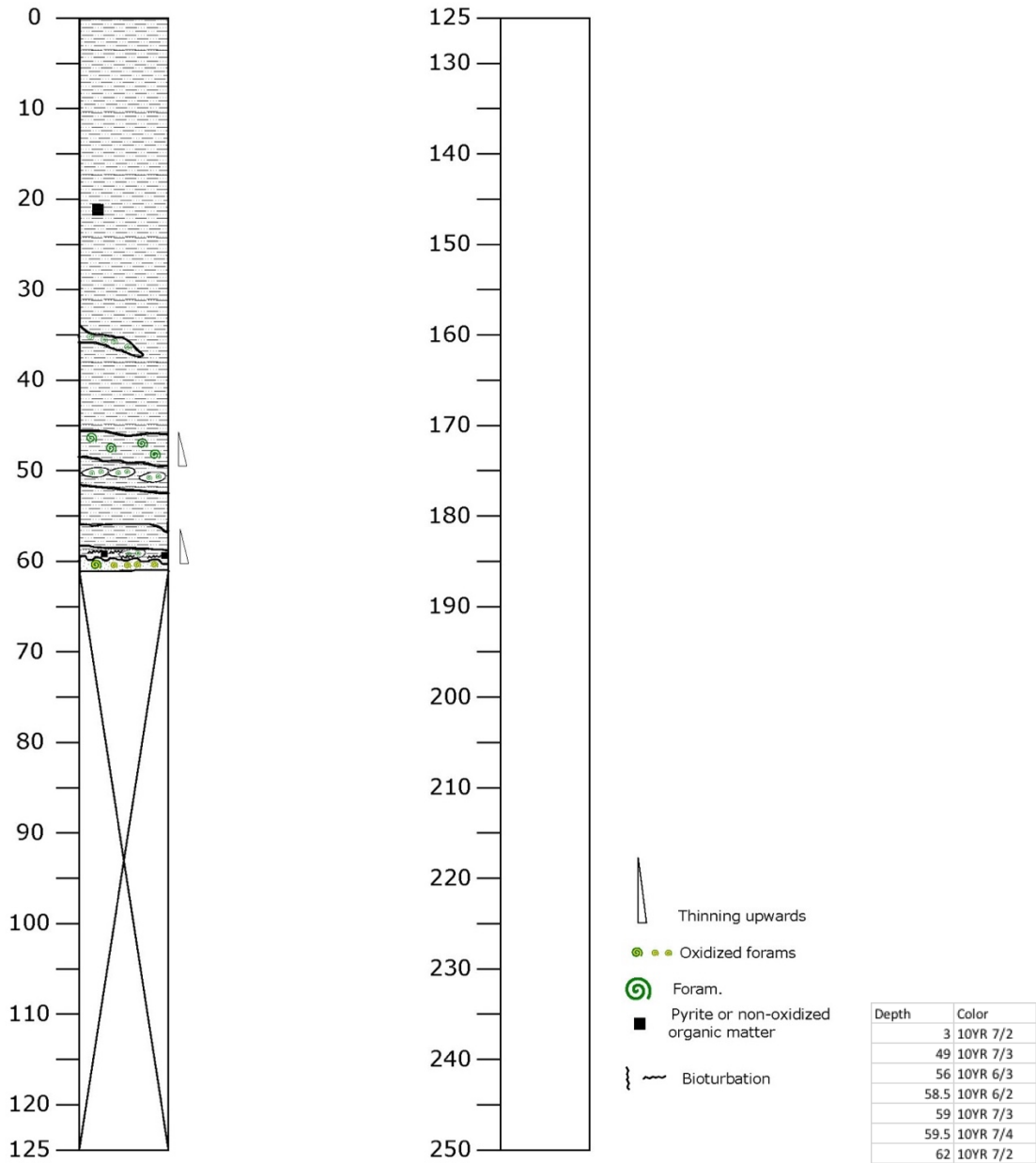
Fig. 12.3.63 Core description GC-41 with Munsell colour code.

88-GC41#1
(7 – 62cm)

Fig. 12.3.64   Core photo of GC-41.
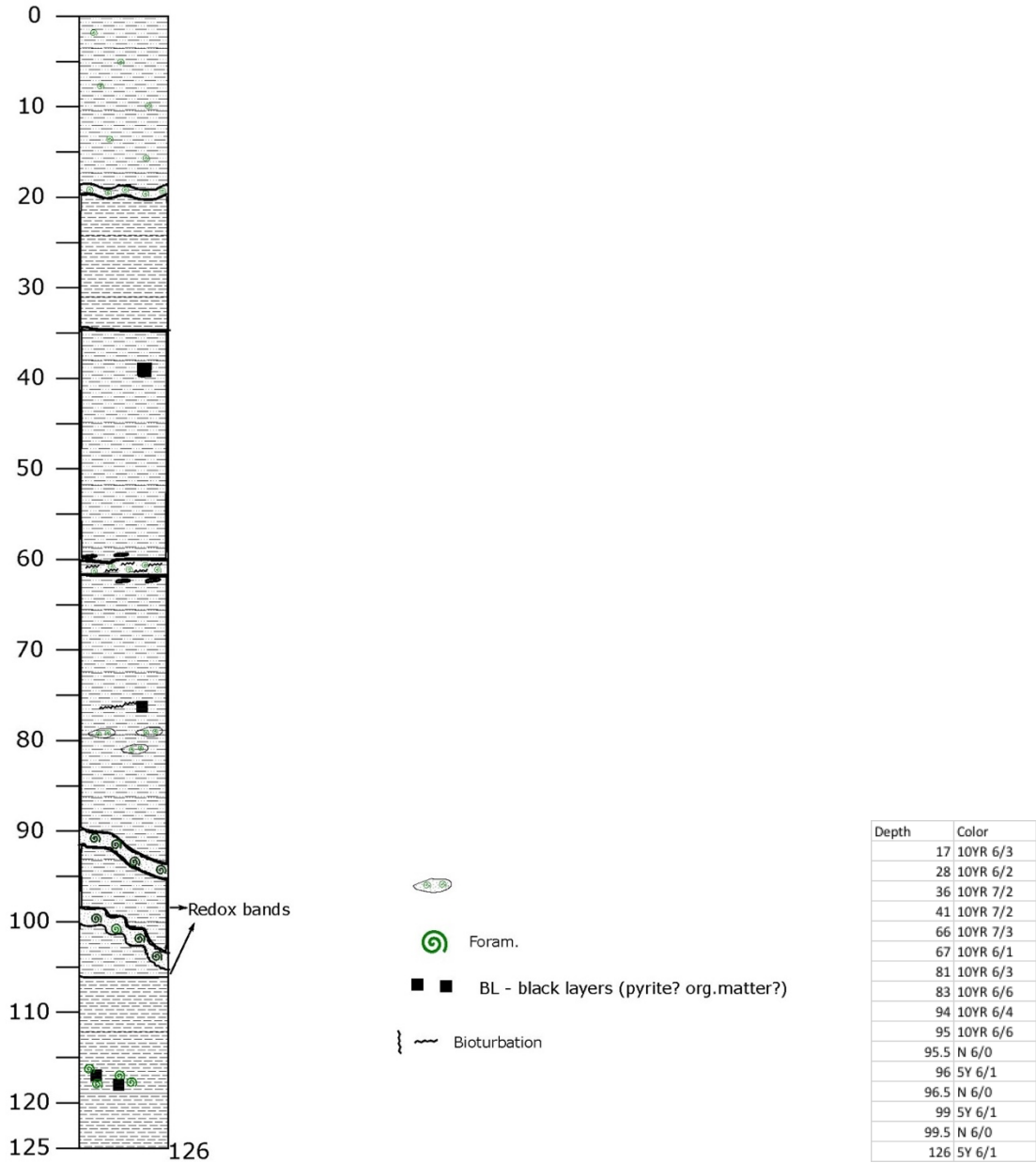
Fig. 12.3.65 Core description GC-42 with Munsell colour code.
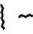
Fig. 12.3.66   Core photo of GC-42.

GRAVITY CORE LOG   **M162**

Date: 2020/04/03 Hour: 09h27 Lat: 37º 14.755 N   Lon: 14º 55.967 W
Station: 91   WA- 5 GC- 43   Depth: 3547 m

Depth	Color
12	10YR 7/3
16	10YR 6/2
21	10YR 7/3
50	10YR 7/2
61	10YR 7/3
73	10YR 6/3
75	10YR 6/4
80	2.5Y 7/4
84	2.5Y 7/2
84.5	2.5Y 6/4
90	2.5Y 7/4
91.5	N 6/0
93.5	5GY 6/1
94	N 6/0
126	5Y 6/1
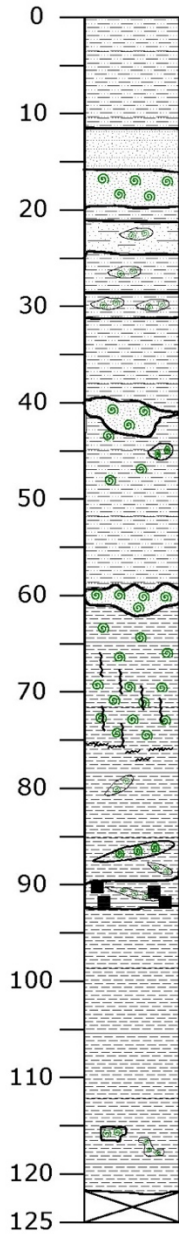
Foram sand nodule

Bioturbation

Black streaks, pyrite or organic matter

Foram.

Fig. 12.3.67 Core description GC-43 with Munsell colour code.

91-GC43#1
(0 – 100cm)

91-GC43#2
(100 – 126cm)
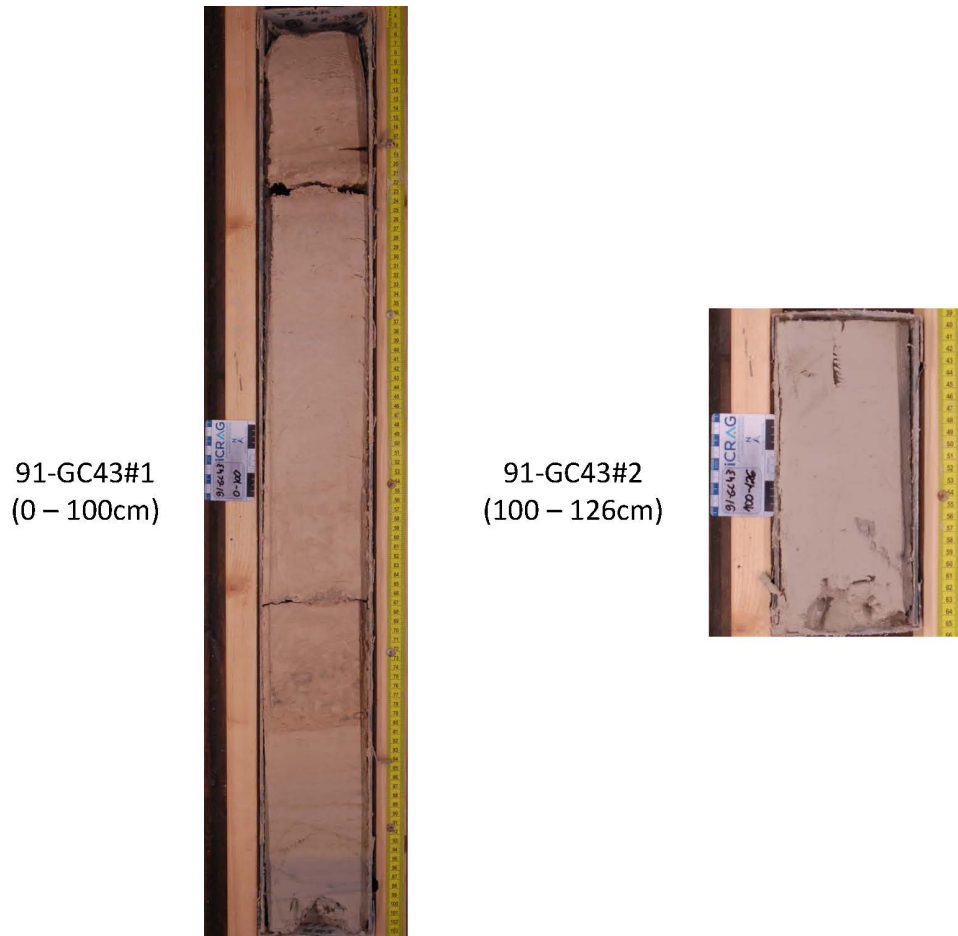
Fig. 12.3.68   Core photo of GC-43.

GRAVITY CORE LOG   **M162**

Date: 2020/04/03 Hour: Lat: 37º 14.753 N   Lon: 14º 55.966 W
Station: 92   WA- 5   GC- 44   Depth: 3547

Depth	Color
27	10YR 6/3
55	10YR 7/2
62	10YR 7/3
63	10YR 5/1
73	10YR 6/3
79	10YR 6/4
87	2.5YR 6/2
91	N6/
115	5YR 6/1
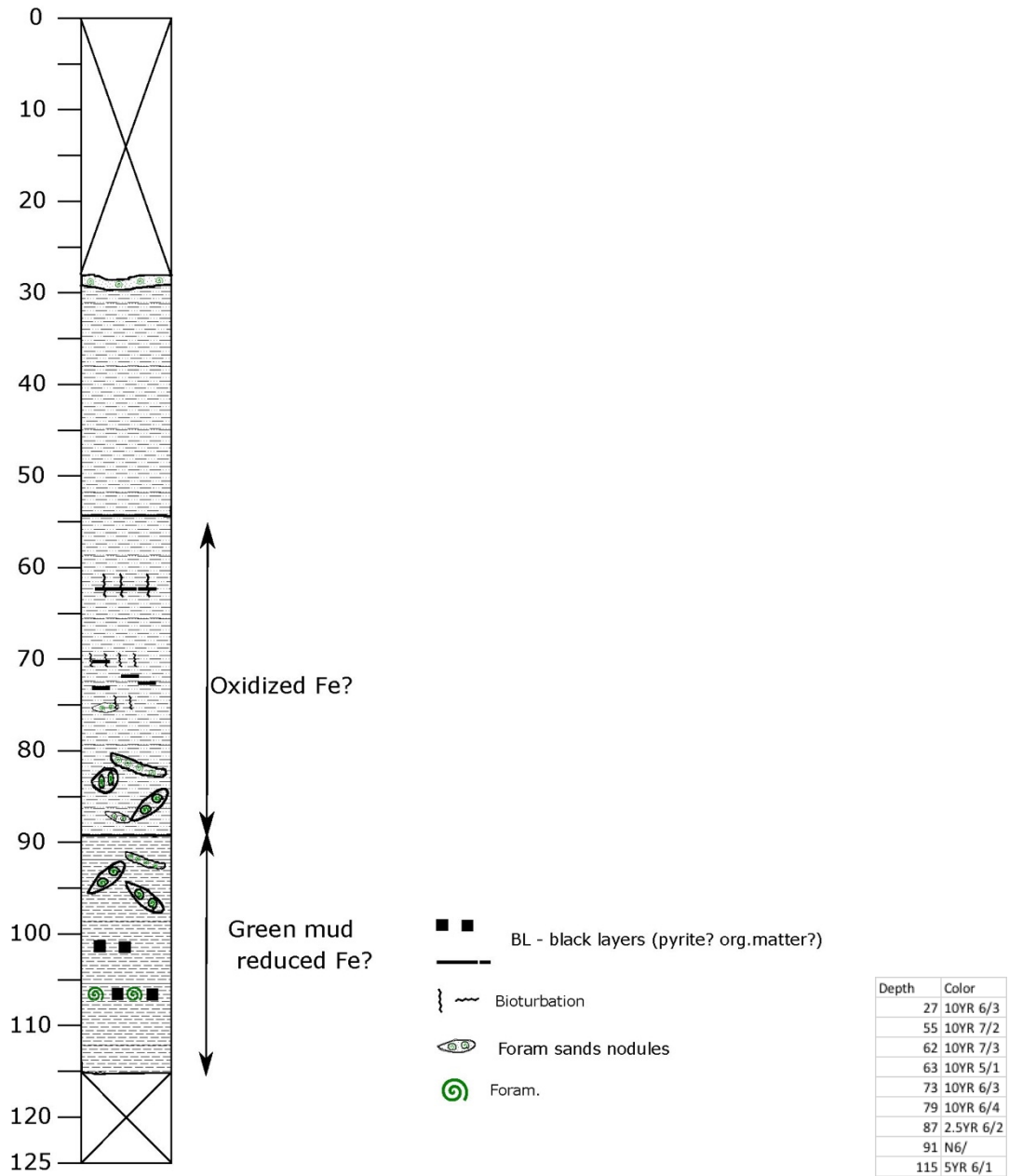
Fig. 12.3.69 Core description GC-44 with Munsell colour code.

92-GC44#1
(0 – 128cm)

Fig. 12.3.70   Core photo of GC-44.
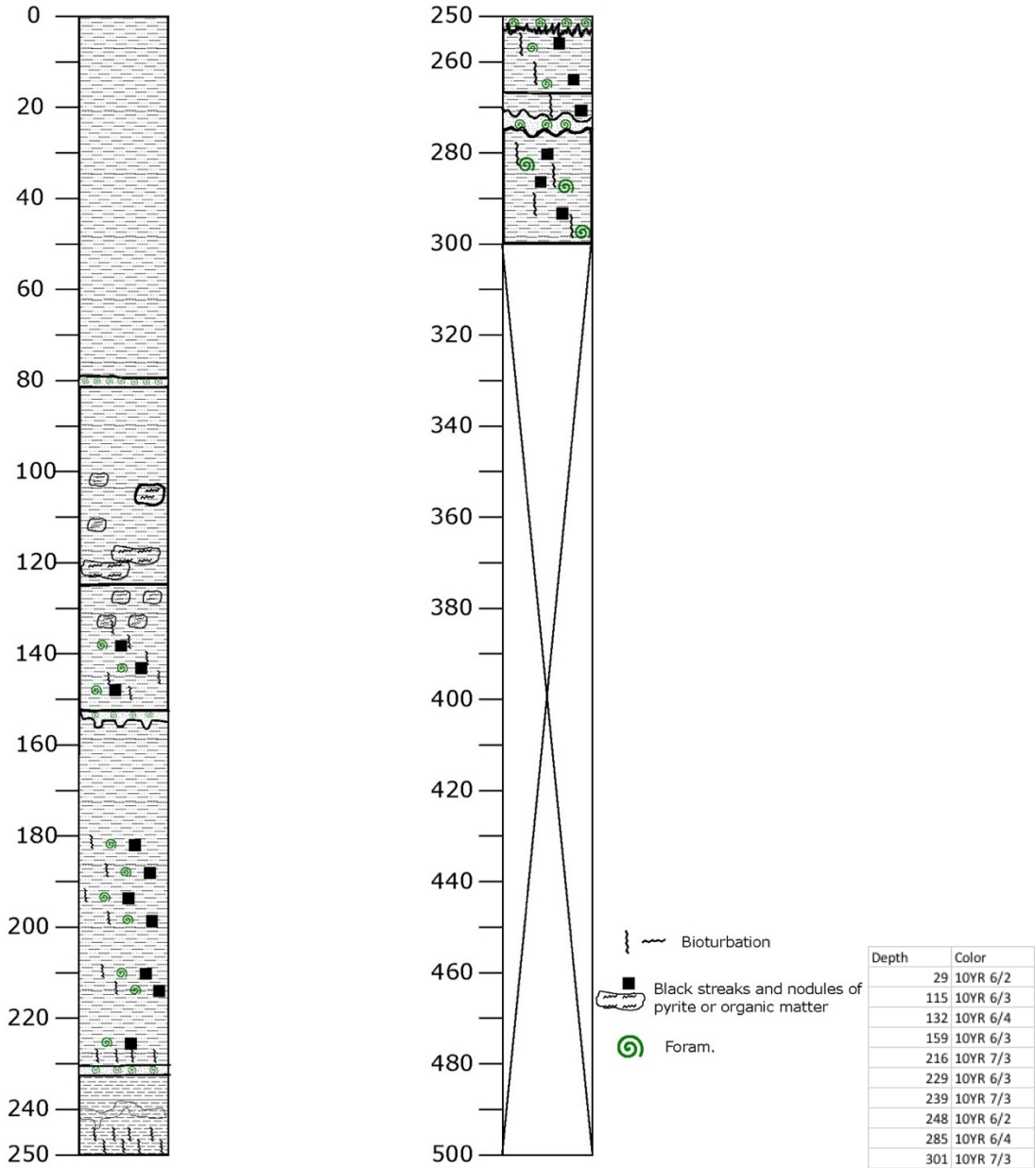
Fig. 12.3.71 Core description GC-45 with Munsell colour code.

94-GC45#1
(0 – 100cm)

94-GC45#2
(100 – 200cm)

94-GC45#3
(200 – 300cm)
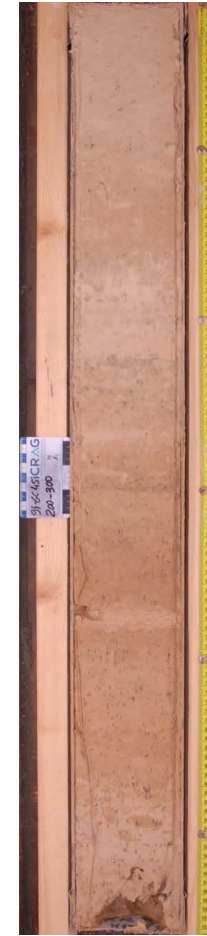
Fig. 12.3.72		Core photo of GC-45.
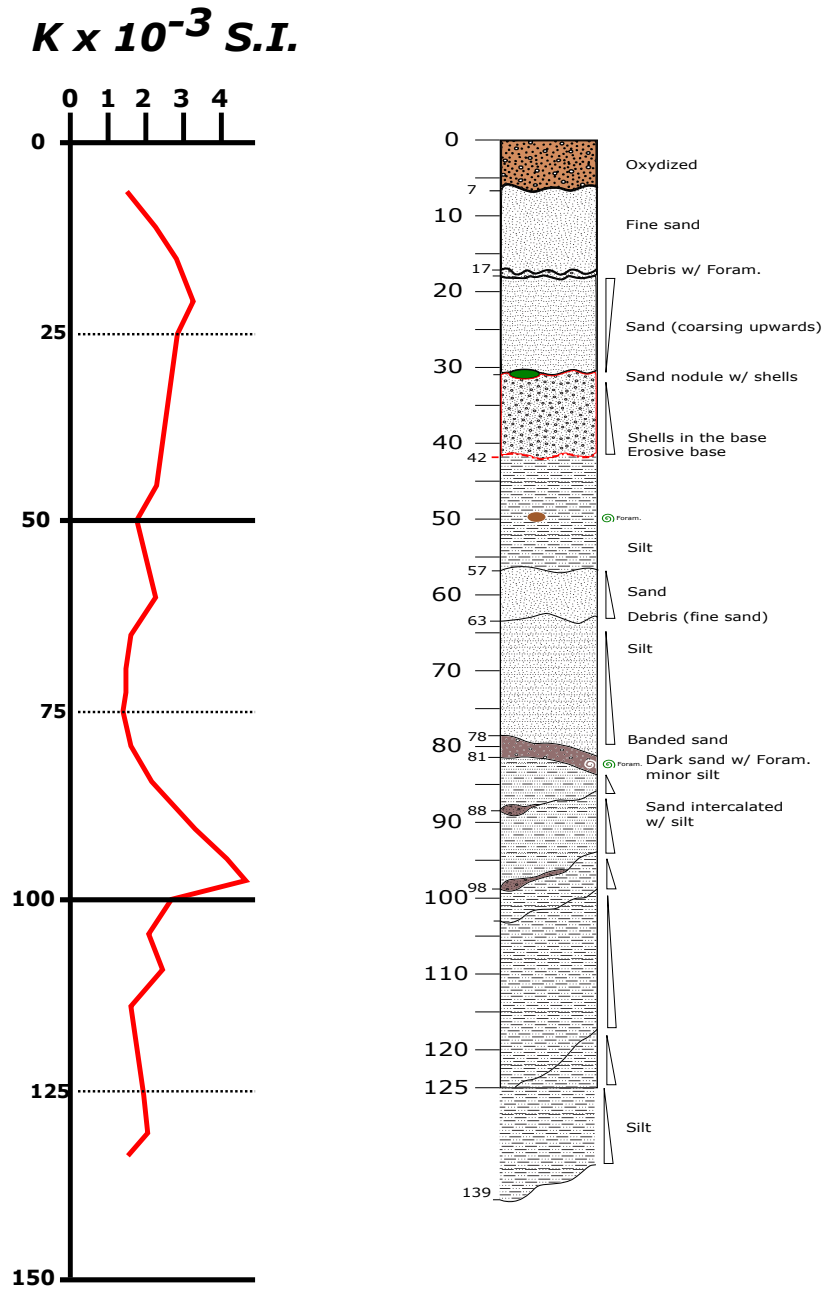
Fig. 12.3.73 Magnetic susceptibility compared with sediment description for GC-1.
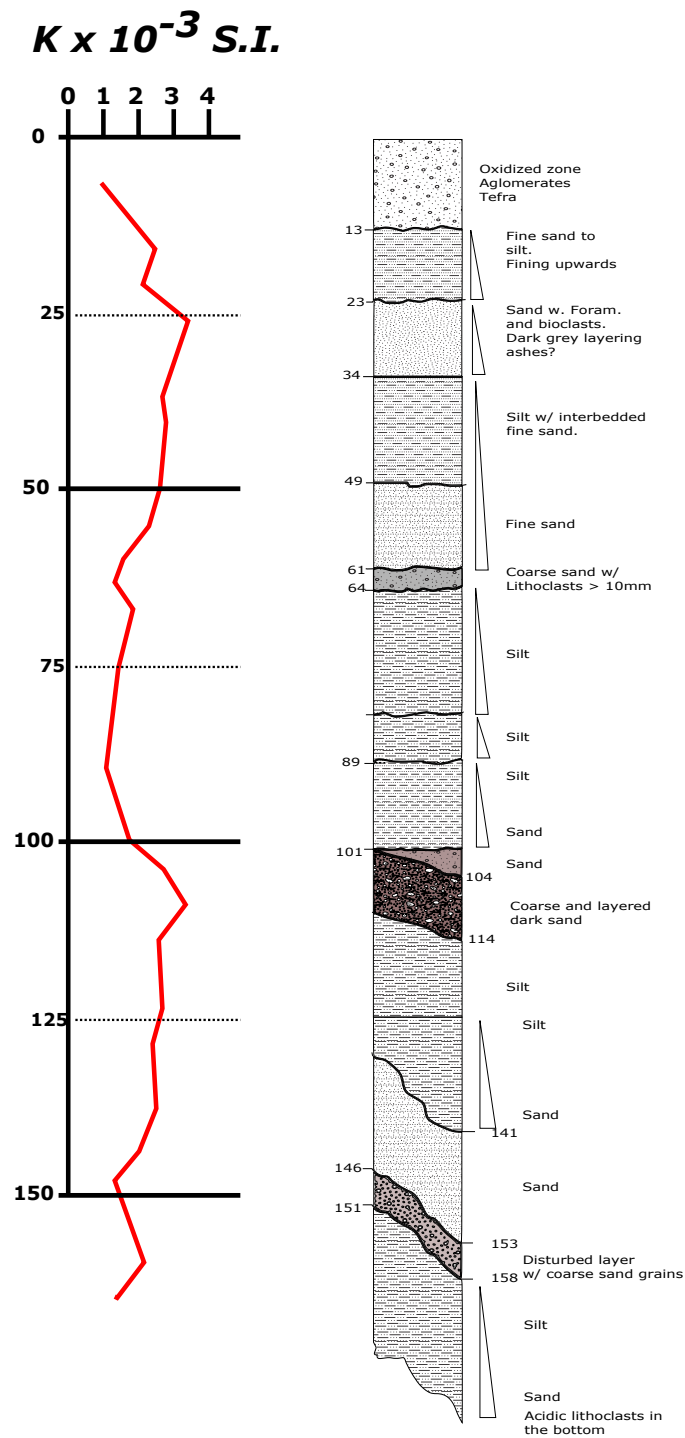
Fig. 12.3.74 Magnetic susceptibility compared with sediment description for GC-2.
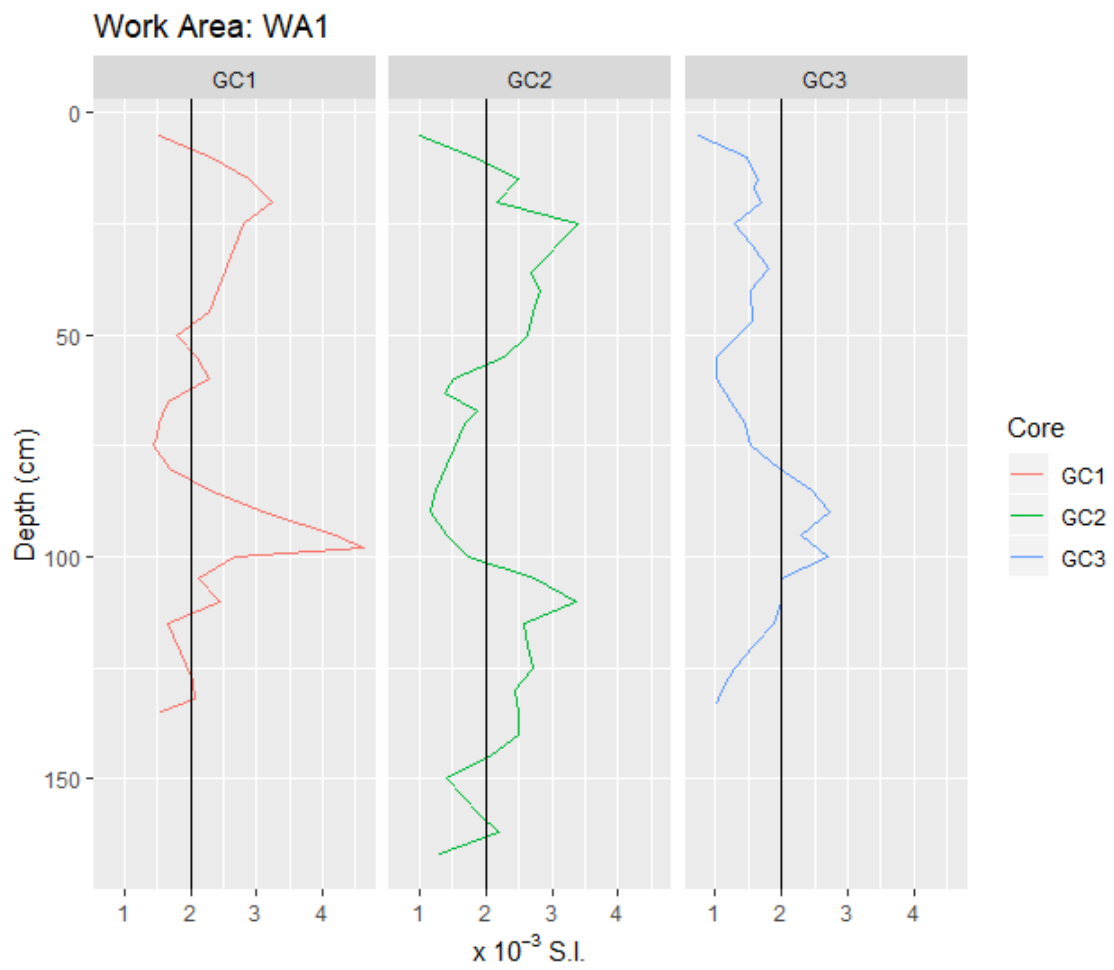
Fig. 12.3.75 Magnetic susceptibility for WA1. Intercept line at 2×10^{-3} S.I.
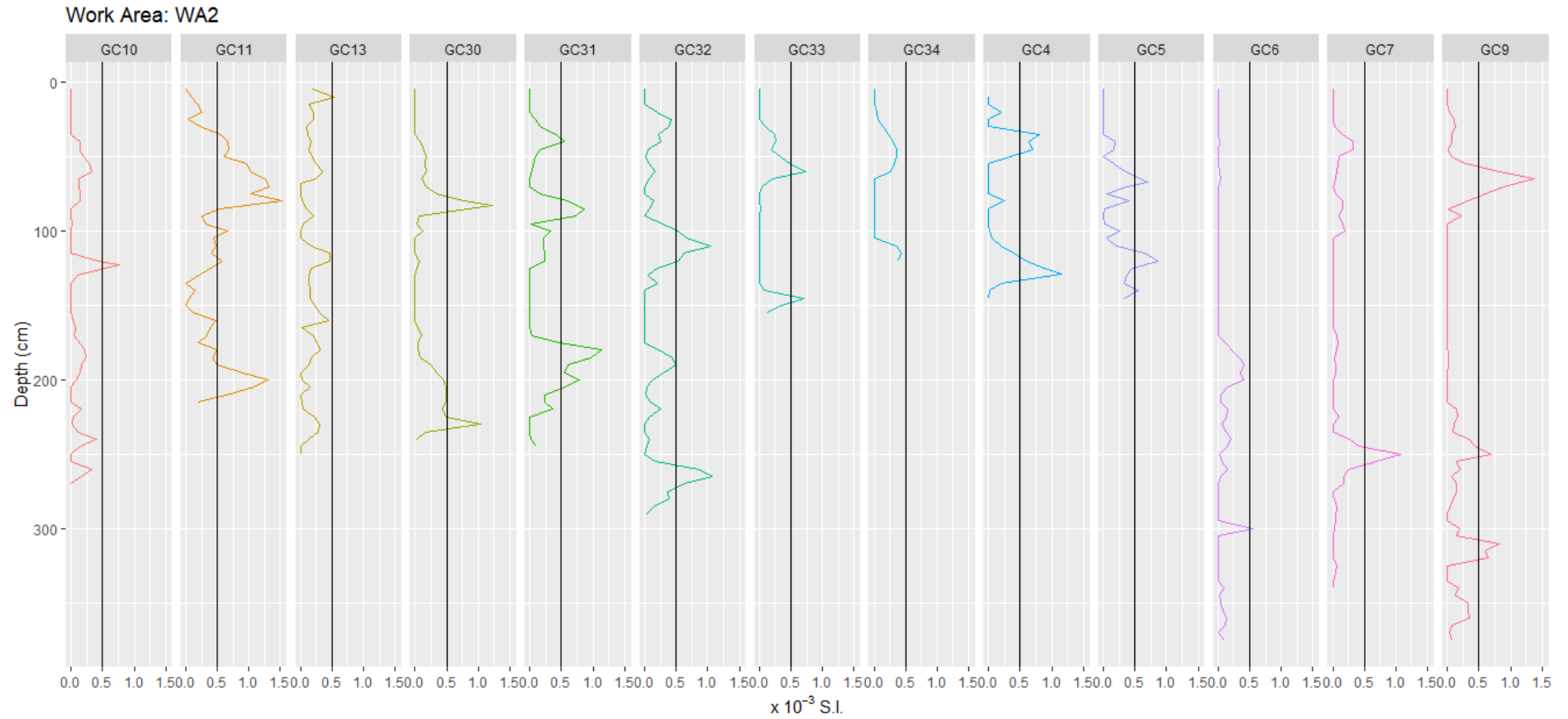
Fig. 12.3.76   Magnetic susceptibility for WA2. Intercept line at 0.5×10^{-3} S.I.
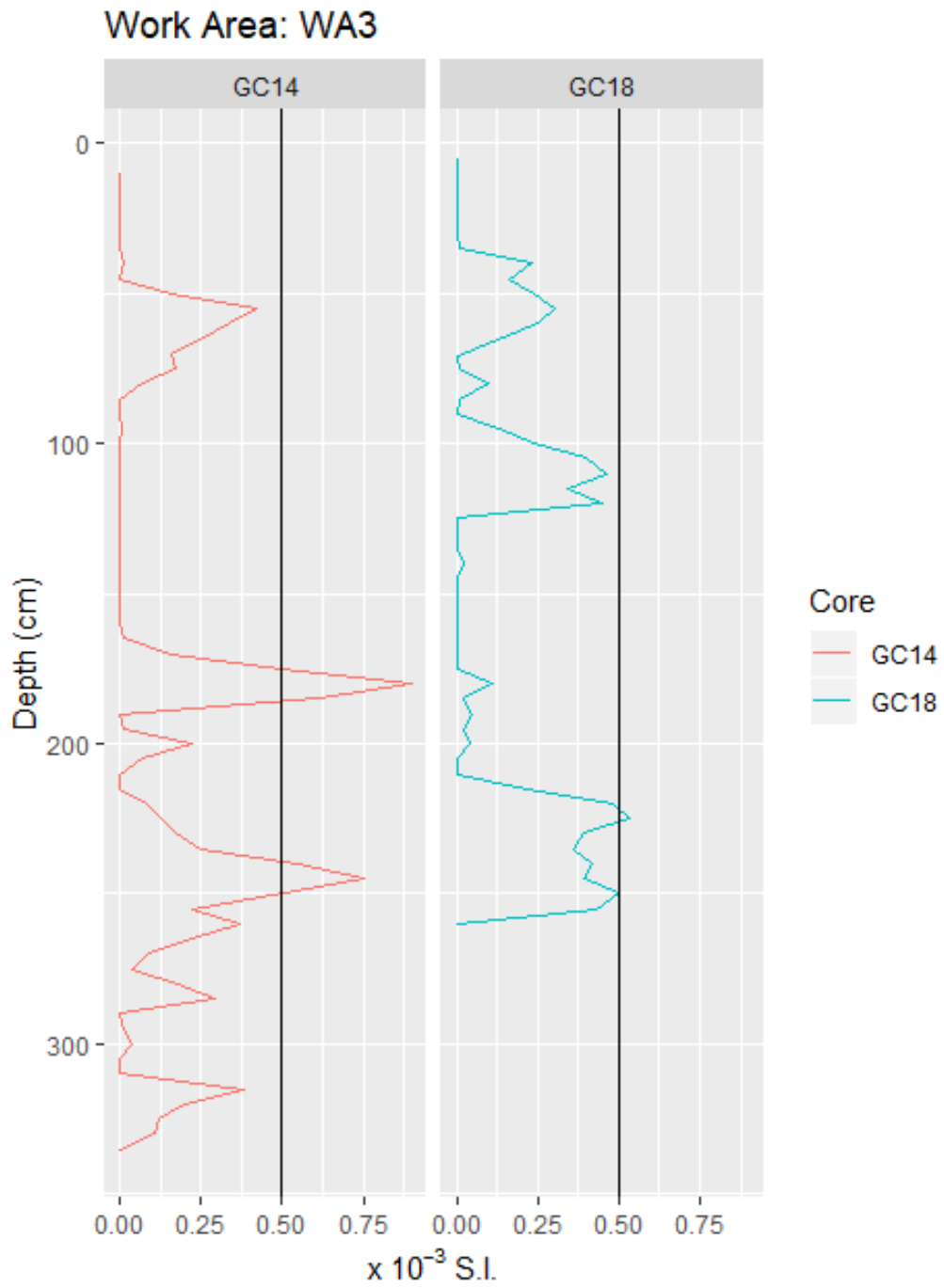
Fig. 12.3.77 Magnetic susceptibility for WA3. Intercept line at 0.5×10^{-3} S.I.
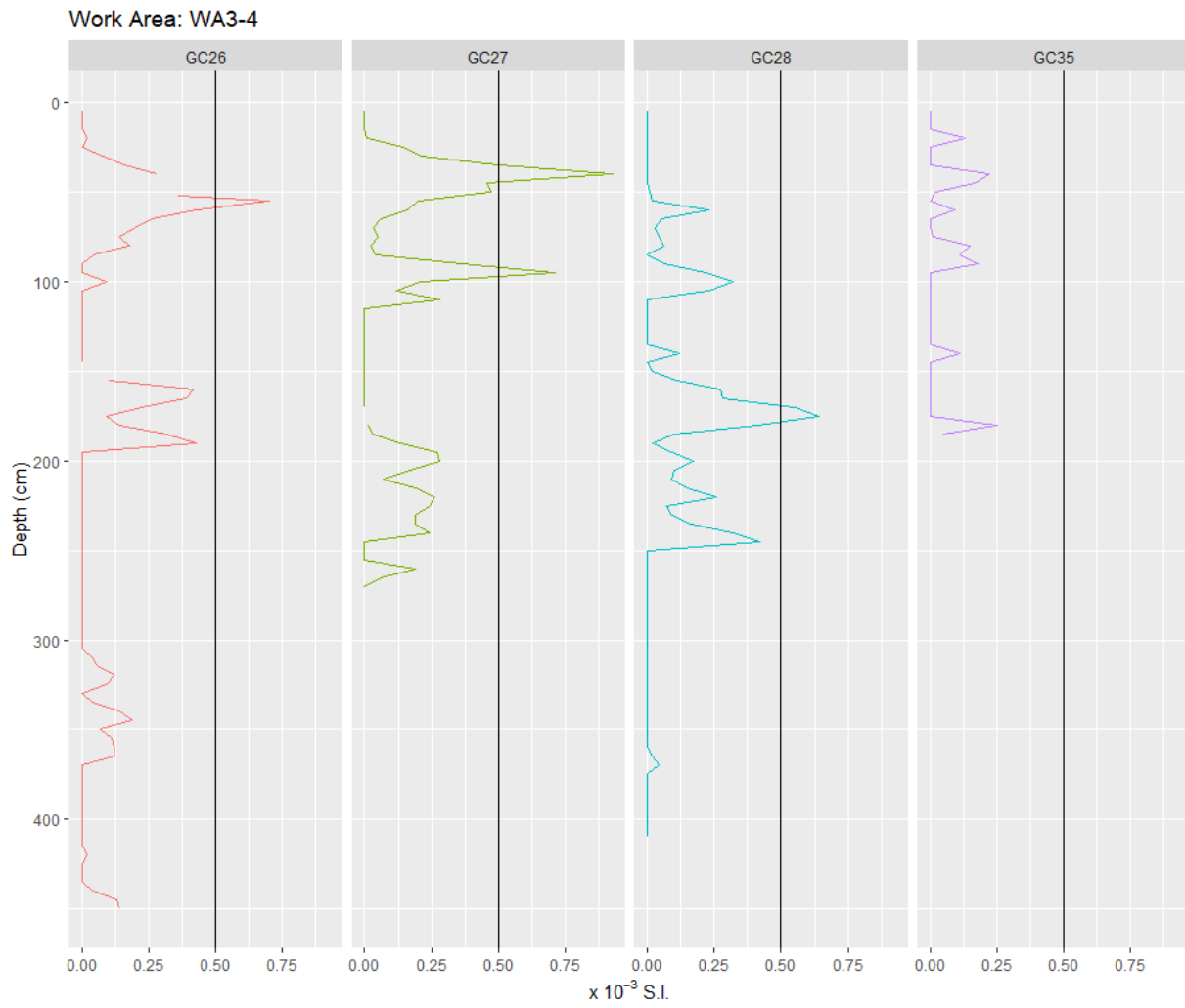
Fig. 12.3.78 Magnetic susceptibility for WA3-4. Intercept line at 0.5×10^{-3} S.I.
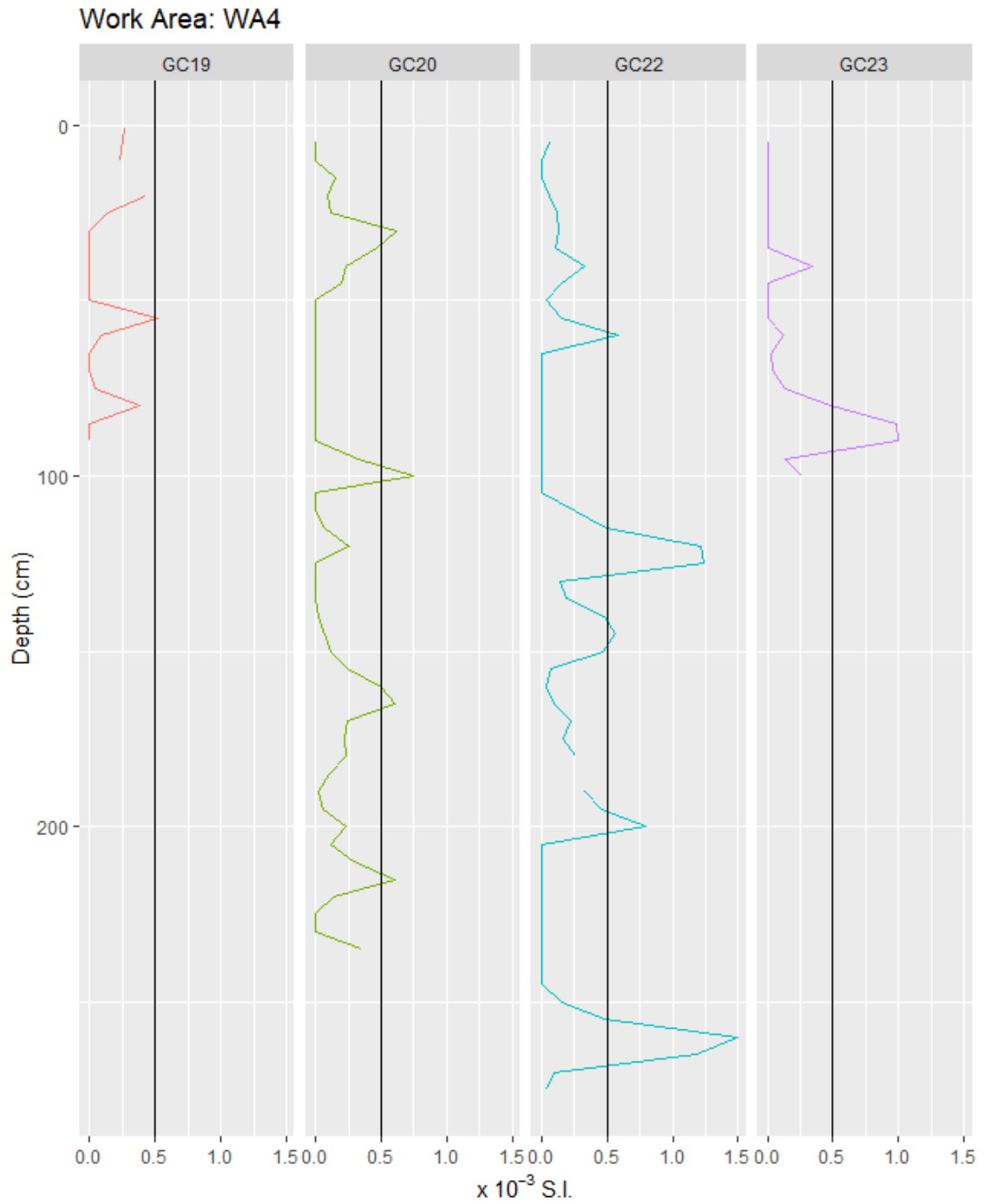
Fig. 12.3.79   Magnetic susceptibility for WA4. Intercept line at 0.5×10^{-3} S.I.
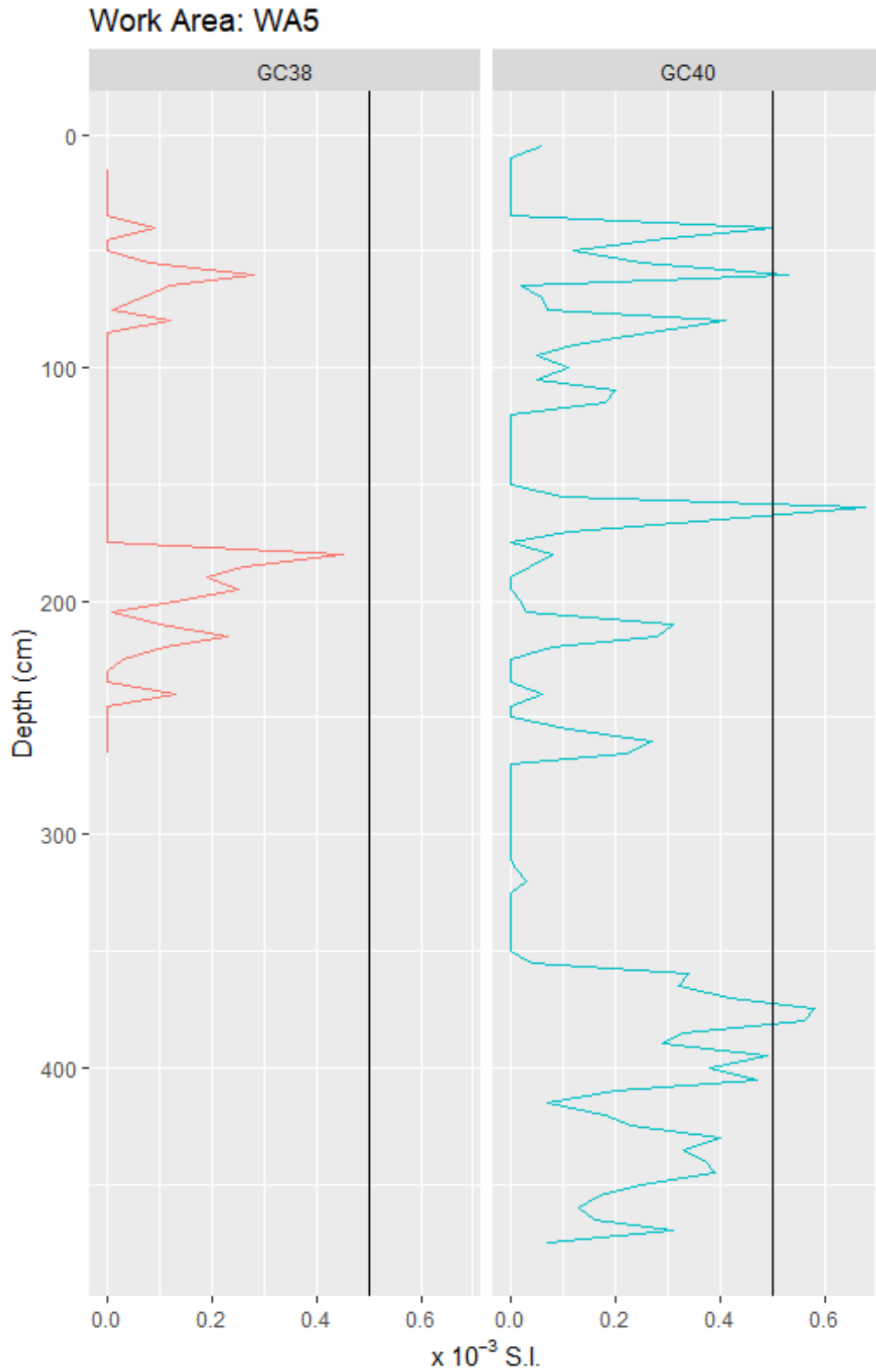
Fig. 12.3.80   Magnetic susceptibility for WA5. Intercept line at 0.5×10^{-3} S.I.
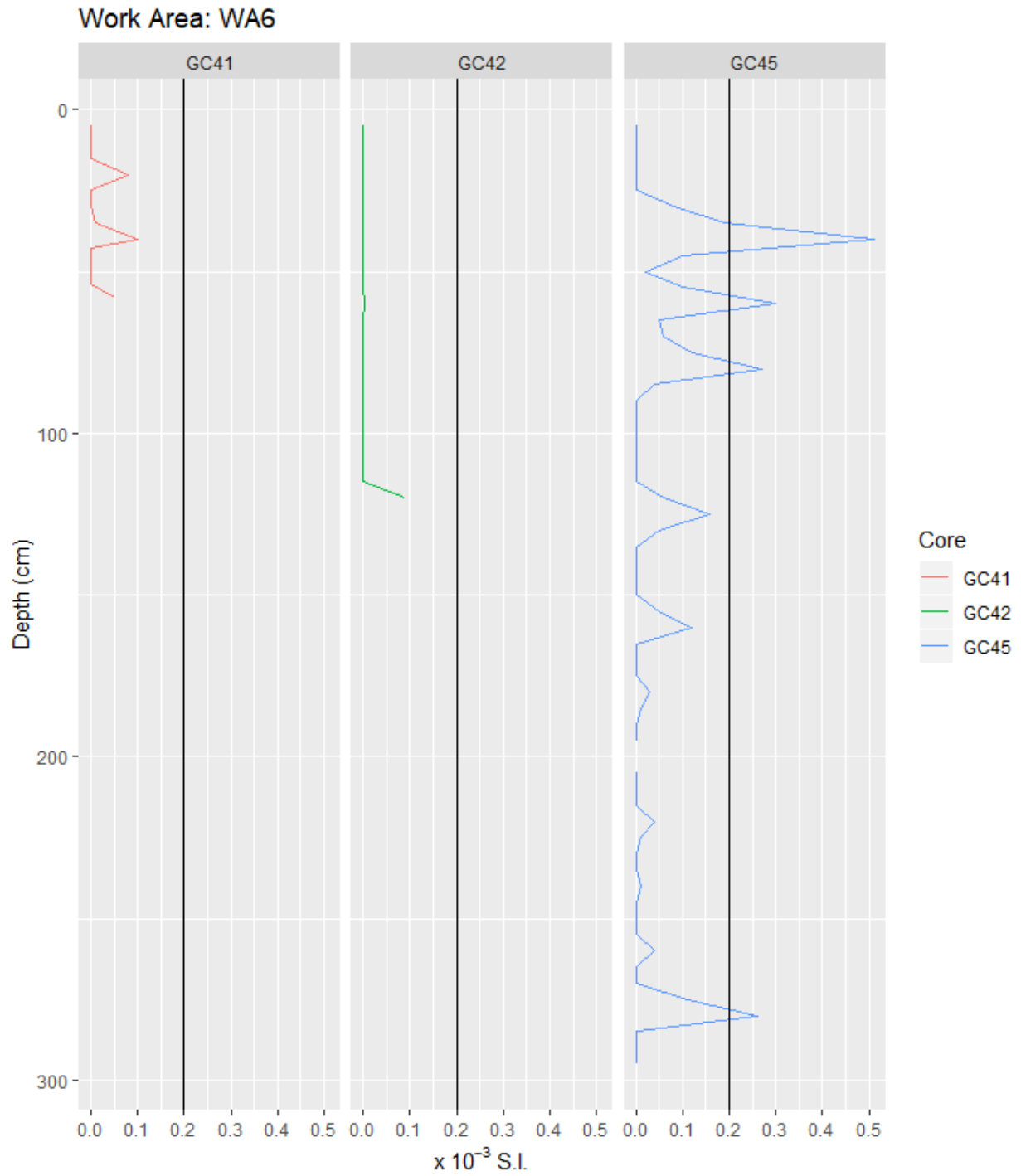
Fig. 12.3.81   Magnetic susceptibility for WA6. Intercept line at 0.2×10^{-3} S.I.
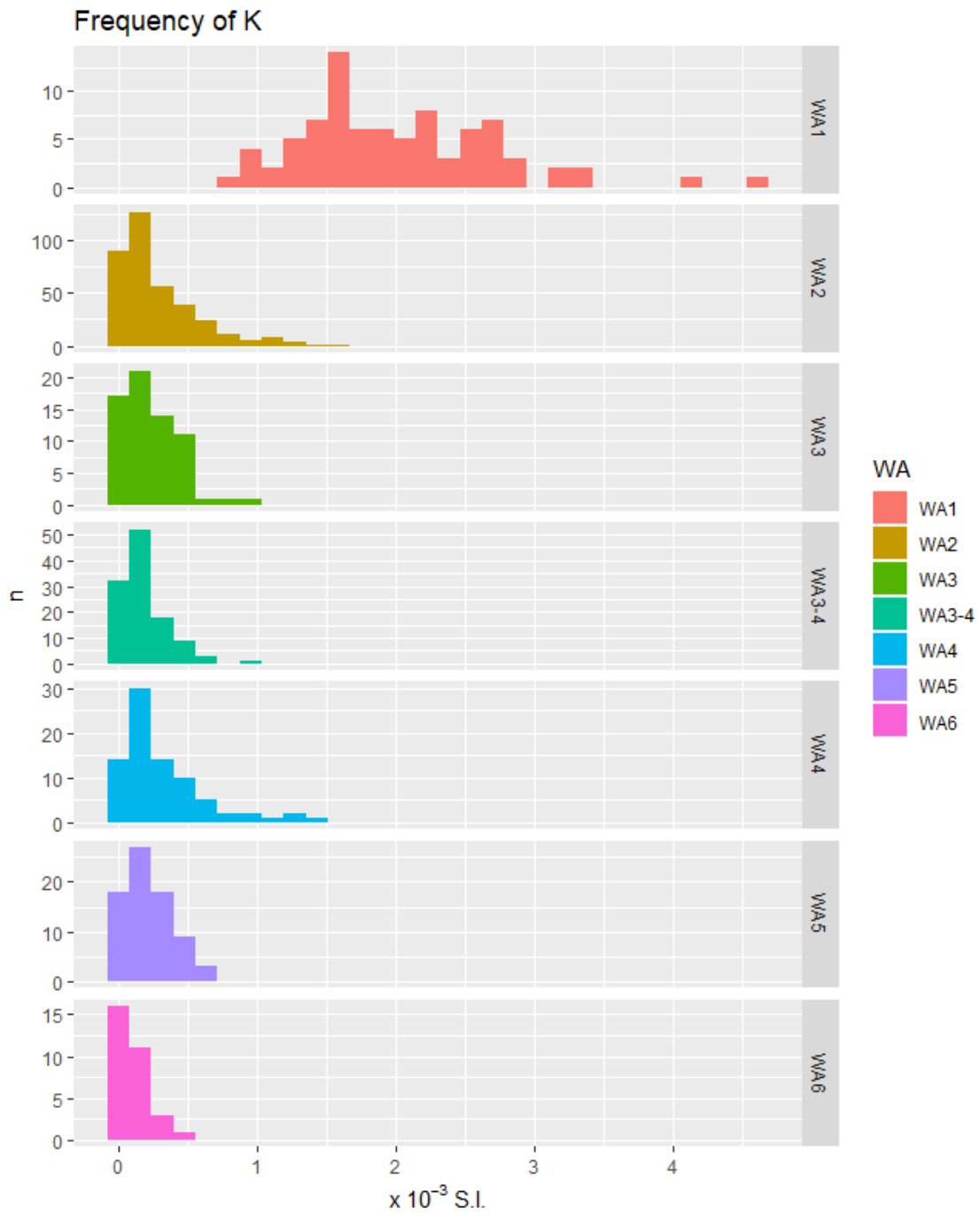
Fig. 12.3.82   Frequency (n) plot of susceptibility values for each work area.

Tab. 12.3.1 Simple descriptive statistics of the susceptibility data for each gravity core (GC)

GC Nº	n	mean	sd	median	min	max	range	skew	kurtosis
GC1	25	2,31	0,816	2,13	1,43	4,62	3,19	1,243	1,033
GC2	31	2,14	0,645	2,19	1,00	3,39	2,39	-0,006	-1,031
GC3	27	1,64	0,505	1,55	0,74	2,72	1,98	0,499	-0,390
GC4	26	0,24	0,343	0,02	0,00	1,16	1,16	1,220	0,181
GC5	27	0,23	0,251	0,18	0,00	0,86	0,86	0,815	-0,399
GC6	67	0,06	0,116	0,00	0,00	0,56	0,56	2,453	5,854
GC7	61	0,08	0,160	0,01	0,00	1,07	1,07	4,140	21,499
GC9	71	0,16	0,266	0,04	0,00	1,37	1,37	2,332	5,695
GC10	50	0,10	0,151	0,02	0,00	0,77	0,77	2,244	6,158
GC11	41	0,52	0,403	0,48	0,00	1,53	1,53	0,732	-0,372
GC13	47	0,16	0,138	0,15	0,00	0,54	0,54	0,814	0,122
GC14	65	0,13	0,196	0,01	0,00	0,90	0,90	1,949	3,709
GC18	51	0,14	0,181	0,02	0,00	0,53	0,53	0,803	-0,988
GC19	17	0,12	0,175	0,00	0,00	0,52	0,52	1,045	-0,457
GC20	46	0,16	0,200	0,10	0,00	0,75	0,75	1,290	0,767
GC22	54	0,23	0,356	0,10	0,00	1,49	1,49	1,971	3,268
GC23	20	0,18	0,308	0,02	0,00	1,00	1,00	1,797	1,976
GC26	88	0,07	0,130	0,00	0,00	0,70	0,70	2,319	5,920
GC27	53	0,14	0,193	0,06	0,00	0,93	0,93	1,960	4,395
GC28	80	0,07	0,133	0,00	0,00	0,64	0,64	2,267	5,078
GC30	45	0,19	0,279	0,06	0,00	1,22	1,22	1,991	3,801
GC31	47	0,24	0,301	0,11	0,00	1,13	1,13	1,231	0,550
GC32	56	0,21	0,270	0,08	0,00	1,06	1,06	1,550	1,772
GC33	31	0,13	0,206	0,00	0,00	0,74	0,74	1,712	2,023
GC34	23	0,14	0,168	0,00	0,00	0,43	0,43	0,520	-1,630
GC35	37	0,04	0,072	0,00	0,00	0,25	0,25	1,526	0,984
GC38	50	0,05	0,098	0,00	0,00	0,45	0,45	2,099	4,301
GC40	89	0,15	0,176	0,07	0,00	0,68	0,68	1,023	-0,022
GC41	12	0,02	0,036	0,00	0,00	0,10	0,10	1,240	-0,199
GC42	22	0,00	0,019	0,00	0,00	0,09	0,09	4,067	15,249
GC45	56	0,05	0,096	0,00	0,00	0,51	0,51	2,753	8,561

Tab. 12.3.2 Simple descriptive statistics of the susceptibility data for each work area (WA)

WA Nº	n	mean	sd	median	min	max	range	skew	kurtosis
WA1	83	2,03	0,712	1,90	0,74	4,62	3,88	0,921	1,299
WA2	592	0,18	0,264	0,06	0,00	1,53	1,53	2,103	4,710
WA3	116	0,13	0,189	0,02	0,00	0,90	0,90	1,519	1,982
WA3-4	258	0,08	0,143	0,00	0,00	0,93	0,93	2,504	7,739
WA4	137	0,19	0,285	0,07	0,00	1,49	1,49	2,233	5,359
WA5	139	0,11	0,159	0,02	0,00	0,68	0,68	1,400	1,086
WA6	90	0,03	0,079	0,00	0,00	0,51	0,51	3,490	14,646

12.4   Appendix 4 – Meiofauna samples

Tab. 12.4.1   Collected samples from gravity cores for meiofauna community identification, DNA and granulometry analysis.

Sample #	Date	Sample ID	Sampled Layer [cm]	DNA samples	Granulometry samples
1	07.03.2020	M-162-3, GC 1	0-3		
2	07.03.2020	M-162-3, GC 1	3.0-10.0		✓
3	07.03.2020	M-162-4, GC 2	0.0-1.0		✓
4	07.03.2020	M-162-4, GC 2	1.0-5.0		✓
5	07.03.2020	M-162-4, GC 2	>5		✓
6	07.03.2020	M-162-4, GC 2	superstitial water		
7	07.03.2020	M-162-5, GC 3	0-5+superst. water		✓
8	07.03.2020	M-162-5, GC 3	5.0-10.0		✓
9	07.03.2020	M-162-5, GC 3	10.0-20.0		✓
10	12.03.2020	M-162-15, GC 4	0-1		✓
11	12.03.2020	M-162-15, GC 4	1.0-4.0		✓
12	12.03.2020	M-162-15, GC 4	4.0-6.0		✓
13	12.03.2020	M-162-15, GC 4	6.0-10.0		✓
14	12.03.2020	M-162-16, GC 5	0-1		✓
15	12.03.2020	M-162-16, GC 5	1.0-4.0		✓
16	12.03.2020	M-162-16, GC 5	4.0-6.0		✓
17	12.03.2020	M-162-16, GC 5	6.0-10.0		✓
18	12.03.2020	M-162-17, GC 6	0-1		✓
19	12.03.2020	M-162-17, GC 6	1.0-4.0		✓
20	12.03.2020	M-162-17, GC 6	4.0-6.0		✓
21	12.03.2020	M-162-17, GC 6	6.0-10.0		✓
22	13.03.1920	M-162-19-GC 7	0-1	✓	✓
23	13.03.1920	M-162-19-GC 7	1.0-4.0		✓
24	13.03.1920	M-162-19-GC 7	4.0-6.0		✓
25	13.03.1920	M-162-19-GC 7	6.0-10.0		✓
26	13.03.1920	M-162-21-GC 9	0-1	✓	✓
27	13.03.1920	M-162-21-GC 9	1.0-4.0		✓
28	13.03.1920	M-162-21-GC 9	4.0-6.0		✓
29	13.03.1920	M-162-21-GC 9	6.0-10.0		✓
30	14.03.1920	M-162-23-GC 10	0-1	✓	✓
31	14.03.1920	M-162-23-GC 10	1.0-4.0		✓
32	14.03.1920	M-162-23-GC 10	4.0-6.0		✓
33	14.03.1920	M-162-23-GC 10	6.0-10.0		✓
34	16.03.1920	M-162-29-GC 11	0-1	✓	✓
35	16.03.1920	M-162-29-GC 11	1.0-4.0		✓
36	16.03.1920	M-162-29-GC 11	4.0-6.0		✓
37	16.03.1920	M-162-29-GC 11	6.0-10.0		✓
38	17.03.1920	M-162-32-GC 12	0-1	✓	✓
39	17.03.1920	M-162-32-GC 12	1.0-4.0		✓
40	17.03.1920	M-162-32-GC 12	4.0-6.0		✓
41	17.03.1920	M-162-32-GC 12	6.0-10.0		✓
42	17.03.1920	M-162-33-GC 13	0-1	✓	✓
43	17.03.1920	M-162-33-GC 13	1.0-4.0		✓
44	17.03.1920	M-162-33-GC 13	4.0-6.0		✓
45	17.03.1920	M-162-33-GC 13	6.0-8.0		✓
46	18.03.1920	M-162-35-GC 14	0-1	✓	✓

Sample #	Date	Sample ID	Sampled Layer [cm]	DNA samples	Granulometry samples
47	18.03.1920	M-162-35-GC 14	1.0-4.0		✓
48	18.03.1920	M-162-35-GC 14	4.0-6.0		✓
49	18.03.1920	M-162-35-GC 14	6.0-8.0		✓
50	18.03.1920	M-162-37-GC 15	0-1	✓	
51	18.03.1920	M-162-37-GC 15	1.0-4.0		✓
52	18.03.1920	M-162-37-GC 15	4.0-6.0		✓
53	18.03.1920	M-162-37-GC 15	6.0-8.0		
54	19.03.1920	M-162-41-GC 18	0-1	✓	
55	19.03.1920	M-162-41-GC 18	1.0-4.0		✓
56	19.03.1920	M-162-41-GC 18	4.0-6.0		✓
57	19.03.1920	M-162-41-GC 18	6.0-10		
58	20.03.2020	M-162-43-GC 19	0-1	✓	
59	20.03.2020	M-162-43-GC 19	1.0-4.0		✓
60	20.03.2020	M-162-43-GC 19	4.0-6.0		✓
61	20.03.2020	M-162-43-GC 19	6.0-10		
62	20.03.2020	M-162-40-GC 20	0-1		
63	20.03.2020	M-162-40-GC 20	1.0-4.0		✓
64	20.03.2020	M-162-40-GC 20	4.0-6.0		✓
65	20.03.2020	M-162-45-GC 21	0-1	✓	
66	20.03.2020	M-162-45-GC 21	1.0-4.0		✓
67	20.03.2020	M-162-45-GC 21	4.0-6.0		✓
68	21.03.1920	M-162-47-GC 22	0-1	✓	
69	21.03.1920	M-162-47-GC 22	1.0-4.0		✓
70	21.03.1920	M-162-47-GC 22	4.0-6.0		✓
71	21.03.1920	M-162-48-GC 23	0-1	✓	
72	21.03.1920	M-162-48-GC 23	1.0-4.0		✓
73	21.03.1920	M-162-48-GC 23	4.0-6.0		✓
74	24.03.1920	M-162-57-GC 26	0-1	✓	
75	24.03.1920	M-162-57-GC 26	1.0-4.0		✓
76	24.03.1920	M-162-57-GC 26	4.0-6.0		✓
77	24.03.1920	M-162-58-GC 27	0-1	✓	
78	24.03.1920	M-162-58-GC 27	1.0-4.0		✓
79	24.03.1920	M-162-58-GC 27	4.0-6.0		✓
80	25.03.1920	M-162-62-GC 28	0-1	✓	
81	25.03.1920	M-162-62-GC 28	1.0-4.0		✓
82	25.03.1920	M-162-62-GC 28	6.0-8.0		✓
83	27.03.1920	M-162-65-GC 30	0-1	✓	
84	27.03.1920	M-162-65-GC 30	1.0-4.0		
85	27.03.1920	M-162-65-GC 30	4.0-6.0		✓
86	27.03.1920	M-162-65-GC 30	6.0-10		✓
87	27.03.1920	M-162-66-GC 31	0-1	✓	
88	27.03.1920	M-162-66-GC 31	1.0-4.0		✓
89	27.03.1920	M-162-66-GC 31	4.0-6.0		✓
90	27.03.1920	M-162-67-GC 32	20.0-21.0	✓	✓
91	27.03.1920	M-162-67-GC 32	21.0-28.0		✓
92	28.03.2020	M-162-69-GC 33	0-1	✓	
93	28.03.2020	M-162-69-GC 33	1.0-4.0		
94	28.03.2020	M-162-69-GC 33	4.0-6.0		✓
95	28.03.2020	M-162-69-GC 33	6.0-8.0		✓
96	28.03.2020	M-162-70-GC 34	0-1	✓	
97	28.03.2020	M-162-70-GC 34	1.0-4.0		
98	28.03.2020	M-162-70-GC 34	4.0-6.0		✓
99	28.03.2020	M-162-70-GC 34	6.0-8.0		✓

Sample #	Date	Sample ID	Sampled Layer [cm]	DNA samples	Granulometry samples
100	29.03.1920	M-162-72-GC 35	0-1	✓	
101	29.03.1920	M-162-72-GC 35	1.0-4.0		
102	29.03.1920	M-162-72-GC 35	4.0-6.0		✓
103	29.03.1920	M-162-72-GC 35	6.0-8.0		✓
104	30.03.1920	M-162-76-GC 36	mixed		✓
105	30.03.1920	M-162-77-GC 37	0-1	✓	
106	30.03.1920	M-162-77-GC 37	1.0-4.0		✓
107	30.03.1920	M-162-77-GC 37	4.0-6.0		✓
108	01.04.1920	M-162-80-GC 39	0-1	✓	
109	01.04.1920	M-162-80-GC 39	1.0-4.0		
110	01.04.1920	M-162-80-GC 39	4.0-6.0		✓
111	01.04.1920	M-162-80-GC 39	6.0-10.0		✓
112	01.04.1920	M-162-82-GC 40	0-1	✓	
113	01.04.1920	M-162-82-GC 40	1.0-4.0		
114	01.04.1920	M-162-82-GC 40	4.0-6.0		✓
115	01.04.1920	M-162-82-GC 40	6.0-10.0		✓
116	03.04.1920	M-162-94-GC 45	0-1	✓	
117	03.04.1920	M-162-94-GC 45	1.0-4.0		
118	03.04.1920	M-162-94-GC 45	4.0-6.0		✓
119	03.04.1920	M-162-94-GC 45	8.0-10.0		✓
Total			**119**	**26**	**88**

Tab. 12.4.2 Collected samples from VMUCs for meiofauana community identification, DNA, pore water and granulometry analysis.

Date	Sample ID	Core N°	Sampled Layer [cm]	Sample type	Granulometry samples
08.03.2020	M-162, VMUC 1	1	0-3	meiofauna	
08.03.2020	M-162, VMUC 1	1	3.0-6.0	meiofauna	
08.03.2020	M-162, VMUC 1	1	6.0-10.0	meiofauna	✓
08.03.2020	M-162, VMUC 1	2	0-3	meiofauna	
08.03.2020	M-162, VMUC 1	2	3.0-6.0	meiofauna	
10.03.2020	M-162, VMUC 2	1	0-1	meiofauna, R1	
10.03.2020	M-162, VMUC 2	1	1.0-4.0	meiofauna, R1	
10.03.2020	M-162, VMUC 2	1	4.0-6.0	meiofauna, R1	
10.03.2020	M-162, VMUC 2	1	0-1	meiofauna, R2	
10.03.2020	M-162, VMUC 2	1	1.0-4.0	meiofauna, R2	
10.03.2020	M-162, VMUC 2	1	4.0-6.0	meiofauna, R2	
10.03.2020	M-162, VMUC 2	1	0-1	meiofauna, R3	✓
10.03.2020	M-162, VMUC 2	1	1.0-4.0	meiofauna, R3	✓
10.03.2020	M-162, VMUC 2	1	4.0-6.0	meiofauna, R3	✓
10.03.2020	M-162, VMUC 2	2	0-1	DNA	
10.03.2020	M-162, VMUC 2	2	1.0-4.0	DNA	
10.03.2020	M-162, VMUC 2	2	4.0-6.0	DNA	
10.03.2020	M-162, VMUC 2	2	0-1	O_2-conc.	
10.03.2020	M-162, VMUC 2	2	1.0-4.0	O_2-conc.	
10.03.2020	M-162, VMUC 2	2	4.0-6.0	O_2-conc.	
10.03.2020	M-162, VMUC 2	2	0-1	fatty acids (PW)	
10.03.2020	M-162, VMUC 2	2	1.0-4.0	fatty acids (PW)	
10.03.2020	M-162, VMUC 2	2	4.0-6.0	fatty acids (PW)	
02.04.2020	M-162, VMUC 3	1	0-1	meiofauna	
02.04.2020	M-162, VMUC 3	1	1.0-4.0	meiofauna	
02.04.2020	M-162, VMUC 3	1	4.0-10.0	meiofauna	
02.04.2020	M-162, VMUC 3	1	0-1	DNA	
02.04.2020	M-162, VMUC 3	1	1.0-4.0	DNA	
02.04.2020	M-162, VMUC 3	1	4.0-10.0	DNA	
02.04.2020	M-162, VMUC 3	2	1	O_2-conc.	
02.04.2020	M-162, VMUC 3	2	3	O_2-conc.	
02.04.2020	M-162, VMUC 3	2	5	O_2-conc.	
02.04.2020	M-162, VMUC 3	2	7	O_2-conc.	
02.04.2020	M-162, VMUC 3	2	1	fatty acids, meth.	
02.04.2020	M-162, VMUC 3	2	3	fatty acids (PW)	
02.04.2020	M-162, VMUC 3	2	5	fatty acids (PW)	
02.04.2020	M-162, VMUC 3	2	7	fatty acids (PW)	
02.04.2020	M-162, VMUC 3	2	0-1	meiofauna	✓
02.04.2020	M-162, VMUC 3	2	1.0-4.0	meiofauna	✓
02.04.2020	M-162, VMUC 3	2	4.0-6.0	meiofauna	✓
02.04.2020	M-162, VMUC 3	2	6.0-10.0	meiofauna	✓
02.04.2020	M-162, VMUC 3	2	0-1	DNA	
02.04.2020	M-162, VMUC 3	2	1.0-4.0	DNA	
02.04.2020	M-162, VMUC 3	2	4.0-6.0	DNA	
02.04.2020	M-162, VMUC 3	2	6.0-10.0	DNA	
02.04.2020	M-162, VMUC 3	3	0-1	meiofauna	
02.04.2020	M-162, VMUC 3	3	1.0-4.0	meiofauna	
02.04.2020	M-162, VMUC 3	3	0-1	DNA	
02.04.2020	M-162, VMUC 3	3	1.0-4.0	DNA	
Total meiofauna				**23**	

Tab. 12.4.3   Collected samples for meiofauna identification and DNA at ancient layers.

Date	Station ID	Core number	Layer [cm]	Baseline for sampling	DNA
29.03.2020	M-162-67	32	93-193	123-133 cm	✔
29.03.2020	M-162-67	35	93-193	117-121	✔
29.03.2020	M-162-23	10	173-273	197	✔
29.03.2020	M-162-23	10	173-273	203	✔
29.03.2020	M-162-44	20	43-143	104-113	✔

12.5   Appendix 5 – Pore water oxygen measurements

Tab. 12.5.1 Oxygen concentrations.

Core	Depth [cmbsf]	O2 [µM]
GC01	10	9.51
GC01	30	10
GC01	60	9.3
GC01	100	9.1
GC01	130	10.68
GC02	41	11.4
GC02	83	10.6
GC02	123	10.3
GC02	133	10.93
GC03	20	#N/A
GC03	50	#N/A
GC03	60	#N/A
GC03	90	#N/A
GC03	120	#N/A
GC04	20	275.4
GC04	30	275.9
GC04	50	274.9
GC04	76	163.8
GC04	96	283.5
GC04	116	227.4
GC04	136	261.23
GC05	15	195.63
GC05	30	261.06
GC05	50	255.07
GC05	70	70.25
GC05	90	90.84
GC05	110	110.37
GC05	130	146.59
GC06	10	312.59
GC06	30	204.6
GC06	50	133.36
GC06	70	98.19
GC06	90	
GC06	110	20.1
GC06	130	12.1
GC06	150	0
GC06	170	0
GC06	190	0
GC06	210	0
GC06	230	0
GC06	250	0
GC06	270	0
GC06	290	0
GC06	310	0

Core	Depth [cmbsf]	O2 [µM]
GC06	330	0
GC06	350	0
GC07	10	337.4
GC07	30	166.1
GC07	45	122.9
GC07	73	#N/A
GC07	93	42
GC07	113	14.7
GC07	133	1
GC07	173	#N/A
GC07	193	0
GC07	213	0
GC07	233	#N/A
GC07	273	#N/A
GC07	293	0
GC07	313	0
GC07	333	0
GC09	20	332.4
GC09	40	221.4
GC09	60	199.1
GC09	70	129.4
GC09	102	300.16
GC09	122	171.1
GC09	142	130.1
GC09	162	85.7
GC09	202	214.3
GC09	222	128.36
GC09	242	167.52
GC09	262	226.3
GC09	302	169.6
GC09	322	160.75
GC09	342	166.67
GC09	362	143.97
GC10	20	198.1
GC10	40	128.3
GC10	60	82.2
GC10	83	42.25
GC10	103	33.32
GC10	123	0
GC10	143	0
GC10	163	0
GC10	193	0
GC10	213	127
GC10	233	43.3
GC10	253	44.36
GC11	10	281
GC11	20	197.14
GC11	37	256.6

Core	Depth [cmbsf]	O2 [µM]	Core	Depth [cmbsf]	O2 [µM]
GC11	57	193.8	GC20	133	117.4
GC11	77	184.9	GC20	153	86.59
GC11	97	172.8	GC20	173	67.75
GC11	117	210.9	GC20	193	48.52
GC11	137	235.4	GC20	213	36.45
GC11	157	171.7	GC20	228	31.06
GC11	177	156.8	GC22	10	375.31
GC11	197	226.24	GC22	30	152.39
GC11	217	155.4	GC22	50	129.61
GC14	10	265	GC22	70	77.61
GC14	20	202.16	GC22	91	65.53
GC14	30	150.5	GC22	111	54.5
GC14	40	103.1	GC22	131	39.76
GC14	60	53.25	GC22	151	31.1
GC14	80	28.6	GC22	166	87.7
GC14	100	38.89	GC22	191	80.41
GC14	120	0	GC22	211	54.67
GC14	140	0	GC22	231	61.8
GC14	170	0	GC22	251	65.7
GC14	190	0	GC22	261	80.99
GC14	210	0	GC22	268	36
GC14	230	0	GC23	10	228.58
GC14	270	0	GC23	30	180.22
GC14	290	0	GC23	50	124.33
GC14	310	0	GC23	70	114.12
GC14	330	0	GC23	85	124.18
GC15	10	402.6	GC23	90	117.25
GC15	20	272.6	GC23	100	110.52
GC15	30	159.37	GC26	10	209.85
GC15	40	120.14	GC26	20	170.19
GC15	50	102.9	GC26	30	116.98
GC15	77	127.6	GC26	38	96.89
GC15	97	71.19	GC26	59	80.46
GC15	117	101.05	GC26	79	51.04
GC15	137	13.28	GC26	99	36.67
GC15	152	7.08	GC26	119	15.43
GC15	177	4.25	GC26	134	12.06
GC15	197	2.05	GC26	159	21.01
GC15	217	4.35	GC26	179	13.35
GC15	237	45.56	GC26	199	31.35
GC20	10	185.22	GC26	219	52.18
GC20	29	136.1	GC26	239	9.59
GC20	53	85.5	GC26	259	12.68
GC20	73	76.9	GC26	279	16.22
GC20	93	51.02	GC26	299	20.48
GC20	113	156.53	GC26	319	10.41
GC20	123	158	GC26	339	2.49

Core	Depth [cmbsf]	O2 [µM]	Core	Depth [cmbsf]	O2 [µM]
GC26	359	11.47	GC30	196	0
GC26	379	11.21	GC30	216	0
GC26	399	43	GC30	236	0
GC26	419	18.5	GC31	20	168.65
GC27	10	199.52	GC31	40	100.73
GC27	30	135.38	GC31	61	81.14
GC27	60	86.17	GC31	81	66.38
GC27	86	87.35	GC31	101	105.25
GC27	106	56.38	GC31	121	74.45
GC27	126	39.81	GC31	141	57.65
GC27	146	28.56	GC31	161	48.31
GC27	166	19.13	GC31	181	52.29
GC27	186	16.22	GC31	201	33.31
GC27	206	30.76	GC31	221	146.13
GC27	226	14.71	GC31	241	122.25
GC27	246	41.1	GC32	10	107.47
GC27	266	24.4	GC32	30	58.02
GC28	12	184.13	GC32	50	36.25
GC28	33	102.64	GC32	70	24.19
GC28	43	71.74	GC32	85	22.33
GC28	53	46.76	GC32	103	29.47
GC28	63	33.53	GC32	123	5.81
GC28	73	25.51	GC32	143	112.6
GC28	93	15.21	GC32	163	80.16
GC28	113	5.33	GC32	183	52.35
GC28	133	0	GC32	203	24.42
GC28	153	0	GC32	223	12.1
GC28	173	0	GC32	243	9.44
GC28	193	0	GC32	263	5.45
GC28	213	0	GC32	283	10.48
GC28	233	0	GC33	10	270.18
GC28	253	0	GC33	30	115.39
GC28	273	0	GC33	50	81.61
GC28	293	0	GC33	73	47.5
GC28	313	0	GC33	93	28.14
GC28	333	0	GC33	113	20.48
GC28	353	0	GC33	133	54.21
GC28	373	0	GC33	153	20.14
GC28	393	0	GC34	15	231.62
GC28	413	0	GC34	41	119.11
GC30	25	120.34	GC34	61	94.46
GC30	56	62.35	GC34	81	75.67
GC30	76	46.31	GC34	101	64.38
GC30	96	28.14	GC34	121	120
GC30	116	22.39	GC35	10	190.18
GC30	136	0	GC35	30	138.46
GC30	156	0	GC35	50	114.32
GC30	176	0	GC35	70	100.66

Core	Depth [cmbsf]	O2 [µM]	Core	Depth [cmbsf]	O2 [µM]
GC35	80	89.17	GC40	334	0
GC35	103	79.41	GC40	354	0
GC35	123	135.18	GC40	374	0
GC35	143	116.54	GC40	394	0
GC35	163	97.5	GC40	414	0
GC35	183	108.51	GC40	434	0
GC37	10	254.19	GC40	454	0
GC37	30	211.87	GC40	474	0
GC37	51	178.3	GC42	15	109.38
GC37	71	193.53	GC42	35	10.29
GC37	91	175.64	GC42	41	0
GC37	111	181.17	GC42	46	0
GC37	126	169.89	GC42	56	30
GC38	20	282.5	GC42	71	19.36
GC38	40	136.23	GC42	86	0
GC38	55	91.17	GC42	101	0
GC38	80	52.55	GC42	116	0
GC38	100	35.55	GC43	5	149.47
GC38	120	20.37	GC43	10	97.1
GC38	140	13.4	GC43	13	56.49
GC38	160	9.81	GC43	18	30.53
GC38	180	5.26	GC43	22	20.51
GC38	200	2.36	GC43	26	17.34
GC38	220	8.46	GC43	30	8.51
GC38	240	1.99	GC43	35	0
GC38	260	5.05	GC43	45	0
GC39	20	245.33	GC43	65	13.55
GC39	35	214.85	GC43	68	8.55
GC39	50	185.37	GC43	74	7.36
GC40	20	205.1	GC43	80	0
GC40	30	140.5	GC43	90	0
GC40	40	109.29	GC43	108	0
GC40	50	88.44	GC43	117	0
GC40	60	73	GC45	10	130.01
GC40	70	55.2	GC45	30	91.55
GC40	94	35.12	GC45	50	62.32
GC40	114	18.37	GC45	70	43.82
GC40	134	10.93	GC45	90	31.64
GC40	154	8.33	GC45	110	25.23
GC40	174	4.63	GC45	130	14.34
GC40	194	2.16	GC45	150	22.03
GC40	214	2.45	GC45	170	12.21
GC40	234	1.93	GC45	190	16.37
GC40	254	1.64	GC45	210	14.5
GC40	274	3.11	GC45	230	14.67
GC40	294	2.5	GC45	250	12.52
GC40	314	0.5	GC45	270	10.59

Core	Depth [cmbsf]	O2 [µM]
GC45	290	8.76
VMUC02	0.5	281.9
VMUC02	1.5	260
VMUC02	2	255.11
VMUC02	4	161.56
VMUC02	5	232.37
VMUC02	5.5	217.03
VMUC02	6	220.1
VMUC03	1	261.17
VMUC03	3	178.56
VMUC03	5	132.18
VMUC03	7	107.31

12.6   Appendix 6 – Pore water and sediment samples for geochemical analyses

Tab. 12.6.1   Collected pore water samples for geochemical analyses.

Station	Device	#	Samples	Noble gas samples	H₂S	PO₄³⁻	H₄SiO₄	NH₄⁺	TA	Cl⁻	SO₄²⁻	Br⁻	δ¹³C	δ¹⁸O/δD	ICP	DIC	IC	CH₄-C₅H₁₂	δ¹³C (CH₄)	Rn	Squeeze cakes	Physical properties
									Parameter measured onboard						Subsamples							
3	GC	1	16	-	-	x	x	x	x	x	x	x	x	x	x	x	x	x	x	-	x	x
4	GC	2	15	-	-	x	x	x	x	x	x	x	x	x	x	x	x	x	x	x	x	x
5	GC	3	11	-	-	x	x	x	x	x	x	x	x	x	x	x	x	x	x	x	x	x
10	VMUC	2	9/5[1]	-	-	x	x	x	x	x	x	x	x	x	x	x	x	x	x	x	x	x
15	GC	4	12	-	-	x	x	x	x	x	x	x	x	x	x	x	x	x	x	x	x	x
16	GC	5	13	-	-	x	x	x	x	x	x	x	x	x	x	x	x	x	x	x	x	x
17	GC	6	26	-	-	x	x	x	x	x	x	x	x	x	x	x	x	x	x	x	x	x
19	GC	7	21/21[1]	-	-	x	x	x	x	x	x	x	x	x	x	x	x	x	x	x	x	x
20	GC	8	4	7	-	x	x	x	x	x	x	x	x	x	x	x	x	x	x	x	x	x
21	GC	9	19	-	-	x	x	x	x	x	x	x	x	x	x	x	x	x	x	x	x	x
23	GC	10	19	-	-	x	x	x	x	x	x	x	x	x	x	x	x	x	x	x	x	x
29	GC	11	14	-	-	x	x	x	x	x	x	x	x	x	x	x	x	x	x	x	x	x
33	GC	13	13	-	-	x	x	x	x	x	x	x	x	x	x	x	x	x	x	x	x	x
35	GC	14	21	-	-	x	x	x	x	x	x	x	x	x	x	x	x	x	x	x	x	x
36	GC	15	16	-	-	x	x	x	x	x	x	x	x	x	x	x	x	x	x	x	x	x
41	GC	18	1	-	-	x	x	x	x	x	x	x	x	x	x	x	x	x	x	x	x	x
43	GC	19	9	-	-	x	x	x	x	x	x	x	x	x	x	x	x	x	x	x	x	x
44	GC	20	13	-	-	x	x	x	x	x	x	x	x	x	x	x	x	x	x	x	x	x
45	GC	21	2	-	-	x	x	x	x	x	x	x	x	x	x	x	x	x	x	x	x	x
47	GC	22	17	-	-	x	x	x	x	x	x	x	x	x	x	x	x	x	x	x	x	x
48	GC	23	7	-	-	x	x	x	x	x	x	x	x	x	x	x	x	x	x	x	x	x
57	GC	26	24/5[1]	-	-	x	x	x	x	x	x	x	x	x	x	x	x	x	x	x	x	x
58	GC	27	14	-	-	x	x	x	x	x	x	x	x	x	x	x	x	x	x	x	x	x
62	GC	28	22/10[1]	-	-	x	x	x	x	x	x	x	x	x	x	x	x	x	x	x	x	x
64	GC	29	6	9	-	x	x	x	x	x	x	x	x	x	x	x	x	x	x	x	x	x
65	GC	30	13/9[1]	-	-	x	x	x	x	x	x	x	x	x	x	x	x	x	x	x	x	x
66	GC	31	13/7[1]	-	-	x	x	x	x	x	x	x	x	x	x	x	x	x	x	x	x	x
67	GC	32	15	-	-	x	x	x	x	x	x	x	x	x	x	x	x	x	x	x	x	x
69	GC	33	10	-	-	x	x	x	x	x	x	x	x	x	x	x	x	x	x	x	x	x
70	GC	34	9	-	-	x	x	x	x	x	x	x	x	x	x	x	x	x	x	x	x	x
72	GC	35	12	-	-	x	x	x	x	x	x	x	x	x	x	x	x	x	x	x	x	x
76	GC	36	2	-	-	-	x	x	x	x	x	x	x	x	x	x	x	x	x	x	x	x
77	GC	37	10	-	-	-	x	x	x	x	x	x	x	x	x	x	x	x	x	x	x	x
78	GC	38	14	-	-	-	x	x	x	x	x	x	x	x	x	x	x	x	x	x	x	x
80	GC	39	6	-	-	-	x	x	x	x	x	x	x	x	x	x	x	x	x	x	x	x
82	GC	40	24/12[1]	-	-	-	x	x	x	x	x	x	x	x	x	x	x	x	x	x	x	x
82	VMUC	3	11	-	-	-	x	x	x	x	x	x	x	x	x	x	x	x	x	x	x	x
90	GC	42	11/7[1]	-	-	-	x	x	x	x	x	x	x	x	x	x	x	x	x	x	x	x
91	GC	43	11/9[1]	-	-	-	x	x	x	x	x	x	x	x	x	x	x	x	x	x	x	x
92	GC	44	2	4	-	-	x	x	x	x	x	x	x	x	x	x	x	x	x	x	x	x
94	GC	45	16	-	-	-	x	x	x	x	x	x	x	x	x	x	x	x	x	x	x	x

Tab. 12.6.2 Sediment samples for adsorbed hydrocarbon gas analyses and lipid biomarker studies.

Station	Device	#	Noble gas samples	Adsorbed Gas samples		Biomarker samples	Microbiology				
				CH_4-C_5H_{12}	$\delta^{13}C$ (CH_4-C_5H_{12})		DNA	Microbial Activity	DNA Backup	H_2 Incubation	H_2 Extraction
3	GC	1	-	3	3	8	4	16	2	4	4
4	GC	2	-	4	4	-	4	16	2	4	4
5	GC	3	-	3	3	8	4	16	2	4	4
10	VMUC	2	-	-	-	-	12	24	6	12	12
15	GC	4	-	3	3	9	4	-	-	4	4
16	GC	5	-	3	3	9	4	16	2	4	4
17	GC	6	-	10	10	23	8	32	4	8	8
19	GC	7	-	10	10	23	8	32	4	8	8
20	GC	8	7	4	4	-	-	-	-	-	-
21	GC	9	-	6	6	-	8	-	4	-	-
23	GC	10	-	4	4	12	6	24	3	6	6
29	GC	11	-	3	3	-	6	24	3	6	6
33	GC	13	-	3	3	-	4	16	2	4	4
35	GC	14	-	4	4	28	8	32	4	8	8
36	GC	15	-	3	3	16	6	24	3	6	6
41	GC	18	-	1	1	-	-	-	-	-	-
43	GC	19	-	2	2	-	-	-	-	-	-
44	GC	20	-	3	3	11	6	24	3	6	6
45	GC	21	-	2	2	-	-	-	-	-	-
47	GC	22	-	3	3	20	6	24	3	6	6
48	GC	23	-	1	1	6	-	-	-	-	-
57	GC	26	-	5	5	25	10	40	5	10	10
58	GC	27	-	3	3	13	6	24	3	6	6
62	GC	28	-	5	5	26	10	40	5	10	10
64	GC	29	9	-	-	6	-	-	-	-	18
65	GC	30	-	3	3	6	6	24	3	6	-
66	GC	31	-	3	3	-	6	24	3	6	-
67	GC	32	-	3	3	-	6	24	3	6	-
69	GC	33	-	2	2	7	4	16	2	4	-
70	GC	34	-	2	2	-	4	-	2	-	-
72	GC	35	-	2	2	-	4	16	2	4	-
76	GC	36	5	2	2	-	-	-	-	-	-
77	GC	37	-	2	2	15	4	16	2	4	-
78	GC	38	-	3	3	12	6	24	3	6	-
80	GC	39	-	1	1	-	2	-	1	-	-
82	GC	40	-	5	5	41	10	40	5	10	-
82	VMUC	3	-	-	-	-	10	-	-	-	-
90	GC	42	-	2	2	11	4	16	2	4	-
91	GC	43	-	2	2	-	4	16	2	4	-
92	GC	44	5	-	-	8	-	-	-	-	-
94	GC	45	-	3	3	18	6	24	3	6	-

12.7   Appendix 7 – Heat flow measurements

Tab. 12.7.1 Heat flow sites and data.

ID	Latitude DD MM.MMM	Longitude DD MM.MMM	Temp. Gradient [mK/m]	TC [W/Km]
HF2001P01	37 58.884	-26 04.218	NaN	1.230
HF2001P02	37 58.722	-26 04.452	NaN	1.230
HF2001P03	37 58.560	-26 04.704	94.35	1.228
HF2001P04	37 58.416	-26 04.944	NaN	1.230
HF2001P05	37 58.254	-26 05.178	112.66	1.230
HF2001P06	37 58.092	-26 05.418	NaN	1.230
HF2001P07	37 57.990	-26 05.586	NaN	1.230
HF2001P08	37 57.834	-26 05.796	NaN	1.230
HF2001P09	37 57.690	-26 06.042	NaN	1.230
HF2001P10	37 57.366	-26 06.498	NaN	1.230
HF2002P01	37 04.383	-21 18.727	NaN	1.000
HF2002P02	37 04.755	-21 18.735	113.55	1.000
HF2002P03	37 05.188	-21 18.783	92.41	0.976
HF2002P04	37 05.905	-21 18.826	96.86	1.020
HF2002P05	37 06.710	-21 18.874	92.08	1.000
HF2002P06	37 07.271	-21 18.935	119.57	1.221
HF2002P07	37 08.141	-21 18.989	NaN	1.000
HF2002P08	37 09.673	-21 19.168	NaN	1.000
HF2003P01	37 20.952	-21 20.326	NaN	1.340
HF2004P01	37 20.838	-21 20.260	NaN	0.900
HF2004P02	37 20.212	-21 20.245	NaN	0.900
HF2004P03	37 19.791	-21 20.207	88.60	1.360
HF2004P04	37 19.375	-21 20.178	NaN	0.900
HF2004P05	37 18.971	-21 20.146	49.07	1.335
HF2004P06	37 18.415	-21 20.085	NaN	0.900
HF2004P07	37 18.030	-21 20.331	NaN	0.900
HF2005P01	36 59.108	-21 18.082	99.84	1.000
HF2005P02	37 00.146	-21 18.218	NaN	1.000
HF2005P03	37 00.460	-21 18.263	NaN	1.000
HF2005P04	37 00.790	-21 18.320	76.36	1.000
HF2005P05	37 01.338	-21 18.391	137.76	1.000
HF2005P06	37 01.913	-21 18.466	66.26	1.000
HF2005P07	37 04.435	-21 18.720	99.31	1.011
HF2006P01	37 09.763	-21 19.243	53.96	1.135
HF2006P02	37 10.568	-21 19.332	NaN	1.130
HF2006P03	37 11.697	-21 19.443	199.72	1.130
HF2007P01	36 53.699	-23 40.868	61.69	1.120
HF2007P02	36 53.935	-23 40.925	82.73	1.100
HF2007P03	36 54.177	-23 40.982	78.40	1.029
HF2007P04	36 54.479	-23 41.042	NaN	1.100
HF2007P05	36 54.727	-23 41.113	NaN	1.100
HF2007P06	36 55.023	-23 41.171	NaN	1.100
HF2007P07	36 55.323	-23 41.230	NaN	1.100
HF2008P01	37 09.025	-20 21.932	66.22	1.021
HF2008P02	37 09.2803	-20 21.897	71.21	1.020
HF2008P03	37 09.535	-20 21.853	67.22	1.020
HF2008P04	37 09.772	-20 21.812	70.03	1.066
HF2008P05	37 10.032	-20 21.779	71.39	1.020
HF2008P06	37 10.303	-20 21.738	67.14	1.020
HF2008P07	37 10.548	-20 21.704	64.59	1.063
HF2008P08	37 10.809	-20 21.658	70.25	1.020
HF2008P09	37 11.060	-20 21.621	67.69	1.020

ID	Latitude DD MM.MMM	Longitude DD MM.MMM	Temp. Gradient [mK/m]	TC [W/Km]
HF2008P10	37 11.323	-20 21.580	57.79	1.020
HF2008P11	37 11.566	-20 21.545	64.43	1.020
HF2008P12	37 11.823	-20 21.503	56.93	1.020
HF2009P01	37 35.208	-20 29.596	43.73	1.019
HF2009P02	37 35.441	-20 29.584	56.88	1.020
HF2009P03	37 35.671	-20 29.585	76.81	1.189
HF2009P04	37 35.758	-20 29.560	77.42	1.020
HF2009P05	37 35.851	-20 29.578	65.75	1.020
HF2009P08	37 36.631	-20 29.560	71.64	1.020
HF2010P01	37 32.220	-18 38.651	69.23	1.412
HF2010P02	37 31.914	-18 38.698	50.71	1.100
HF2010P03	37 31.673	-18 38.818	69.20	1.177
HF2010P04	37 31.441	-18 38.881	53.47	1.100
HF2010P05	37 31.200	-18 39.005	61.26	1.109
HF2010P06	37 30.898	-18 39.141	50.90	1.100
HF2010P07	37 30.659	-18 39.188	88.74	1.100
HF2010P08	37 30.415	-18 39.307	85.60	1.100
HF2010P09	37 30.116	-18 39.426	NaN	1.100
HF2010P10	37 29.994	-18 39.488	NaN	1.100
HF2011P01	36 52.553	-21 17.190	26.53	1.141
HF2011P02	36 52.799	-21 17.223	NaN	1.100
HF2011P03	36 53.045	-21 17.256	NaN	1.100
HF2011P04	36 53.316	-21 17.292	NaN	1.100
HF2011P05	36 53.558	-21 17.323	NaN	1.100
HF2011P06	36 53.814	-21 17.357	49.71	1.229
HF2011P07	36 54.053	-21 17.391	40.23	1.100
HF2011P08	36 54.301	-21 17.426	NaN	1.100
HF2011P09	36 54.545	-21 17.459	69.22	1.100
HF2011P11	36 55.021	-21 17.525	NaN	1.100
HF2011P12	36 55.517	-21 17.590	NaN	1.100
HF2011P13	36 55.790	-21 17.627	83.97	1.100
HF2012P01	37 04.752	-21 18.345	65.21	1.045
HF2012P02	37 04.605	-21 17.988	NaN	0.900
HF2012P03	37 04.678	-21 17.927	NaN	0.900
HF2012P04	37 04.677	-21 17.268	373.54	0.900
HF2013P01	37 27.794	-18 25.671	108.93	1.333
HF2013P02	37 27.814	-18 25.351	73.96	1.034
HF2013P03	37 27.813	-18 25.016	82.23	1.043
HF2014P01	37 28.187	-16 00.452	72.34	1.076
HF2014P02	37 28.247	-16 00.842	66.45	1.229
HF2014P03	37 28.317	-16 01.244	76.76	1.100
HF2015P01	37 22.742	-15 35.884	24.96	1.260
HF2015P02	37 23.003	-15 35.861	81.00	0.889
HF2015P03	37 23.169	-15 35.807	85.35	1.100
HF2016P01	37 14.551	-14 55.344	NaN	0.900
HF2016P02	37 14.747	-14 55.894	NaN	0.900
HF2016P03	37 14.952	-14 56.497	NaN	0.900
HF2016P04	37 15.169	-14 57.138	NaN	0.900
HF2017P01	37 30.309	-14 55.094	60.72	1.154
HF2017P02	37 30.212	-14 55.113	60.38	1.150
HF2017P03	37 30.097	-14 55.129	52.73	1.144
HF2017P04	37 29.972	-14 55.149	53.74	1.150
HF2017P05	37 29.863	-14 55.158	61.16	1.150
HF2017P06	37 29.749	-14 55.178	59.64	1.178